INTERFACIAL AND TRANSPORT PHENOMENA IN CLOSED-CELL FOAMS

A Thesis

Submitted to the Faculty

of

Purdue University

by

Laurent Pilon

In Partial Fulfillment of the

Requirements for the Degree

of

Doctor of Philosophy

December 2002

Imagination is more important than Knowledge.

Albert Einstein

ACKNOWLEDGMENTS

During the completion of my doctoral work, I have had the chance, pleasure and honor to work, meet, and live with wonderful people who made undelible marks in my intellectual and personal life.

I am, first of all, all indebted to my advisor Professor Raymond Viskanta for the freedom, constant support, and encouragements he gave me through out the completion of my doctoral work. His extensive knowledge, professionalism, ethic, availability, patience, and kindness will always be a source of inspiration and an example. I would like to thank my academic brother and dear friend Professor Andrei Fedorov who convinced me to start studying for the doctorate while he was a post-doctoral scientist in the Heat Transfer Laboratory at Purdue. I cannot acknowledge these two men without thanking their wives Birute (Barbara) Viskanta and Lena Polovnikova for their kindness and constant encouragements. The working and affectionate environment in which I had the privilege to evolve is beyond what a graduate student could dream of. I found more than a stimulating professional environment, I found a Family.

I am grateful to Professor Doraiswami Ramkrishna for introducing me to population balance theory with patience and kindness and for always being available and prompt to discuss my research and answer my questions. I would like to express my gratitude to Professor Jay Gore and Professor Ganesan Narsimhan for their constructive comments and assistance during the course of my research work and for serving in my PhD examining committee. The assistance of Professors Jayathi Murthy and Joe D. Hoffman in my numerical work is greatly appreciated. I also want to thank Professor Lefteri Tsoukalas for his support and encouragement.

I would like to express my gratitude to Dr. Dominique Baillis and Professor Jean-François Sacadura from the Center for Thermal Sciences of Lyon, France (Centre

Thermique de Lyon) for welcoming me in their laboratory to perform measurements of radiation characteristics of fused quartz containing bubbles. I thank very much their graduate student Jaona Randrianalisoa.

I wish to acknowledge the Department of Thermal-Hydraulics and Physics of the French Atomic Energy Commission (CEA) for giving me the opportunity to come and work at Purdue as part of my French national service. Partial financial support from the Department of Energy - Office of Energy Efficiency and Renewable Energy through Argonne National Laboratory during the three years of my doctoral work is especially acknowledged with thanks. Engineers and researchers from Osram Sylvania, Techneglas, and Owens Corning provided the glass samples as well as helpful criticisms and feedbacks. I would also like to thank the member of the staff at Purdue and in particular John Pirolo from the Purdue Glass Laboratory for sharing his expertise on glass and for letting me use his laboratory equipments, Fran Beard for her everyday cheerfulness and helpfulness, the staff of the School of Mechanical Engineering for their assistance and their professionalism. My appreciation is also extended to my fellow graduate students in the Heat Transfer Laboratory, and to my dear friend Rafael Gomez for helping me with the preparation of the quartz samples and many other aspects of my research.

My life over the last three years consisted of many encounters with fellow students from all over the world whose diversity and intelligence made my life so rich and enjoyable. I am grateful to all my friends for sharing not only the numerous great moments but also the few difficult ones. My affection goes especially to Edie and Rafael with whom I had the pleasure to share most of my free time. I thank my sister Dominique for her support and encouragement all along my studies.

Most of all, I would like to dedicate this dissertation to my mother for all the sacrifices she made for us and for strongly believing in the power of education to positively transform the life of individuals and particularly that of her children.

TABLE OF CONTENTS

Page

Page

Page

Page

Page

LIST OF TABLES

LIST OF FIGURES

Figure Page

Figure Page

Figure Page

Figure Page

ABSTRACT

Pilon, Laurent. Ph.D., Purdue University, December, 2002. Interfacial and Transport Phenomena in Closed-Cell Foams. Major Professor: Raymond Viskanta.

The present study can be divided in three different parts: (1) foam dynamics, (2) thermal radiation transfer through foams and semitransparent media containing bubbles, and (3) bubble transport in three-dimensional liquid laminar flow.

The first part aims at better understanding and predicting (i) the transient growth, (ii) the steady state foam thickness, and (iii) the onset of formation of foams produced by injecting bubbles in a column containing a foaming liquid at rest. First, a model for the transient growth based on the mass conservation equation for the gas phase is proposed. Second, the governing equation for the transient foam thickness has been non-dimensionalized, and two dimensionless numbers have been identified to describe the formation and stability of liquid foams at steady state. Finally, the model for predicting the onset of foaming is derived from the one-dimensional drift-flux model. Experimental data have been collected from the literature and cover a wide range of experimental conditions and thermophysical properties. The models predictions were systematically compared with available experimental data and show very good agreement.

The dissertation presents a general formulation of the radiation characteristics of semitransparent media containing gas bubbles. Sample calculations for the spectral radiation characteristics of soda-lime silicate glass containing bubbles are discussed. Results clearly show that the presence of bubbles strongly affects the radiation characteristics of the semitransparent media containing entrapped gas bubbles, particularly if bubbles, void fractions, and spectral absorption coefficient of the continuous phase are small. Spectral bi-directional transmittance and reflectance of fused quartz sam-

ples containing bubbles have been measured experimentally. The data were used to retrieve the spectral absorption and extinction coefficients, and the scattering phase function by an inverse method. Model predictions were compared against experimental data.

Finally, a model for bubble transport in three-dimensional liquid laminar flow has been developed based on population balance theory. It accounts for growth or shrinkage of bubbles containing one or several gases diffusing in and out of the bubbles. A numerical scheme based on the modified method of characteristics (or inverse marching method) has been developed, validated, and applied to bubble transport in three-dimensional gravity driven flow of molten glass.

1. INTRODUCTION

Closed-cell foams consist of gas bubbles separated from one another by a thin membrane of a continuous condensed phase. The condensed phase can be solid or liquid. Among foams having solid membranes, the polymeric foams are the most commonly used [1]. Solid foams can be rigid or flexible, and the cell geometry can be open or closed. Liquid foams, on the other hand, are flexible closed-cell foams consisting of gas bubbles entrapped in a liquid matrix. They are frequently encountered as a by-product in chemical processes (oil refinery, food processes), in bioprocessing (protein separation, bioreactors) and materials processing (steel, aluminum, glass). They can also be generated for special applications such as firefighting or shaving.

The objective of this chapter is not to present an exhaustive literature review of the different aspects of interfacial and transport phenomena in closed-cell foams treated in this document, but, instead, to present an overview of the scientific and technological rationale. It is followed by a brief description of the physical phenomena taking place in liquid foams and their consequences on the foam morphology and volumetric gas fraction. The chapter concludes with a statement of the specific objectives of the research along with the organization of the document.

1.1. Motivations For the Present Work

Solid closed-cell foams are usually rigid and mostly used for thermal insulation in the construction and refrigeration industries as well as in industrial processes. The matrix oftn consists of polymers but glass foams have started appearing on the market. Indeed, closed-cell foams are very effective thermal insulators due to entrapped blowing agents used for foaming and that have a low thermal conductivity. Unfortunately, the thermal insulating characteristics and dimensional stability of rigid

closed-cell foams decay significantly with age due to the outward diffusion of the low conductivity gas and the inward diffusion of higher conductivity air constituents [2,3].

In liquid foams, bubbles are either generated by chemical reactions taking place within the liquid or injected in the liquid through a single nozzle, a multinozzle inlet or a porous medium. In bioreactors, bubbles are generated by an air sparger placed beneath the agitator to aerate the culture medium [4]. In the presence of surface active agents, foam may be formed and act as a cushion preventing bursting bubbles from damaging the cells at the liquid surface. In modern electric arc furnaces, foam is often required to shield the refractories from the arc, to protect the liquid metal from the atmosphere, and to help stabilize the arc [5]. In protein separation, proteins acting as surfactants concentrate in the foam that is collected to produce a solution with higher protein concentration [6]. The thermal insulation properties of foams are used in firefighting by covering the surrounding of a blaze with foam thus preventing the fire from expanding and setting on fire surrounding trees, houses, and other precious or flammable materials by thermal radiation [7, 8].

However, foam is not always desired as it may disrupt the production and affects essential transport phenomena and the product quality. Industrial processes which bring gases and liquids together often form foams that can block the flow or damage pumps. The petroleum and chemical processing industries are therefore interested in controlling or destroying foams. In glass-melting furnaces, foam produced by chemical reactions taking place within the melt is often undesirable since it reduces the heat transfer rates from the combustion space to the melt thereby increasing the operating temperature, the NO_x-formation rate, the energy consumption, and the wear of the refractories [9–13].

In all the above applications, transport phenomena in closed-cell foams, wether it is mass, heat or radiation transfer, are essential either for controlling and optimizing the process and the product quality or for reaching desired performance. Such transport phenomena are the focus of the work described in this document. The thickness of the foam layer is the most obvious parameters that can significantly affect such

transport phenomena. Unlike solid foams, the inner stucture of liquid foams constantly evolve with time and their thickness can change significantly depending on the operating or surrounding conditions. Therefore, the dynamics of liquid foams is considered first. Then, radiation transport in closed-cell foams is studied. Finally, rationale for studying bubble transport in three-dimensional gravity driven flow is treated.

1.1.1. Foam Dynamics

The transient behavior of foams is of particular importance in food, chemical, and materials processing that require constant adjustement of the operating parameters to meet the production needs. For example, in glass melting furnaces, operators have to constantly adapt the pull rate, the feeding of the batch and the firing rate as a function of the production needs. Such changes affect the foam layer thickness that grows or decays accordingly. Even though the physical phenomena taking place in the formation of a foam layer appear to have been identified and are qualitatively understood, the modeling of the transient behavior of pneumatic foams have been concerned mainly with the decay of standing foams [14–19]. One should also mention that parametric studies of the transient and steady-state foam behaviors have been performed [14], but very little validation against experimental data has been reported [18,19]. Finally, the observation that the solution of the model equations for the foam decay available in the literature are highly dependent on the initial conditions provides an additional motivation for studying the formation of the foam layer from a liquid surface free of foam.

The transient behavior of liquid foams can be divided in three different regimes. For small superficial gas velocities the foam layer reaches a steady-state, i.e, the burst rate of the bubbles at the top of the foam is compensated by the supply of bubbles at the bottom. This regime is of particular interest to bioreactors and materials processing such as iron or steel manufacturing [5, 9, 20–30]. The most popular

approach used to predict the steady-state foam thickness consists of performing a dimensional analysis based on Buckingham's Pi theorem [20–23, 29, 30]. However, the correlation developed fails to predict the steady-state thickness of foams generated from liquids other than molten steel [26–28].

Experimental data used to study the transient and steady-state behavior of liquid foams indicate that liquid foams do not form for any arbitrarily small gas flow rate. Laimbock [9] has observed that a minimum superficial gas velocity should be reached to initiate foaming of molten glass. The same observations have been made for different aqueous solutions [26, 31–35], as well as for molten steel [5, 20–24, 29, 30]. Whether foam is desirable or not, it is of fundamental and practical interest to understand the foaming process and to predict the conditions under which foam starts forming in order to operate a process under the most favorable conditions. However, to the best of my knowledge, no self-contained model able to predict the minimum superficial gas velocity for onset of foaming j_m has been reported in the literature. The only attempt has been to determine the transition from the homogeneous bubbling regime to the foaming regime on a flow map plotting the void fraction versus the Froude number [35]. The map provides "an estimate" of the minimum superficial gas velocity for onset of foaming as a function of the void fraction in the bubbly flow and of the container diameter. Moreover, the drift-flux model has been used to qualitatively describe the occuring of a foam layer on top of bubbly flow under steady-state conditions [36] but it fails to explain the existence of a non-zero minimal superficial gas velocity for onset of foaming.

1.1.2. Radiation Characteristics of Semitransparent Media Containing Bubbles

Transport phenomena and in particular thermal radiation transfer at elevated temperature in solids or liquids can be strongly affected by the presence of foams and entrapped bubbles. Foam or bubbles can strongly reflects and back-scatters the incident thermal radiation due to the multitude of gas/liquid interfaces from which

photons will reflect or refract [13, 37]. The refractive-index mismatch at the bubble interface is large so multiple scattering is unavoidable. This gives bulk foam samples their familiar white opaque appearance except for very dry and slowly evolving foams or for bulk liquid with small bubble concentrations [37]. Thermal radiation transfer through semitransparent media containing bubbles including foams is of interest to many practical engineering applications ranging from meteorology and firefighting to materials processing and characterization.

For example, thermal emission data from ocean surface is currently assessed for retrieval of wind speed and direction assuming a smoothly varying surface profile [38]. However, under high wind conditions, the presence of breaking water waves, foam patches, and bubbles will affect the emissivity of the ocean surface leading to errors in the retrieval of the wind speed and directions [38]. Moreover, the cost and quality of nearly all commercial glass products are determined by the performance of the glass melting and delivery systems which, in turn, depends on the efficiency of heat transfer from the hot combustion space to the raw materials and to the glass melt [13]. Heat transfer by thermal radiation accounts for the major fraction of the energy supply that is needed for the fusion and melting of the raw batch materials [39]. However, the foam layer covering part of the molten glass acts as a good insulator. This forces the glass manufacturers to consume more fuel and reach higher temperatures in the combustion space in order to melt the batch, to activate the refining reactions, and to obtain the required glass bath temperatures for producing high glass quality. Higher combustion space temperatures not only increase the operating costs, due to a larger fuel consumption, but also increase NO_x emissions and the wear of the furnace refractories [13]. Finally, the use of photon transport in liquid foams has been suggested for noninvasive probing of their time dependent inner structure [37, 40, 41]. Previous studies have been based on simplifying assumptions and assumed photon transport in foams as a diffusion process [37, 40–45]. However, such an assumption is not valid for thin or weakly absorbing materials such as glass in the spectral range between 0.2 and about 4 μm [46, 47].

1.1.3. Bubble Generation and Transport in Three-Dimensional Gravity Driven Flow

The bubble size distribution and their concentration (expressed as the volumetric gas fraction) have been identified as critical parameters that can strongly affect the transport phenomena in foams and in particular thermal radiation transfer through the change in apparent radiation characteristics of the continuous phase [11, 12]. In order to predict the bubble size distribution and void fraction, it is essential to investigate the bubble transport in the liquid phase before they reach the liquid/foam interface. Moreover, such a study enables one to predict the superficial gas velocity reaching the interface. With this information on hand, one can determine if the conditions for foaming are reached, the transient regime of the foam as well as the transient foam thickness and eventually the steady-state foam thickness if the superficial gas velocity is small enough.

Before presenting the objectives of the doctoral work and describing in details the original analysis developed for each one of the above topics, it is appropriate to explain the interfacial and transport phenomena taking place in liquid foams as well as their effects on the foam morphology.

1.2. Physical Description of Liquid Foams

Liquid foams generated at the surface of a liquid are constantly evolving systems with complex interfacial and transport phenomena occuring simultaneously or consecutively. A brief description of these phenomena and there consequences on the foam morphology are presented.

1.2.1. Foam Structure

Foams consist of an ensemble of bubbles of different sizes. The bubble size distribution at the bottom of the foam layer depends on the injection systems [48]. Bubbles can take different shapes and polyhedral and spherical bubbles often coexist within the foam layer as illustrated in Figure 1.1. The polyhedral bubbles tend to be located

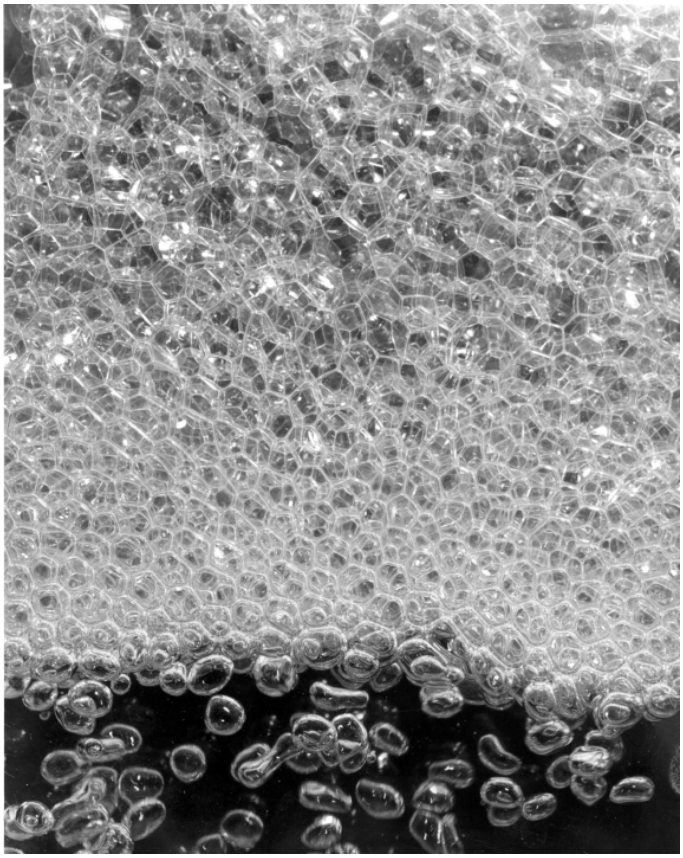

Figure 1.1. Photograph of liquid foams (courtesy of J.J. Cilliers, UMIST, UK).

at the top of the foam while the spherical ones are at its bottom [49,50]. Even though polyhedral bubbles can adopt different geometries, they all obey a few rules known as the Plateau's laws [14]: (i) three and only three films meet at an edge at an angle of 120^o, (ii) four and only four edges (Plateau border channels) meet at a point at an angle of 109^o. It has been observed that a regular dodecahedron nearly satisfies Plateau's laws and is considered as an idealized polyhedral bubble [14].

1.2.2. Physical Phenomena

We consider the situation when a foam layer is generated from bubbles rising to the surface of a liquid at rest. As bubble rise to the liquid free surface, they entrain

a certain amount of liquid that gets trapped to form a film between the rising bubble and the surrounding atmosphere (at the onset of foaming) or between the rising bubble and another bubble in the foam. If the bubble supply is maintained, bubbles move up into the foam layer as they are pushed by incoming bubbles. When bubbles reach the top of the foam, they eventually burst thus releasing the liquid contained in the lamellae that flows down into the foams. The life of "an average" bubble within the foam layer can be visualized by looking at an instant image of a liquid foam layer (see Figure 1.1) from the liquid/foam interface to the top of the foam layer. Between the liquid/foam interface and the top of the foam layer several physical phenomena occur simultaneously or consecutively. These phenomena are:

(i) *Gravity drainage* of the liquid through the Plateau borders opposed by the viscous forces.

(ii) *Drainage* of the liquid in the films driven by the capillary pressure due to the curvature of the adjacent Plateau channels and opposed by the disjoining pressure consisting of the Van der Waals attractive forces, the repulsive electrical double layer and the hydration forces [14]. Drainage in the foam eventually stops when the effect of the capillary forces (or Plateau border suction) balances the effect of gravity [14, 51].

(iii) *Coalescence* of two adjacent bubbles as a result of the rupture of the film separating them. Coalescence causes the mean bubble size to increase and the number of bubbles as well as the interfacial area of the foam to decrease.

(iv) *Interbubble gas diffusion*[1] from small bubbles (higher pressure) to large bubbles (lower pressure). This causes the small bubbles to become smaller and the large bubbles to become larger provided that the solubility and the diffusion coefficient of the gas in the liquid phase are large enough. A theoretical analysis by Narsimhan and Ruckenstein [15] indicates that interbubble gas diffusion is significant only at the top of the foam where the bubble lamellae are thin.

[1]Also called Ostwald ripening or disproportionation

(v) *Gibbs-Marangoni effect* in thin liquid films and foams results in a decrease of the surface excess surfactant concentration caused by stretching an interface, hence in an increase in surface tension (Gibbs effect); the surface tension gradient thus created causes liquid to flow toward the stretched region, thereby providing both a "healing" force and also a resisting force against further thinning (Marangoni effect).

It has been observed for different types of liquid phase (molten glass [9] and aqueous solutions [16]) that bubbles do not necessarily burst when the lamellae reach their critical thickness. Instead, they remain in a so-called metastable state until they burst. Thus, the rupture of lamellae occurs due to two independent and consecutive processes. The first stage in the rupture of the film is its thinning due to drainage, and the second stage is the tear of the film probably due to random molecular collisions [52]. According to Hrma [53], the lifetime of a bubble cannot be determined from the thickness of its lamellae, and the characteristic time of rupture can be expressed as a function of two characteristic times: (i) the characteristic time of drainage τ_d, and (ii) the lifetime of the critically thin film τ_c [52, 53]:

$$\tau = \tau_d + \tau_c \tag{1.1}$$

The lifetime τ_c depends on the properties of the fluid and on the bubble radius, but it is independent of the gas supply [53]. If τ_c equals zero, the foam is said to be evanescent, that is, bubbles burst as soon as their lamellae reach the critical thickness. In general, τ_c is non-zero and the foam is said to be metastable [53].

1.2.3. Foam Porosity

As a result of gravity drainage, the foam becomes "dryer" and the porosity, defined as the ratio of the local volume of gas to the volume of foam, increases from the bottom to the top of the foam layer. It is usually assumed [14, 15, 48] that the porosity at the bottom of the foam is constant with time and equals 0.74 corresponding to the

maximum packing of spherical bubbles of the same size. In reality the porosity varies with time from zero as bubbles start reaching the surface of the liquid to its steady-state value. Hartland and Barber [54] have observed that even though the liquid holdup close to the liquid/foam interface varies with time, it rapidly reaches a steady state while the foam is still growing. In other words, the characteristic time for the porosity at the bottom of the foam required to reach a steady state is negligible compared to that of the foam thickness. Therefore, assuming that the porosity at the bottom of the foam is constant with time is an acceptable approximation.

1.3. Objectives of the Present Study

The present study can be divided in three major parts:

1. **Foam Dynamics**

   Several aspects of the dynamics of liquid foams are considered:

   - *Transient foam thickness of liquid-gas foams.* The objective is to develop a model for predicting the thickness of a foam layer during its formation, i.e., from the beginning of the gas injection onward. A simple yet physically sound approach based on the first principles is preferred to the solution of a complex system of differential equations accounting for drainage, bubble coalescence, and interbubble gas diffusion. Such an approach is justified by the fact that (1) very little work on transient foam formation has been previously carried out and validated against experimental data, and (2) in the case of transient growth the formulation of boundary and initial conditions for existing governing equations are not available.
   - *Steady-state thickness of gas-liquid foams.* The goal is to develop a model for predicting the steady-state foam thickness as a function of the thermophysical properties of the system, the bubble size, and the superficial gas velocity. The effects of the temperature (uniform across the foam), the initial liquid height, and the type of gas are investigated as well. The

study is based on dimensional analysis of the conservation equation of the liquid phase in the foam commonly refered as the drainage equation.

- *Minimum superficial velocity for onset of foaming.* The objective is to provide physical explanations of the experimental facts and to develop a quantitative self-contained model which gives the minimum superficial gas velocity as a function of the physicochemical properties of the two phases and the operating conditions using the drift-flux model and paying particular attention to bubble coalescence.

2. **Radiation Characteristics of Semitransparent Media Containing Bubbles**

   Considering the wide range of applications and the fundamental interests, the doctoral work aims at modeling the radiation transfer through semitransparent media containing bubbles including foams for weakly absorbing materials for which rigorous formulation of the radiative transfer equation must be used. The objectives of the work can be summarized as follows:

   - Model the radiation characteristics of semitransparent media containing bubbles.
   - Perform experimental measurements of spectral bi-directional transmittance and reflectance of fused quartz containing bubbles and use inverse method to retrieve the radiation characteristics of fused quartz containing bubbles.
   - Validate the theoretical model against the experimental data.

3. **Generation and Transport of Bubbles in Three-Dimensional Laminar Gravity Driven Flow**.

   The study aims at developing a general framework for predicting the bubble density function, the bubble radius and gas molar fraction in three-dimensional laminar liquid flow. The specific goals are:

- Develop a model for bubble transport in three-dimensional laminar gravity driven flow using population balance theory.
- Develop a numerical algorithm for solving the governing equations for the bubble density function using the method of characteristics and the inverse marching method.
- Validate the numerical scheme against known solutions and apply it to bubble transport in three-dimensional laminar gravity driven flow of molten glass.

1.4. Scope of the Document

This document can be divided in three parts. First, different aspects of foam dynamics are modeled with careful experimental validation. Analysis of the transient behavior of liquid foams is presented in Chapter 2. Then, the model for predicting the steady-state foam thickness of liquid-gas foams is presented in Chapter 3 along with comparisons with experimental data. Model for the superficial gas velocity for onset of foaming and validation against experimental data are described in Chapter 4. Then, the theoretical analysis predicting the radiation characteristics of semitransparent media containing bubbles followed by the experimental results and the model validation are presented in Chapters 5 and 6. Finally, Chapter 7 describes the model for bubble transport in three-dimensional laminar flow. The numerical solutions of the bubble transport model are presented in Chapter 8 for the specific application to glass melting furnaces.

The document is arranged in such a way that each chapter can be read independently as each one contains its own literature review, nomenclature, analysis, and results.

2. ANALYSIS OF TRANSIENT THICKNESS OF LIQUID/GAS FOAMS

2.1. Introduction

As already discussed, the transient behavior of foams is of particular importance for processes that require constant adjustement of the operating parameters leading to changes in the foam thickness with time. Moreover, foam decay has been studied extensively whereas foam formation has received little interest. The objective of the present work is to develop a model based on first principles for predicting the thickness of a foam layer during its formation, i.e., between the beginning of the gas injection until the foam reaches a steady state.

2.2. Current State of Knowledge

Several models describing the transient behavior of pneumatic foams are available in the literature and have been reviewed recently [14]. Most of them consist of solving a system of differential equations for the foam thickness and for the local foam porosity or the liquid hold-up [14, 17]. The fundamental governing equation called "the drainage equation" is based on the local mass conservation of the liquid phase [14]. The one-dimensional formulation of the drainage equation in terms of the foam porosity at height z and time t, $\phi(z,t)$, is written as follows [14]:

$$\frac{\partial \phi}{\partial t} = \frac{\partial}{\partial z}(\phi q_{PB}) \tag{2.1}$$

where q_{PB} is the volumetric flux of the liquid phase through the Plateau border channels at location z and time t. Assuming that (1) the foam bed consists of dodecahedron bubbles of the same size, (2) the Plateau borders are randomly oriented, (3) the drainage through the Plateau borders due to film thinning is negligible compared

to that due to gravity [see Ref. [14] and [17] for additional discussion], (4) coalescence of bubbles and Ostwald ripening within the foam are absent, (5) surface tension is constant, (6) the wall effects are negligible, and (7) the foam is under isothermal conditions, an expression for the volumic flow rate through the Plateau border $q_{PB}(z,t)$ is given by [see Chapter 3 Equation (3.9)]:

$$\begin{aligned} q_{PB}(z,t) &= 3.632 \times 10^{-3} c_v \frac{[1-\phi(z,t)]^2}{\phi(z,t)} \left\{ \frac{\rho g r^2}{\mu} + \right. \\ &\left. \frac{1.3957}{\alpha} \frac{\sigma r^2}{\mu} \frac{\partial}{\partial z} \left[\left(\frac{\phi(z,t)}{(1-\phi(z,t))r^2} \right)^{\frac{1}{2}} \right] \right\} \end{aligned} \tag{2.2}$$

where ρ is the liquid density, μ is the liquid viscosity, σ is the surface tension of the gas/liquid system, and r is the bubble radius. In this equation α equals $\sqrt{0.644}/0.322$, and the velocity coefficient c_v (dimensionless) accounts for the mobility of the walls of a Plateau border channel and has been computed by Desai and Kumar [55]. In most of their calculations, Ruckenstein and coworkers used $c_v = 1$ [14]. The initial porosity distribution in the foam and two boundary conditions are needed to solve Equations (2.1) and (2.2). The porosity at the bottom of the foam layer $\phi(z_2,t)$ is traditionally assumed to be constant and equal to 0.74 and the volumetric flux q_{PB} is assumed to be zero at the top of the foam [18, 19]. Two approaches have been used to determine the initial porosity in the studies of the decay of standing foams. Narsimhan [17] used a quasi-steady state model to compute the initial porosity as a function of the location in the pneumatic foam. His analysis is based on the assumption that the loss of liquid by gravity drainage is compensated by the liquid entrained with the rising bubbles. On the other hand, Bhakta and Ruckenstein [19] solved the drainage equation using moving boundaries during the foam formation. The latter model compares better with experimental data for the decay of pneumatic foams than the quasi-steady state approach indicating that "the unsteady nature of foam formation cannot be ignored" [19]. Thus, the solution for foam decay has been proven to be highly sensitive to the initial bubble size distribution in the foam [14]. However, it is difficult to obtain or predict the initial bubble size distribution either experimentally, analytically or numerically [14, 56].

More sophisticated models have been proposed that account for coalescence of bubbles as well as interbubble gas diffusion and require the solution of an additional equation for the local average film thickness of the lamellae as a function of position in the foam [14, 15]. These models assume that the neighboring bubbles coalesce as soon as the thickness of the lamellae reaches the critical film thickness, i.e., the foam is assumed to be evanescent.

Another possible approach to deal with transient behavior of foams is the use of population balance theory. Narsimhan and Ruckenstein [48] developed such a model accounting for drainage, coalescence, and interbubble gas diffusion. Drainage is treated assuming dodecahedron bubbles while the treatment of interbubble gas diffusion is based on spherical bubbles. Such assumptions have been judged to be inevitable given the complexity of the system, and this model is difficult to extend to transient problems [14]. More recently, Hartland and co-workers [32, 57] have developed a transient population balance equation by accounting for drainage and interbubble gas diffusion and neglecting coalescence. However, the population balance equations available in the literature for bubbles in foams [48, 57] assume that the number density function is smooth, differentiable with respect to time and space coordinates [see Ref. [58] for more details]. In other words, "the population balance equation is to be viewed as an averaged equation" [58] that is valid when the population is large enough to consider its behavior as deterministic, i.e., the deviation about the average is negligible [58]. However, the validity of the above mentioned models [48, 57] can be questionable in the upper part of the foam where only a small number of bubbles is present. For such small populations a stochastic approach seems to be more appropriate [58] but is not available in the literature.

Even though the physical phenomena taking place in the formation of a foam layer appear to have been identified and are qualitatively understood, the modeling of the transient behavior of pneumatic foams have been concerned mainly with the decay of standing foams [14–19]. One should also mention that parametric studies

of the transient and steady-state foam behaviors have been performed [14], but very little validation against experimental data has been reported [18, 19].

Moreover, all the models assume that bubbles are dodecahedron in shape and are continuously bursting at the top of the foam layer. Although such assumptions are valid for the decay of standing foams, they are difficult to justify during the foam formation, particularly at an early stage [14]. The polyhedral shape assumption does not account for the fact that as drainage, coalescence and Ostwald ripening take place the foam porosity increases from 0.74 to values close to unity, requiring the bubble to change from spherical to polyhedral shape. Such a change in shape is particularly important in the transient formation of the foam.

Finally, the observation that the solution of the model equations for the foam decay available in the literature are highly dependent on the initial conditions provides an additional motivation for studying the formation of the foam layer from a liquid surface free of foam to a steady-state foam layer.

In the present work, an attempt is made to develop a simple model for predicting the transient thickness of a foam layer generated by bubbling a gas in a foaming solution. A simple yet physically sound approach based on the first principles is preferred to the solution of a complex system of differential equations accounting for drainage, bubble coalescence, and interbubble gas diffusion.

2.3. Analysis

Following Hartland and Barber [54], the experimental data for the formation of pneumatic foams can be classified in three different types of transient behavior depending on the superficial gas velocity (see Figure 2.1 for illustration):

1. For low superficial gas velocity, the foam thickness increases almost linearly with time until it reaches a steady state. Small and slow transient fluctuations of the foam thickness around the steady-state thickness are observed.

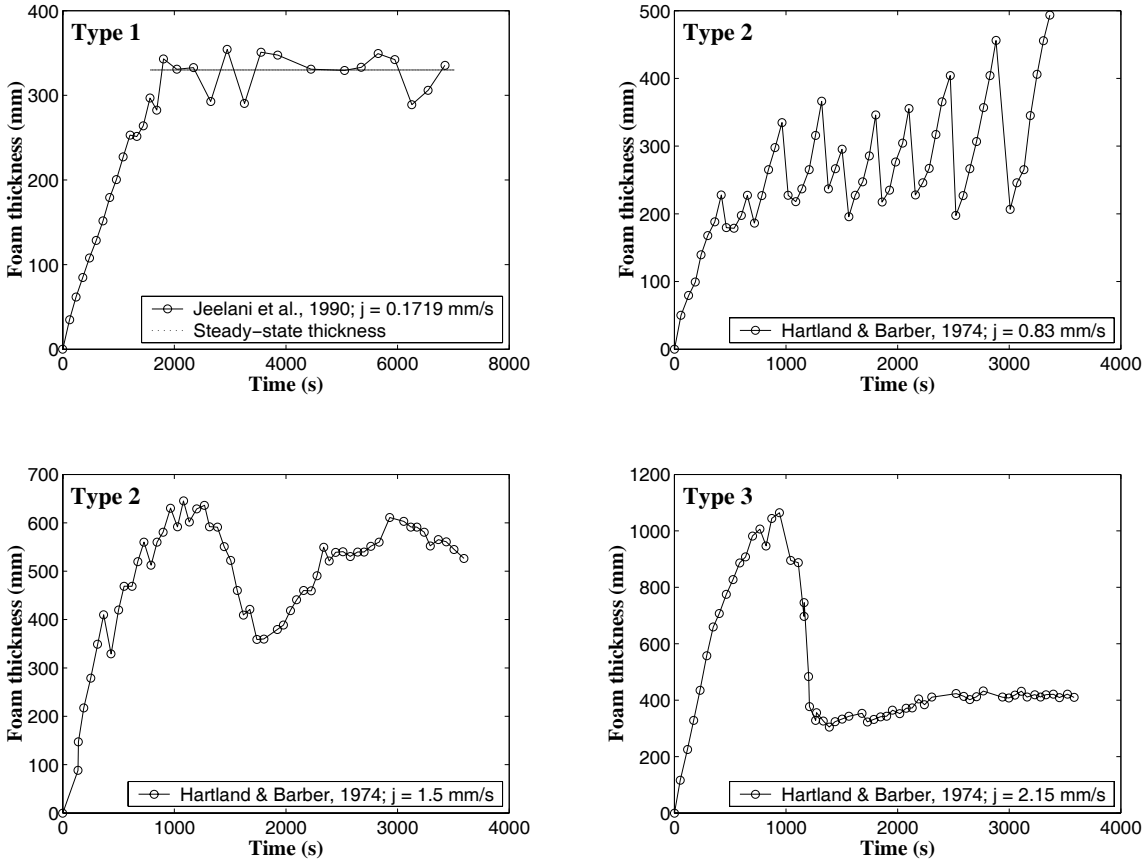

Figure 2.1. Different types of transient during foam formation.

2. For intermediate superficial gas velocity, the foam thickness increases linearly with time until the foam enters a cycle of successive collapse and growth. Unlike the previous type, the fluctuations of the foam thickness with time are such that one cannot consider the foam as being at a steady state. Note that as the flow rate increases, the oscillations tend to be smoother but their amplitude remains significant. Hartland and Barber [54] divided this type of transient behavior into two different regimes: the first one characterized by sudden oscillations, and the second one characterized by smoother oscillations. Here, we do not make the distinction since the overall behavior is similar, i.e., no apparent steady state can be defined due to large oscillations of the foam thickness with time.

3. For large superficial gas velocity, the foam thickess increases almost linearly with time but after some time the foam breaks down into a froth [54]. The froth height is lower than that of the foam for similar conditions. Hartland and Barber [54] attributed this to turbulence and other factors that cause the film at the top of the foam to rupture at greater thicknesses. At higher gas flow rates, no foam is observed and the dispersion becomes a froth right immediately as indicated by Hartland and Barber [54].

Experimental data do not permit the definition of a general criteria between the three different transient behaviors. Such a criteria would depend on the thermophysical properties of the liquid and gas phases, on the superficial gas velocity, on the container size and shape, and other factors.

2.3.1. Mass Conservation Equation

In this section, we present a model for predicting the foam thickness as a function of time during the foam generation. The analysis uses the following simplifying assumptions:

1. The problem is one-dimensional and transient, i.e., the foam porosity is a function of time and the vertical position only [14].

2. The wall effects are negligible.

3. The foam is isothermal.

4. During the transient formation of the foam layer, no bubbles burst at the surface of the foam.

Let us consider a container of constant cross-sectional area A containing a solution at rest as schematically represented in Figure 2.2. Initially (i.e., at $t = 0$) gas bubbles are injected at the bottom of the container at a constant superficial gas velocity j. We also assume that the gas flux j is large enough to generate foam. Let $H(t)$ be the

height of the foam at any time t. The coordinate system is chosen with the origin located at the top of the foam as shown in Figure 2.2.

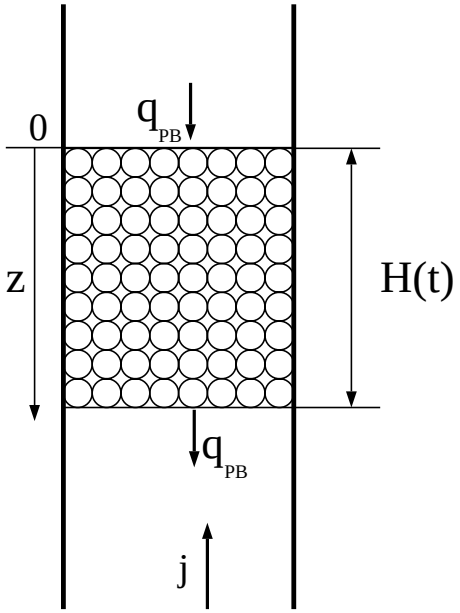

Figure 2.2. Schematic of a foam layer generated by bubbling and coordinate system with notations.

According to the above assumptions, the mass conservation of the gas phase within the foam can be expressed as

$$\frac{dm_g(t)}{dt} = \rho_g j A \qquad \text{if } t \leq \tau \tag{2.3}$$

where ρ_g is the density of the gas phase, j the volumetric gas flux or superficial gas velocity, and τ the time for the foam thickness to reach a steady state. The total mass of gas retained within the foam $m_g(t)$ can be expressed as a function of the gas density ρ_g and the foam porosity $\phi(z)$:

$$m_g(t) = \int_0^{H(t)} \rho_g \phi(z,t) A dz \tag{2.4}$$

Assuming that the gas density and the container area are constant, Equations (2.3) and (2.4) can be combined and simplified to become

$$H(t)\bar{\phi}(t) = jt \qquad \text{if } t \leq \tau \tag{2.5}$$

where $\bar{\phi}$ is the instantaneous average foam porosity defined as

$$\bar{\phi}(t) = \frac{1}{H(t)} \int_0^{H(t)} \phi(z,t) \mathrm{d}z \tag{2.6}$$

According to Equation (2.5), the transient foam thickness can be predicted if one knows the evolution of the instantaneous average (over height) foam porosity $\bar{\phi}(t)$ with time.

2.3.2. Porosity Profile in the Foam Layer

In this section, we develop an approximate expression for the porosity profile in the foam layer as a function of time t and location z. We choose a second order polynomial to represent the local porosity distribution $\phi(z,t)$:

$$\phi(z,t) = a_0 + a_1 \left[\frac{z}{H(t)}\right] + a_2 \left[\frac{z}{H(t)}\right]^2 \tag{2.7}$$

where the coefficients a_0, a_1, and a_2 are generally functions of time, unless self-similar solution is obtained. Three conditions are needed to determine these three coefficients and they are obtained from the boundary conditions at the top and bottom of the foam layer:

$$\phi[H(t),t] = \phi_2 \tag{2.8}$$

$$\phi(0,t) = \phi_1(t) \tag{2.9}$$

$$\left.\frac{\partial \phi(z,t)}{\partial z}\right|_{z=0} = 0 \tag{2.10}$$

Equation (2.8) states that the porosity at the bottom of the foam is constant, as previously discussed, and is taken as 0.74 corresponding to the maximum packing of spherical bubbles of identical size. Equation (2.9) indicates that the porosity at

the top of the foam is a function of time only. The third condition [Equation (2.10)] reflects the fact that, in most cases, drainage of liquid occurs in the lower part (bottom) of the foam layer and this eventually stops at the top of the foam layer when the gradient of the capillary pressure balances the gravity force [14, 51]. Then, only coalescence may cause the foam porosity to increase at the top of the foam [14], but it is speculated to occur only when the foam is sufficiently drained and the lamella thickness is less than about 100 nm [15]. The drainage flow rate induced by the rupture of the foam lamellae is extremely small, thereby making the porosity $\phi(z,t)$ change very little and, thus, the partial derivative $\partial\phi(z,t)/\partial z$ can be assumed to vanish at the top of the foam (i.e., at z=0) as given by Equation (11). Several models and numerical simulations of the foam liquid holdup using boundary conditions different from Equation (2.10) [14,15,59] have been presented in the literature. They all predict that "the liquid holdup decreases rapidly near the foam/pool liquid interface and less in the rest of the [foam] bed" [15]. Predicted porosity profiles computed for foaming solutions with different viscosity, surface tension, and bubble radius indicate that Equation (2.10) is a reasonable first order approximation. It should be noted that the boundary conditions [Equation (2.10)] can also be deduced by using the well known condition of zero velocity or zero flow rate of the liquid though the Plateau borders at the top of the foam [i.e., $q_{PB}(z=0,t)=0$] [14]. In addition it must be assumed that the radius does not change with the location z and the porosity is unity at the top of the foam layer.

Using the boundary conditions, Equations (2.8) to (2.10) and solving Equation (2.7) for the parameters a_0, a_1, and a_2 results in the following porosity profile within the foam:

$$\phi(z,t) = \phi_1(t) + [\phi_2 - \phi_1(t)] \left[\frac{z}{H(t)}\right]^2 \tag{2.11}$$

The average foam porosity corresponding to this profile can be computed using Equation (2.6):

$$\bar{\phi}(t) = \frac{2\phi_1(t) + \phi_2}{3} \tag{2.12}$$

At the beginning of the foam growth, the bottom and the top of the foam are superimposed and the gas volume fraction at the top of the foam is similar to that at the bottom. As the foam grows and gravity drainage takes place, the porosity at the top increases until the thickness of the lamellae and the porosity at the top reach their respective critical values for which bubbles start bursting. Moreover, Jeelani *et al.* [31] reported porosity values at the top of the foam approaching unity for steady-state foams. Therefore, it is believed that $\phi_1(t)$ varies between ϕ_2 at the beginning of the foam formation and its maximum values taken as unity at steady state.

The next step in the present analysis is to model the evolution of $\phi_1(t)$ and thus $\bar{\phi}(t)$ with time. Three different models are considered in the following sections: the average porosity (i) is constant with time, (ii) is an exponential function of time, and (iii) is obtained by approximate solution of the drainage equation.

i) Constant Porosity at the Top

The simplest approach is to assume that the porosity at the top of the foam $\phi_1(t)$ does not change with time and equals the arithmetic mean of its minimum and its maximum values. In agreement with the experimental observations, we assume that $\phi_{1,min} = 0.74$ and $\phi_{1,max} \approx 1.0$. In this case $\phi_1(t)$ is taken to be 0.86, and according to Equation (2.12) the average foam porosity is $\bar{\phi}(t) = 0.82$.

ii) Exponential Variation of ϕ_1 with Time

The characteristic time for reaching the steady-state foam thickness should be identical to the characteristic time for the porosity at the top of the foam to reach a critical value beyond which bubbles start bursting at the top. Let τ be the characteristic time for the foam thickness to reach a steady state, then the change of the porosity $\phi_1(t)$ with time can be expressed as:

$$\phi_1(t) = \phi_{1,max} + (\phi_{1,min} - \phi_{1,max})e^{-t/\tau} \tag{2.13}$$

The value for τ can be obtained by solving Equation (2.5) for the case $H(t = \tau) = H_\infty$ where H_∞ is the steady-state foam thickness:

$$\tau = \frac{\bar{\phi}(\tau)H_\infty}{j} = \frac{H_\infty}{j}\left\{\frac{2}{3}\phi_{1,max} + (\phi_{1,min} - \phi_{1,max})e^{-1} + \frac{1}{3}\phi_2\right\} \tag{2.14}$$

Again, assuming that $\phi_2 = \phi_{1,min} = 0.74$ and $\phi_{1,max} = 1.0$, we obtain

$$\tau = \frac{0.85 H_\infty}{j} \tag{2.15}$$

An expression for the steady-state thickness H_∞ can be found in Chapter 3 for foams generated from high viscosity fluids. Two dimensionless numbers have been identified as describing the effect of surface tension, viscosity, density, bubble radius, and superficial gas velocity. However, all the experimental data for transient foam behavior collected from the literature are concerned with low viscosity solutions, and nitrogen is used as the filling gas, except for one set of experimental data reported by Hartland *et al.* [32] who used xenon. But, as shown in Chapter 3, in the case of nitrogen bubbled in low viscosity solutions, the same approach as that used for high viscosity solutions can be used. Thus, a correlation for the steady-state thickness of foams generated by bubbling nitrogen into low viscosity solutions has been developed using the two dimensionless parameters previously mentioned:

$$\frac{H_\infty}{r_0} = \frac{213,177}{Ca} \left(\frac{Fr}{Re} \right)^{1.77} \tag{2.16}$$

where Re, Fr, and Ca are the Reynolds, Froude and Capillary numbers, respectively, defined as:

$$Re = \frac{\rho_c (j - j_m) r_0}{\mu}, \qquad Fr = \frac{(j - j_m)^2}{g r_0}, \qquad Ca = \frac{\mu (j - j_m)}{\sigma} \tag{2.17}$$

where j_m is the superficial gas velocity for onset of foaming, μ is the viscosity of the foaming solution, r_0 is the radius of the bubbles at the bottom of the foam, and σ is the surface tension. Since all the experimental data sets for transient foam thickness except one were obtained by bubbling nitrogen in low viscosity solutions, the value of the steady-state foam thickness can be substituted into Equation (2.14) to give the following expression for τ as the function of the thermophysical properties and the superficial gas velocities:

$$\tau = 1.812 \times 10^5 \frac{\sigma}{j r_0^{2.54}} \frac{[\mu (j - j_m)]^{0.77}}{(\rho g)^{1.77}} \tag{2.18}$$

Finally, having determined the characteristic time for the foam to reach a steady state τ, the average foam porosity can be expressed as a function of time t, $\phi_{1,min} = 0.74$, and $\phi_{1,max} = 1.0$, as follows:

$$\bar{\phi}(t) = 0.91 + 0.17e^{-t/\tau} \tag{2.19}$$

iii) Approximate Solution of the Drainage Equation

The drainage equation [Equations (2.1) and (2.2)] is solved approximately by the series method [60] using the following boundary conditions:

$$\phi[H(t), t] = \phi_2 \tag{2.20}$$

$$q_{PB}(0, t) = 0 \tag{2.21}$$

where q_{PB} is the volumetric flux of the liquid phase through the Plateau border channels at location z and time t. Note that at the top of the foam the velocity of the fluid through the Plateau border due to gravity drainage must be zero since no liquid enters the foam at the top [19], therefore, $q_{PB}(0, t) = 0$. Integrating Equation (2.1) with respect to the space variable from $z = 0$ to $z = H(t)$ and using the above boundary conditions together with the Leibnitz rule yields:

$$\frac{\mathrm{d}}{\mathrm{d}t}\left(\int_0^{H(t)} \phi \mathrm{d}z\right) - \phi_2 \frac{\mathrm{d}H(t)}{\mathrm{d}t} = \phi_2 q_{PB}[H(t), t] \tag{2.22}$$

where $q_{PB}[H(t), t]$ is the flux of liquid through the Plateau borders at the foam/liquid interface. Substituting the expression for the average porosity $\bar{\phi}(t)$ given by Equation (2.6) into Equation (2.22) leads to the following differential equation:

$$\frac{\mathrm{d}}{\mathrm{d}t}[\bar{\phi}H) - \phi_2 \frac{\mathrm{d}H}{\mathrm{d}t} = \phi_2 q_{PB}[H(t), t] \tag{2.23}$$

The flux of liquid through the Plateau borders at the foam/liquid interface $q_{PB}[H(t), t]$ can be found by substituting Equation (2.11) into Equation (2.2) and assuming that $\phi_2 = 0.74$ and the change in the bubble radius with location is negligible, then Equation (2.23) becomes

$$H\frac{\mathrm{d}}{\mathrm{d}t}(\bar{\phi}H) - 0.74H\frac{\mathrm{d}H}{\mathrm{d}t} = AH - B(\phi_1(t) - 0.74) \tag{2.24}$$

where

$$A = 2.46 \times 10^{-4} c_v \frac{\rho g r^2}{\mu} \tag{2.25}$$

$$B = 1.10 \times 10^{-2} c_v \frac{\sigma r}{\mu} \tag{2.26}$$

Equation (2.24) has two unknowns [$\bar{\phi}(t)$ and $H(t)$]. Thus, one needs an additional equation to complete the problem formulation. One can use Equation (2.5) to obtain the following system of equations for $\bar{\phi}(t)$ and $H(t)$ as dependent variables:

$$\frac{\mathrm{d}}{\mathrm{d}t}(\bar{\phi}H) = j \tag{2.27}$$

$$H\frac{\mathrm{d}}{\mathrm{d}t}(\bar{\phi}H) - 0.74H\dot{H} = AH - \frac{3}{2}B(\bar{\phi} - 0.74) \tag{2.28}$$

The initial conditions are:

$$\bar{\phi}(t=0) = \phi_2 \tag{2.29}$$

$$H(t=0) = 0 \tag{2.30}$$

Integrating Equation (2.27) and substituting the expression for the foam thickness $H(t)$ ($=jt/\bar{\phi}$) into Equation (2.28) yields:

$$j^2 t\bar{\phi}(\bar{\phi} - 0.74) + 0.74j^2t^2\frac{\mathrm{d}\bar{\phi}}{\mathrm{d}t} = Ajt\bar{\phi}^2 - \frac{3}{2}B(\bar{\phi} - 0.74)\bar{\phi}^3 \tag{2.31}$$

We now have a single non-linear first-order ordinary differential equation [Equation (2.31)] that can be solved approximately or numerically.

An approximate solution for early times of the foam formation is sought using the series method [60]. We assume that the average porosity $\bar{\phi}(t)$ can be expressed as a Taylor series during the initial phase of the foam formation (i.e., t is small):

$$\bar{\phi} = \sum_{i=0}^{\infty} b_i t^i \tag{2.32}$$

Substituting this expression in Equation (2.31) and identifying the first three terms in t^i gives:

$$b_0 = \phi_2, \qquad b_1 = \frac{2}{3}\left(\frac{Aj}{B\phi_2}\right), \qquad b_2 = -j\phi_2(A + 2j)b_1 \tag{2.33}$$

The Taylor series in Equation (2.32) needs to be truncated for practical calculations. If only the first two terms are retained, the approximate solution of the low O(1) order could be only obtained and this approximation is valid as long as the time interval is between 0 and $o(b_1/b_2)$. On the other hand, if more precise solution with a second order of approximation [e.g., O(2)] is sought, the first three terms in the series need to be retained in Equation (2.32), albeit this more precise solution is valid over much shorter time interval between $t = 0$ and $t = o(b_2/b_3)$. Unfortunately, the upper limit of time for validity of the second-order approximation [i.e., $o(b_2/b_3)$] is a very small number (tenths of a second), and no experimental data fall into this time interval to warrant any further discussion and use of the second-order approximation. Thus, the cruder first order model (i.e., $\phi = b_0 + b_1 t$) that is valid for a much longer time interval is used in this study to provide meaningful comparison with available experimental data.

2.4. Results and Discussion

2.4.1. Validation Against Experimental Data

Table 2.1 summarizes the experimental conditions for the studies reported in the literature and concerned with transient foam thickness.

2.4.1.1. Low Superficial Gas Velocity

Figures 2.3 shows typical experimental data for the transient foam thickness with the type 1 behavior obtained with a nitrogen flux of j=0.1719 mm/s in a solution of 10% glycerine + water + 80 mg/l of Marlophen-89 [31]. The predictions of Equation (2.5) are also plotted by assuming an average porosity $\bar{\phi}$ of 0.74 and 0.91. As one can see, the experimental data fall between these two extreme cases. The assumption that no bubbles burst at the surface of the foam during the transient growth is

valid for transients of type 1. It appears that the steady-state thickness is reached shortly after the mass conservation equation for the gas phase [Equation (2.5)] is no longer satisfied. The only possible reason for the equation not to be valid is if the bubbles at the top of the foam start bursting or if the gas contained in the bubble at the top of the foam diffuses to the atmosphere. However, the sudden change in the transient foam thickness toward its steady-state value indicates that the responsible phenomena is abrupt and suggests that the bursting of the bubbles at the top is a major event causing the foam to rapidly reach a steady state thickness.

It is also interesting to note that at the early stage of the foam formation, the

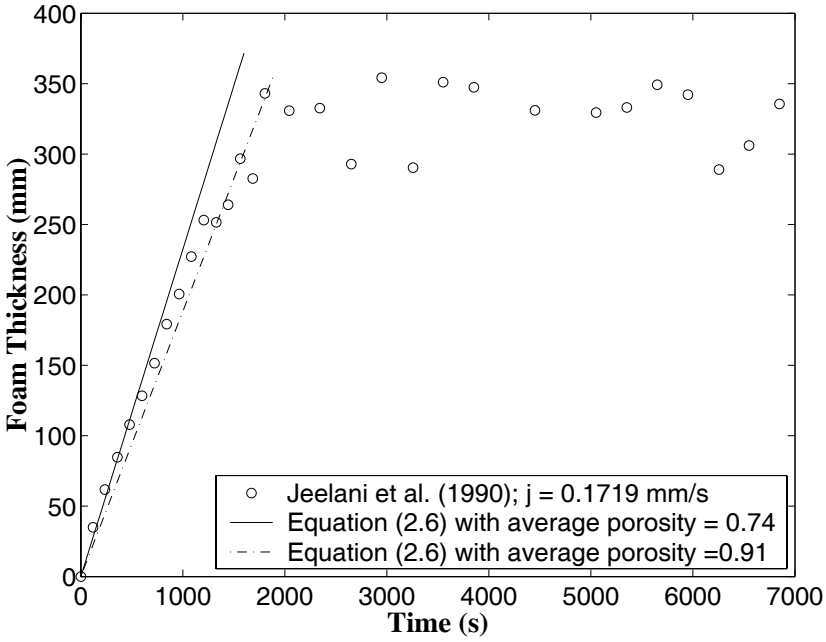

Figure 2.3. Comparison between the model predictions using the limiting values for the average porosity $\bar{\phi}$ and typical experimental data for nitrogen flux j=0.1719 mm/s in 10% glycerine + water + 80 mg/l of Marlophen-89, (Jeelani *et al.*, 1990).

experimentally measured thickness follows Equation (2.5) with $\bar{\phi} = 0.74$ and, at a later stage, it tends toward the predictions of Equation (2.5) with $\bar{\phi} = 0.91$. Similar plots were obtained for other type 1 transients. This can be explained by the fact that as the liquid phase leaves the foam at the bottom as a result of drainage, the

average porosity increases causing the slope dH/dt to slightly decrease with time. At the same time, the bubbles change from spherical to polyhedral shape.

Figures 2.4 compares the experimental data for the transient foam thickness in the case of the low superficial gas velocities with the predictions of the present work obtained with the three different models previously presented. Good agreement is obtained for all three models and particularly when the average porosity is assumed constant and equal to 0.82. Note that there were not enough data at the beginning of the foam formation to fully assess the validity of the approximate solution of the drainage equation which is valid when the time t is small. Moreover, as observed in Figure 2.3, the experimental data fall within the predictions of Equation (2.5) using the extreme values for $\bar{\phi}$ of 0.74 and 0.91, and the difference between the predictions of the two limiting cases is relatively small. Therefore, even the simplest models expressed in terms of average quantities (e.g., porosity) will produce sufficiently accurate results even though it ignores some key physical processes taking place during foam formation (e.g., coalescence and Ostwald ripening). Consequently, a simpler approach is preferred and for practical purposes, the average foam porosity can be taken as constant and equal to 0.82.

Figure 2.5 shows the average foam porosity deduced from experimental data for low superficial gas velocities by using Equation (2.5). A maximum value of 0.91 was imposed when the foam thickness reaches a steady state. It is worth noting that the typical variation with time of the average porosity features a sharp increase in the early stage of the foam formation, then a plateau follows where it does not change significantly, and finally an increase toward its maximum value. This can be explained by the fact that at the beginning, the foam formation is dominated by drainage due to gravity which eventually stops when balanced by the capillary forces (Plateau border suction effects). The foam internal structure does not change significantly for a certain length of time until some films rupture within the foam. The plateau may be due to the stochastic character of film rupture requiring a random time for the first film to rupture. Then, coalescence and drainage of the broken films through

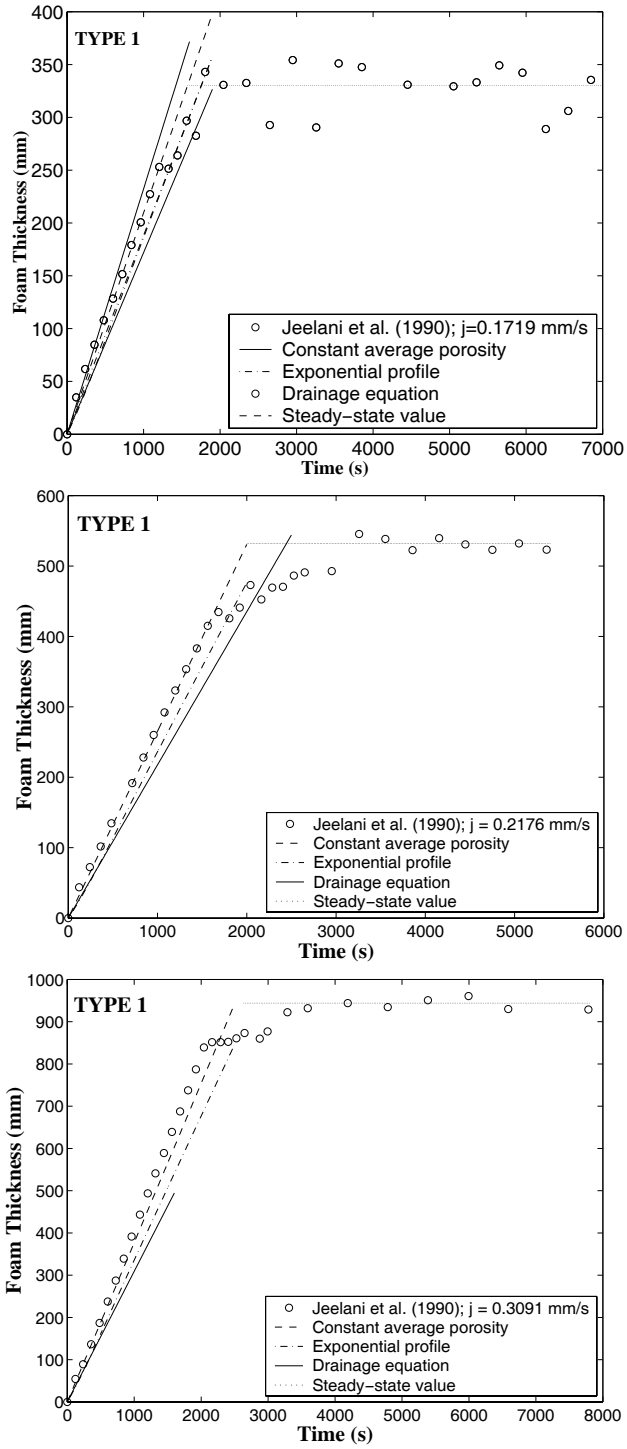

Figure 2.4. Comparison of the model predictions with experimental data for nitrogen flux of j=0.1719 mm/s (top), j=0.2176 mm/s (center), and j=0.3091 mm/s (bottom) in 10% glycerine + water + 80 mg/l of Marlophen-89 (Jeelani *et al.*, 1990).

the Plateau border channels take place making the average foam porosity increase again. Note that such an analysis is traditionally applied to the foam porosity [14] at a given location, but it seems that it is also valid for the average foam porosity. All the models reported in the literature [14, 15, 17, 48] describe drainage, coalescence, and interbubble gas diffusion as occuring simultaneously and continuously in the foam layer. According to Figure 2.5, this hypothesis does not seem to be valid for foam formation. Gravity drainage dominates initially during the formation of the foam layer. However, only a few experimental data are available to fully assess the validity of the drainage equation during the drainage dominated regime of the foam formation. Only when the films separating the bubbles are thin enough, coalescence and interbubble gas diffusion can occur [15]. Therefore, the first part of the transient foam formation would consist of gravity drainage only while the second part should depend on gravity drainage and coalescence, as well as interbubble gas diffusion.
Moreover, two different characteristic times for drainage and film rupture or coalescence within the foam seem to prevail and can be measured from Figure 2.5. The first increase in the average porosity corresponds to the drainage only and appears to be the same for the three different cases, i.e, the characteristic time for drainage (τ_d) is independent of the superficial gas velocity. The duration of the plateau, i.e., the lifetime of the critically thin film (τ_c), however, seems to increase with the superficial gas velocity. This may be due to the fact that as the superficial gas velocity increases, the foam thickness increases and acts as a cushion protecting the bubbles already drained in the upper part of the foam from disturbances occuring at the liquid/foam interface. The larger the superficial gas velocity, the thicker is the absorbing "cushion". Note also that according to Figure 2.5, the characteristic time for drainage is significantly smaller than the lifetime for the critically thin film.

To assess the effect of the gas contained is the bubble, only two experimental data sets were found in the literature. Jeelani *et al.* [31] and Harland *et al.* [32] reported the variation of the foam thickness with time for a superficial gas velocity of j=0.3091 mm/s in a solution of 10% glycerine + water containing 80 mg/l and 120 mg/l of

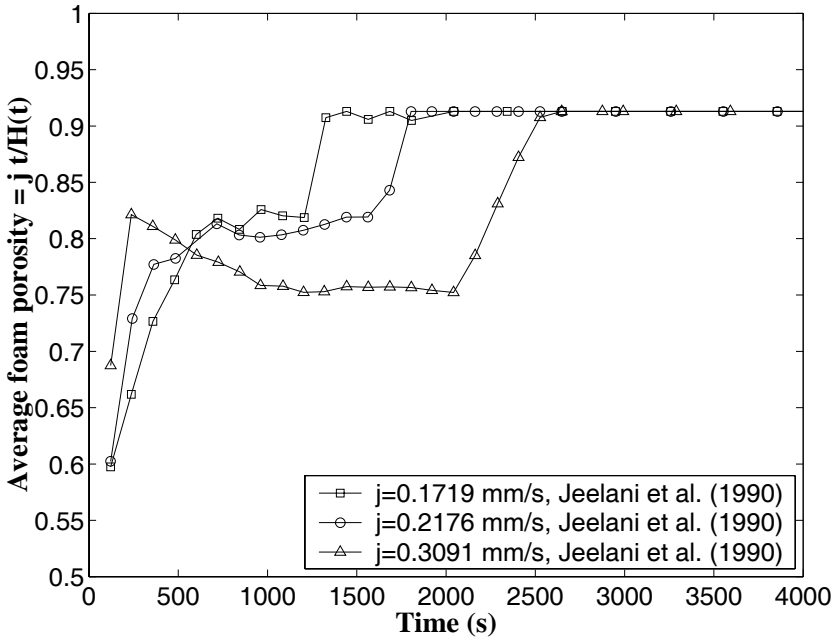

Figure 2.5. Evolution of the average porosity with time for nitrogen flux of j=0.2176 mm/s in 10% glycerine + water + 80 mg/l of Marlophen-89 (Jeelani *et al.*, 1990).

Marlophen-89 and with nitrogen and xenon as the filling gas, respectively. According to Equation (2.5) both systems should behave identically since the superficial gas velocity is the same. However, Figure 2.6 shows that when xenon is injected in the solution the transient foam thickness deviates significantly from the predictions of Equation (2.5), whereas this equation is valid for nitrogen. Even though the amount of surfactant added to the solution is different, the differences in surface tension, density or viscosity between the two solutions are negligible (see Table 3.2 for a summary of the thermophysical properties). Therefore, the difference in the transient behavior can only be explained by the type of gas injected in the solutions. Detailed analysis of the physical properties of nitrogen and xenon reported by Hartland *et al.* [32] indicates that xenon and nitrogen have similar diffusion coefficients in the liquid phase, but the solubility of xenon is seven times larger than that of nitrogen. Furthermore, Harland *et al.* [32] reported that the Sauter mean diameter increases sharply from the bottom to the top of the foam when xenon is injected while it does

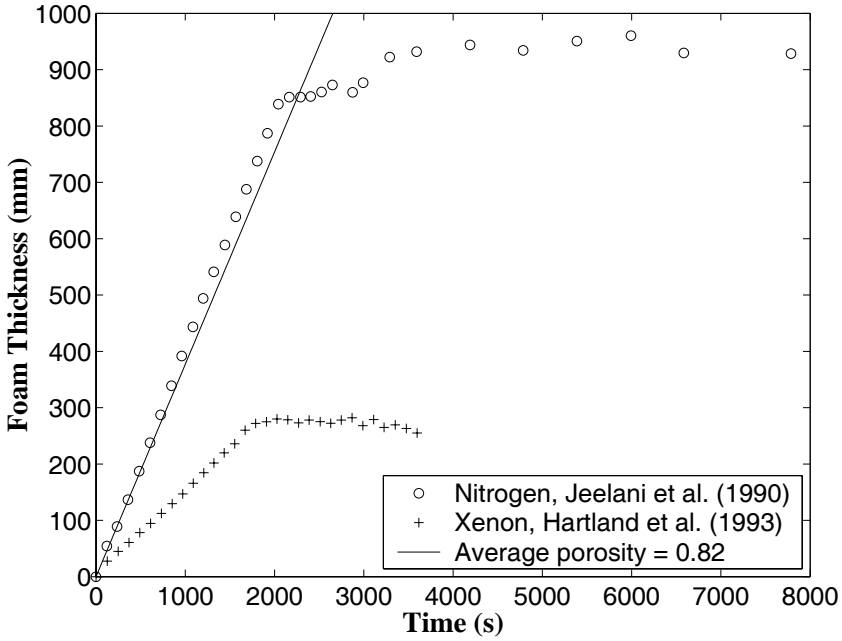

Figure 2.6. Comparison of the evolution of the foam thickness with time for nitrogen and xenon flux of j=0.3091 mm/s in 10% glycerine + water + 80 mg/l of Marlophen-89 (Jeelani *et al.*, 1990).

not change significantly with nitrogen. This can be explained by the enhanced mass transfer from smaller to larger bubbles as the solubility increases. As suggested by Harland *et al.* [32], the interbubble gas diffusion occuring with xenon leads to larger and more unstable bubbles at the top of the foam that tend to burst faster leading to an early deviation from Equation (2.5). For high solubility gases, Ostwald ripening and bursting of the bubbles at the top of the foam should be accounted for to obtain correct predictions of foam dynamics.

2.4.1.2. Intermediate and Large Superficial Gas Velocity

Figure 2.7 shows the evolution of the foam thickness with time for intermediate superficial gas velocity. One can see that the model predictions deviate from the experimental data. More precisely, the bubbles at the top of the foam seem to collapse

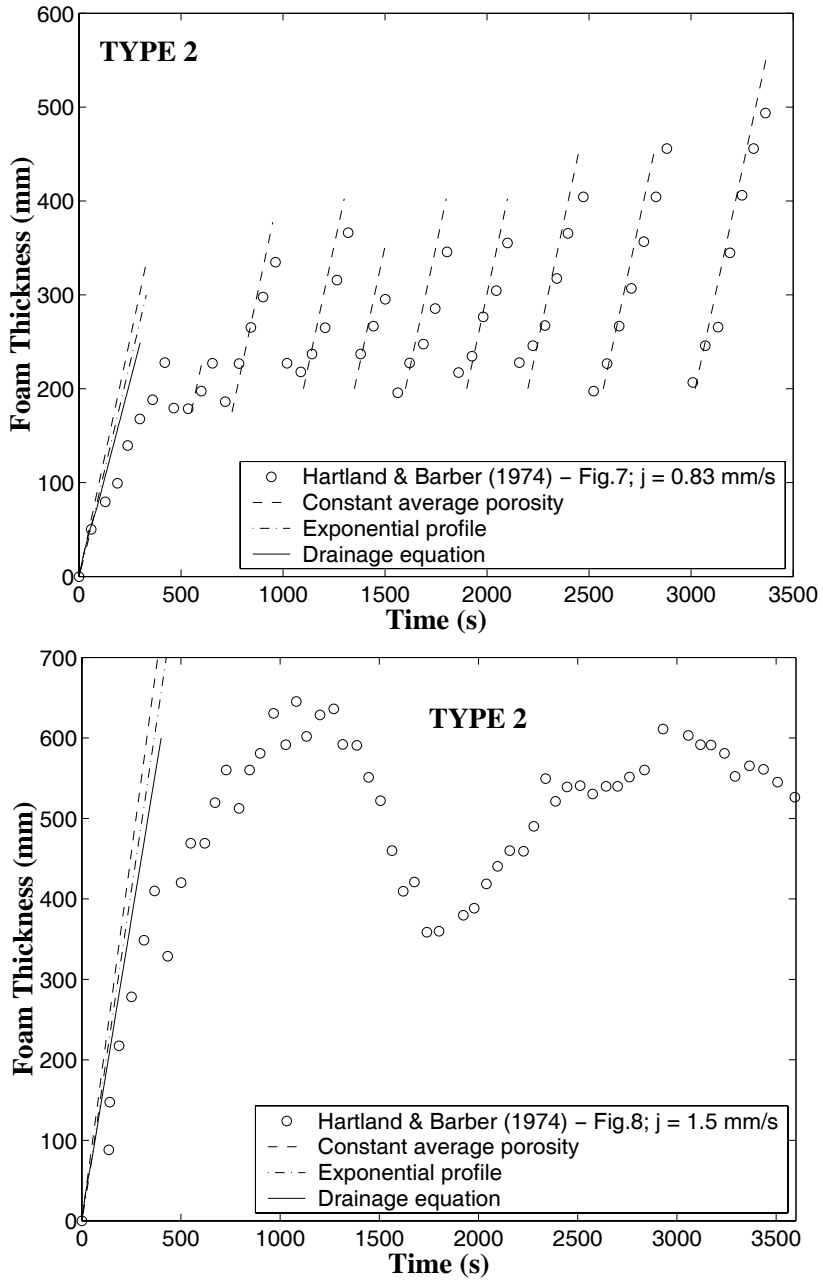

Figure 2.7. Evolution of the foam thickness with time for nitrogen flux of j=0.83 mm/s (top) and 1.5 mm/s (bottom) in a solution containing 800 g sucrose, 0.52l glycerol, 1.l distilled water, 600 mg/l aerosol OT (Hartland & Barber, 1974).

before the foam reaches a steady state. This is believed to be due to the larger gas flow rates that create disturbances in the liquid and at the liquid/foam interface causing the film at the top of the foam to rupture at larger thicknesses. This phenomena is amplified for large superficial gas velocity where foam changes quickly to a steady state froth as suggested by Hartland and Barber [54] (see Figures 2.8 and 2.9). Therefore, transients of type 2 feature a bifurcating behavior between two possible steady states: (i) steady-state foam and (ii) steady-state froth. Oscillations of the foam thickness with time at intermediate superficial gas velocity are discussed in the next section.

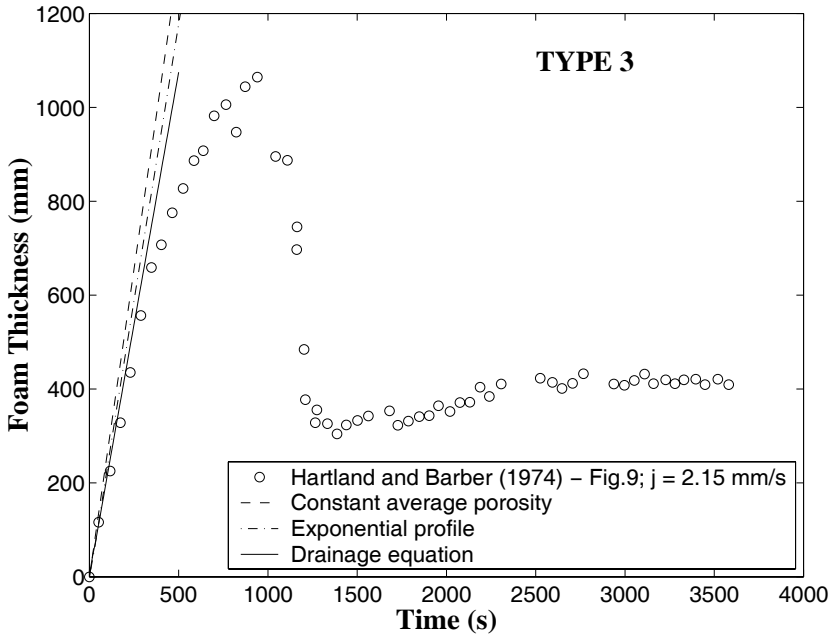

Figure 2.8. Comparison of the model predictions with experimental data for nitrogen flux of j=2.15 mm/s in a solution containing 800 g sucrose, 0.52l glycerol, 1.l distilled water, 600 mg/l aerosol OT (Hartland & Barber, 1974).

2.4.2. Oscillations of the Foam Thickness with Time

For low superficial gas velocity (type 1), the steady-state foam thickness oscillates slightly around its mean value, but it was not possible to identify any periodicity,

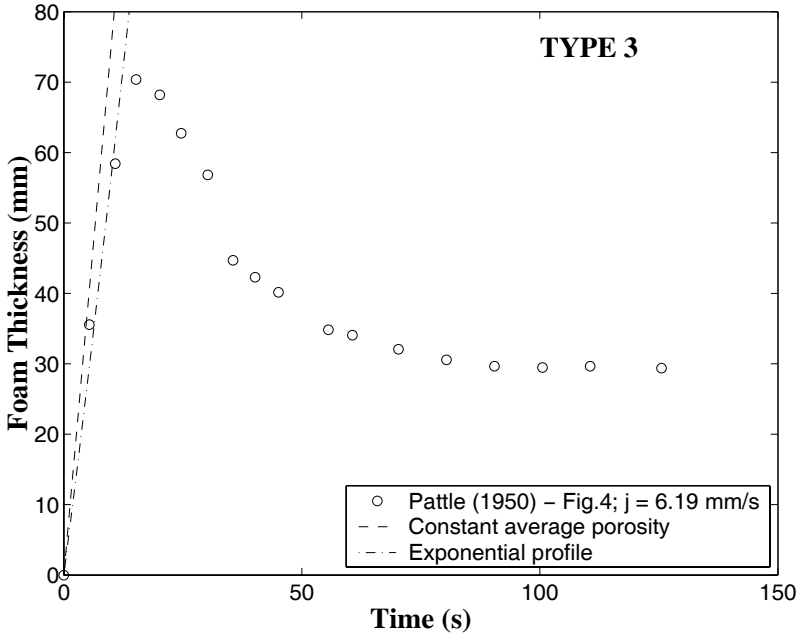

Figure 2.9. Evolution of the foam thickness with time for nitrogen flux of j=6.2 mm/s in 0.3% gum arabic + 1.5% isobutyl alcohol in water solution (Pattle, 1950).

possibly, due to a small sampling rate. However, for intermediate superficial gas velocity (type 2) it is believed that the foam thickness oscillates significantly due to the discrete character of the bubble rupture at the top of the foam. Several mechanisms explaining such a behavior can be suggested:

1. The first bubble bursting at the top of the foam generates a high velocity liquid jet that breaks up into a number of small drops as observed for a single bubble bursting at a free surface [4]. Those drops, when falling back on top of the foam, cause the bubbles sufficiently drained to burst almost simultaneously in a chain reaction. Note that this rupture mechanism has been observed for small single bubbles [less than 5 mm in diameter [4]] bursting at the free surface of a liquid. No jet was observed for large bubbles indicating that the pressure inside the bubble has to be high enough to generate a jet that later breaks up into drops [4]. Moreover, the collapse of standing foams has been observed to be discontinuous [16], and $H(t)$ is a step function rather than a continous function

of time [16]. The stages of collapse were longer for higher surface tension and lower viscosity [16]. This can be explained in terms of the proposed mechanism, by virtue of the fact that the viscosity tends to slow down the jet due to viscous dissipation [4], and the surface tension increases the energy released when the bubbles burst. Note that in the experimental data set reported in Figures 2.4 [31], the mean diameter of the bubbles at the top of the foam increases with the superficial gas velocity but remains less than 3.2 mm indicating that the bubbles could generate a jet when bursting.

2. The first bubble bursting at the top of the foam creates a pressure wave (detonation) propagating through the foam. The magnitude of the detonation depends on the bubble size and is larger for small bubbles since their inside pressure is larger than that of large bubbles. The viscous forces limit the propagation of the pressure wave and a larger surface tension increases the amplitude of the detonation.

For both mechanisms the bubbles that still have thick lamellae can stand the disturbance and act as a protection preventing the entire foam from collapsing. This is confirmed by experimental observation on cells cultivated in a bioreactor that undergo severe damages due the burst of small bubbles close to the free surface [4]. However, the damage is significantly reduced in the presence of a slowly draining foam covering the free surface of the reactor [4]. For low superficial gas velocities and as observed in Figures 2.4, oscillations around the steady-state thickness tend to decrease as the superficial gas velocity increases. Similarly, for intermediate superficial gas velocity (type 2 transients), the oscillations are larger for smaller superficial gas velocity as shown in Figure 2.7, even though no steady state can be observed. This can be explained by the fact that as the superficial gas velocity increases, the steady-state foam thickness increases as well as the residence time of the bubbles in the foam allowing them to coalesce more. Thus, increasing the superficial gas velocity causes the bubbles at the top to increase in diameter and their inside pressure to decrease. Hence,

the rupture of large bubbles does not trigger the burst of other bubbles as much as does the rupture of smaller bubbles. For thick foams, the bubbles at the top of the foam have a large mean diameter and their rupture can be considered as an isolated event that may generate neither a jet nor a strong detonation. Therefore, the oscillations of the foam thickness become smoother as the superficial gas velocity increases. The major difference between type 1 and type 2 transients can be attributed to the agitation in the liquid phase at the foam/liquid interface that increases with higher superficial gas velocity.

It is interesting to note (in Figure 2.7) that during the first few instants of the foam thickness growth, the experimental data deviate significantly from the predictions of Equation (2.5), i.e., bubbles start bursting soon after the beginning of the foam formation. At some point in time the foam suffers its first collapse and starts a cycle of linear growth with time followed by sudden and periodic collapses. Unlike the initial growth, the secondary growths closely follow Equation (2.5), i.e., no bubble burst at the top of the foam. As mentioned by Harland and Barber [54], below a certain height (i.e., 200 mm) the foam appeared to be stable and the collapse stopped when this height is reached and the foam starts growing again. It is believed that the 200 mm layer of stable foam acts as a cushion for the upper part and absorbs the agitation at the foam/liquid interface created by the rising bubbles. As a consequence to this "cushion", the upper part of the foam can grow without being affected by the agitation at the liquid/foam interface. The foam grows like in a transient of type 1 and follows Equation (2.5). When the first bubble bursts, it makes the unstable part of the foam collapse in a chain reaction down to 200 mm. The fact that at each growth the foam reaches a higher and higher thickness was attributed to the washing of dust and impurities on the tube walls that previously prevented the foam to grow [54].

2.5. Conclusions

This chapter presents a simple, experimentally validated approach to analyze the transient formation of a foam layer produced by injecting gas bubbles in a foaming solution. Three different regimes in the transient growth of the foam have been identified as a function of the superficial gas velocity: (i) at low superficial gas velocities, the foam thickness increases linearly with time and quickly reaches a steady state, (ii) at intermediate superficial gas velocities, the foam thickness exhibits large oscillations with time and never reaches a steady state, and (iii) at large superficial gas velocity, the foam thickness initially increases linearly and then suddenly collapses into a steady-state froth.

The proposed model is based on the mass conservation equation for the gas phase in the foam combined with three different models for the average porosity: (1) a constant average porosity of 0.82, (2) an exponential variation of average porosity with time, and (3) an approximate solution of the drainage equation. This model enables one to better understand the physical mechanisms that occur during the foam formation and the effects of the superficial gas velocity on the foam dynamics. The analysis provides the framework for more fundamental and detailed studies of the foam formation and leads to the following conclusions:

1. For practical calculations, a linear model given by Equation (2.5) with a constant average porosity equal to 0.82 can be used. The model predictions show very good agreement with experimental data for low superficial gas velocity and provide an upper limit for the foam thickness in the case of an intermediate and large superficial gas velocity.

2. In most of the experimental data used in the present work interbubble gas diffusion can be neglected. However, we also observed that for gases with large solubility in the liquid phase, interbubble gas diffusion could play an important role and should be accounted for. Thus, further experimental and modeling work is needed to better understand the effect of interbubble gas diffusion on

the transient foam thickness.When the gas solubility in the foaming solution is high, the Ostwald ripening effect becomes dominant, especially when the bubble size is small and the bubbles are polydispersed. In this case, the interbubble mass transfer becomes significant, and the proposed model may not be valid.

3. For intermediate superficial gas velocity featuring large transient oscillations of the foam thickness, two different mechanisms could be suggested to explain the foam dynamics. The first bubble bursting at the top of the foam generates either (1) a high velocity liquid jet that breaks up into a number of small drops, or (2) a pressure wave (detonation) propagating through the foam. Both mechanisms cause the bubbles sufficiently drained to burst in a chain reaction and explain qualitatively the experimental observations. However, more careful observations and measurements have to be performed in order to experimentally validate these mechanisms. The addition of salts to a surfactant solution and the Gibbs-Marangoni effect may have a profound effect on the film/interface stability, and this effect on the dynamics of the foam growth needs to be further investigated.

4. Additional work is needed on modeling the characteristic time for drainage and the lifetime of a critically thin lamellae. The mechanical effect of the disturbances at the liquid/foam interface on the total foam thickness should also be investigated.

5. The present work also contributes to better understanding of the decay of standing foams that was proven to be very sensitive to the bubble size distribution in the foam layer at the instant the gas supply is shut off [56]; the bubble size distribution at the beginning of the foam decay can only be determined in the limit of the dynamic foam growth, which is analyzed in this chapter.

NOMENCLATURE

A	Area of the container
a_i	Coefficients of the polynomial expansion of $\bar{\phi}$ in terms of z [Equation (2.7)]
b_i	Coefficients of the polynomial expansion of $\bar{\phi}$ in terms of t [Equation (2.32)]
c_v	Dimensionless parameter, Equation (2.2)
g	Specific gravity
$H(t)$	Transient foam thickness
j	Superficial gas velocity
j_m	Superficial gas velocity for onset of foaming
m	Mass
q_{PB}	Mass flow rate through the Plateau border
r	Local bubble radius in the foam
r_0	Average bubble radius in the foam
R	Universal gas constant $= 8.314 J/molK$
t	Time
z	Downward vertical elevation (see Figure 2.2)

Dimensionless numbers

Ca	Capillary number, defined in Equation (2.17)
Fr	Froude number, defined in Equation (2.17)
Re	Reynolds number, defined in Equation (2.17)

Greek symbols

α	Parameter, $= \sqrt{0.644}/0.322$, Equation (2.2)
ϕ	Foam porosity (volumetric gas fraction)
$\bar{\phi}(t)$	Average foam porosity
ϕ_1	Porosity at the top of the foam
ϕ_2	Porosity at the bottom of the foam
μ	Dynamic viscosity
ρ	Density
σ	Surface tension

τ	Characteristic time required to reach steady-state conditions
τ_c	Lifetime of the critically thin film
τ_d	Characteristic time for drainage

Subscripts

g	Refers to gas
max	Refers to the maximum value
min	Refers to the minimum value

Table 2.1. Summary of experimental conditions for studies reported in the literature and concerned with transient foam thickness.

Solution	**Dimensions I.D. & H_0**	**Gas**	**Gas flux (mm/s)**	σ **(mN/m)**	μ **(mPa · s)**	ρ **(kg/m^3)**	**T (^{o}C)**	**r_0 (mm)**	**Type Foam**	**Ref.**
Water + sucrose AR + glycerol SLR + aerosol OT	I.D.= 6.15cm H_0= N.A.	N_2	0. to 0.82	26	20	1220	30	3.9	1, 2, and 3	[54]
Water + 10% glycerin Marlophen 89 and 812	I.D.= 10cm H_0= 45cm	Xe	0.09 to 0.3091	32.0 to 41.1	1.22	1014	20	0.5 to 0.78	1	[32]
Water + 10% glycerin Marlophen 89 and 812	I.D.= 10cm H_0= 45cm	N_2	0.09 to 0.3091	32.0 to 41.1	1.22	1014	20	0.5 to 0.78	1	[31]
0.3% gum arabic + water + 1.5% isobutyl alcohol		Air	6.2	260	N/A	N/A	Room temp.	0.7 to 1.	3	[61]

3. STEADY-STATE FOAM THICKNESS

3.1. Introduction

As discussed in the previous chapter, for small superficial gas velocities the foam thickness grows almost linearly until it reaches a steady-state. Then, the burst of the bubbles at the top of the foam is compensated by the supply of bubbles at the bottom. The objective of this chapter is to develop a model for predicting the steady-state foam thickness as a function of the thermophysical properties of the system, the bubble size, and the superficial gas velocity. The effects of the temperature (uniform across the foam), the initial liquid height, and the type of gas are also investigated.

3.2. Analysis

3.2.1. Current State of Knowledge

The first model predicting the steady-state foam height as a function of the superficial gas velocity j[1] has been proposed by Bikerman [62]. He suggested that below a critical superficial gas velocity j_{cr}, the steady-state foam thickness H_∞ increases linearly with the gas flux:

$$H_\infty = \Omega j \qquad \text{if } j \leq j_{cr} \tag{3.1}$$

where Ω is a constant called the "unit of foaminess" or "foaming index" and is considered to be a physical characteristic of the liquid corresponding to the residence time of a bubble in the foam. Beyond the critical mass flux j_{cr}, the entrainment of the

[1]The superficial gas velocity is defined as the gas flow rate in m^3/s divided by the cross sectional area of the container in m^2.

liquid into the foam by rising bubbles cannot be balanced by drainage and the foam thickness increases without limit. However, experimental data for viscous oils [53, 63] indicate that the transition from a steady-state foam to a constantly growing foam is not abrupt at $j = j_{cr}$ but continuous, thereby indicating that the "unit of foaminess" Ω in Equation (3.1) is not constant but increases as the mass flux j increases. Lin and Guthrie [64] observed that for low gas influx, a bubbly flow prevails, bubbles are small and spherical or ellipsoidal, and the foam thickness increases linearly with the superficial gas velocity, i.e., Equation (3.1) is valid. However, for higher gas influx, bubbles coalesce and churn-turbulent flow regime is observed with spherical-cap bubbles forming while rising to the surface, and the foam tends to be unstable, i.e., the foam thickness decreases with the gas flow rate. Moreover, Laimbock [9] has observed that foaming of soda-lime silicate glass at different temperatures was not possible for arbitrarily small gas flow rate; instead, a minimum superficial gas velocity j_m should be reached to initiate foaming. The same observations have been made for different solutions of water and glycerol [26, 31]. Application of Equation (3.1) to actual iron smelters was also questioned by Lin and Guthrie [64]; therefore, Equation (3.1) does not appear to be a general and satisfactory relation for describing the foaming behavior of liquids.

Watkins [65] has considered a cylindrical container filled with lubricating oils and in which air was injected at a constant flow rate. He observed that steady-state conditions could not be reached and that experimental results were not repeatable. He also noticed that foam rupture is neither random nor dependent on the foam thickness [65]. This led him to assume that the mass flow rate of gas leaving the foam due to the rupture of bubbles at the top layer of the foam is proportional to the area of the container. He also concluded that it is very unlikely for steady-state conditions to be observed in cylindrical containers. To systematically observe steady-state conditions, Watkins [65] suggested the use of a conical container so that the area of the container can change as foam thickness reaches a steady state. The experiments confirmed the validity and satisfactory repeatability of this approach. These findings

have been confirmed experimentally by other studies on mineral oil [66]. Monsalve and Schechter [56] also observed the poor reproducibility of their measurements, but they attributed it to the fact that the foam collapse is very sensitive to the initial bubble size distribution in the foam, a factor difficult to control.

Jeelani *et al.* [31] proposed a model for the steady-state foam thickness accounting for the binary coalescences taking place within the foam. The steady-state foam thickness was expressed as a functions of the thermophysical properties of the liquid phase, the binary coalescence time, and the average foam porosity. The binary coalescence time as well as the average foam porosity were determined experimentally from the measurements of the average bubble diameter along the foam height. Good agreement was found between the model's predictions and the experimental data for aqueous foams stabilized with glycerinate and surfactants. Unfortunately, most of the other experimental studies of steady-state foam thickness did not provide the variation of the average bubble diameter along the foam height and neither the binary coalescence time nor the average foam porosity can be determined, making impossible to validate the model for other solutions.

More recently, Hrma [53] developed a model for a steady-state foam blanket. The foam behavior is described in terms of two limiting gas fluxes: the threshold flux j_m corresponding to the minimum gas flux required to generate foam and the critical flux j_{cr} corresponding to the breakdown of steady-state conditions. Then, three different regimes can be identified: (1) If $j < j_m$, the gas flux j reaching the liquid surface is not sufficient to create a foam layer. If $j = j_m$, the foam layer consists of a monolayer of bubbles whose thickness is $2r_0$, where r_0 is the average radius of the bubbles. (2) If $j_m < j \leq j_{cr}$, the foam is steady and its thickness increases as the gas influx increases according to the following expression [53],

$$H_\infty = 2r_0 + 2r_0 b_h \left[\frac{1/j_m - 1/j_{cr}}{1/j - 1/j_{cr}} - 1 \right] \tag{3.2}$$

where r_0 is the average radius of bubbles in the foam, and b_h is a constant depending on the gravitational drainage and on the survival time of a critically thin film separating the foam from the atmosphere. (3) If $j \geq j_{cr}$, the excess of mass flux

over j_{cr} cannot be released at the top of the foam and has to be stored within the foam. Thus, the foam volume grows continuously and a steady state is never reached until all available liquid is dispersed in the foam [53]. Beyond a certain mass flux, vent holes may start developing within the foam, the foam thickness stops growing and may even start decreasing [31, 65]. Hrma [53] suggested that Equation (3.1) proposed by Bikerman [62] is only valid for evanescent foams for which the liquid lamellae separating the bubbles in the foam rupture as soon as the critical thickness of the foam is reached and for very small superficial gas velocity (i.e., $j \ll j_{cr}$). In that case, Eqs. (3.1) and (3.2) are equivalent as long as $b_h = 1$ and $\Omega \approx 2r_0/j_m$. Hrma [53] also suggested that Watkins' experiments [65] were characterized by similar threshold and critical gas fluxes ($j_m \simeq j_{cr}$) such that only a narrow range of fluxes j were able to generate a steady-state foam blanket. Moreover, several experimental studies [20, 21, 23, 26, 29–31] have shown that it is possible to obtain a steady-state foam within a cylindrical container of constant area filled with different fluids (see Table 3.1). Even if Hrma's model [53] provides an insight into the mechanism of foam formation and stability by explaining qualitatively reported experimental data, it cannot be used to predict the steady-state foam thickness due to the lack of either analytical or semi-empirical expressions for the critical mass flux and the parameter b_h as a function of thermophysical properties of the system.

A series of studies on slag foams in iron and steelmaking processes has been carried out to predict the steady-state foam thickness [20–24,29,30]. All the experiments consisted of bubbling argon in a cylindrical tank containing liquid CaO-SiO_2-FeO-MgO-Al_2O_3 slags at high temperatures. First, Ito and Fruehan [29] showed that the steady-state foam thickness for CaO-SiO_2-FeO slags is independent of the inside diameter of the container as long as it is larger than 3 cm. They also performed a dimensional analysis based on the Buckingham-Pi theorem to relate the unit of foaminess Ω, the liquid viscosity μ, the liquid density ρ, and the surface tension σ. Two dimensionless numbers were identified, and the foaming index Ω was found to be proportional to the ratio $(\mu/\sqrt{\sigma\rho})$ [30]. Jiang and Fruehan [23] confirmed the pre-

vious work, but suggested a different empirical constant of proportionality between Ω and $\mu/\sqrt{\sigma\rho}$. However, although the average bubble radius has been identified as an important parameter for the steady-state foam thickness [64], it was not considered in Ito and Fruehan's [29, 30] or in Jiang and Fruehan's [23] work. This point has been recognized by Zhang and Fruehan [20], and the dimensional analysis using Buckingham-Pi theorem has been performed again by adding the average bubble diameter D_0. Three dimensionless groups were identified, and a power type of law was assumed to relate them. Experimental data suggested the following semi-empirical expression for the unit of foaminess Ω [20]:

$$\Omega = 115\frac{\mu^{1.2}}{\sigma^{0.2}\rho D_0^{0.9}} \tag{3.3}$$

Equation (3.3) merits further discussion:

- Comparison between the measured and the experimental foam indices Ω for slag foams was plotted in logarithmic scale (Figure 17 in Ref. [20]), and after careful analysis, significant discrepancies (up to a factor 3 between predicted and experimental unit of foaminess) have been noted.

- Most of the studies [20–24, 29, 30] rely on the validity of Equation (3.1) which seems to be appropriate for slag foams but has been proven erroneous for other foaming solutions [9, 53, 61, 63] (see previous comments about Equation (3.1)).

- The semi-empirical Equation (3.3) is based on the experimental data obtained for slag foams of similar solutions containing CaO, FeO, SiO_2, MgO, and Al_2O_3, for which thermophysical properties (in particular the density and the surface tension), and the average bubble diameter do not vary significantly (see Table 3.1). Thus, the effects of density and surface tension on the steady-state foam thickness were not fully investigated. Therefore, in general one should not expect Equation (3.3) to be valid for other systems having very different thermophysical properties or average bubble diameters.

- Ghag *et al.* [26] studied pneumatic foams formed by bubbling nitrogen in different solutions containing water, glycerinate (78 to 95 vol.%), and SDBS as the surfactant. The authors showed that "there was a poor correlation" between their experimental data and Equation (3.3) proposed by Zhang and Fruehan [20]. Experimental results indicate that the foaming index predicted by Equation (3.3) should be more sensititive to changes in surface tension and that the exponent associated with the average bubble diameter D_0 was a major cause of the discrepancies.

From these observations, Ghag *et al.* [27, 28] examined three models for the unit of foaminess using the Buckingham-Pi theorem and assuming that Equation (3.1) is valid. They performed the same analysis as that by Zhang and Fruehan [20] but replaced the equilibrium surface tension by (1) the surface tension depression, (2) the Marangoni dilational modulus, and (3) the effective elasticity for solutions following Langmuir behavior. They concluded that the best of the three models was the one using the effective elasticity provided that the solution follows Langmuir behavior. Due to the complexity of the models and the fact that effective elasticity is not available to fully validate the model for a wide range of experimental conditions and solutions, it will not be discussed further.

Other authors [64, 67] modeled the steady-state foam thickness based on the mass and momentum conservation equations with applications to slag foaming in steel manufacturing. The validation of those models against experimental data appears to be limited and will not be discussed further.

Finally, a detailed model has been proposed to predict the thickness of pneumatic foams [14]. Figure 3.1 shows a schematic of a typical foam layer formed by injection of gas at the bottom of a vertical column containing a foaming liquid. For this

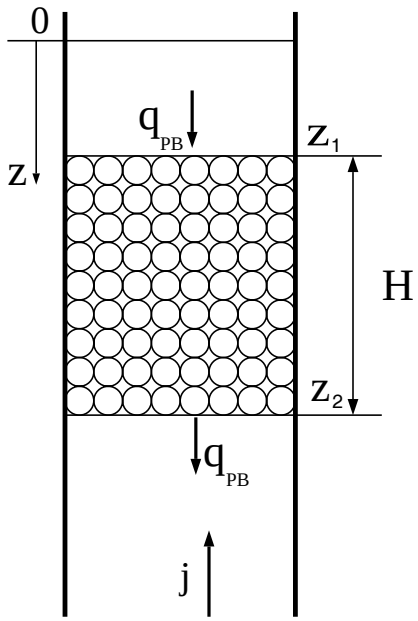

Figure 3.1. Schematic of a foam layer generated by bubbling and coordinate system with notations.

arrangement, Bhakta and Ruckenstein [14] proposed the following expression for z_1 and z_2, the vertical coordinates of the top and bottom of the foam, respectively:

$$\frac{\mathrm{dz_1}}{\mathrm{dt}} = \frac{\phi(z_1,t)q_{PB}(z_1,t)}{1-\phi(z_1,t)} \tag{3.4}$$

$$\frac{\mathrm{dz_2}}{\mathrm{dt}} = \frac{j}{\phi(z_2,t)} - q_{PB}(z_2,t) \tag{3.5}$$

where j is the superficial gas velocity, $\phi(z,t)$ is the volume fraction of gas (or porosity), and $q_{PB}(z,t)$ is the mass flow rate of liquid through the Plateau border at location z and time t. Since the total foam thickness can be expressed as $H_\infty = (z_2 - z_1)$ one obtains

$$\frac{\mathrm{dH}}{\mathrm{dt}} = \frac{\mathrm{d(z_2 - z_1)}}{\mathrm{dt}} = \frac{j}{\phi(z_2,t)} - q_{PB}(z_2,t) - \frac{q_{PB}(z_1,t)\phi(z_1,t)}{1-\phi(z_1,t)} \tag{3.6}$$

The first term on the right-hand side represents the increase of the foam thickness due to the incoming gas while the last two terms represent the decrease of the foam thickness due to the liquid leaving the foam through the Plateau borders and the gas leaving the foam due to bubble rupture at the top of the foam, respectively.

Assuming that (1) the foam bed consists of dodecahedron bubbles of the same size, (2) the Plateau borders are randomly oriented, (3) the drainage through the Plateau borders due to film thinning is negligible compared to that due to gravity (see Ref. [14, 17] for additional discussion), (4) coalescence of bubbles and Ostwald ripening within the foam are absent, (5) surface tension is constant, (6) the wall effects are negligible, and (7) the foam is under isothermal conditions, an expression for the volumic flow rate through the Plateau border $q_{PB}(z,t)$ is given by [15, 48]:

$$q_{PB}(z,t) = \left(\frac{3}{15}\right) N r n_p a_p u \tag{3.7}$$

where r is the bubble radius, N is the number of bubble per unit volume, n_p is the number of Plateau borders per bubble, a_p is the cross-sectional area of a Plateau border, and u is the velocity of the fluid through the Plateau border due to gravity drainage. An simplified expression for those parameters has been developed by Narsimhan and coworkers [15, 17] and can be reformulated as follows:

$$\begin{aligned} N &= \frac{3\phi}{4\pi r^3}, & n_p &= 10, \\ a_p &= \frac{4\pi r^3/3}{0.816 r n_p}\left(\frac{1-\phi}{\phi}\right), & u &= \frac{c_v a_p}{20\sqrt{3}\mu}\left[\rho g + \sigma \frac{d}{dz}\left(\frac{1}{\alpha a_p^{1/2}}\right)\right] \end{aligned} \tag{3.8}$$

where α is a dimensionless constant[2] [17], and the velocity coefficient c_v (dimensionless) accounts for the mobility of the walls of a Plateau border channel and has been computed by Desai and Kumar [55]. In most of their calculations, Ruckenstein and coworkers used $c_v = 1$ [14]. Combining Equation (3.7) with Equation (3.8) yields,

$$q_{PB}(z,t) = 3.632\times10^{-3} c_v \frac{[1-\phi(z,t)]^2}{\phi(z,t)}\left\{\frac{\rho g r^2}{\mu} + \frac{1.3957}{\alpha}\frac{\sigma r^2}{\mu}\frac{\partial}{\partial z}\left[\left(\frac{\phi(z,t)}{(1-\phi(z,t))r^2}\right)^{\frac{1}{2}}\right]\right\}$$

Equation (3.9) can be solved numerically and simultaneously with the transient equation for the foam porosity at height z and time t, $\phi(z,t)$ [14]. The porosity at the bottom of the foam layer $\phi(z_2,t)$ is assumed to be constant and equal to 0.74. The steady-state foam thickness is then obtained from the limit of the transient calculations ($t \to \infty$). However, this method for calculating the steady-state foam thickness

[2] $\alpha a_p^{1/2}$ represents the radius of curvature of the Plateau border [17].

may be time and resource consuming, and thus does not appear to be satisfactory for practical applications. Moreover, the solution has been proven to be highly sensitive to initial conditions [14] that are difficult to obtain either experimentally, analytically or numerically.

In the present work, an attempt is made to develop a general correlation capable of predicting the steady-state foam thickness for a wide variety of systems having widely different thermophysical properties and average bubble diameters. Instead of using Buckingham-Pi theorem, the governing Eqs. (3.6) and (3.9) for the foam thickness are properly scaled to obtain an expression for the steady-state foam thickness.

3.2.2. Dimensional Analysis

In this study, we assume isothermal conditions and that thermophysical properties are constant across the foam layer. We also assume that limitations and assumptions used to develop Eqs. (3.6) and (3.9) are valid. Eqs. (3.6) and (3.9) are nondimensionlized by using the following independent dimensionless variables:

$$z^* = \frac{z}{H_\infty}, \qquad r^* = \frac{r}{r_0}, \qquad j^* = \frac{j}{(j - j_m)}, \qquad t^* = \frac{t}{\tau} \tag{3.9}$$

where H_∞ is the steady-state foam thickness, r_0 is the average bubble radius, j_m is the superficial gas velocity of onset of foaming, and τ is the characteristic time for the foam formation. Substituting Eqs. (3.9) in Eqs. (3.6) and (3.9) yields

$$\begin{aligned}\frac{H_\infty}{\tau}\frac{\mathrm{dH}^*}{\mathrm{dt}^*} \quad &= \frac{j - j_m}{\phi(z_2^*)} j^* - 3.632 \times 10^{-3} c_v \frac{\rho g r_0^2}{\mu} r^{*2} \left[\frac{[1 - \phi(z_2^*, t^*)]^2}{\phi(z_2^*, t^*)} + 1 - \phi(z_1^*, t^*) \right] - \\ &\quad 5.069 \times 10^{-3} \alpha c_v \frac{\sigma r_0}{\mu H_\infty} r^* \left\{ \frac{[1 - \phi(z_2^*, t^*)]^2}{\phi(z_2^*, t^*)} \frac{\partial}{\partial z^*} \left[\left(\frac{\phi(z^*, t^*)}{(1 - \phi(z^*, t^*)) r^{*2}} \right)^{\frac{1}{2}} \right]_{z_2^*} + \right. \\ &\quad \left. [1 - \phi(z_1^*, t^*)] \frac{\partial}{\partial z^*} \left[\left(\frac{\phi(z^*, t^*)}{(1 - \phi(z^*, t^*)) r^{*2}} \right)^{\frac{1}{2}} \right]_{z_1^*} \right\}\end{aligned} \tag{3.10}$$

A further simplification can be obtained by chosing the characteristic time $\tau = H_\infty/(j - j_m)$; then, Equation (3.10) becomes

$$\begin{aligned}\frac{\mathrm{dH}^*}{\mathrm{dt}^*} &= \frac{j^*}{\phi(z_2^*)} - 3.632\times10^{-3} c_v \Pi_1 r^{*2}\left[\frac{[1-\phi(z_2^*,t^*)]^2}{\phi(z_2^*,t^*)} + 1 - \phi(z_1^*,t^*)\right] - \\ & 5.069\times10^{-3}\frac{\alpha c_v}{\Pi_2} r^* \left\{ \frac{[1-\phi(z_2^*,t^*)]^2}{\phi(z_2^*,t^*)} \frac{\partial}{\partial z^*}\left[\left(\frac{\phi(z^*,t^*)}{(1-\phi(z^*,t^*))r^{*2}}\right)^{\frac{1}{2}}\right]_{z_2^*} + \right. \\ & \left. [1-\phi(z_1^*,t^*)]\frac{\partial}{\partial z^*}\left[\left(\frac{\phi(z^*,t^*)}{(1-\phi(z^*,t^*))r^{*2}}\right)^{\frac{1}{2}}\right]_{z_1^*} \right\} \end{aligned} \tag{3.11}$$

where the two dimensionless parameters Π_1 and Π_2 can be identified:

$$\Pi_1 = \frac{\rho g r_0^2}{\mu(j-j_m)} \qquad \text{and} \qquad \Pi_2 = \frac{\mu H_\infty (j-j_m)}{\sigma r_0} \tag{3.12}$$

Π_1 can be interpreted as the ratio of the gravitational force to the viscous force on an average bubble of radius r_0 having a velocity $(j - j_m)$. Π_2 corresponds to the ratio of the viscous force to the surface tension force times the ratio of the steady-state foam characteristic height to the bubble characteristic dimension:

$$\Pi_1 = \frac{\rho g r_0^3}{\mu(j-j_m)r_0} = \frac{\text{gravitational force}}{\text{viscous force}} = \frac{Re}{Fr} \tag{3.13}$$

$$\Pi_2 = \frac{\mu(j-j_m)r_0}{\sigma r_0} \times \left(\frac{H_\infty}{r_0}\right) = \frac{\text{viscous force}}{\text{surface tension force}} \times \left(\frac{H_\infty}{r_0}\right) = Ca\left(\frac{H_\infty}{r_0}\right) \tag{3.14}$$

where Re, Fr, and Ca are the Reynolds, Froude and Capillary numbers, respectively, defined as:

$$Re = \frac{\rho_c (j-j_m) r_0}{\mu}, \qquad Fr = \frac{(j-j_m)^2}{g r_0}, \qquad Ca = \frac{\mu(j-j_m)}{\sigma} \tag{3.15}$$

The relationship between Π_1 and Π_2 is assumed to follow a power law, i.e.,

$$Ca\left(\frac{H_\infty}{r_0}\right) = K\left(\frac{Re}{Fr}\right)^n \tag{3.16}$$

where K and n are constant parameters determined from experimental data. Then, an expression for the steady-state foam thickness H_∞ can be deduced. Note that the choice of a power law to relate the dimensionless numbers Π_1 and Π_2 is arbitrary, but it

presents the advantage of capturing a wide variety of possible functional relationship between Π_1 and Π_2.

3.3. Results and Discussion

3.3.1. Results

Figure 3.1 shows a schematic of a typical experimental setup used to generate pneumatic foams by gas injection into a foaming liquid. An inert gas is injected in a foaming solution through a porous frit, a single or a multiple orifice nozzle at a constant superficial gas velocity, j. The container walls may have an effect on the foam growth [31, 54], and the container is often rinsed several times with the foaming solution before taking the measurements [31]. The gas is bubbled through the solution for several hours to ensure the saturation of the solution [32]. The steady-state foam thickness H_∞ is measured after more than 30 minutes to guarantee that a steady state is achieved [26, 31, 32]. The average bubble radius is typically obtained by means of a scale attached to the container and video images or photographs. Experimental data reported in the literature were collected and used to validate the dimensional analysis and to obtain the parameters K and n in Equation (3.16). Table 3.1 summarizes the experimental conditions used in the studies concerned with the steady-state thickness of foams formed by bubbling gas in a container filled with high viscosity foaming solutions. Most of the thermophysical properties of iron slags studied by Fruehan and coworkers [20–24, 29, 30] were computed from available models proposed in the literature and summarized in Ref. [68]. Data summarized in Table 3.1 were used to determine the parameters K and n. For the experimental data obtained by Zhang and Fruehan [22] for a 30%CaO-60%SiO_2-10%CaF_2 slag bubbled with argon, hydrogen, and helium, the dimensionless numbers Π_1 and Π_2 were computed assuming that the type of gas has little effect on the surface tension of the binary system gas/slag as observed by Hartland *et al.* [32] for 10% glycerinate + water + 120 mg/l of Marlophen

89 (see Table 3.2). The steady-state foam thickness from Fruehan and coworkers [20–24, 29, 30] results has been computed to account for the fact that the true foam thickness H_∞ was not measured but instead the distance h from the top of the foam to the initial level of liquid at rest. The foam thickness H_∞ was deduced from the experimental data for h by using the expression [29] $h = H_\infty \phi$ (obtained by writing the mass conservation equation for the liquid phase) and assuming $\phi = 0.8$. Note that the choice of $\phi = 0.8$ is based on experimental data for slag foams [64], and on the observation that the porosity "was between 0.7 and 0.9 and almost independent of the position in the foam" [29]. Moreover, parametric studies have shown that values of ϕ between 0.7 and 0.9 have little influence on the results both qualitatively and quantitatively. Indeed, the values obtained for the parameter K are 2932, 2905, and 2881, and -1.79, -1.80, and -1.81 for the parameter n, using the values of porosities $\phi = 0.7$, 0.8, and 0.9, respectively. Thus, considering the experimental uncertainties and that of the thermophysical properties, the choice of $\phi = 0.8$ to treat Fruehan and coworkers' data seems to be acceptable.

The superficial gas velocity for the onset of foaming j_m was determined assuming a linear relationship between the steady-state foam thickness H_∞ and the gas flux j such that $H_\infty = a(j - j_m)$ as shown in Figure 3.2. From Table 3.1 one can see that experimental studies have covered a wide range of density, viscosity, surface tension, and average bubble radius for more than 120 experimental data points. The dimensionless parameters Π_1 [$=Re/Fr$] and Π_2 [$=Ca\,(H_\infty/r_0)$] cover the range of 80 to 5030 and of 5×10^{-4} to 0.76, respectively. Figure 3.3 shows the relationship between the dimensionless parameters Π_1 and Π_2. Equation (3.16) appears to fit experimental data over a wide range of thermophysical properties with $K = 2905$ and $n = -1.80$ with a correlation coefficient $R^2_{corr} = 0.95$. In other words, the following relationship between the two dimensionless numbers has been determined:

$$\frac{H_\infty}{r_0} = \frac{2905}{Ca}\left(\frac{Fr}{Re}\right)^{1.80} \tag{3.17}$$

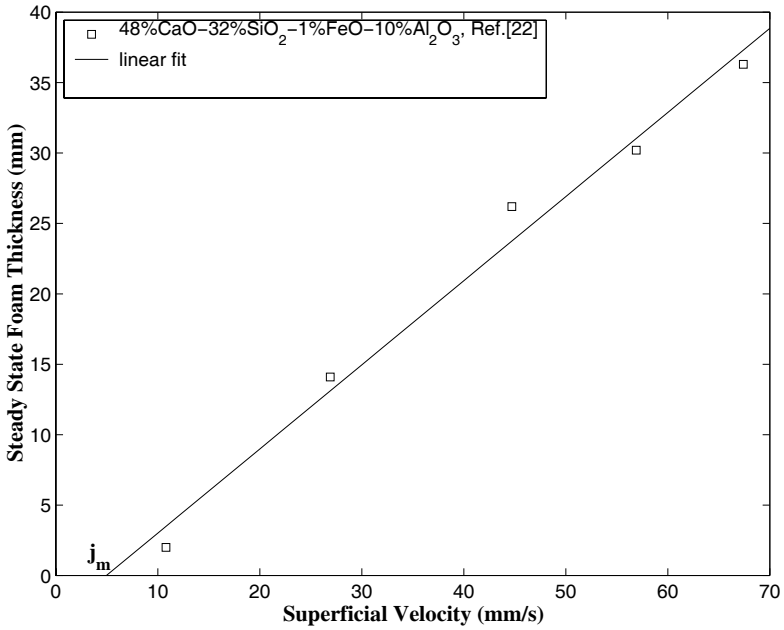

Figure 3.2. Steady state foam thickness vs. superficial argon velocity (Jung and Fruehan, 2000).

Equation (3.17) is general and should be preferred but in order to compare the present model with experimental findings, it is expressed in dimensional form:

$$H_\infty = 2905 \frac{\sigma}{r_0^{2.60}} \frac{[\mu(j - j_m)]^{0.80}}{(\rho g)^{1.80}} \tag{3.18}$$

The following is evident from Equation (3.18):

- The steady-state foam thickness H_∞ appears to be proportional to $(j - j_m)^{0.80}$ confirming the assumption made in determining the minimum superficial gas velocity for foaming j_m, i.e., $H_\infty \propto (j - j_m)$. The velocity j_m should be determined iteratively in general, but this was not judged necessary due to the proximity of the exponent 0.80 to unity and due to the experimental uncertainty in both the thermophysical properties and the experimental conditions; therefore, j_m in Eqs. (3.17) and (3.18) is obtained by assuming a linear relationship between H_∞ and $(j - j_m)$.

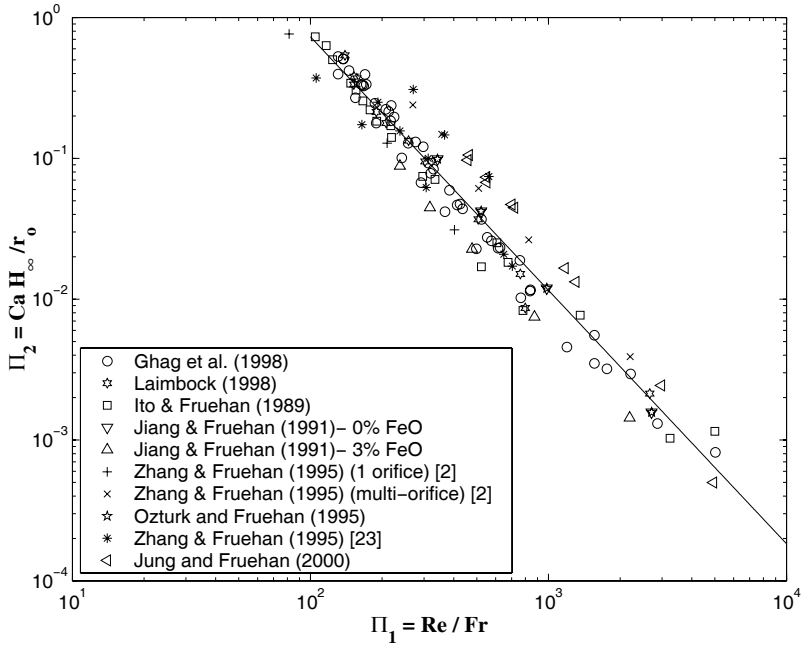

Figure 3.3. Correlation of dimensionless numbers Π_2 vs. Π_1.

- The steady-state foam thickness increases with an increase in the superficial gas velocity j.

- As the viscosity of the liquid phase μ increases, the drainage rate is reduced, the lamellae become thicker and more stable, and thus the foam thickness increases.

- On the contrary, the gravity and/or an increase in the liquid density ρ cause the foam to drain faster and to reduce its steady-state thickness.

- The effect of surface tension appears to be in contradiction with experimental observations: it has been observed that an increase in the surface tension σ tends to reduce the steady-state foam thickness [25,29]. This can be interpreted based on the fact that a decrease in the surface tension reduces the interfacial energy and, therefore, increases the foam stability and the steady-state foam thickness. The contradiction is evident if we assume that the surface tension and the average bubble radius are independent, but in reality they are not. In-

deed, when considering the effect of the surface tension on the foam thickness as suggested by Equation (3.18), one should account for the effect of the bubble radius as well, and, therefore, the ratio $\sigma/r_0^{2.60}$ represents the effect of surface tension. If one assumes that the pressure in the bubble is constant and equal to the pressure of injection in the bubbles, the Young-Laplace equation indicates that the bubble radius is proportional to the surface tension. This has been confirmed by Ogawa *et al.* [69] who observed experimentally that the bubble radius increases linearly with the surface tension. Thus, Equation (3.18) suggests that if the surface tension decreases, the bubble radius decreases by the same order, and the ratio $\sigma/r_0^{2.60}$ increases. Hence, according to Equation (3.17), the foam thickness increases, as the surface tension decreases in agreement with experimental observations.

Figure 3.4 compares the steady-state foam thickness obtained experimentally and calculated from Equation (3.18). One can see that most of the experimental data for highly viscous fluids are predicted by the present model within $\pm 35\%$ error. Note that for molten slags, experimental uncertainties are about $\pm 2\%$ for density, $\pm 10\%$ for surface tension, and about $\pm 25\%$ for viscosity [68]; therefore, models predicting those properties should not be expected to be more accurate. The biggest discrepancies encountered between the experimental steady-state foam thickness and the predictions of the model correspond to studies for which thermophysical properties were not measured but estimated from simple relations [20–24, 29, 30] and for which the bubble radius was visually determined [23, 24]. On the other hand, studies for which thermophysical properties of the solutions were measured [9, 26] show better agreement. Note also that the discrepancies appear to be higher for small steady-state foam thicknesses, i.e., for superficial gas velocities close to j_m. Consequently, given the uncertainty of the thermophysical properties and of the experimental measurements (in particular that for the average bubble radius), and given the wide range of thermophysical properties and experimental conditions, the agreement appears to be remarkably good.

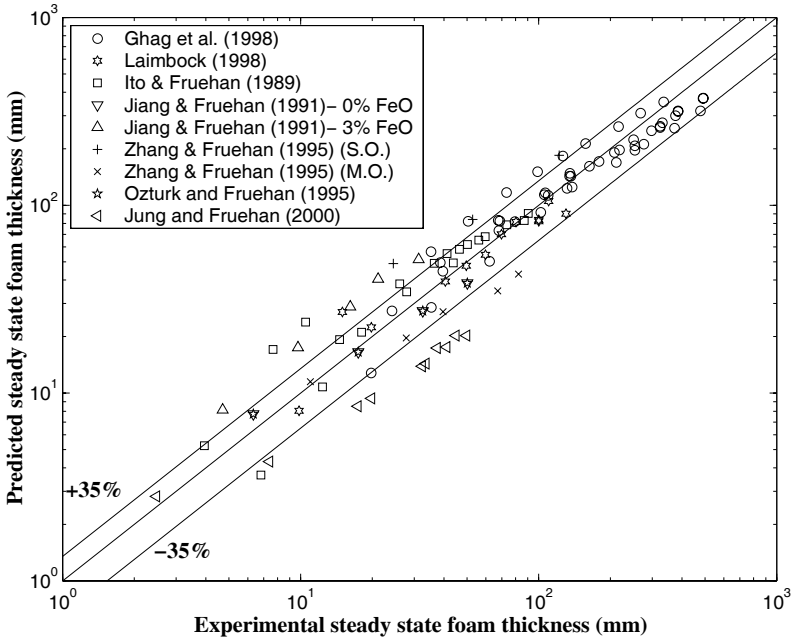

Figure 3.4. Comparison between experimental data and predictions of the steady-state foam thickness. S. O. stands for single orifice and M. O. for multiple orifice nozzle

3.3.2. Discussion

Several parameters have been identified in the literature as having an influence on the steady-state foam thickness:

- the thermophysical properties of the solutions (density, viscosity, surface tension)
- the bubble radius [20, 26]
- the temperature [5, 70] or the temperature gradient across the foam layer
- the dimensions of the container [23]
- the initial liquid height or volume at rest [5, 64, 67]
- the type of gas injected [22, 32]
- the pressure and composition of the surrounding atmosphere [9]

- the solid particules that may be present in the solution [21]

The effects of several of these parameters are discussed in the next few subsections. The present study is concerned with two-phase systems, and the effect of a third phase, like solid particles, will not be considered.

3.3.2.1. Effect of the Bubble Radius

A detailed study on foaming [26] reports the size distributions of bubbles reaching the foam/liquid interface using more than 200 samples. For a solution of water-85 wt.% glycerol and surfactants causing a surface tension depression[3] of 5 mN/m, the mean radius of 0.835 mm and a standard deviation of 0.105 mm were recorded, i.e., in terms of 95% confidence intervals, the bubble radius is 0.835 mm ± 24%. Thus, the bubble size distribution has rather wide tails around the mean value, and this should be accounted for in order to accurately predict the steady-state foam thickness. However, in this work, only the average bubble radius was considered and assumed to be independent of the superficial gas velocity, bearing in mind that it is a first order approach and based on the conclusion of Narsimhan and Ruckenstein [48] that "the symplifying assumption of equal size bubbles can be employed for the prediction of the stability of the foam bed when the inlet bubble size distribution is narrow, especially at high superficial gas velocity, high viscosities, larger inlet mean bubbles sizes".

Experimentally, different average bubble radius can be obtained via different injection systems, e.g., multiorifice nozzles produce smaller bubbles than single orifice nozzles [20], and gas injected through porous materials produces even smaller bubbles (see Table 3.1). It is evident from Equation (3.18) that the average bubble radius has a significant influence on the foam thickness due to an associated exponent of 2.60. Figure 3.5 compares the experimental steady-state foam thickness obtained for glass foams [9] with the model predictions using three different radii: the reported radius,

[3]The surface tension depression $\Delta\sigma$ is defined as the difference between the surface tension of the solution without surfactant σ_0 and that with surfactants σ, i.e. $\Delta\sigma = \sigma_0 - \sigma$.

and the reported radius with ± 10% deviation. One can see that the predictions vary

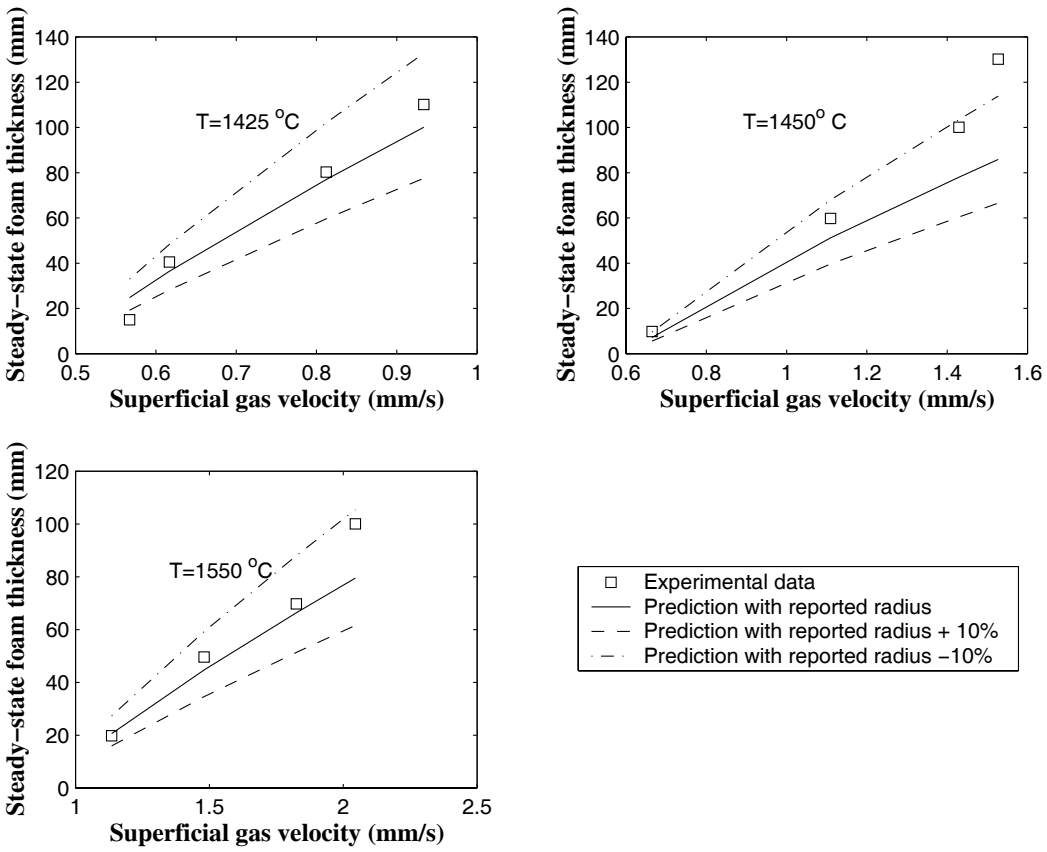

Figure 3.5. Influence of the bubble radius on the model predictions for glass foams (Laimbock, 1998).

significantly depending on the average bubble radius used and that, in this particular case, the experimental data lie within the prediction range. These observations provide further confidence in the model but also call for a more refined model that explicitely accounts for the bubble size distribution rather than using the average bubble radius.

3.3.2.2. Effect of Temperature

Cooper and Kitchener [70] found that foam stability increases with decreasing temperature. They attributed this effect to a higher viscosity as the temperature de-

creases. Actually, the temperature has an effect on all the thermophysical properties of the solution, but its effect on viscosity is by far more significant than that on the density and the surface tension. Our study uses experimental data taken over a wide range of temperatures for different fluids with thermophysical properties that behave distinctly in response to changes in the temperature (see Table 3.1), and predictions appear to be satisfactory. Therefore, the model developed in this study captures, in a satisfactory manner, the effect of the temperature on the steady-state foam thickness. In glass melting and other industrial furnaces, the foam layer may be subject to a large temperature gradient but its effect on the steady-state foam thickness remains to be explored.

3.3.2.3. Effect of the Container Dimensions and the Initial Liquid Height

As already mentioned, experimental data indicate that the container inside diameter has no influence on the steady-state foam thickness of iron slags if it is larger the 3 cm [29]. The experimental data used in the present work corresponds to such conditions (see Table 3.1 and it is assumed that the wall effect is negligible (I.D. $>$ 3 cm). Ozturk and Fruehan [5] found that the foaming index increases slightly with the initial slag depth and concluded that the steady-state foam thickness "is almost independent of the slag volume", but recognized that more experiments are needed to fully assess the effect of the initial liquid height. However, additional systematic studies showed that the steady-state foam thickness increases with the increase in the initial liquid height [64, 67]. On the other hand, Lin and Guthrie [64] observed that the initial liquid height had no effect for large initial liquid depth ($\geq$ 30 cm for water/air systems).

The correlation developed in the present work does not use explicitely the initial liquid height; however, we speculate that this height has an influence on the steady-state foam thickness through the superficial gas velocity for the onset of foaming j_m. Indeed, if the liquid depth is large enough, bubbles have time to reach their terminal

velocity and the onset of foaming should not depend significantly on the initial liquid height. On the contrary, if the initial liquid depth is small, the velocity at which bubbles reach the interface will depend on the initial liquid depth. Note that in the present study, j_m has been determined experimentally, i.e., if our speculation is correct, the effect of the initial liquid height, if any, has been accounted for. Although experimental work showed the existence of non-zero superficial gas velocity for the onset of foaming j_m [9, 26], to the best of our knowledge, no model for j_m has been proposed in the literature.

3.3.2.4. Effect of the Surrounding Atmosphere

The present study used data for foams generated under air at atmospheric pressure. However, two parameters characterizing the surrounding atmosphere can influence the steady-state foam thickness: (i) the total pressure, and (ii) the atmosphere chemical composition. An increase in the total pressure imposed at the top of the foam layer limits significantly the steady-state foam thickness [10]. Cable *et al.* [71] studied the foaming behavior of binary silicate melts and conclude that the atmosphere composition had a significant effect on the foam. They experimentally observed that no glass foam was observed in pure nitrogen atmosphere and that glass foams are more stable in pure oxygen atmosphere, confirming visual observations [9]. Kappel *et al.* [10] also showed that increasing the partial pressure of water on top of the glass foam destabilizes it. Injection of different gases on the top of the foam is a technique widely used in glass manufacturing to destroy the foam layer formed on the surface of the glass melt. The effect of the surrounding atmosphere has not been fully evaluated experimentally and should be further assessed.

3.3.2.5. Effect of the Gas Type Contained in the Bubbles

The thermophysical properties of the system affected by the type of gas bubbled in the solution are the surface tension, the gas diffusion coefficient and the gas solubility

in the liquid phase. For viscous liquids, foam lamellae are thick due to a slow drainage, therefore, Ostwald ripening and coalescence should not have a significant effect on the steady-state foam thickness. This is confirmed by the present work: data for relatively high viscosity fluids ($\mu > 46$ mPa·s) reported in Figure 3.3 and summarized in Table 3.1 follow the same trend and are characterized by the same experimental parameters K and n, even though obtained for different gases (air, helium, hydrogen, argon, nitrogen). The effect of the type of gas on viscous fluids has been studied by Zhang and Fruehan [22] who showed that the steady-state thickness of slag foam was affected neither by the gas pressure nor by the density of the gas inside the bubbles. Instead, the unit of foaminess obtained for different gases varied linearly with the viscosity of the gas contained in the bubbles, but the authors did not propose any physical interpretation of this effect. They also observed that there was "no change in the appearance as well as the size of the bubble cells in the foam no matter what type of gas was used". Further, they reported a relatively narrow bubble size distribution centered around a mean value of 13 mm $\pm$ 11.5%. These experimental observations indicate that no coalescence or Ostwald ripening was taking place within the slag foam (viscous fluid). Considering the uncertainties for the thermophysical properties and for the experimental data, one can conclude that the type of gas contained in the bubbles has little effect on the behavior of foams generated from viscous liquids. Then, the model developed in the present work gives satisfactory results.

For low viscosity fluids, however, such as those used by Hartland and coworkers [31, 32, 54], the foam lamellae become thin and coalescence and gas diffusion effects may play a significant role. Table 3.2 summarizes the conditions of studies concerned with the steady-state thickness of low viscosity fluids.Hartland *et al.* [32] showed that for low viscosity solutions, the foam height was reduced for gases of high solubility due to interbubble gas diffusion that tend to create bigger and less stable bubbles which can coalesce or burst within the foam and cause the foam to collapse. Results reported by Hartland and coworkers [31, 32, 54] for different gases injected in different low viscosity solutions are reproduced in Figure 3.6 in terms of the dimen-

sionless numbers Π_1 and Π_2. Table 3.3 summarizes relevant experimental conditions

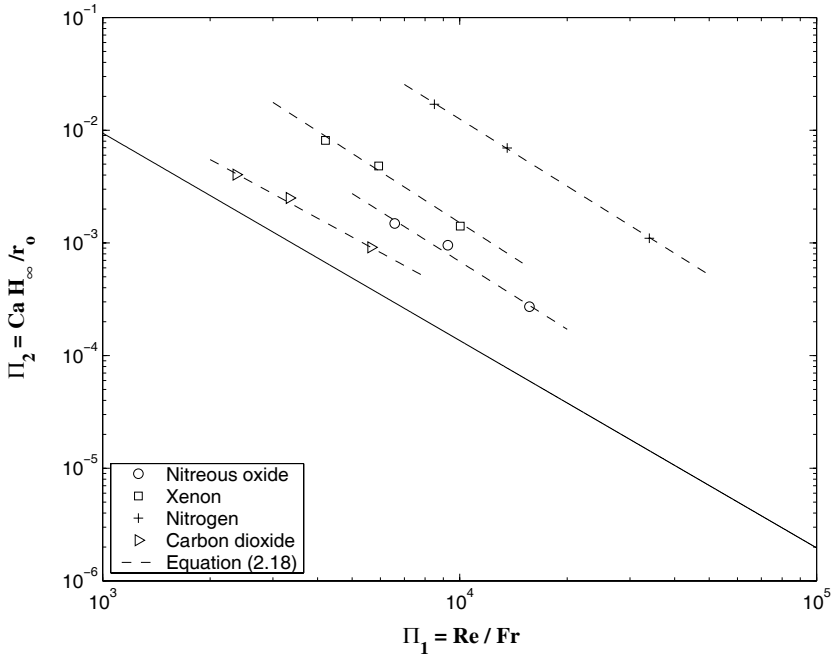

Figure 3.6. Correlation of dimensionless numbers Π_1 and Π_2 for different gases injected into low viscosity solutions.

and the experimental constants K and n. Note that for data reported by Hartland *et al.* [32] the size distribution and the average bubble radius change drastically along the foam height. More precisely, the bubble size distribution has a narrow bell shape at the bottom of the foam and flattens out toward the top as small bubbles become smaller and large bubbles become larger due to interbubble gas diffusion and bubble coalescence. Therefore, the discrepancies between the experimental data for low viscosity fluids and the present work [Equation (3.16)] can be explained by the fact that the bubbles size distribution is described by a single parameter r_0 taken as the average bubble radius at the bottom of the foam layer. While this approach seems to be sufficient for highly viscous fluids for which the porosity and the bubble size distribution are almost uniform across the foam layer [22,29], it is not satisfactory for low viscosity fluids where bubble coalescence and disproportionation are significant.

Moreover, it is worth noting that for the low viscosity solutions summarized in Tables 3.2 and 3.3, the parameter K changes with the type of gas while n is almost the same for all gases and is close to the exponent 1.80 found for highly viscous fluids. It is also interesting to remark that experimental data obtained for nitrogen bubbled in different low viscosity fluids and with bubbles of different radii occupy the same region of the Π_2 vs. Π_1 plot (Figure 3.6).

Finally, these findings tend to indicate that the deviation from the model developed in the present work should depend on the bubble size distribution and on the intrinsic properties of the gas phase. In other words, a third dimensionless number should be introduced by extending Equation (3.6) for the transient foam thickness to account for Ostwald ripening, bubble coalescence and other phenomena involving the gas phase, as well as for a non-uniform bubble size distribution within the foams. Note that these considerations have been neglected in the development of Eqs. (3.6) and (3.9) proposed by Bhakta and Ruckenstein [14] and by Narsimhan and Ruckenstein [15, 17]. The third dimensionless number would, then, depend on the thermophysical properties of the gas (e.g., solubility in the liquid phase, diffusion coefficient, etc.) and hopefully enable one to collapse the data on a single line as presented in this chapter for high viscosity fluids.

3.4. Conclusions

This chapter presents an approach to predict the thickness of pneumatic foams under steady-state and isothermal conditions. The governing equation for the transient foam thickness has been employed and a dimensional analysis has been performed. Two dimensional numbers have been identified as necessary to describe the formation and stability of this type of foam:

$$\Pi_1 = \frac{Re}{Fr} \qquad \text{and} \qquad \Pi_2 = Ca \times \frac{H_\infty}{r_0}$$

Physical interpretation of the dimensionless numbers has been proposed and the power-law type relation has been assumed between Π_1 to Π_2. Experimental data have

been used to determine the empirical paramaters of the correlation (i.e., $\Pi_2 = K\Pi_1^n$). The resulting semi-empirical model has been validated by comparing its predictions with available data covering a wide range of viscosity, density, surface tension, gas superficial velocity, and average bubble radius, with the following conclusions:

1. The relationship between the dimensionless parameters can be expressed as:

$$\frac{H_\infty}{r_0} = \frac{2905}{Ca}\left(\frac{Fr}{Re}\right)^{1.80}$$

   This equation is valid for foams formed from high viscosity liquids bubbled with nitrogen, air, and argon injected through single, multi-orifice nozzles or porous medium, and featuring the following thermophysical property and experimental condition ranges:

   - 46 mPa·s $< \mu <$ 12100 mPa·s,
   - 1200 kg/m^3 $< \rho <$ 3000 kg/m^3,
   - 69.5 mN/m $< \sigma <$ 478 mN/m,
   - $0 < j <$ 40 mm/s,
   - 0.7 mm $< r_0 <$ 20 mm.

2. Comparison between the developed semi-empirical correlation and the experimental data yields reasonable agreements (within 35% error) given the broadness of the bubble radius distribution around the mean value, the uncertainty of the experimental data and of the thermophysical properties.

3. Predictions are very sensitive to the average bubble radius and a more refined model is still needed which should be supported by a careful experimental studies.

4. The effects of the initial liquid height and of the surrounding atmosphere and that of the type of gases contained in the bubbles remain to be studied.

NOMENCLATURE

a_p	Cross-sectional area of a Plateau border
b_h	Parameter in Equation (3.2)
c_v	Dimensionless parameter, Equation (3.8)
D_0	Average bubble diameter in the foam ($= 2r_0$)
g	Specific gravity
H	Foam thickness
H_0	Initial height of the liquid in the container
H_∞	Steady-state foam thickness
j	Superficial gas velocity
j_{cr}	Critical superficial gas velocity
j_m	Superficial gas velocity for onset of foaming
K	Constant defined experimentally, Equation (3.16)
n	Constant defined experimentally, Equation (3.16)
n_p	Number of Plateau borders per bubble
N	Number of bubble per unit volume
q_{PB}	Mass flow rate through the Plateau border
r_0	Average bubble radius in the foam
R	Universal gas constant $= 8.314 J/molK$
R^2_{corr}	Correlation coefficient
T	Temperature
t	Time
u	Velocity of the fluid through the Plateau border due to gravity drainage
z	Downward vertical elevation (see Figure 3.1)

Dimensionless numbers

Ca	Capillary number, defined in Equation (3.15)
Fr	Froude number, defined in Equation (3.15)
Re	Reynolds number, defined in Equation (3.15)

Greek symbols

α	Dimensionless parameter, Equation (3.8)
β	Constant
ϕ	Foam porosity (volumetric gas fraction)
μ	Dynamic viscosity of the liquid phase
Ω	Unit of foaminess, constant defined experimentally, Equation (3.1)
$\Pi_{1,2}$	Dimensionless groups
ρ	Density
σ	Surface tension
τ	Characteristic time to reach steady-state conditions

Subscripts

1	Refers to the top of the foam layer
2	refers to the bottom of the foam layer

Superscript

$*$	Refers to dimensionless properties

Table 3.1. Summary of experimental data for steady-state foam thickness for high viscosity fluids reported in the literature.

Solution	**Dimensions I.D. & H_0**	**Gas**	**Nozzle type**	**Gas flux (mm/s)**	σ **(mN/m)**	μ **(mPa · s)**	ρ **(kg/m^3)**	**T (^{o}C)**	**r$_0$ (mm)**	**Ref.**
40%CaO-40%SiO_2	I.D.= 9.2cm	Argon	Single &	0 to	463.	398	2743	1500	7.8 to	[20]
5% FeO-15%Al_2O_3	H_0= 4.5cm		Multiple	50					13.5	
48%CaO-32%SiO_2	I.D.= 4.1cm	Argon	Single	0 to	477.2	381	2733	1600	12	[5]
10%FeO-10%Al_2O_3	H_0= 4.2cm			30.						
75 SiO_2-15 NaO_2	I.D.= 6.5cm	Air	Single	0 to	297.7 to	7450 to	2346.6 to	1425 to	15 to	[9]
-10 CaO (wt.%) glass	H_0= 2.cm			2.5	307.7	12100	2358.6	1500	20	
water + 78% to 95%	I.D.= 10.7cm	N_2	Pyrex®	0.83 to	69.5 to	46.5 to	1204 to	20	0.7 to	[26]
glycerinate +SDBS	H_0= 16.7cm		disk	1.5	72.3	520.8	1251		1.1	
30% FeO-42% SiO_2	I.D.= 3.2/5 cm	Argon	Single	0 to	477.9	1605	3055	1300	12	[29]
-28% CaO	H_0= N.A.			27.0						

Table 3.1. continued.

Solution	**Dimensions I.D. & H_0**	**Gas**	**Nozzle type**	**Gas flux (mm/s)**	σ **(mN/m)**	μ **(mPa · s)**	ρ **(kg/m^3)**	**T (^{o}C)**	**r$_0$ (mm)**	**Ref.**
3% FeO	I.D.= 9.2cm	Argon	Single	0 to	477.2	381	2733	1500	12	[23]
(CaO/SiO_2=1.25)	H_0= 4.5cm			30.3						
0% FeO	I.D.= 9.2cm	Argon	Single	0 to	472.8	396	2693	1500	12	[23]
(CaO/SiO_2=1.25)	H_0= 4.5cm			40.4						
30%CaO-60%SiO_2	I.D.= 4.1cm	Argon	Single	0 to	338	533 [72]	2534	1400 or	13	[21, 22]
10%CaF_2	H_0= 4.5cm	He, H_2		40.				1500		
34.78%CaO-33.76%SiO_2	I.D.= 4.5cm	Argon	Single	0 to	502	270	2958	1600	17	[24]
22.52%FeO-8.94%MgO	H_0= 4cm			67.3						
37.39%CaO-35.57%SiO_2	I.D.= 4.5cm	Argon	Single	0 to	493	291	2936	1600	17	[24]
20.87%FeO-6.17%MgO	H_0= 4cm			67.4						

Table 3.2. Summary of experimental data for steady-state foam thickness for low viscosity fluids reported in the literature.

Solution	**Dimensions I.D. & H_0**	**Gas**	**Nozzle type**	**Gas flux (mm/s)**	σ **(mN/m)**	μ **(mPa · s)**	ρ **(kg/m^3)**	**T (^{o}C)**	**r$_0$ (mm)**	**Ref.**
water + 10% glycerin	I.D.= 10cm	N_2	Frit	0.09 to	32.0 to	1.22	1014	20	0.5 to	[31]
Marlophen 89 and 812	H_0= 45cm		glass	0.31	41.1				0.78	
water + sucrose AR +	I.D.= 6.15cm	N_2	multiple	0. to	26	20	1220	30	3.9	[54]
glycerol SLR + aerosol OT	H_0= N.A.			0.82						
water + 10% glycerin	I.D.= 10cm	N_2, NO_x	Frit	0.09 to	32.0 to	1.22	1014	20	0.5 to	[32]
Marlophen 89 and 812	H_0= 45cm	Xe, CO_2	glass	0.3091	41.1				0.78	[32]

Table 3.3. Values of parameters K and n obtained from experimental data and relevant properties for different gases injected in low viscosity fluids.

Solution	**Concentration**	**Gas**	σ **(mN/m)**	μ **(mPa · s)**	ρ **(kg/m^3)**	**r$_0$ (mm)**	K	n	**Ref.**
water + 10% glycerin + Marlophen 89	120	N_2	32.1	1.22	1014	0.5	2.94×10^6	-2.04	
water + 10% glycerin + Marlophen 89	80	N_2	35.4	1.22	1014	0.5	4.13×10^8	-2.45	[31]
water + 10% glycerin + Marlophen 89	40	N_2	41.1	1.22	1014	0.5	4.94×10^5	-1.88	
water + 10% glycerin + Marlophen 812	80	N_2	35.4	1.22	1014	0.5	1.06×10^7	-2.08	
water + sucrose AR + glycerol SLR + aerosol OT	120	N_2	26	20	1220	3.9	8.37×10^5	-1.90	Hartland & Barber [54]
water + 10% glycerin + Marlophen 89	120	N_2	32.1	1.22	1014	0.5	1.05×10^6	-1.98	
water + 10% glycerin + Marlophen 89	120	NO_x	31	1.22	1014	0.5	6.85×10^4	-2.00	[32]
water + 10% glycerin + Marlophen 89	120	Xe	31.52	1.22	1014	0.4	2.19×10^5	-2.04	
water + 10% glycerin + Marlophen 89	120	CO_2	31.13	1.22	1014	0.3	2.82×10^3	-1.73	

4. MINIMUM SUPERFICIAL GAS VELOCITY FOR ONSET OF FOAMING

4.1. Introduction

In one-dimensional two-phase flow, the area-averaged superficial velocities for the gas and liquid phases denoted j_f and j_g, respectively, can be expressed as a function of the area-averaged velocities of the liquid v_f and gas phase v_g and of the area-averaged void fraction α [36]:

$$j_g = \alpha v_g \qquad \text{and} \qquad j_f = (1-\alpha)v_f \tag{4.1}$$

The superficial velocities of the gas and the liquid phases can also be expressed as a function of the volumetric flow rates:

$$j_g = \frac{Q_g}{A} \qquad \text{and} \qquad j_f = \frac{Q_f}{A} \tag{4.2}$$

where Q_g and Q_f are the volumetric flow rates of the gas and liquid phases, respectively, while A is the cross-sectional area of the container. Thus, the superficial velocities j_g and j_f can be easily monitored experimentally. Finally, the velocity of the center of volume of the mixture j can be expressed as

$$j = j_g + j_f \tag{4.3}$$

The so-called drift velocity is defined as the relative velocity of the gas phase with respect to the velocity of the center of volume of the mixture [36]. The drift velocity V_{gj} and the associated drift flux j_{gf} are given, respectively, by [36, 73]:

$$V_{gj} \equiv v_g - j \qquad \text{and} \qquad j_{gf} \equiv \alpha V_{gj} \tag{4.4}$$

As previously discussed, foaming does not occur for any arbitrarily small superficial gas velocity. Instead, a minimum superficial gas velocity j_m is required to initiate

foaming [9, 35, 53]. Bukur *et al.* [33] showed that the history of the system has a strong influence on the foam formation. Their main experimental observations can be summarized as follows: (1) foam is obtained when the superficial gas velocity is slowly increased from zero to values larger the minimum superficial gas velocity for onset of foaming j_m; (2) if the gas phase is injected instantaneously at a superficial gas velocity exceeding j_m, foam is not generated; (3) foam grows as the superficial gas velocity is increased beyond j_m but disappear beyond a critical value, then only bubbly flow is present in the column; (4) finally, foam forms again if the superficial gas velocity decreases below a second critical value. Graphically, the foam thickness or the gas hold-up in the bubble column features an hysteresis when plotted as a function of the superficial gas velocity [33].

The drift flux j_{gf} for different two-phase flow regimes can be written in the general form as [36]

$$j_{gf} = K v_\infty \alpha (1-\alpha)^n \tag{4.5}$$

where K is a parameter depending on the bubble radius and v_∞ is the velocity of a single bubble of radius r rising in a quiescent liquid. The present study is concerned with a gas-liquid flow with the liquid phase at rest. Thus, the superficial liquid velocity vanishes, i.e., j_f=0. Then, according to Equation (4.3) the area-averaged superficial gas velocity j_g equals j. Then, from Equations (4.3) and (4.4) the drift flux can be expressed as

$$j_{gf} = (1-\alpha) j_g \tag{4.6}$$

Figure 4.1 shows the drift flux j_{gf} plotted versus the void fraction α as given by Equations (4.5) (solid line) and (4.6)(dashed line). One can observe that for any positive superficial gas velocity j_g, Equations (4.5) and (4.6) are simultaneously satisfied for two different values of the void fraction, i.e., there are two functioning points as previously discussed by Wallis [36]. The first functioning point falls into the bubbly flow regime (low void fraction) and the second functioning point into the foamy regime (large void fraction). The foam occupies the upper part of the column and coexists with a bubbly region at the lower part as observed experimentally.

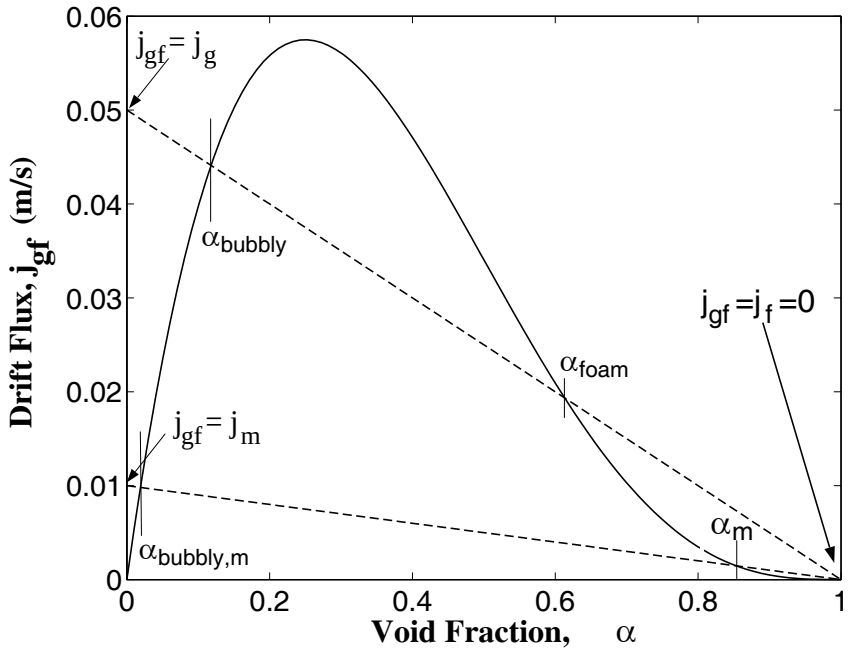

Figure 4.1. Functioning points obtained from Equations (4.5) (solid line) and (4.6) (dashed line) for superficial gas velocities j_g of 0.01 m/s and 0.05 cm/s with $j_f = 0$ m/s.

Experimental observations also indicate that pneumatic foams do not form for any arbitrarily small gas flow rate. Laimbock [9] has observed that a minimum superficial gas velocity should be reached to initiate foaming of molten glass. The same observations have been made for different aqueous solutions [26, 31–35], as well as for molten steel [5, 20, 22–24, 29, 30]. Figure 4.2 shows a typical plot of the steady-state foam thickness H_∞ as a function of the superficial gas velocity j_g and demonstrate the existence of a minimum superficial gas velocity for onset of foaming j_m. However, the drift-flux model predicts that the two functioning points always exist. Hence, a foam layer should form for any arbitrary small superficial gas velocity. This conclusion is obviously in contradiction with experimental observations discussed previously. Wallis attributed this to the instability of the foam leading to "rapid bubble bursting and agglomeration" [36]. The coexistence of a slug flow and a foam layer at the top of the bubble column has not been observed experimentally due to both reduced number of

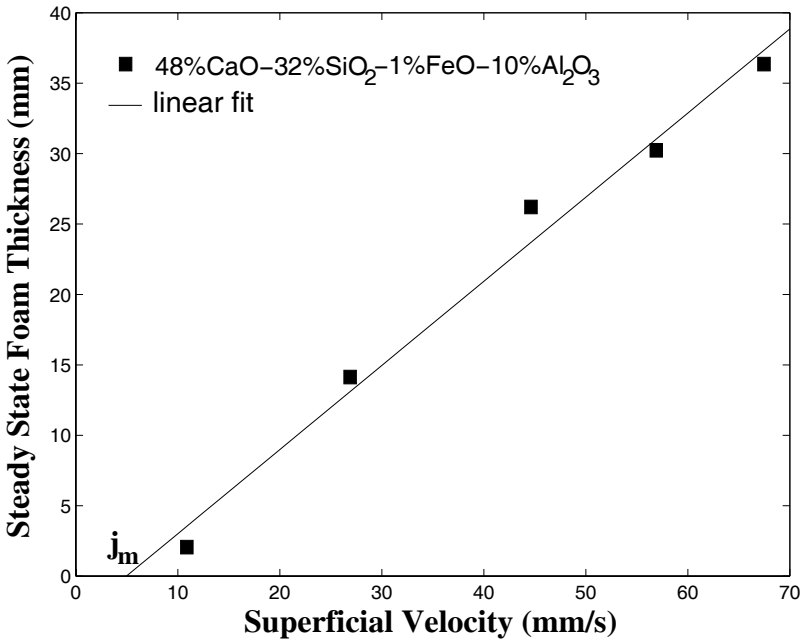

Figure 4.2. Typical plot of the steady state foam thickness vs. superficial argon velocity (based on data reported by Jung and Fruehan, 2000).

small bubbles and the agitation caused by slug bubbles bursting at the free surface and breaking the foam layer.

Whether foam is desirable or not, it is of fundamental and practical interest to understand the foaming process and to predict the conditions under which foam starts forming in order to operate a process under the most favorable conditions. The minimum superficial gas velocity for onset of foaming j_m should be determined as a function of the physicochemical properties of the two phases and the operating conditions. However, to the best of my knowledge, no self-contained model able to predict the minimum superficial gas velocity for onset of foaming j_m has been reported in the literature. The only attempt has been to determine the transition from the homogeneous bubbling regime to the foaming regime on a flow map plotting the void fraction versus the Froude number [35]. The map predicts "an estimate" of the minimum superficial gas velocity for onset of foaming as a function of the void fraction in the bubbly flow and of the container diameter. Moreover, the drift-flux model alone

fails to explain the existence of a minimal superficial gas velocity for onset of foaming as observed experimentally.

The objective of the present work is to provide physical explanations of the experimental facts and develop a quantitative self-contained model which gives the minimum superficial gas velocity as a function of the physicochemical properties of the two phases and the operating conditions by using the drift-flux model and paying particular attention to bubble coalescence.

4.2. Analysis

4.2.1. Physical Phenomena

In gas-liquid flow, bubbles of different sizes and velocities may collide resulting in the thinning of the film separating them. Collisions between two bubbles may lead either to the coalescence due to the rupture of the film or to bouncing and separation of the bubbles [74]. The coalescence rate of bubbles depends on the frequency of collision and on the probability that bubbles coalesce upon collision. The frequency of collisions depends on the liquid flow and on the hydrodynamic interactions between the bubbles and the liquid phase [75]. On the other hand, coalescence upon collision takes place when the collision duration time t_c is larger than the time to drain the film between bubbles t_d. In the limiting cases, the thinning of the film separating two colliding bubbles is dominated by either viscous or inertial forces. Finally, the probability of coalescence P should tend to unity when the ratio t_d/t_c is small and to zero when the ratio t_d/t_c is large. An expression for the probability of coalescence as a function of the collision duration time t_c and the drainage time t_d has been suggested [75]:

$$P = exp(-t_d/t_c) \tag{4.7}$$

The Weber number is commonly used in the studies of bubble coalescence [34, 74, 76] and represents the ratio of the inertial forces to the surface tension forces [74]:

$$We = \frac{\rho_f V^2 r}{\sigma} \tag{4.8}$$

where V is the relative velocity of centers of colliding bubbles. In pure water, Duineveld [74] observed three different bubble interaction behaviors: (1) when the Weber number based on the relative approaching velocity and denoted We_a is less than 0.18, bubbles coalesce; (2) for We_a larger than 0.18, and for Weber number We_∞ based on the terminal velocity of a single bubble v_∞ less than 3.3, bubbles bounce at the first contact but eventually coalesce; (3) for We_a and We_∞ larger than 0.18 and 3.3, respectively, bubbles bounce at the first collision and separate. Finally, experimental observations in low viscosity liquids show that bubble coalescence is inhibited when surfactants or electrolytes are added to the pure solution and is even terminated above a certain surfactant concentration [74, 76, 77].

Similarly, a single bubble reaching a free interface can either merge with the interface almost instantaneously (for small approaching velocities) or bounce back one or several times before stabilizing at the free interface to finally burst (for large approaching velocities). Kirkpatrick and Lockett [76] found that for Weber numbers larger than 0.5 (based on the bubble velocity) bubbles bounce one or several times before coalescing with the interface. They also showed that bubble coalescence is identical in doubly distilled water and in tap water. However, the presence of electrolyte inhibited coalescence of the bubble with the free interface [76].

Chesters [75] proposed an expression for the collision duration time t_c and for the drainage time t_d in both the viscous and the inertial dominated limiting cases assuming that bubbles have the same radius and both gas viscosity and van der Waals

forces can be ignored. In each limiting case, the ratio of the collision duration time t_c and for the drainage time t_d can be written as [75]

$$t_d/t_c = \left(\frac{\rho_f V^2 r}{32\sigma}\right)^{1/2} \quad \text{for inertia controlled drainage } (Re_\infty \leq 24) \tag{4.9}$$

$$t_d/t_c = \frac{3\mu}{\sqrt{2\sigma\rho_f r}} \quad \text{for viscosity controlled drainage } (Re_\infty > 24) \tag{4.10}$$

where V is the relative velocity of centers of colliding bubbles and r the average bubble radius. In the present work, r is assumed to be the average bubble radius at the liquid free surface, thus accounting for eventual bubble growth due to pressure change and coalescence taking place between the injection system and the liquid surface. Then, V is taken as the terminal velocity v_∞ of a single bubble of identical size rising in an infinite medium as suggested by Duineveld [74]. It can be interpreted as the relative velocity between the center of a rising bubble and that of a bubble at rest at the liquid free surface. The transition between the inertia and the viscosity controlled drainage regimes was assumed to occur when the corresponding characteristic time ratios given by Equation (4.9) and (4.10) are equal, i.e., when $Re_\infty = 24$. The ratio of the collision duration time t_c to the drainage time t_d can be seen as the scaling of the inertial or the viscous forces to the surface tension forces. Note that for inertia dominated drainage, the ratio of the characteristic times t_d/t_c is proportional to the square root of the dimensionless Weber number given by Equation (4.8). It is also interesting to note that in the viscosity dominated regime, the ratio t_d/t_c does not depends on the bubble velocity.

Finally, Figure 4.1 indicates that the void fraction for the functioning point in the foamy regime decreases as the superficial gas velocity increases. This suggests that as the superficial gas velocity increases, the bubbles at the top of the liquid column are less packed and their frequency of collision is reduced. Moreover, as the superficial gas velocity increases, the average bubble velocity increases while the probability of coalescence upon collision decreases in the case of inertia dominated drainage. For viscosity controlled drainage, the probability of coalescence is independent of the superficial gas velocity. In summary, increasing the superficial gas velocity, reduces

one or both components of the coalescence rate: 1) the frequency of collision and 2) the probability of coalescence for inertia dominated drainage. For a given combination of superficial gas velocity and void fraction, the coalescence rate is reduced enough to allow foam formation. Therefore, there exists a minimum superficial gas velocity and a corresponding maximum void fraction α_m for onset of foaming beyond which the foam is unstable and disappears instantaneously from the liquid interface. For void fraction smaller than α_m, bubbles are stable and do not coalesce enabling the formation of a foam layer. The conditions for onset of foaming are reached by increasing the superficial gas velocity beyond j_m, i.e., by reducing the void fraction above the liquid surface below α_m.

4.2.2. Modeling

The drift flux j_{gf} has been identified as a key variable in dealing with sedimentation, fluidization, and extraction experiments [78] and is expressed, in general, in terms of the terminal velocity v_∞ of a single bubble of radius r rising in an infinite volume of liquid, of the area-averaged void fraction α of the two-phase mixture, and of the physicochemical properties of the two phases [73].

As previously discussed, the present study is concerned with a gas-liquid flow for which the superficial liquid velocity vanishes, i.e., j_f=0. Moreover, the wall shear stresses are small and can safely be neglected as suggested by Wallis [36] and by Guitian and Joseph [79]. Therefore, the flow can be described as a vertical gravity dominated flow with no wall shear. Thus, the velocity and void fraction profiles at any given cross-section perpendicular to the two-phase flow are assumed to be uniform [36].

Expressions of the drift flux j_{gf} for different two-phase flow regimes along with the transition criteria as a function of the physicochemical properties of the system can be found in the literature. The analysis by Ishii and co-workers [78, 80] is based on

the dimensionless bubble radius r^* and on the viscosity number N_μ which represents the scaling of the viscous forces by the surface tension forces:

$$r^* = r\left[\frac{\rho_f(\rho_f-\rho_g)g}{\mu_f^2}\right]^{1/3} \qquad \text{and} \qquad N_\mu = \frac{\mu_f}{\sigma}\left[\frac{(\rho_f-\rho_g)g\sigma}{\rho_f^2}\right]^{1/4} \tag{4.11}$$

where σ is the surface tension of the gas/liquid system and μ_f and ρ_f are the dynamic viscosity and the density of the liquid phase, respectively. The average bubble radius and the specific gravity are denoted r and g, respectively. The Reynolds number of a single bubble of radius r rising in an infinite liquid with the terminal velocity v_∞ can be expressed as [78]

$$Re_\infty = \frac{2r\rho_f v_\infty}{\mu_f} \tag{4.12}$$

Three different regimes of gas-liquid systems are considered in the present study: (1) *the viscous regime* in which bubbles are spherical and a complete similarity exists between the expressions of the drag coefficient for a single particle system and for a multiparticle system, (2) *the distorted particle regime* in which the bubbles are distorted and the drag on an individual bubble is strongly affected by the wake generated by the other bubbles, and (3) *the churn-turbulent regime* in which the distorted bubbles influence not only the other bubbles but also the surrounding liquid. Expressions for the drift flux j_{gf} and for the terminal velocity v_∞ are available for each one of these regimes [78].

The viscous regime, can be divided in two sub-regimes namely, the Stokes' flow regime and the wake regime. In the Stokes' flow sub-regime ($Re_\infty \ll 1$) the drift flux can be expressed as [78]

$$j_{gf} = v_\infty \alpha(1-\alpha)^3 \tag{4.13}$$

with

$$v_\infty = \frac{2}{9}\frac{(\rho_f-\rho_g)gr^2}{\mu_f} \tag{4.14}$$

In the wake sub-regime, i.e., for larger Reynolds numbers ($Re_\infty \geq 1$), the drift flux is given by [78]

$$j_{gf} = v_\infty \alpha(1-\alpha)^3\left[\frac{1+\psi(r^*)}{1+\psi(r^*)(1-\alpha)^{9/7}}\right] \tag{4.15}$$

where $\psi(r^*)$ is a function of the dimensionless radius r^* and defined as

$$\psi(r^*) = 0.55\left[(1+0.08r^{*3})^{4/7}-1\right]^{0.75} \tag{4.16}$$

The terminal velocity of a single bubble rising in an infinite medium v_∞ is obtained from the force balance equating the buoyancy force to the drag force. The correlation for the drag coefficient as a function of the Reynolds number Re_∞ proposed by Ishii and Zuber [78] is used and the following non-linear equation is solved for v_∞

$$\frac{8(\rho_f-\rho_g)gr}{3\rho_f v_\infty^2} = \frac{24}{Re_\infty}(1+0.1Re_\infty^{0.75}) \tag{4.17}$$

Note that the Stokes' flow sub-regime is asymptotic to the wake regime in the limiting case when the Reynolds number Re_∞ is much smaller than unity. The transition between the viscous regime and the distorted bubble regime is expressed in terms of the viscosity number at the transition denoted $N_\mu|_t$ and given by

$$N_\mu|_t = 0.11\left[\frac{1+\psi(r^*)}{\psi(r^*)^{8/3}}\right] \tag{4.18}$$

For $N_\mu \leq N_\mu|_t$ the bubbles are spherical and the flow is in the viscous regime whereas for $N_\mu > N_\mu|_t$ the bubbles are distorted and the flow is in the distorted bubble regime.

In the distorted bubble regime the drift flux and the terminal velocity of a single bubble are expressed, respectively as [78],

$$j_{gf} = v_\infty\alpha(1-\alpha)^3\left[\frac{18.67}{1+17.67(1-\alpha)^{9/7}}\right] \approx v_\infty\alpha(1-\alpha)^{1.75} \tag{4.19}$$

and

$$v_\infty = \sqrt{2}\left[\frac{(\rho_f-\rho_g)g\sigma}{\rho_f^2}\right]^{1/4} \tag{4.20}$$

In the churn-turbulent regime, the drift flux and the terminal velocity of a single bubble are given, respectively, by [78]

$$j_{gf} = v_\infty\alpha(1-\alpha)^{1/4} \tag{4.21}$$

and

$$v_\infty = \sqrt{2}\left[\frac{(\rho_f-\rho_g)gr}{\rho_f^2}\right]^{1/4} \tag{4.22}$$

According to Ishii and Zuber [78], the transition from the distorted bubble regime to the churn-turbulent flow regime occurs for void fraction of 0.3. However, they

recognize that in case of batch processes, such as these presently under consideration, "detailed coalescence mechanisms and surface contaminations become important in determining the transition criterion", and the distorted bubble regime can remain even at high void fractions like in foams.

A general expression of the drift flux for the above described two-phase flow regimes can be derived from Equations (4.13) to (4.22):

$$j_{gf} = v_\infty f(r^*)\alpha(1-\alpha)^n \tag{4.23}$$

where $f(r^*)$ is a function of the dimensionless radius r^* and of the flow regime. Table 4.1 summarizes the expression for the terminal velocity v_∞ of a single bubble, the function $f(r^*)$, and the parameter n for gas-liquid mixtures in the three different flow regimes considered.

As discussed by Wallis [36] and Ishii and Zuber [78], there exists a maximum value of the void fraction up to which expressions for the drift flux j_{gf} and hence Equations (4.13) to (4.22) are valid. This maximum value depends on the shape of the particles and the nature of their interactions [36]. For gas/liquid systems, the flexibility of the bubble/liquid interface leads to negligible particle-particle interaction forces and the above expressions for the drift flux and for the superficial gas velocity for onset of foaming j_m in the different flow regimes are still valid for values of the void fraction α very close to unity, including foams or dense packing regimes [36, 78, 80]. Moreover, the drift-flux model has been validated for gas-liquid bubbly flow featuring void fraction close to unity such as foams [34, 36, 78–80]. Therefore, the drift-flux model can be used with confidence for predicting the onset of foaming since ideally, the onset of foaming corresponds to the situation when bubbly or churn-turbulent flow regimes with low void fraction prevail and coexist with only a single layer of packed bubbles accumulating at the free surface as shown in Figure 4.3. Here α_m corresponds to the maximum void fraction for onset of foaming. Then, combining

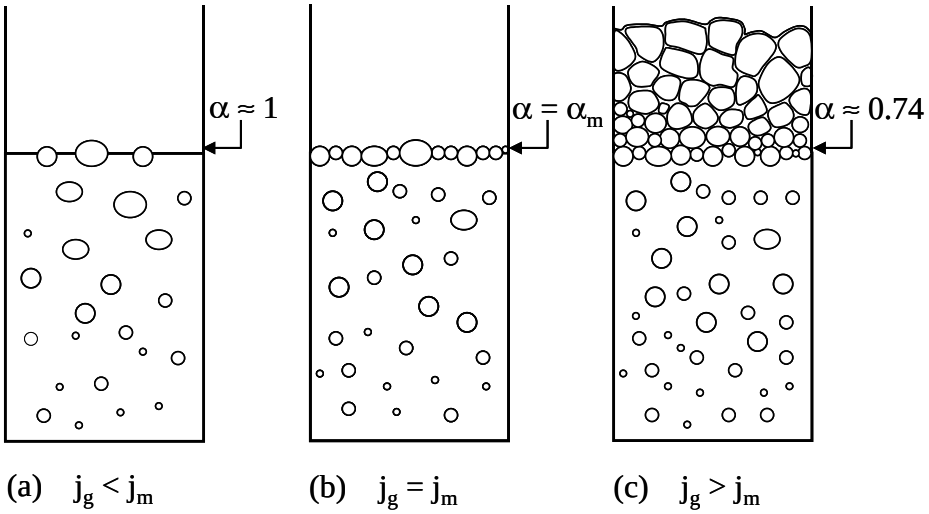

Figure 4.3. Schematic of the behavior of a foaming solution as the superficial gas velocity is increased (a) bubbly flow without foam, (b) onset of foaming, (c) developed foam layer.

Equations (4.6) and (4.23) at the onset of foaming, i.e., when $\alpha = \alpha_m$ leads to the following expression for the superficial gas velocity for onset of foaming j_m

$$j_m = v_\infty f(r^*)\alpha_m(1-\alpha_m)^{n-1} \tag{4.24}$$

where $f(r^*)$, r^* are summarized in Table 4.1.

Based on physical arguments, coalescence of rising bubbles with bubbles at rest at the liquid free surface has been identified as the main physical phenomena controlling foam formation. On the other hand, an expression for the minimum superficial gas velocity for onset of foaming j_m has been derived from the drift-flux model as a function of the maximum void fraction for onset of foaming α_m, operating conditions, and physicochemical properties of the two phases. To confirm this analysis, the model predictions should be compared against experimental data.

4.3. Results and Discussion

4.3.1. Experimental Data

The experimental data reported in Chapter 3 are also used in the present study. Additional data were obtained from the literature [34]. The minimum superficial gas velocity for onset of foaming j_m was determined experimentally by extrapolating the data for the steady-state foam thickness H_∞ as a function of the superficial gas velocity j_g and by assuming a linear relationship [i.e., $H_\infty \propto (j_g - j_m)$] as suggested in Chapter 3. Figure 4.2 shows a typical example of such an extrapolation used to determine j_m. The bubble shape and velocity v_∞ as well as the associated value of the parameter n were determined based on information summarized in Table 4.1. Note that the shape of the bubbles derived from Ishii's criteria agree with different models based on other dimensionless numbers than the viscosity number (see Ref. [81], p.27). Even though no transition criteria between the distorted bubble and the churn-turbulent regimes has been given, experimental data reported by Pino *et al.* [34] were assumed to feature a churn-turbulent regime as described by the authors. The radii of the bubbles for data reported by these researchers were found based on the following correlation relating the bubble radius to the gas flow rate [see Ref. [36], Equation (9.5), p.245]:

$$r = 0.648 \left(\frac{Q_g^2}{g} \right)^{1/5} \tag{4.25}$$

In molten steel slags, the bubbles were assumed to reach their terminal velocity before reaching the free interface, i.e., in less than 50 mm. This should be considered as a first order approximation that can be justified by the small values of the bubble sizes and terminal velocities. Finally, Equation (4.24) indicates that the knowledge of either j_m or α_m leads to the determination of the other. Finding α_m from j_m appears to be more reliable in the present analysis since a small uncertainty in α_m can lead to a significant error in the value of j_m, particularly in the foamy regime. In contrast, uncertainty in the experimentally determined value of j_m leads to a small

variation in α_m. Consequently, the maximum void fraction for onset of foaming α_m was obtained from the experimental data of j_m based on Equation (4.24). Table 4.2 summarizes the physicochemical properties and flow regimes for data collected from the literature. As one can see, experimental data cover a wide range of fluids, physicochemical properties, bubble sizes and shapes, flow regimes, and hydrodynamic conditions.

4.3.2. Regimes for Onset of Foaming

Figure 4.4 shows the plot of the minimum liquid hold-up for onset of foaming ($= [1 - \alpha_m]$) as a function of the ratio of the drainage time to the collision time t_d/t_c. Similarly, Figure 4.5 shows the variation of the minimum liquid hold-up as a

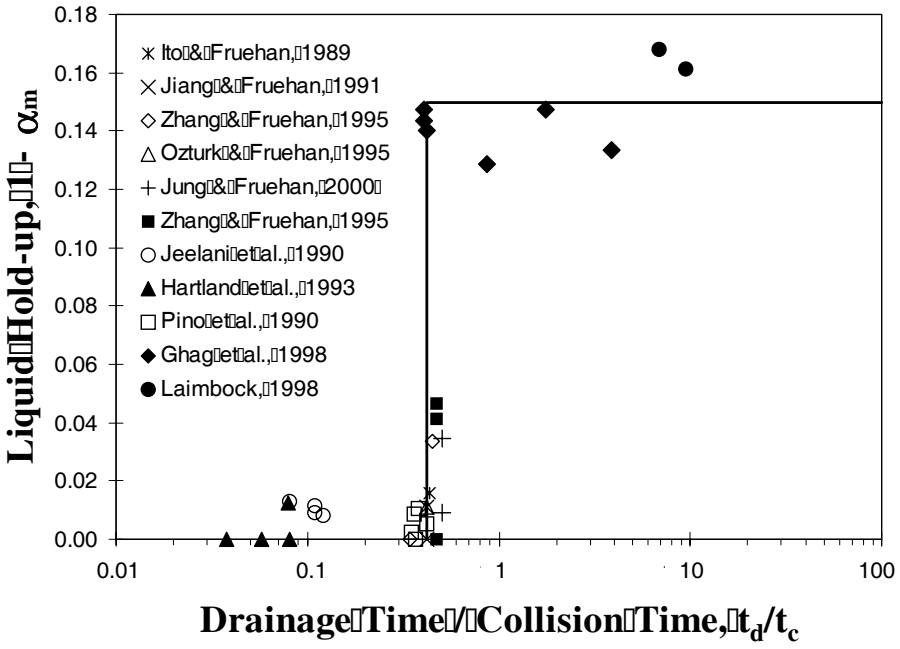

Figure 4.4. Liquid hold-up for onset of foaming (1-α_m) as a function of the characteristic time ratio t_d/t_c.

function of the probability of coalescence of a rising bubble with a bubble at rest at

the free surface as given by Equations (4.7), (4.9), and (4.10). In both figures, one

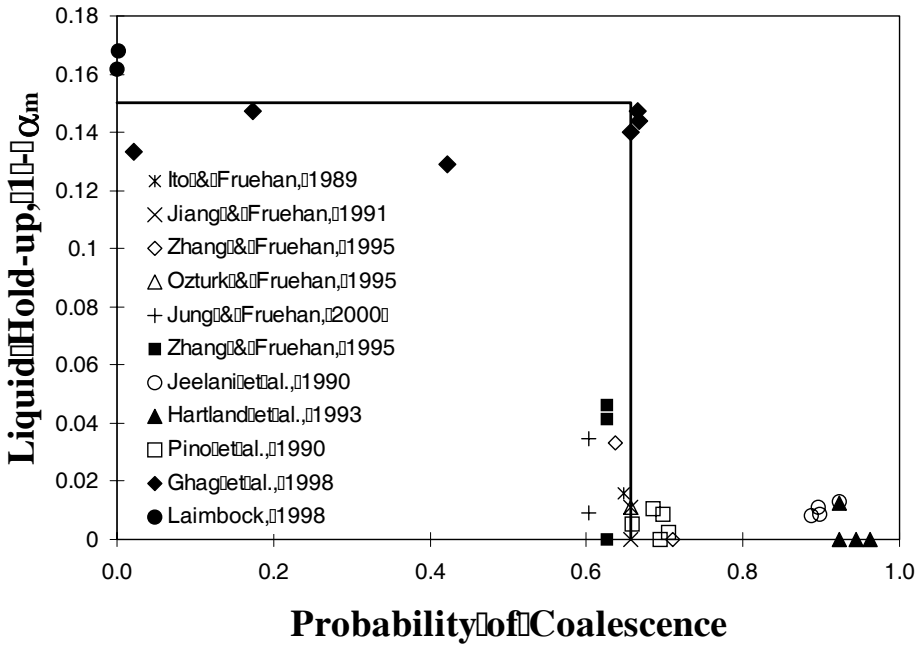

Figure 4.5. Liquid hold-up for onset of foaming (1-α_m) as a function of the probability of coalescence between rising bubbles and bubbles at rest at the liquid free surface.

can see a sharp transition in the liquid hold-up for onset of foaming corresponding to a characteristic time ratio of 0.42 and a probability of coalescence of 66 %. For the inertia dominated drainage, the transition expressed in terms of Weber number based on the terminal velocity occurs for $We_\infty = 5.6$. This value should be compared with $We_\infty = 3.3$ found by Duineveld for total inhibition of bubble coalescence in pure water [74], bearing in mind that inhibition of coalescence occurs over a range of Weber numbers and depends on the liquid properties.

Moreover, it is interesting to note that the void fraction for onset of foaming α_m obtained for large characteristic time ratio t_d/t_c (i.e., for small probability of bubble coalescence) is about 0.85. This is consistent with the fact that the onset of foaming corresponds to a physical situation between an interface free of foam and a layer of foam with a void fraction of 0.74 at the liquid/foam interface as schematically repre-

sented in Figure 4.3. In the former case, the void fraction above the liquid/surrouding interface is unity while in the latter case it corresponds to the maximum packing of spheres of same size. Experimental data indicate that, in the regime of low probability of bubble coalescence, bubbles are spherical and viscous forces dominate the thinning of the film separating bubbles.

Since the parameter n is empirically determined, a sensitivity study has been performed with an estimated $\pm 20\%$ error in the value of n given in Table 4.1. The results show similar trend as that previously discussed with a regime transition occuring at the same characteristic time ratio of 0.42. For large characteristic time ratio t_d/t_c, the average void fraction for onset of foaming α_m varies between 0.78 and 0.92 while that for large characteristic time ratio is larger than 0.99.

We speculate that coalescence of rising bubbles with a bubble at rest at the liquid free surface is a key phenomenon in the onset of foaming. If rising bubbles coalesce instantaneously with the bubble(s) at rest at the free surface, the bubble resulting from single or multiple coalescences becomes too large to be stable and bursts. Only a few large bubbles are present at the liquid free surface at a given time and foam cannot form. If bubble coalescence is somehow inhibited then, bubbles can accumulate at the liquid free surface and a foam layer starts forming.

For small characteristic time ratio ($t_d/t_c < 0.42$) and large probability of coalescence ($P > 66\%$) bubbles tend to coalesce more leading to larger bubbles that are forced to change from spherical to polyhedral shape in order to be stable [82]. Foams consisting of polyhedral bubbles can assume void fraction for onset of foaming α_m close to unity. In the static foam layer surfactants stabilize the liquid lamellae separating the bubbles thus reducing the probability of coalescence of bubbles and enabling the foam to be stable at large void fractions. In contrast, if bubble coalescence is strongly inhibited because of slow drainage and/or Plateau suction effects, bubbles keep their spherical shape and the maximum void fraction should correspond to the maximum packing of identical spheres (i.e., 0.74). The drift-flux model predicts that foam should form for any arbitrarily small superficial gas velocity and for

small superficial gas velocities the foam should have a void fraction close to unity (see Figure 4.1). The disagreement with experimental observations described earlier can be explained as follows: (1) for large bubble coalescence probability (i.e., small t_d/t_c), the functioning point predicted by the drift-flux model is unstable due to large unstable bubbles present and quickly bursting at the free surface and (2) for small bubble coalescence probability (i.e., large t_d/t_c) a functioning point in the foamy regime cannot be reached by the system since bubbles remain spherical leading to a foam morphology that cannot assume void fractions close to unity.

Experimental observations for the inertia dominated drainage showed that an increase in the viscosity of the liquid phase increases the coalescence rate owing to a reduction in the bubble velocity and to the formation of larger stable bubbles as reviewed by Pino *et al.* [34]. Finally, Bukur *et al.* [33] observed that no foam was generated when the liquid viscosity is too large. They attributed this phenomena to the fact that "coalescence increases with the liquid viscosity". Thus, a stable foam layer does not form due to the absence of a large number of small bubbles that coalesced before reaching the interface. These speculations are confirmed by the present analysis. Indeed, for inertia dominated drainage, an increase in the viscosity reduces the bubble velocity and thus the Weber number. Then, according to Equations (4.7) and (4.9), the probability of coalescence of a rising bubble with a bubble at rest at the free surface is close to unity.

Figure 4.6 compares the experimental data for the minimum superficial gas velocity for onset of foaming j_m with the model predictions given by Equation (4.24), using a maximum void fraction α_m of 0.85 in the case of small probability of coalescence ($P < 66\%$) between a rising bubble and a bubble at rest at the liquid free surface. Good agreement between experimental data and the model predictions is found. When the probability of coalescence is larger, the model predictions for j_m appear to be very sensitive to the void fraction α_m for onset of foaming.

The analysis developed in the present work does not use explicitely the initial liquid height; however, we speculate that this height has an influence on the superficial

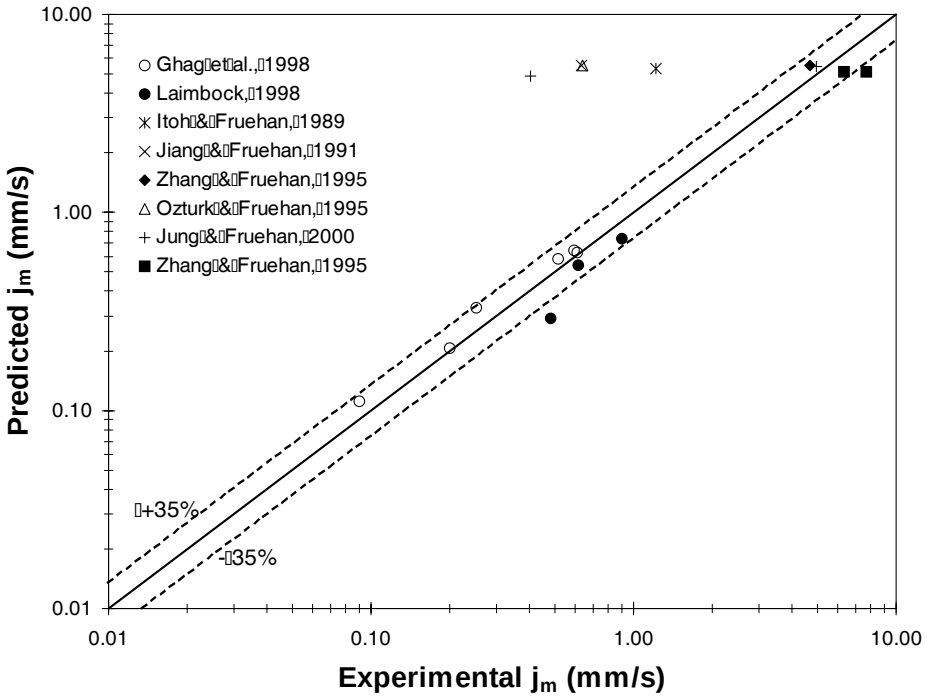

Figure 4.6. Comparison between experimental and predicted minimum superficial gas velocity for onset of foaming for viscosity dominated drainage, i.e., small characteristic time ratio t_d/t_c.

gas velocity for the onset of foaming j_m. Indeed, if the liquid depth is large enough, bubbles have time to reach their terminal velocity, and the onset of foaming should not depend significantly on the initial liquid height. In contrast, if the initial liquid depth is small, the velocity at which bubbles reach the interface will depend on the initial liquid depth. However, determining the approach velocity of a bubble in shallow baths requires the complex analysis of the bubble rise in which transient forces such as the Basset force and the added mass force must be accounted for [73,83]. Unfortunately, the complete formulation of the transient forces acting on a rising bubble is not available at the present time [83]. Moreover, the effect of the liquid height seems to be negligible for the experimental data collected in the literature and used in the present work. Thus, as a first order approximation, the approaching bubble velocity can be assumed to equal the terminal velocity v_∞.

The present study does not consider the effect of the container size on the onset of foaming since the model assumes uniform velocity and void fraction profiles at any given cross-section perpendicular to the two-phase flow. Such an assumption may not be valid for large containers where uniform void fraction and velocity are more difficult to obtain experimentally and where spreading of the foam over the liquid bath may be significant.

Finally, Guitian and Joseph [79] showed that the injection of the liquid phase at the bottom of the column (i.e., co-current flow with $j_f > 0$) delays the foam formation to larger superficial gas velocities and the condition for onset of foaming can be written as

$$j_g = a + bj_f \tag{4.26}$$

where a and b are constants independent of the superficial velocities j_g and j_f. The present work focuses on the constant $a = j_m$ and considered quiescent liquid for which $j_f = 0$.

4.3.3. Steady-State Foam Thickness

In Chapter 3 we have developed a semi-empirical correlation for predicting the steady-state foam thickness of viscous fluids ($\mu \geq 46mPa.s$) based on the dimensional analysis of the drainage equation [14]. It was found that the steady-state thickness H_∞ is proportional to $(j_g - j_m)^{0.8}$ [see Equation (3.17)].

$$H_\infty = 2905 \frac{\sigma}{r_0^{2.6}} \frac{[\mu(j - j_m)]^{0.8}}{(\rho g)^{1.8}} \tag{4.27}$$

where H_∞ is the steady-state foam thickness, r_0 is the average bubble radius at the bottom of the foam layer, σ is the surface tension of the liquid/gas system, j is the superficial gas velocity, ρ is the density of the liquid phase, and g is the specific gravity. However, j_m was determined from experimental data such as those shown in Figure 4.2 which limits the prediction capability of Equation (4.27). Figure 4.7 compares the experimental data for the steady-state foam thickness with the predictions of Equation (4.27) combined with the present model for the superficial gas velocity j_m

for experimental data having characteristic time ratio $t_d/t_c \geq 0.42$. The superficial gas

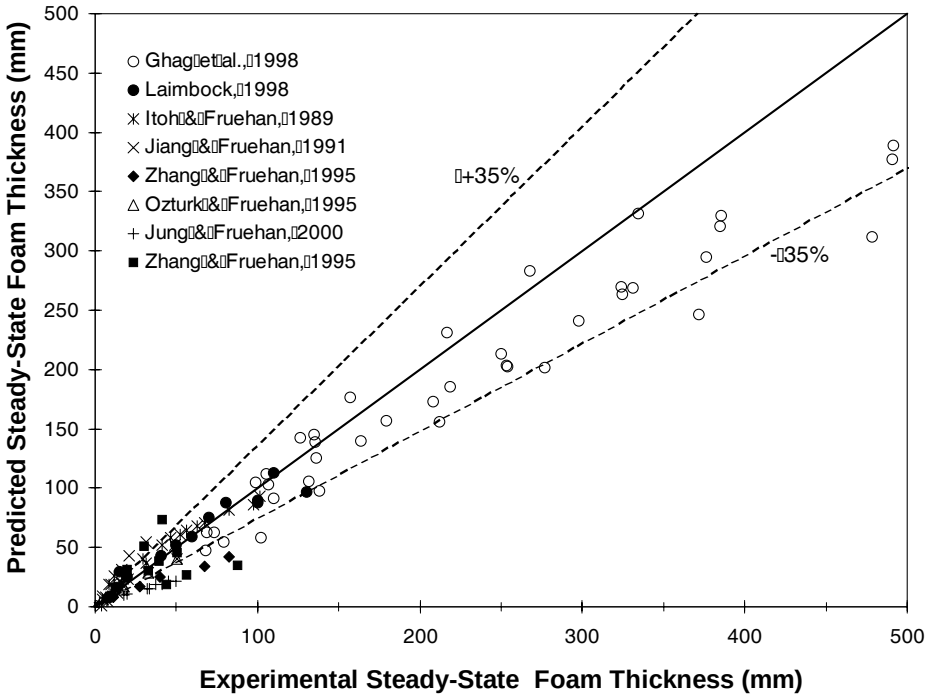

Figure 4.7. Comparison between experimental and predicted steady-state thickness for viscosity dominated drainage, i.e., small characteristic time ratio t_d/t_c.

velocity for onset of foaming was determined from Equation (4.24) using a maximum void fraction for onset of foaming α_m equals to 0.85. Given the complexity of the physical phenomena taking in liquid/gas foams, Figure 4.7 indicates that the model gives reasonable and similar predictions for the steady-state foam thickness as those obtained when j_m was determined experimentally. Note that (1) the smaller the probability of bubble coalescence, i.e., the larger the characteristic time ratio t_d/t_c, the better the model's predictions, and (2) the largest deviations from the experimental data occur for small gas influxes, i.e., for small steady-state foam thicknesses. The model's predictions for the steady-state foam thickness falls within $\pm$ 35% error bound for characteristic time ratio $t_d/t_c > 0.5$. Therefore, the present work completes the formulation of a self-contained model for the steady-state thickness of pneumatic

foams generated from viscous fluids over a wide range of physicochemical properties and operating conditions (see Table 4.2).

4.4. Concluding Remarks

A model is presented for predicting the superficial gas velocity for onset of foaming. The analysis has provided better understanding of the physical mechanisms responsible for foam formation. It is based on the one-dimensional drift-flux model for gravity driven flow with no wall shear. Inhibition of coalescence between rising bubbles and bubbles at rest at the free interface has been identified as a key mechanism for explaining the onset of foaming. Expression for the probability of coalesce can be found in the literature [75]. The experimental data collected from the literature and covering a wide range of physicochemical properties, bubble sizes and shapes, and flow regimes is the basis of the model. The following conclusions can be drawn from the results obtained:

- Two different regimes for the onset of foaming have been identified: (1) for low probability of coalescence, i.e., large characteristic time ratio t_d/t_c, bubble coalescence is strongly inhibited, and the foam formation occurs for relatively large void fractions of about 0.85, and (2) for large probability of coalescence, i.e., small characteristic time ratio t_d/t_c, bubbles tend to coalesce more leading to their distortion and the onset of foaming for void fractions close to unity.

- A semi-empirical correlation for the superficial gas velocity for onset of foaming j_m at low probability of coalescence between rising bubbles and bubbles at rest at the free surface ($P < 0.66$) is given by Equation (4.24). The associated maximum void fraction for onset of foaming α_m is equal to 0.85. Good agreement between the model predictions and experimental data is observed for both the superficial gas velocity for onset of foaming j_m and the steady-state foam thickness when $j_g > j_m$.

NOMENCLATURE

A	Container cross-sectional area
C_D	Drag coeffficient
g	Specific gravity
j	Superficial velocity
j_{gf}	Drift flux
K	Constant, Equation (4.5)
n	Constant determined experimentally, Equation (4.5)
N_μ	Viscosity number, Equation (4.11)
Q	Volumetric flux
Re	Reynolds number, Equation (4.12)
r	Bubble radius
r^*	Dimensionless bubble radius, Equation (4.11)
t_c	Bubble collision duration time
t_d	Characteristic time for drainage
v	Velocity
V	Relative velocity of centers of colliding bubbles
V_{gj}	Drift velocity
We	Weber number, Equation (4.8)

Greek symbols

α	Void fraction
σ	Surface tension
μ	Dynamic viscosity
$\psi(r^*)$	Function of the dimensionless bubble radius r^*, Equation (4.16)
ρ	Density

Subscripts

g	Refers to the gas phase
f	Refers to the liquid phase
m	Refers to the minimum conditions for onset of foaming

t	Refers to the transition between spherical and distorted bubbles
∞	Refers to conditions of a single bubble rising in an infinite medium

Table 4.1. Parameters for the prediction of the superficial gas velocity for onset of foaming as given by Equation (4.24).

Regime	**Terminal velocity** v_∞	$f(r)$	**Parameter** n	**Transition Criteria**
Viscous	$\frac{2}{9}\frac{(\rho_f-\rho_g)gr^2}{\mu_f}$ $\frac{8\Delta\rho}{3\rho_f v_\infty^2}=\frac{24}{Re_\infty}(1+0.1Re_\infty^{0.75})$	1 $\left[\frac{1+\psi(r^*)}{1+\psi(r^*)(1-\alpha)^{9/7}}\right]$	3	$N_\mu \le N_\mu\vert_t$ and $Re_\infty \ll 1$ $N_\mu \le N_\mu\vert_t$ and $Re_\infty > 1$
Distorted bubble	$\sqrt{2}\left[\frac{(\rho_f-\rho_g)g\sigma}{\rho_f^2}\right]^{1/4}$	1	1.75	$N_\mu > N_\mu\vert_t$
Churn-turbulent	$\sqrt{2}\left[\frac{(\rho_f-\rho_g)g\sigma}{\rho_f^2}\right]^{1/4}$	1	1/4	$r < [\sigma/(\rho_f-\rho_g)g]^{1/3}$

Table 4.2. Summary of experimental data for minimum superficial velocity for onset of foaming reported in the literature.

Solution	**Gas**	σ **(mN/m)**	μ_f **(mPa · s)**	ρ **(kg/m^3)**	$\mathbf{r}_0$ **(mm)**	**Two-Phase Flow Regime**	t_d/t_c **range**	**Ref.**
40%CaO-40%SiO_2 5% FeO-15%Al_2O_3	Argon	463.	398	2743	7.8 to 13.5	distorted bubble	≈ 0.47	Zhang & Fruehan [20]
48%CaO-32%SiO_2 10%FeO-10%Al_2O_3	Argon	477.2	381	2733	12	distorted bubble	0.42	Ozturk & Fruehan [5]
75 SiO_2-15 NaO_2 -10 CaO (wt.%) glass	Air	297.7 to 307.7	7450 to 12100	2346.6 to 2358.6	15 to 20	viscous (Stokes)	6.9 to 12.4	Laimbock [9]
water + 78% to 95% glycerinate +SDBS	N_2	69.5 to 72.3	46.5 to 520.8	1204 to 1251	0.7 to 1.1	viscous (Stokes)	0.42 to 3.9	Ghag *et al.* [26]
30% FeO-42% SiO_2 -28% CaO	Argon	477.9	1605	3055	12	distorted bubble	0.43	Ito & Fruehan [29]
3% FeO (CaO/SiO_2=1.25)	Argon	477.2	381	2733	12	distorted bubble	0.42	Jiang & Fruehan [23]
0% FeO (CaO/SiO_2=1.25)	Argon	472.8	396	2693	12	distorted bubble	0.42	Jiang & Fruehan [23]

Table 4.2. Continued.

Solution	**Gas**	σ **(mN/m)**	μ_f **(mPa · s)**	ρ **(kg/m^3)**	$\mathbf{r}_0$ **(mm)**	**Two-Phase Flow Regime**	t_d/t_c **range**	**Ref.**
30%CaO-60%SiO_2 10%CaF_2	Argon He, H_2	338	533 [72]	2534	13	distorted bubble	0.47	Zhang & Fruehan [21, 22]
34.78%CaO-33.76%SiO_2 22.52%FeO-8.94%MgO	Argon	502	270	2958	17	distorted bubble	0.51	Jung & Fruehan [24]
37.39%CaO-35.57%SiO_2 20.87%FeO-6.17%MgO	Argon	493	291	2936	17	distorted bubble	0.51	Jung & Fruehan [24]
water + 10% glycerinate Marlophen 89 and 812	N_2	32.0 to 41.1	1.22	1014	0.5 to 0.78	viscous (wake)	0.08 to 0.12	Jeelani *et al.* [31]
water + sucrose AR + glycerol SLR + aerosol OT	N_2	26	20	1220	3.9	distorted bubble	0.41	Hartland & Barber [54]
water + 10% glycerinate Marlophen 89 and 812	N_2, NO_x Xe, CO_2	32.0 to 41.1	1.22	1014	0.5 to 0.78	viscous (wake)	0.04 to 0.08	Hartland *et al.* [32]
tap water, aqueous glycerine, kerosen, kerosen +surfactants	air	20.4 to 72.2	0.89 to 3.42	808 to 1104	3.4 to 5.7	viscous (wake)	0.35 to 0.42	Pino *et al.* [34]

5. RADIATION CHARACTERISTICS OF SEMITRANSPARENT MEDIA CONTAINING GAS BUBBLES

5.1. Introduction

Transport phenomena occuring in foams depend obviously and significantly on the foam thickness. The previous three chapters presented different aspects of foam dynamics, from onset of foaming to steady state and have focused on predicting the transient and steady-state foam thickness. The part of the dissertation pays attention to transport phenomena and in particular on thermal radiation transfer through semitransparent media containing bubbles.

Most previous studies on radiation transfer through closed-cell foams assumed either that the matrix is non-absorbing and use the diffusion theory of photons [37, 40, 41] or that the foam is optically thick and scattering is isotropic so that Rosseland diffusion approximation is valid [84]. Then, an effective thermal conductivity accounting for conduction and radiation can be defined [42–45]. For strongly absorbing materials such as metalic or polyurethane foams the latter approach appears to give satisfactory results. However, the Rosseland diffusion approximation has to be relaxed for weakly absorbing materials such as glass in the spectral region from 0.2 to about 4μm [46, 47]. Only recently, Fedorov and Viskanta [11, 12] have presented a theoretical model for radiation transfer through foams by solving the radiative transfer equation (RTE) analytically using the Schuster-Schwarzschild two-flux approximation and accounting for absorption and multiple scattering in the foam layer but neglecting emission. The authors presented a model for the radiation characteritics of foams but focused their attention on the apparent transmittance, reflectance, and absorptance of glass foams.

The present analysis aims at extending the previous studies [11, 12] to the entire range of volumetric void fraction f_v from dense materials without bubbles ($f_v = 0$) to foams consisting of spherical bubbles ($f_v = 0.74$). Indeed, in metal, polymers, ceramics, and glass materials processing and manufacturing situations, gas bubbles can form in liquid and solid phases and their concentration (i.e.,the void fraction) can vary significantly depending on the location in the liquid and on the operating conditions. Similarly, emission of thermal radiation by the ocean surface is affected not only by the foam patches but also by bubbles generated either by the breaking waves or within the ocean and rising at the surface. Unlike previous studies [11, 12], this chapter focuses on intrinsec radiation characteristics, i.e., the spectral absorption, scattering, and the scattering phase function of media containing bubbles. The validity of the model for the spectral absorption, scattering, and the scattering phase function is discussed and results of samples calculations for the most common glass, i.e., for soda-lime silicate, are presented. Experimental results and model validations are given in the next chapter.

5.2. Analysis

Consider heat transfer within an horizontal layer of continuous condensed phase containing bubbles as shown in Figure 5.1. In general, convection (due to the motion of bubbles), conduction, and radiation heat transfer are present and should be considered. We further assume that the continuous condensed phase is a solid or a slowly moving liquid and is essentially isothermal. Then, the first two modes of heat transfer can be safely neglected in comparison to heat transfer by radiation. When gas bubbles are moving with the liquid phase, a time-averaged void fraction and bubble size distribution should be used. In addition, we assume the following: (1) all bubbles are spherical, (2) the scattering of a single bubble is not affected by the presence of its neighbors (independent scattering); and (3) the radiation field within the liquid layer is incoherent (i.e., scattering centers are randomly distributed

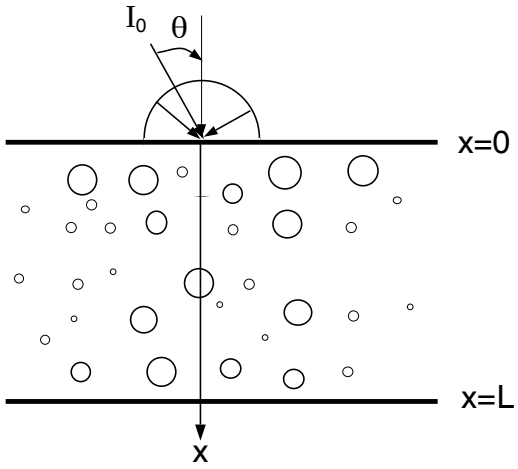

Figure 5.1. Schematic of the idealized liquid layer containing bubbles and the coordinate system.

with zero-phase correlation). Then, radiative transfer within an absorbing, emitting, and independently scattering medium is governed by the integro-differential equation expressed in dimensionless optical coordinates [84, 85],

$$\frac{\mathrm{d}I_\lambda}{\mathrm{d}\tau_\lambda} = [1-\omega_\lambda(\hat{s})]I_{b\lambda}[T(\hat{s})] - I_\lambda(\hat{s},\hat{\Omega}) + \frac{\omega_\lambda(\hat{s})}{4\pi}\int_{\hat{\Omega}'=4\pi} I_\lambda(\hat{s},\hat{\Omega}')\Phi_\lambda(\hat{s},\hat{\Omega}'\rightarrow\hat{\Omega})d\hat{\Omega}' \quad (5.1)$$

Here, $\hat{s}$ is the local spatial coordinate unit vector, $\hat{\Omega}$ is a line-of-sight direction, and $I_{b\lambda}$ is Planck's blackbody function. The spectral optical thickness τ_λ and single scattering albedo ω_λ are defined, respectively, as

$$\tau_\lambda = \int_0^s (\kappa_\lambda+\sigma_\lambda)ds = \int_0^s \beta_\lambda ds \quad (5.2)$$

$$\text{and} \qquad \omega_\lambda = \frac{\sigma_\lambda}{\kappa_\lambda+\sigma_\lambda} = \frac{\sigma_\lambda}{\beta_\lambda} \quad (5.3)$$

where κ_λ, σ_λ, and β_λ $(=\kappa_\lambda+\sigma_\lambda)$ are the absorption, scattering, and extinction coefficients, respectively. The scattering phase function $\Phi_\lambda(\hat{s},\hat{\Omega}'\rightarrow\hat{\Omega})$ represents the probability of scattering of the radiation from a beam propagating in the direction $\hat{\Omega}'$ to the direction $\hat{\Omega}$, and it is normalized such that

$$\frac{1}{4\pi}\int_{\hat{\Omega}'=4\pi}\Phi_\lambda(\hat{s},\hat{\Omega}'\rightarrow\hat{\Omega})d\hat{\Omega}' = 1 \quad (5.4)$$

Equation (5.1) indicates that the extinction, absorption, and scattering coefficients together with the scattering phase function and the single scattering albedo are major parameters of the radiation transfer. Thus, the following subsections of the paper are devoted to characterization of the continuous phase layer with dispersed gas bubbles and to the development of detailed models for its effective radiation characteristics.

The objective of this work is to explore the effect of the bubble radius, the bubble size distribution, and the void fraction on the radiation characteristics of glass containing spherical gas bubbles with different bubble size distributions and to gain understanding of their importance on radiative transfer in glass.

Let $m_\lambda^d = n_\lambda^d - ik_\lambda^d$ and $m_\lambda^c = n_\lambda^c - ik_\lambda^c$ be the spectral complex indices of refraction of the dispersed phase (i.e., gas bubbles), and of the continuous phase, respectively. The following sections present the formulations for predicting the spectral radiation characteristics of glass containing monodispersed and polydispersed bubbles.

5.2.1. Prediction of Spectral Radiation Characteristics for Monodispersed Bubbles

We assume here that all the bubbles entrapped in the glass melt have a uniform radius a. Then, the effective extinction coefficients (due to absorption and scattering) and the scattering phase function for the layer can be expressed as [11]

$$\begin{aligned}
\kappa_\lambda &= \pi Q_{abs}^d(a)a^2 N_T + \left[\kappa_\lambda^c - \pi Q_{abs}^c(a)a^2 N_T\right] \\
&= \kappa_\lambda^c - \pi[Q_{abs}^c(a) - Q_{abs}^d(a)]a^2 N_T \qquad (5.5) \\
\sigma_\lambda &= \pi Q_{sca}^d(a)a^2 N_T \qquad (5.6) \\
\beta_\lambda &= (\kappa_\lambda + \sigma_\lambda) = \kappa_\lambda^c - \pi[Q_{abs}^c(a) - Q_{ext}^d(a)]a^2 N_T \qquad (5.7)
\end{aligned}$$

where $Q_{abs}(a)$, $Q_{sca}(a)$, and $Q_{ext}(a)$ denote the absorption, scattering, and extinction efficiency factors and scattering phase function, respectively, for a sphere of radius a, while the superscripts "d" and "c" refers to the dispersed and the continuous phase, respectively. N_T is the total number of bubbles per unit volume, that can be expressed

as a function of the void fraction f_v and of the foam and continuous densities, ρ_f and ρ_c, respectively:

$$N_T = \frac{3f_v}{4\pi a^3} = \frac{3}{4\pi a^3}\left(1 - \frac{\rho_f}{\rho_c}\right) \tag{5.8}$$

Moreover, for independent scattering, the phase function in a cloud of uniform bubbles $\Phi_\lambda(\Theta)$ is the same as that for a single particle $\phi(a, \Theta)$ [84], it is also the same for a bubble cloud, i.e.,

$$\Phi_\lambda(\Theta) = \phi(a, \Theta) \tag{5.9}$$

Note that the absorption coefficient of the continuous phase κ_λ^c in Equation (5.5) can be calculated from the imaginary part (k_λ^c) of the complex index of refraction (m_λ^c) as

$$\kappa_\lambda^c = 4\pi\eta_0 k_\lambda^c \tag{5.10}$$

where $\eta_0 = \nu/c_0 = 1/(n_\lambda^c \lambda)$ is the wavenumber of the wave with a frequency ν and phase velocity equal to a speed of light in vacuum c_0.

5.2.2. Spectral Radiation Characteristics for Polydispersed Bubbles

Figure 5.1 shows a schematic diagram of layer of continuous condensed phase containing bubbles of different sizes. In glass melt these bubbles may be generated during the batch fusion and fining reactions [86]. Suppose that all bubbles are spherical (in the case of distorted bubbles one can define an equivalent sphere which preserves the gas void volume) and their size (radius a) distribution is given by the so-called modified gamma function (Ref. [84], pp. 393-394):

$$n(a) = A \times a^\gamma \times exp\left(-B \times a^\delta\right), \qquad 0 \le a < \infty \tag{5.11}$$

The distribution function vanishes at $a = 0$ and $a \to \infty$ and it reaches its maximum at the bubble radius $a_{max} = (\gamma/\delta B)^{1/\delta}$. The four constants A, B, γ and δ are taken positive and real, and they must be determined from measurable quantities such as total number of bubbles per unit volume,

$$N_T = \int_0^\infty n(a)da = A\int_0^\infty a^\gamma \times exp\left(-B \times a^\delta\right) da = \frac{A\Gamma\left(\frac{\gamma+1}{\delta}\right)}{\delta B^{(\gamma+1)/\delta}} \tag{5.12}$$

and the bubble density (i.e., the total volume of bubbles per unit volume or the bubble volume fraction) is given by

$$f_v = \int_0^\infty \frac{4}{3}\pi a^3 n(a)da = \frac{4\pi A\Gamma\left(\frac{\gamma+4}{\delta}\right)}{3\delta B^{(\gamma+4)/\delta}} \tag{5.13}$$

Here, $\Gamma(z)$ is the *gamma* function $\left(=\int_0^\infty e^{-t}t^{z-1}dt\right)$, and it is tabulated by Abramowitz and Stegun [87]. Note also that the constants γ and δ are usually chosen to be integers.

In the present case, we also assume that all bubbles have the same optical properties throughout the layer and their size distribution function $n(a)$ is known. Then, the effective extinction coefficients (due to absorption and scattering) and the scattering phase function for the medium containing bubbles can be expressed as [11]

$$\begin{aligned}
\kappa_\lambda &= \pi\int_0^\infty Q^d_{abs}(a)a^2n(a)da + \left[\kappa^c_\lambda - \pi\int_0^\infty Q^c_{abs}(a)a^2n(a)da\right] \\
&= \kappa^c_\lambda - \pi\int_0^\infty [Q^c_{abs}(a) - Q^d_{abs}(a)]a^2n(a)da \qquad (5.14)\\
\sigma_\lambda &= \pi\int_0^\infty Q^d_{sca}(a)a^2n(a)da \qquad (5.15)\\
\beta_\lambda &= (\kappa_\lambda + \sigma_\lambda) = \kappa^c_\lambda - \pi\int_0^\infty [Q^c_{abs}(a) - Q^d_{ext}(a)]a^2n(a)da \qquad (5.16)
\end{aligned}$$

and

$$\Phi_\lambda(\Theta) = \frac{\pi}{\sigma_\lambda}\int_0^\infty Q^d_{sca}(a)\phi(a,\Theta)a^2n(a)da \tag{5.17}$$

In calculating the spectral coefficients, most of the computer time is used in evaluating the efficiency factors Q_{abs}, Q_{sca} and Q_{ext} from the Mie theory. In multidimensional and spectral radiative transfer analysis this type of approach becomes impratical. Therefore, it is desirable to have simple approximations for the efficiency factors. The changes in the scattering pattern due to changes in the bubble size should be accounted for in the prediction of the radiation characteristics of the layer containing bubbles. Figure 5.2 shows the different limiting cases in the $\rho - \chi$ domain where simple analytical expressions for $Q_{abs}(a)$, $Q_{sca}(a)$, $Q_{ext}(a)$ and $\phi(a,\Theta)$ are available in the literature.

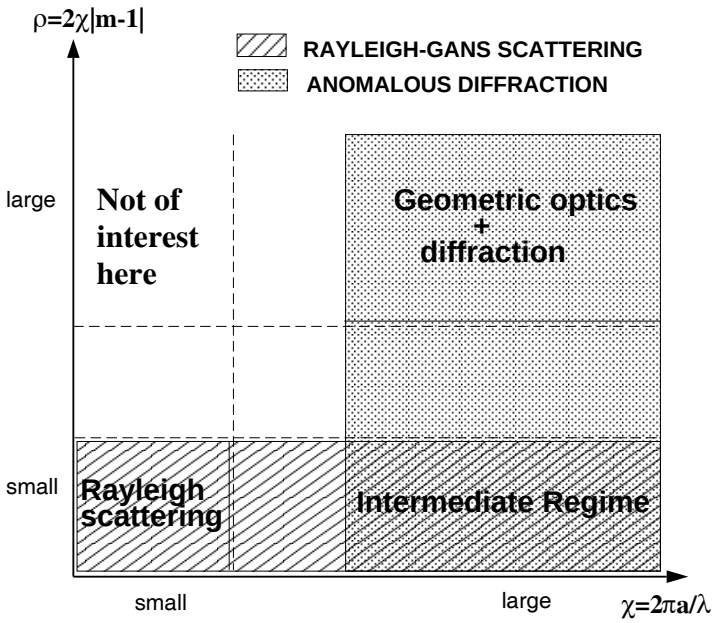

Figure 5.2. Summary of the limiting cases in the $\rho - \chi$ domain.

For spheres with index of refraction close to 1, the $\rho - \chi$ domain can be divided into two limiting cases [88]:

- *The Rayleigh-Gans scattering domain* corresponds to a near-dielectric sphere with (1) $k \approx 0$, (2) a refractive index of refraction close to unity i.e., $|m-1| \ll 1$, and such that (3) the phase lag suffered by the central ray that passes through the sphere along a full diameter is small i.e., $\rho = 2\chi|m-1| \ll 1$. Then, reflectivity is negligible and the radiation passes through the sphere unattenuated and unrefracted [88]. The Rayleigh-Gans scattering domain can itself be divided into two limiting cases namely, $\chi \to 0$ (Rayleigh scattering) and $\chi \to \infty$ ("intermediate regime").

- *The anomalous-diffraction domain* is characterized by $\chi \to \infty$ and $m \to 1$ corresponding to a straight transmission and subsequent diffraction according to Huygens' principle [88]. The anomalous-diffraction domain can also be divided into two limiting cases, namely, $\rho \to 0$ ("intermediate regime") and $\rho \to \infty$

("geometrical optics + diffraction regime"). Note that the Rayleigh-Gans domain and the anomalous diffraction domain overlap in the so-called "intermediate regime".

The present work is concerned with relatively large bubbles and wavelengths between 0.4 μm and 10μm for which the anomalous diffraction is valid. In this region of the $\rho - \chi$ domain, the large gas bubbles are relatively weak absorbers of radiation and mostly act as the strong radiation scatterers. In this case, the approximate analytical expressions for extinction (absorption and scattering) efficiency factors for a weakly absorbing sphere of arbitrary size can be used as derived by van de Hulst (see Ref. [88], p. 179),

$$\begin{aligned} Q_{ext}(\rho', m) = 2 \quad &- \quad 4\,\frac{cos(g)}{\rho'} \times \left[e^{-\rho'\ tan(g)} sin(\rho' - g)\right] \\ &+ \quad 4\left(\frac{cos(g)}{\rho'}\right)^2 \times \left[cos(2g) - e^{-\rho'\ tan(g)} cos(\rho' - 2g)\right] \end{aligned} \tag{5.18}$$

where $\rho' = 2(n-1)\chi = 2(n-1)(2\pi a/\lambda)$ and $g = arctan[k/(n-1)]$ are the van de Hulst's normalized size and absorption parameters, respectively, such that $\rho'^{d} \times tan(g)$ gives the energy absorbed along the axial ray within the sphere. Because of the assumptions of the van de Hulst's theory, the expression overestimates the extinction factor for small spheres and underestimates it for larger spheres. To correct this, Deirmendjian [89] proposed to use a correction factor $(1 + D_i)$. The approach was remarkably successful in improving accuracy of extinction coefficient defined by Equation (5.18), and the specific expressions for D_i can be found in reference [89] (pp. 29-30). The absorption and scattering contributions to the extinction efficiency factor of a single gas bubble are given by the following asymptotic formulae [89]:

$$Q_{abs}(\rho', m) = 1 + \frac{e^{-2\ \rho'\ tan(g)}}{\rho'\ tan(g)} + \frac{e^{-2\ \rho'\ tan(g)} - 1}{2\ [\rho'\ tan(g)]^2} \tag{5.19}$$

and

$$Q_{sca}(\rho', m) = Q_{ext}(\rho', m) - Q_{abs}(\rho', m) \tag{5.20}$$

respectively.

Comparison of the absorption and scattering efficiencies generated using the ap-

proximate expressions given by Equations (5.19) and (5.20) with numerical results obtained from the exact Mie theory (Ref. [89], pp. 30-32) have demonstrated the power of this approach, especially when precise directional scattering pattern and polarizing properties are not desired. Specifically, the results obtained via the corrected van de Hulst's formula $(1 + D_i) \times Q_{ext}$ are accurate within about $\pm 0.05 Q_{ext}$ for a wide range of sphere sizes and indices of refraction. Note that the magnitude of the error increases with an increase in a value of the real part (n_λ^d) of the complex index of refraction for both absorbing and non-absorbing spheres ([89], p. 32). Of course, if the complex index of refraction of the continuous phase (m_λ^c) lies within accuracy limits of the van de Hulst's theory, then Equation (5.19) can be successfully used for calculation of the absorption efficiency factor $Q_{abs}^c(a)$ of the sphere made of the continuous phase as well.

5.3. Results and Discussion

The input parameters for the model include the spectral index of refraction and the spectral absorption coefficient of both the continuous and dispersed phases along with the bubble size distribution and the total number of bubbles per unit volume N_T or the void fraction f_v. Clear soda-lime silicate glass (window glass) is used for the sample calculations, and the spectral variation of the real (n_λ^c) and imaginary part (k_λ^c) of its refractive index $(m_\lambda^c = n_\lambda^c - ik_\lambda^c)$ are taken from the literature [46]. The gas mixture contained inside the gas bubbles is transparent to the incident radiation and its complex index of refraction (m_λ^d) is assumed to be independent of the wavelength and equal to $1.003 - i \cdot 1.0 \times 10^{-10}$. In this section we review the different scattering domains for which simple analytical expressions for the extinction efficiency factors exist. Then, the absorption and extinction coefficients as well as the single scattering albedo of soda-lime silicate glass containing monodispersed and polydispersed bubbles with different size distribution and different void fraction are calculated in the case of anomalous diffraction (large bubbles).

5.3.1. Model Validity for Glass Containing Bubbles

5.3.1.1. Scattering Domains

In defining the limiting cases of the Mie theory for which simple analytical solutions are known, we used the qualitative criteria $\rho \ll 1$ for Rayleigh-Gans scattering and $\chi \gg 1$ for anomalous diffraction. For our particular application the different scattering regimes are delimited arbitrarily as follows,

- Anomalous scattering approximation is assumed to be valid for $\chi \geq 100$. This condition leads to

$$a \geq \frac{100\lambda}{2\pi} \tag{5.21}$$

- The Rayleigh-Gans scattering approximation is assumed to be valid for $\rho \leq 0.01$. For the gas bubbles, this condition is equivalent to

$$a \leq \frac{\lambda}{400\pi\sqrt{(n_\lambda - 1)^2 + (k_\lambda)^2}} \tag{5.22}$$

  Note that unlike the index of refraction of the gas contained in the bubbles, that of the soda-lime silicate glass depends on the wavelength and must be accounted for in defining the scattering domains. The Rayleigh-Gans scattering approximation can be made when the condition expressed by Equation (5.22) is valid for both the dispersed and continuous phase.

- A subdomain of the Rayleigh-Gans scattering approximation is the Rayleigh scattering assumed to be valid when $\rho \leq 0.01$ *and* $\chi \leq 0.01$. For the gas bubbles and glass spheres, these conditions are expressed by Equation (5.22) and

$$a \leq \frac{\lambda}{200\pi} \tag{5.23}$$

According to Equations (5.5), (5.6), and (5.9) one needs to consider the absorption efficiency factor for both gas bubbles and the corresponding glass spheres, and the

scattering efficiency factor and the scattering phase function for the gas bubbles in order to predict the effective radiation characteristics of the glass slab containing bubbles. Figures 5.3 indicates the theory or limiting cases to be used to predict the extinction efficiency factors for both the glass spheres and the gas bubbles in the wavelength-radius domain.

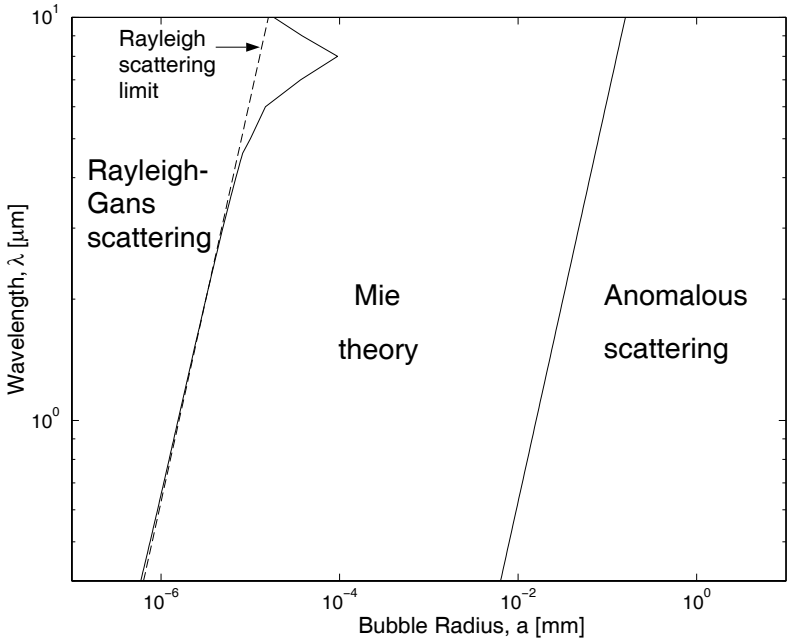

Figure 5.3. Map of the scattering theories and approximations used for determining the extinction efficiency factors Q_{abs}, Q_{sca}, and Q_{ext} of the soda-lime silicate containing gas bubbles.

From Figures 5.4 and 5.3, one can conclude that for bubbles with a $\leq$ 0.1 mm, the radiation characteristics of the glass layer can be predicted from the anomalous diffraction theory.

For bubbles less than 1 nm in diameter, the same radiation characteristics of the glass layer can be estimated from the Rayleigh-Gans scattering theory. However, for bubbles having radii between 1 nm and 0.1 mm and/or if the void fraction is larger than 0.006 the use of the Mie theory and/or the consideration of dependent scattering

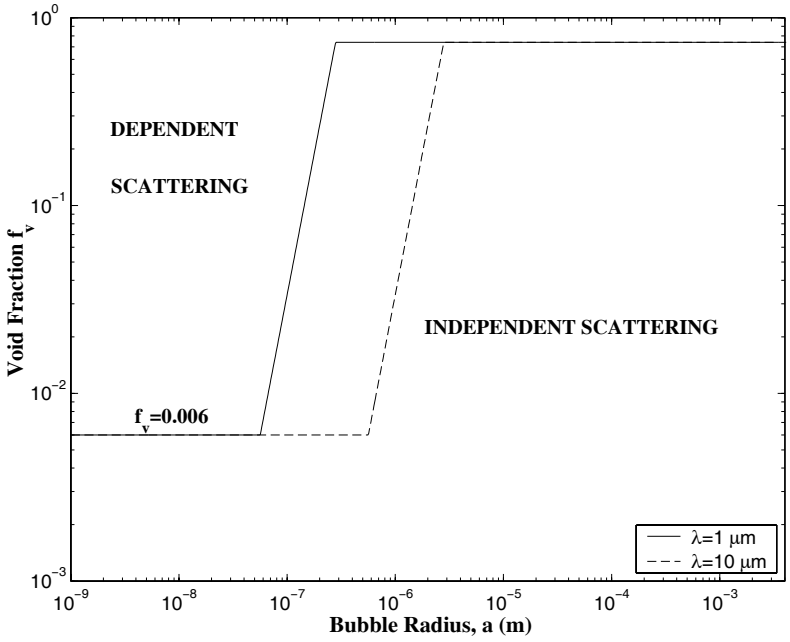

Figure 5.4. Scattering regime map for independent and dependent scattering due to spherical bubbles.

is required for wavelengths between 0.4 μm and 10 μm, making the computation of the apparent absorptance, reflectance and transmittance of the layer considerably more involved. Unfortunately, undertaking the task of solving the Mie theory and/or accounting for dependent scattering is beyond the scope of this work. Therefore, only large bubbles for which the anomalous diffraction theory and the independent scattering assumption are valid will be considered further.

5.3.1.2. Ranges of Interest

The above representation for the effective radiation characteristics is valid only if the scattering by the ensemble of bubbles is *independent*, i.e., scattering by one particle is not affected by the presence of surrounding particles. Tien and Drolen [90] presented a scattering regime map which uses the size parameter ($\chi = 2\pi a/\lambda$) and the volume

fraction (f_v) as the coordinate axis. They showed that the dependent scattering effects may be ignored as long as $f_v < 0.006$ or $c/\lambda < 0.5$. Assuming a cubic lattice of bubbles of pitch p, the condition $c/\lambda < 0.5$ can be expressed in terms of the void fraction as $f_v < (32\pi/3)(a/\lambda) = 16\chi/3$. Figure 5.4 shows the maximum void fraction f_v for independent scattering as a function of the bubble radius a. It suggests that for bubbles larger than 1 μm in diameter, independent scattering can be safely assumed.

It can be shown [91] that bubbles are spherical if their radius a is small compared to the capillary length l_c ($a \ll l_c$) where the capillary length for gas bubbles surrounded by liquid is defined as:

$$l_c = \sqrt{\frac{2\gamma}{(\rho^c - \rho^d)g}} \tag{5.24}$$

Here, γ is the surface tension (=300 mN/m), and ρ^c (=2350 kg/m^3 at around 1400 K [9]) and ρ^d (=1.2 kg/m^3) are the densities of the molten glass and the air, respectively. For soda-lime silicate glass the capillary length is about 4 mm. We assumed that bubbles are spherical for bubble radii up to the capillary length $l_c/4 = 1$ mm.

The spectral region where the thermal radiation is the most important is considered. The wavelength interval from 0.4 μm to 10 μm is chosen since it covers nearly 88% of the thermal radiation emitted by a blackbody at the source temperature of 5800 K and 94.5% at 1200 K. In summary, our study is restricted to the size parameters ($\chi = 2\pi a/\lambda$) ranging from $\chi_{min} = 0.0$ to $\chi_{max} = 3.15 \times 10^6$ and a phase shift, $\rho = 2\chi|m-1|$, that can take values from 0 (|m-1| $\ll 1$ and $\chi \ll 1$) to infinity (|m-1| $\ll 1$ and $\chi \to \infty$). The volume void fraction f_v defined as the ratio of the volume of gas to the total volume can vary between 0 and 0.74 corresponding to the maximum packing of spheres of uniform size, provided that the assumption of dependent scattering is valid.

5.3.2. Radiation Characteristics of the Glass Containing Bubbles

In this section we first discuss the effect of the void fraction and of the bubble radius on the radiation characteritics of soda-lime silicate glass containing bubbles of

uniform size. Then, polydisperse bubble clouds are considered and the results on the effect of their size distribution are presented.

5.3.2.1. Uniform Distribution: Effect of Bubble Radius and Void Fraction

As a concrete example, the spectral absorption and extinction coefficients as well as the single scattering albedo have been predicted for clear soda-lime silicate glass containing monodispersed bubbles for a volumetric void fraction of 0.2. Three different radii a were considered, 0.2 mm, 0.8 mm, and 1.6 mm. Note that in the limiting case when $f_v = 0$, i.e., for dense glass, the scattering coefficient σ_λ and the single scattering albedoω_λ vanish. Table 5.1 summarizes the simulations for monodispersed bubbles and the corresponding number of bubbles contained per cubic centimeter of glass.

From Figure 5.5 one can see that the presence of bubbles reduces the absorption

Table 5.1. Major characteristics of the uniform bubble size distributions.

		f_v =0.2	f_v =0.4	f_v =0.6
Distribution	a $[mm]$	N_T $[\#/cm^3]$	N_T $[\#/cm^3]$	N_T $[\#/cm^3]$
$Uniform1$	0.2	5.97×10^3	1.19×10^4	1.79×10^4
$Uniform2$	0.8	93.3	186.5	279.8
$Uniform3$	1.6	11.7	23.3	35.0

coefficient in the spectral region of 0.4 to 4.5 μm where the absorption coefficient of the glass is relatively small. In this same region, the extinction coefficient is strongly affected by the presence and the size of the bubbles. The scattering is particularly important for smaller bubbles and the single scattering albedo is close to unity. This indicates that the radiative transfer is dominated by scattering rather than by absorption for $0.4 < \lambda < 4.5$ μm. In the spectral region 4.5 to 10 μm, however, the absorption coefficient of the dense glass is large and the presence and the size of the bubbles have little effect of the effective absorption coefficient of the glass layer. In

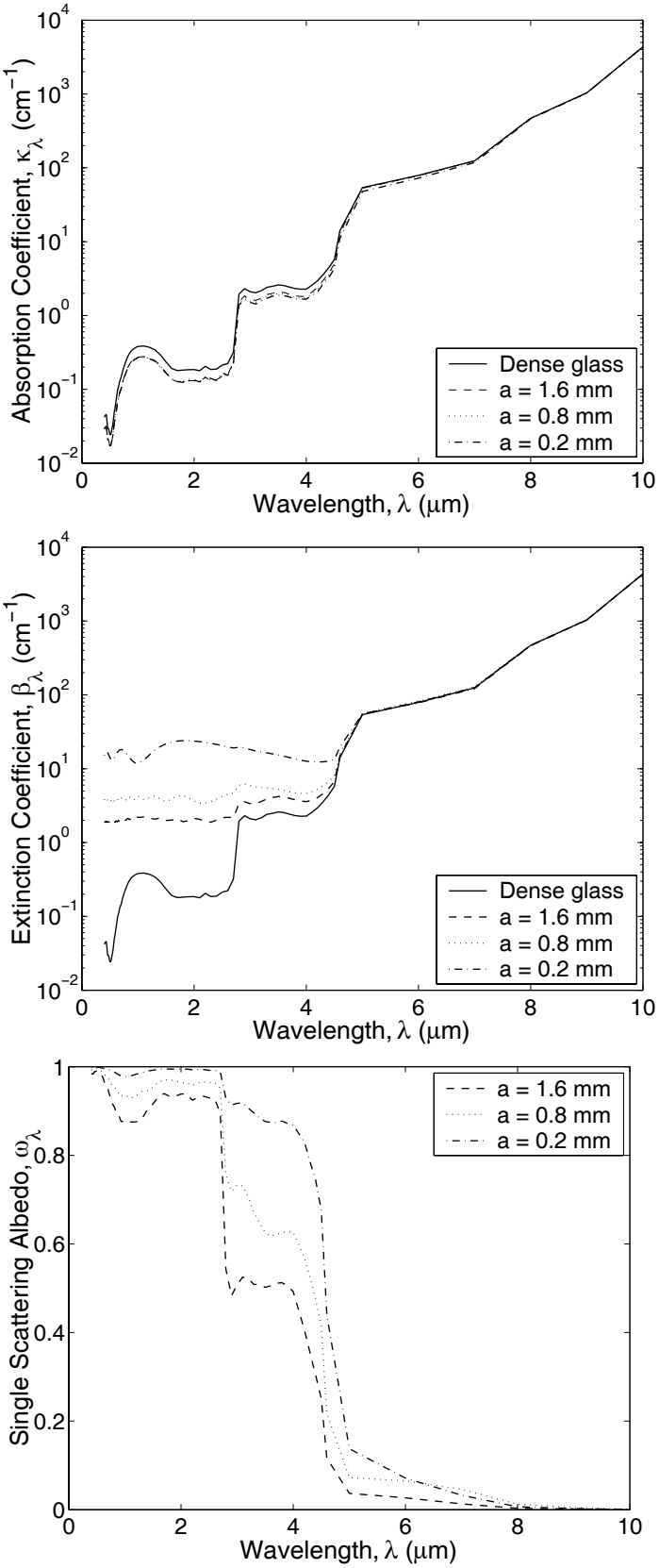

Figure 5.5. Effect of bubble radius on the spectral absorption, extinction coefficients, and single scattering albedo for soda-lime silicate glass with $f_v = 0.2$.

other words, the scattering coefficient is negligible compared with the absorption coefficient and the radiative transfer is dominated by absorption.

Moreover, the absorption coefficient decreases significanlty as the void fraction increases and can be reduced by up to one order of magnitude for void fractions f_v varying from 0.2 to 0.6 (Figure 5.6). In contrast, the extinction coefficient and the single scattering albedo increase as the void fraction or the number of bubbles increase. This can be explained by the fact increasing the void fraction increases the number of scatterers, while the absorption by the two-phase mixture decreases.

5.3.2.2. Effect of Bubble Size Distribution

So far, the bubble size distribution was assumed to be uniform. However, in reality bubbles entrapped in the glass melt are of different diameters. Sample calculations were performed for the spectral radiation characteristics of glass containing different bubble size distributions but with a constant void fraction. Table 5.2 summarizes the conditions simulated and example of bubble size distribution is plotted in Figure 5.7.

Table 5.2. Parameters and major characteristics of the bubble size distribution functions.

					f_v =0.2		f_v =0.6	
Distribution	γ	δ	A	B	a_{max} $[mm]$	N_T $[\#/cm^3]$	a_{max} $[mm]$	N_T $[\#/cm^3]$
Modified Gamma 1	4	1	1.59×10^{10}	80	0.5	116.4	0.5	349.2
Modified Gamma 2	4	1	6.2×10^{7}	40	1.0	14.6	1.0	43.7
Modified Gamma 3	8	1	8.22×10^{13}	80	1.0	24.7	1.0	74.1

The effect of the maximum radius a_{max} and of γ are assessed while the parameter δ is taken to be unity (gamma function). Figure 5.8 shows the absorption and extinction coefficients and the single scattering albedo for different bubble size distributions at void fractions of 0.2. In general, one can see that the bubble size distribution has

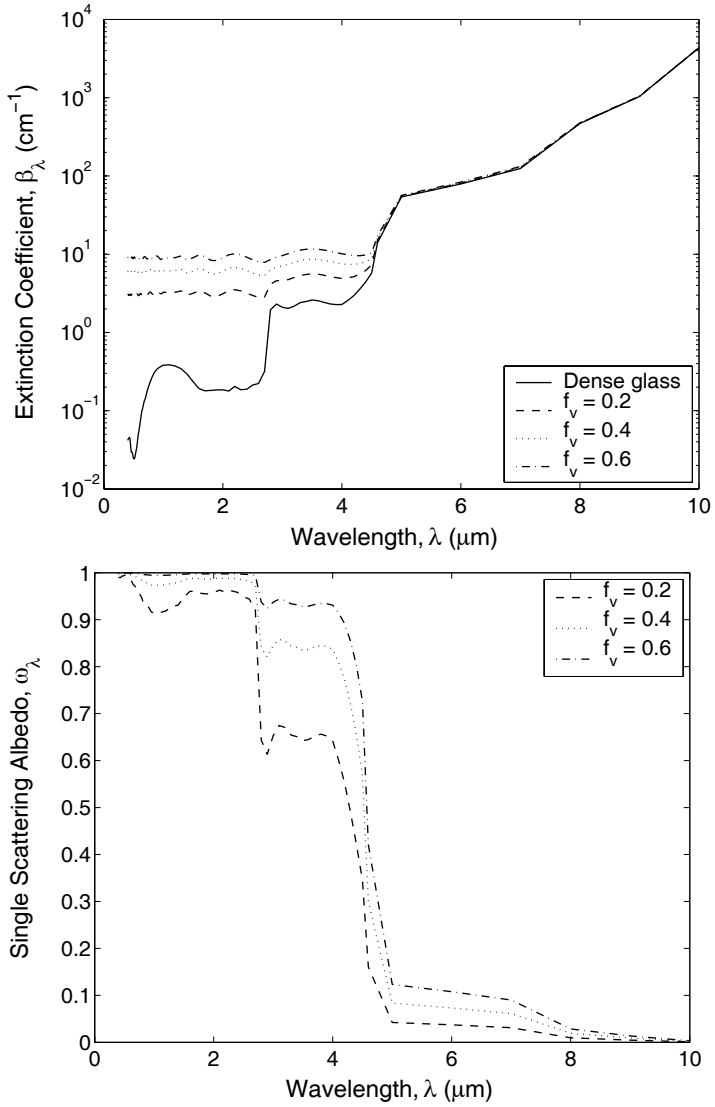

Figure 5.6. Effect of void fraction on the spectral extinction coefficient and single scattering albedo for soda-lime silicate glass containing uniform size bubbles 1 mm in diameter.

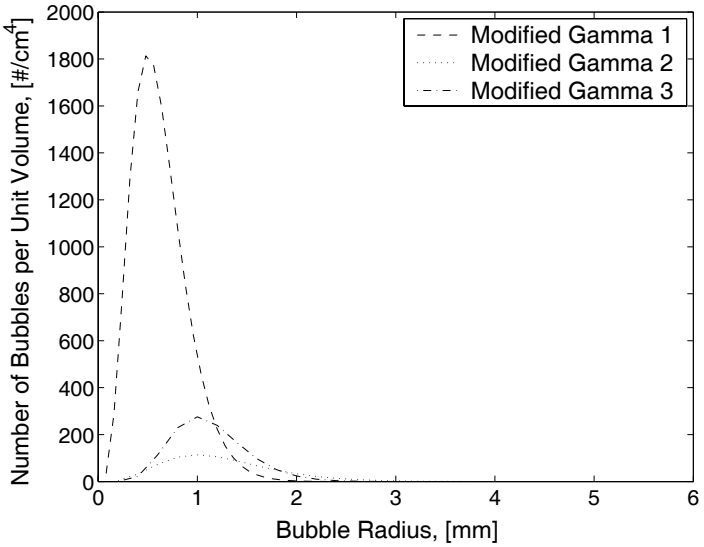

Figure 5.7. Typical bubble size distributions as summarized in Table tdistri-mono-rad for $f_v = 0.2$.

a strong influence on the extinction coefficient and single scattering albedo of glass containing bubbles but very little on the absorption coefficient. Figure 5.9 shows the spectral extinction coefficient and single scattering albedo for soda-lime silicate glass containing gas bubbles following the modified gamma distribution function 1 computed for void fractions of 0.2, 0.4, and 0.6. It is interesting to note that the void fraction seems to affect the extinction coefficient significantly for the wavelength range of $0.4\mu m \leq \lambda \leq 4.5\mu m$. Indeed, increasing in the void fraction from 0.2 to 0.6 leads to an increase of the extinction coefficient by a factor three while the relative effect of the distribution at $f_v = 0.6$ is similar to that at $f_v = 0.2$.

5.4. Concluding Remarks

An analysis of radiative transfer in a semitransparent glass layer containing gas bubbles with application to glass processing and manufacturing is presented. The results of sample calculations performed lead to the following conclusions:

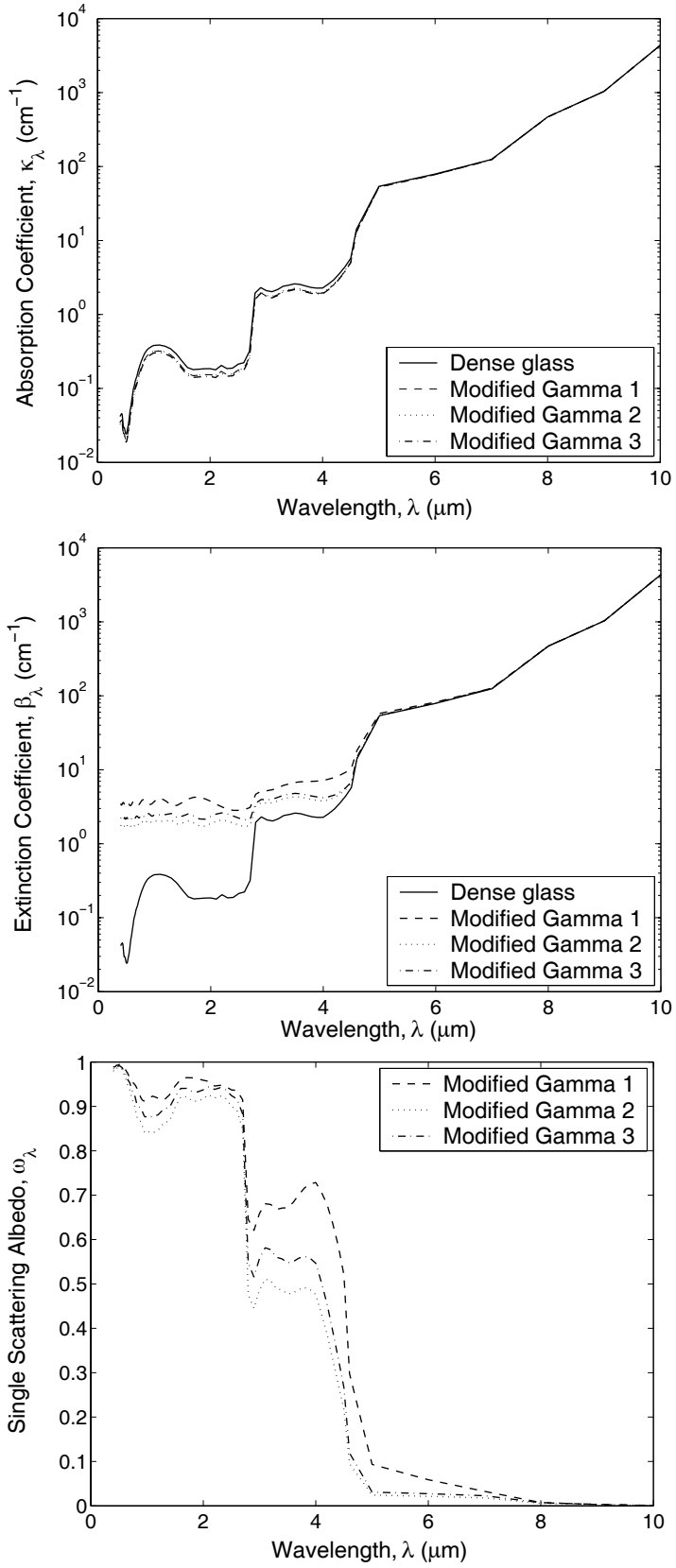

Figure 5.8. Effect of size distribution on the spectral absorption, extinction coefficients, and single scattering albedo of soda-lime silicate glass with $f_v = 0.2$.

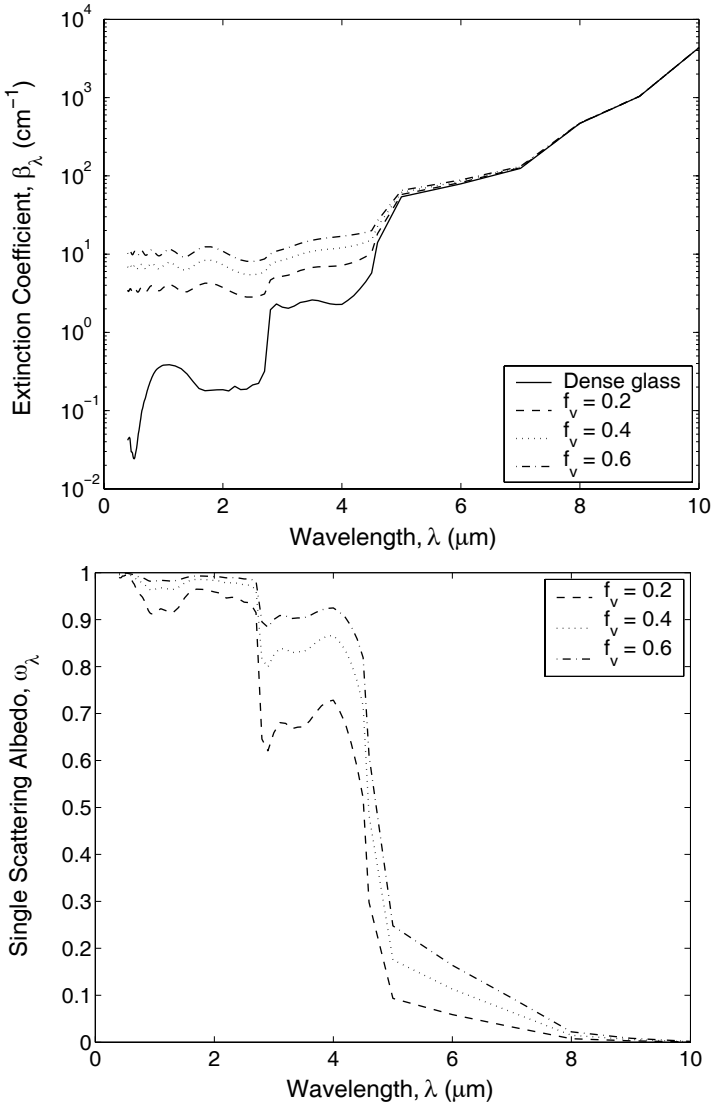

Figure 5.9. Effect of void fraction on the spectral extinction coefficient and single scattering albedo for soda-lime silicate glass containing gas bubbles for modified gamma distribution function 1.

- For gas bubbles smaller than 10 μm in diameter and void fractions larger than 0.006, the Mie theory should be used and/or considerations of dependent scattering are required.

- For gas bubbles larger than 0.1 mm in radius the analysis developed for glass foams by Fedorov and Viskanta [11, 12] can be extended over the entire range of void fractions (from 0 to 0.74).

- Even small void fractions affect the total apparent radiation characteristics of the glass layer containing large bubbles. The effect of the void fraction is even more significant for thicker layers and where the bubble size distribution is not uniform. Therefore, in modeling the radiative heat transfer in glass melting furnaces one should consider the effects of gas bubbles on the radiation characteristics of the glassmelt since bubbles are always present in industrial glass melting furnaces where they exist in large numbers.

- The model could be used as a non-intrusive method for measuring void fraction and bubble size distribution in two-phase flows by using infrared spectroscopy and inverse methods in spectral regions where the liquid phase is slightly absorbing.

NOMENCLATURE

a	bubble radius
c_0	speed of light in vacuum
D	Deirmendjian's correction factor
F	azimuth-averaged scattering phase function
f_v	bubble void volume fraction
g	specific gravity or van de Hulst's absorption parameter, $arctan[k_\lambda^d/(n_\lambda^d - 1)]$
I	radiation intensity
I_b	blackbody radiation intensity
I_0	incident intensity of collimated radiation
Q	efficiency factor
k	imaginary part of the complex index of refraction
l	thickness of the slab
m	complex index of refraction, $n - ik$
N_T	total number of bubbles per unit volume
n	real part of the complex index of refraction
r	reflectivity of the interface
$\hat{s}$	spatial coordinate vector
x	local depth of the slab (Figure 5.1)

Greek symbols

χ	size parameter, $2\pi a/\lambda$
β	extinction coefficient, Equation (5.7)
γ	Surface tension
κ	absorption coefficient, Equation (5.5)
σ	scattering coefficient, Equation (5.6) or Stefan-Boltzmann constant
λ	wavelength of the incident radiation
η	wavenumber of the incident radiation, ν/c_0
ν	frequency of the incident radiation
$\hat{\Omega}$	line-of-sight direction

ω	single scattering albedo, $\sigma_\lambda/(\kappa_\lambda + \sigma_\lambda)$
Φ	effective scattering phase function, Equation (5.9)
ϕ	scattering phase function of the single bubble
φ	azimuth angle
ρ	Density or phase shift, $2\|m-1\|\chi$
ρ'	van de Hulst's normalized size parameter, $2(n-1)\chi$
Θ	scattering angle
τ	optical depth, $\int_0^x(\kappa_\lambda + \sigma_\lambda)dx$

Subscripts

λ	refers to wavelength-dependent quantity
abs	refers to absorption
c	refers to continuous phase
d	refers to dispersed phase
ext	refers to extinction
sca	refers to scattering

Superscripts

d	refers to dispersed phase (gas bubble)
c	refers to the continuous phase

6. EXPERIMENTAL MEASUREMENTS OF RADIATION CHARACTERISTICS OF FUSED QUARTZ CONTAINING BUBBLES

6.1. Introduction

As already mentioned, the RTE describes on a phenomenological level radiation transfer in a continuous, homogeneous medium while porous media consist of a dispersed and a continuous phase and, therefore, are by nature inhomogeneous. However, the theory can still be employed using the effective absorption and scattering coefficients and the effective phase function of the porous medium provided that the porous medium can be treated as homogeneous, i.e., if the pore size to sample dimension ratio is very small. But, currently no quantitative model is available to predict the minimum material thickness beyond which the homogeneous assumption is valid.

The literature contains numerous studies concerned with closed-cell foams such as polyurethane or polystyrene foams [42,43,45,92,93]. All of them consider the medium to be optically thick and isotropically scattering materials for which the Rosseland diffusion approximation is valid. This approach consists of treating the radiative transfer as a diffusion process. Then, one may define a radiative conductivity k_R by [84]

$$k_R = \frac{16n^2T^3}{3\beta_R} \tag{6.1}$$

where σ is the Stefan-Boltzmann constant ($= 5.670 \times 10^{-8}$ W/m^{2}K^4) and n is the effective index of refraction of the heterogeneous medium. The dependence of the latter on wavelength is negligible compared with that of the extinction coefficient β_λ and its value is close to unity [85].The Rosseland-mean extinction coefficient β_R can be computed from its definition,

$$\frac{n^2}{\beta_R} = \frac{\pi}{4\sigma T^3}\int_0^\infty \frac{(n_\lambda^c)^2}{\beta_\lambda}\frac{\mathrm{d}I_{b,\lambda}}{\mathrm{d}T}\mathrm{d}\lambda \tag{6.2}$$

The derivative of the blackbody spectral intensity $I_{b,\lambda}$ with respect to temperature T is given by

$$\frac{\mathrm{d}I_{b\lambda}}{\mathrm{d}T} = \frac{C_1 C_2}{\pi \lambda^6 T^2} \frac{e^{C_2/\lambda T}}{\left(1 - e^{C_2/\lambda T}\right)^2} \tag{6.3}$$

where Planck's first and second radiation constants are $C_1 = 3.742 \times 10^8$ Wμm^4/m^2 and $C_2 = 1.439 \times 10^4$ μmK [94].

When the porous medium cannot be treated as optically thick or isotropically scattering more refined models for radiation characteristics are required. For example, fused quartz or soda-lime silicate glasses are weakly absorbing in the spectral range from 0.2 μm to approximately 4.5μm [46, 95] and the Rosseland diffusion approximation may not be valid. The previous chapter discussed extensively the model for radiation characteristics of semitransparent media containing bubbles proposed by Fedorov and Viskanta [11, 12]. The results for soda-lime silicate glass indicate that scattering of radiation by the bubbles entraped in the glass matrix dominates the radiation transfer in the spectral range 0.3 to 4.5 μm where the glass is weakly absorbing. For longer wavelengths, however, the glass matrix is strongly absorbing and absorption by the matrix dominates the radiation transfer. The model, however, has not been validated and experimental measurements are needed to validate the model.

The present chapter is restriced to radiation characteristics of semitransparent media containing bubbles including closed-cell foams. Experimental evidence on the effect of voids on the radiation characteristics of fused quartz containing bubbles is presented. First, different techniques for measuring the radiation characteristics of porous materials reported in the literature are briefly reviewed. Then, the experimental setup and procedure to retrieve the radiation characteristics by an inverse method are presented. Finally, experimental results are discussed along with a parametric study of the experimental conditions and assumptions made to retrieve the radiation characteristics by inverse method. The second part of the present study presents a quantitative validation of the existing model [11, 12] against experimental data for fused quartz containing bubbles.

6.2. Current State of Knowledge

Established techniques for estimating the radiation characteristics of porous materials consist of measuring some apparent physical quantities of the medium and of using inverse methods to retrieve the radiation characteristics that best fit the experimental data by solving the RTE. Initial values for the radiation characteristics are assumed and the RTE is solved. Then, the calculated and measured apparent properties are compared and a new estimate is made. This procedure is accomplished in an iterative manner until the set of absorption and scattering coefficients and phase function minimizes the difference between the measured and the calculated apparent properties. The major drawbacks inherent to the inverse method is that the problem is ill-posed, i.e., there is no unique solution for the absorption and scattering coefficients and the scattering phase function. Moreover, due to the iterative nature of the method, the initial value for the absorption and scattering coefficients are of major importance if one wants a rapid convergence of the solution. Experimental measurements commonly associated with inverse methods to retrieve the radiation characteristics of porous media are (i) spectral or total, (ii) directional-hemispherical or directional-directional measurements of transmittance and reflectance, and (iii) collimated (normal or not) or diffuse incident radiation. Moreover, several numerical techniques have been used to solve the RTE along with different optimization algorithms to minimize the difference between predictions and experimental data.

Hale and Bohn [96] combined the Monte-Carlo method with importance sampling and a nonlinear least squares convergence technique to compute the absorption and scattering coefficients of reticulated alumina foams from the spectral directional-hemispherical transmittance assuming an isotropic phase function. The directional-hemispherical transmittances of three samples of different thicknesses were measured. The initial guess for the radiation characteristics were obtained from a simplified geometric model.

Hendricks and Howell [97] derived the radiation characteristics of reticulated porous ceramics by measuring their spectral directional-hemispherical transmittance

and reflectance for 0.4μm$< \lambda < 5\mu$m. They used the traditional inverse method with the discrete ordinates method to solve the RTE and a nonlinear-least squares minimization algorithm. They investigated two different phase functions with two unknown parameters. The samples were 1-2 mm thick with 10 to 65 pores per inch (ppi) and a porosity of 80-85%. The authors reported severe computational stability and accuracy requirements and obtained only a few successfully converged optimum solutions, particular for most scattering samples (65 ppi). Moreover, the samples were thin to enable transmittance measurement but the homogeneity assumption may not be valid as reported by Hale and Bohn [96] for similar methods.

Baillis *et al.* [98, 99] combined measurements of bi-directional and directional-hemispherical transmittance and reflectance. They solved the RTE by the discrete ordinates method. Their study shows that a combination of bi-directional and directional -hemispherical measurements provides complementary information and is preferable over either bi-directional or directional-hemispherical measurements. As mentioned by Baillis *et al.* [99], the drawbacks of using bi-directional measurements for highly scattering media is the weakness of the transmitted signal that leads to high experimental uncertainties. On the other hand, directional-hemispherical measurements for a given sample thickness do not permit the estimation of the scattering phase function that often is assumed to be isotropic [100]. Moura *et al.* [101] recovered the spectral radiation characteristics of different semitransparent media from spectral transmittance and reflectance measurements with different angles of incidence. However, the authors assumed that the scattering phase function was azimuthally symmetric which limits the generality of the approach.

All the above mentioned studies have assumed that the porous medium can be treated as homogeneous. Such an assumption leads to the following experimental dilemma: on the one hand, one needs thick enough samples to be able to apply the inverse method using the RTE, yet, on the other hand some porous media are so highly scattering that the signal of the transmitted radiation is very weak even for thin samples, and the experimental uncertainty is very large. Moreover, if a thick

layer is exposed to a high intensity of radiation to obtain stronger signals, the incident radiation may heat up the sample causing non-uniformity in the sample temperature.

To overcome the difficulties related to the homogeneous assumption, Dunn [102] and Subramaniam and Mengüç [103] reported an inverse method using the Monte Carlo method with importance sampling with applications to *inhomogeneous* planar media. Unlike the traditional inverse method, the method described requires only one direct simulation but the optical thickness is either assumed to be known or determined from independent experiments. Moreover, as a statistically based method the Monte Carlo method requires to track a large number of photon bundles and hence large computer resources for a reasonable accuracy [96].

An alternative technique to measure the radiation properties of porous materials has been presented by Yamada, Kurosaki, and co-workers [104,105]. First, Take-Uchi *et al.* [104] presented a method to determine the extinction coefficient, the albedo and the back-scattering fraction factor of fiberglass batting. The albedo and the back-scattering fraction factor were estimated by heating an optically thick sample at 108^{o}C and measuring its normal emittance. The extinction coefficient was determined independently by transmittance measurements of a thinner sample. The analysis is based on the two-flux model and on the assumptions that the radiative properties do not depend on temperature and that the temperature in the medium is uniform. The albedo and the back-scattering fraction factor are determined using the least-square optimization technique. Further simplification has been presented more recently by Yamada and Kurosaki [105] who assumed an isotropic scattering phase function. In both cases, the authors used the fact that the emittance of an optically thick and isotropically scattering medium is independent of the optical thickness and depends only on the albedo and on the back-scattering fraction factor (=0.5 if isotropic scattering is assumed). Finally, the authors recommend the simplified method for highly scattering media rather than for absorbing media since the albedo is very sensitive to emittance and that the latter is larger for strongly absorbing media.

6.3. Experiments

6.3.1. Experimental Setup

Figure 6.1 shows the experimental setup used to measure the spectral bi-directional transmittance and reflectance of the quartz samples containing bubbles and shows the path of the radiation from the radiation source to the detector. A radiation source is

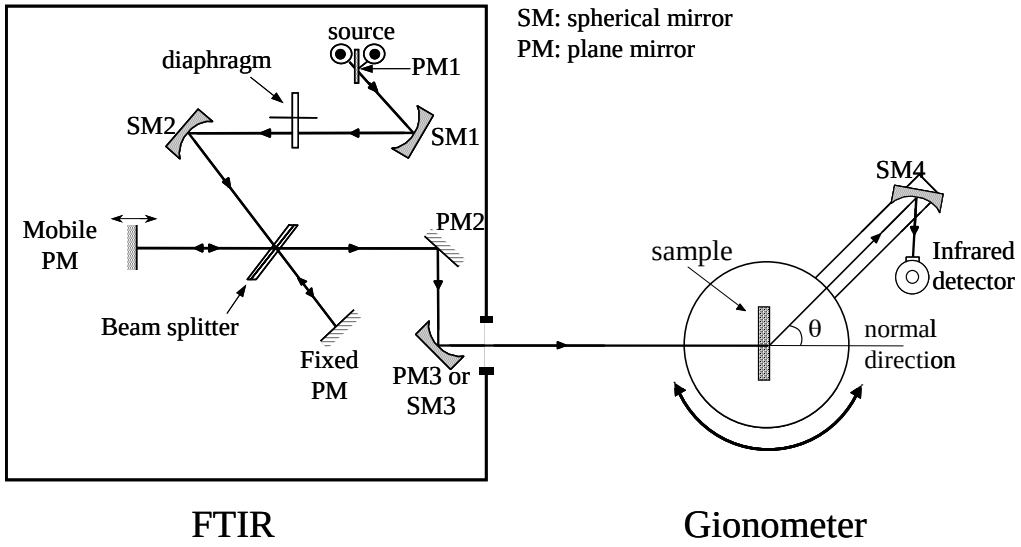

Figure 6.1. Schematic of the experimental apparatus used to measure the spectral transmittance and reflectance.

generated from a Fourier transform infrared spectrometer (FTS 60 A, Bio-Rad, Inc.) operating in the spectral range 1.5-25 μm. The source is distant from the spherical mirror MS1 by twice its focal distance and corresponds to a blackbody emission spectrum at 1300^{o}C emitting a radiation beam 7 mm in diameter. The diaphragm is located in the focal point of mirror MS2 and consists of four cylindrical holes of different radii R_A that determined the divergence half-angle θ_0 of the outcoming beam of the FTIR expressed as

$$\theta_0 = Arctan(\frac{R_A}{f_2}) \tag{6.4}$$

where f_2 is the focal distance of mirror MS2. For a good resolution one needs to reduce the divergence of the beam by reducing the radius of the diaphragm. However, this also reduces the energy of the signal. Thus, a compromise must be found between the energy of the signal leaving the FTIR and the resolution. The optimum diaphragm diameter was found to be 2.7 mm leading to a resolution of 2 cm^{-1} and a divergence half-angle $\theta_0 = 1.27^o$ [106].

The detection system consists of a spherical mirror collecting the transmitted radiation and concentrating it on a liquid nitrogen cooled MCT (HgCdTe) detector (Bio-Rad, Inc. model 997-0038) located at its focal point. The detection system is mounted on a rotating arm enabling the measurement of the spectral bi-directional transmittance and reflectance in any arbitrary direction in the plane of incidence as shown in Figure 6.2. The rotation axis of the goniometer is passing in the plane of

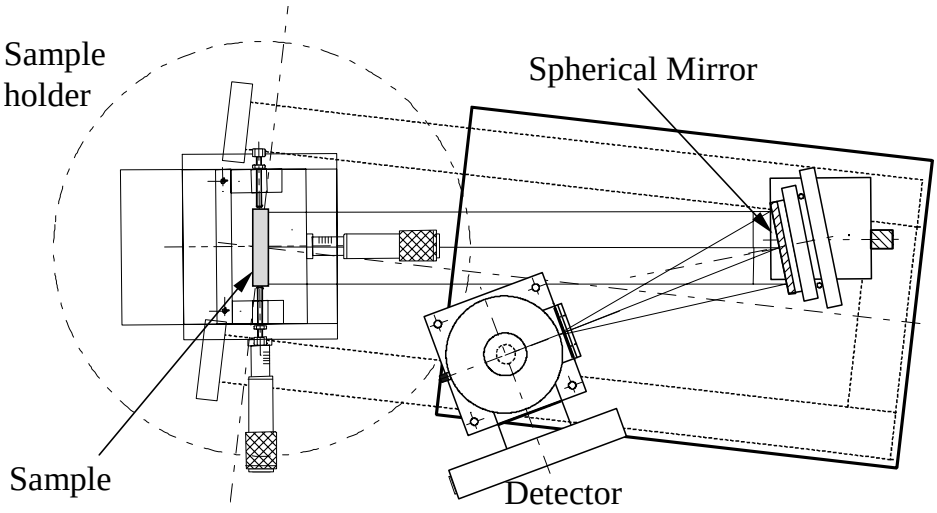

Figure 6.2. Schematic of the rotating arm of the goniometer used to measure the spectral transmittance and reflectance.

the front face of the sample for reflectance measurements and in the plane of the back face for transmittance measurements. The normal incident direction ($\theta = 0^o$) has been determined by finding the location of the maximum signal in the absence of the

sample. The entire system was purged with dry air to avoid infrared absorption by water vapor and carbon dioxide. The radiation emitted by the source is modulated and the detection is synchronized so that the radiation emitted by the sample and the surroundings are not measured.

The bi-directional transmittances and reflectances $T_{e,\lambda}(\theta)$ for normal incidence are defined by

$$T_{e,\lambda}(\theta) = \frac{I_\lambda(\theta)}{I_{\lambda,0}\mathrm{d}\omega_0} \tag{6.5}$$

where $I_\lambda(\theta)$ is the transmitted or reflected intensity in the θ-direction and $I_{\lambda,0}$ is the intensity of the collimated beam normally incident onto the sample within the solid angle $\mathrm{d}\omega_0 = 2\pi(1-cos\theta_0)$. The solid angle of detection is denoted $\mathrm{d}\omega_d = 2\pi(1-cos\theta_d)$ where θ_d is the detection angle measured experimentally as 0.19^o. The spherical mirror obstructs the incident beam and prevents the measurement of the spectral bi-directional reflectance for directions close to $\theta = 180^o$. To overcome this difficulty, the sample holder is rotated by an angle $\theta_a = 5^o$ (see Figure 6.3) enabling the measurement of specular reflection and is equivalent to the measurement for the direction of the quadrature scheme if one assumes that the reflection is independent of the incident angle (for small angles) [107].

Finally, the reflection of the incident radiation by the diaphragm located in front of the sample can significantly affect the reflectance measurements, particularly for small diaphragms. Figure 6.4 shows a schematic of the sample holder used for the transmittance and reflectance measurements. The sample holder consists of two rigid plates having a circular diaphragm between which the sample is placed. Painting the sample holder with an absorbing black paint was not sufficient to minimize such a disturbance. Consequently, the sample holder including the front and back diaphragms were coated with soot particles by placing them in a combustion chamber where ethylene and oxygen burned with an excess of oxygen. Then, the emissivity of the sample holder has been measured and indicates that it behaves as a blackbody across the entire spectral range of the detector. Doermann [106] also showed that assuming a uniform incident radiation intensity may not be valid if the diaphragm

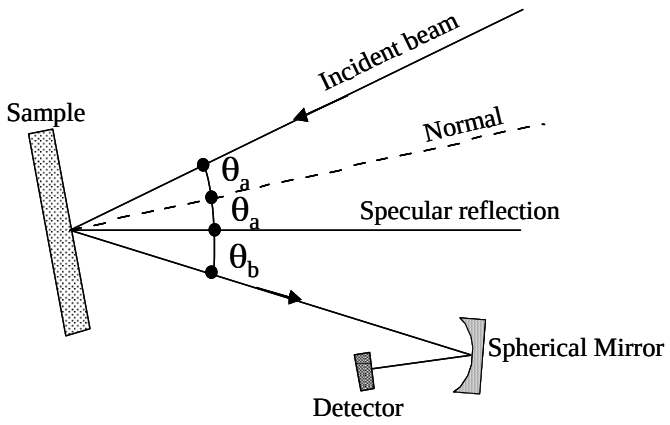

Figure 6.3. Reflectance measurements in the directions between 170^o and 180^o with θ_a=5^o.

placed in front of the sample is too large. Therefore, a compromise should be found in order to find the largest possible diaphragm that would give the largest radiation intensity and signal to noise ratio possible while satisfying the assumption of uniform incident intensity used as a boundary condition in the inversion scheme. The optimum diaphragm diameters was found to be 35 mm leading to a sample thickness to diaphragm diameter ratio between 1/12 and 1/4. In the inversion procedure the radiative transfer equation is solved assuming that the radiation intensity profile of the incident beam falling on the sample is uniform [see boundary condition expressed by Equation (6.8)]. In general, the intensity profile assumes a bell shape with a plateau in the center and a sharp decrease at the edges. The uniformity of the radiation intensity falling onto the sample, i.e., the extent of the plateau in the center of the beam depends both on the spectrophotometer aperture and the size of the diaphragm placed in front of the sample.

6.3.2. Sample Description

In order to experimentally validate the theoretical model proposed and discussed previously [11, 12], fused quartz samples containing bubbles have been prepared and

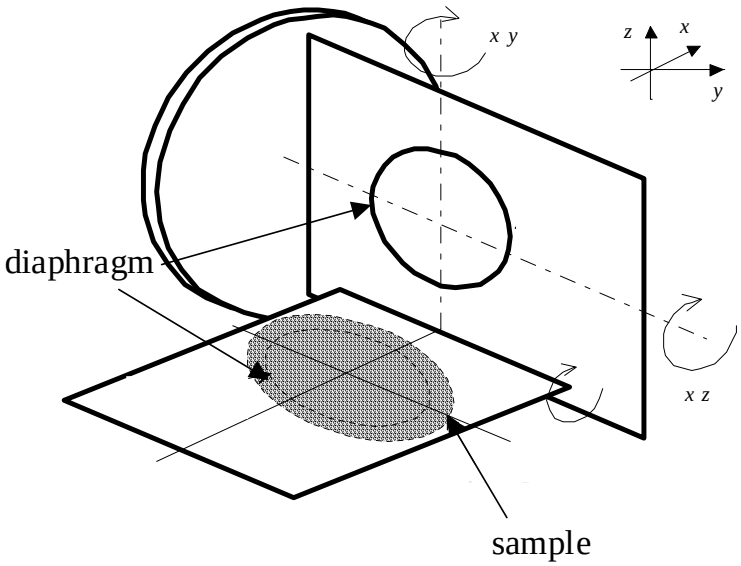

Figure 6.4. Schematic of the sample holder used to measure the spectral transmittance and reflectance.

analyzed. The fused quartz is the Osram Sylvania SG25 Lighting grade containing a negligible hydroxyl content with a maximum of 5 ppm. Samples were cut with a diamond saw from a large piece of quartz collected during the shutdown of an industrial furnace in which the fused quartz is electrically heated in an inert atmosphere of helium and hydrogen. The samples were then ground with a diamond wheel and polished with silicon carbide papers of different grids. Desirable finish was achieved using a rotating cork belt. The samples were cleaned with a 1:1 mixture of sulfuric acid and hydrogen peroxide at 30% for 10 minutes, followed by a 10 minutes rinse in de-ionized water. The samples were finally dried by blowing them with ultra-pure nitrogen. Five samples of different thicknesses (3, 5, 5.6, 6, and 10 mm) have been studied, all having an average void fraction of 0.094 $\pm$ 16% and a 5 cm $\times$ 5 cm cross-section. The samples are cut relatively thin so that (1) the width to thickness ratio is large enough to assure one-dimensional radiative transfer, and (2) the transmitted signal to noise ratio is large enough for the measurements to be meaningful. Due to the small thickness, the sample thickness to average bubble diameter ratio

is small and inhomogeneities exist. However, the cross-sectional area of the incident beam is large (about 35 mm) compared with the average cross-sectional area of the bubbles. Therefore, the radiation encounters numerous bubbles as it passes through the sample leading to an averaging effect that smoothes out the inhomogeneities as confirmed by Baillis and Sacadura [100]. In other words, the radiation characteristics κ_λ, σ_λ, β_λ and $\Phi(\theta)$ recovered from the bi-directional transmittance and reflectance measurements vary little with the sample thickness, i.e., the local inhomogeneities do not affect the results of the inversion and the homogeneous assumption is valid.

Figure 6.5 shows a photograph of a typical sample 3 mm thick. The bubble size

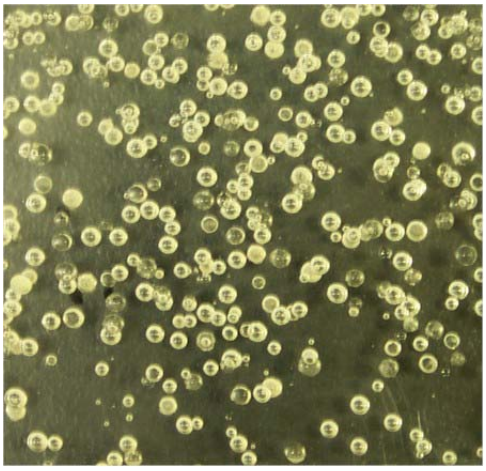

Figure 6.5. Digital photograph of a fused quartz sample containing bubbles (porosity $\approx$ 10%).

distribution was determined from the analysis of more than 120 images of individual

bubbles such as that presented in Figure 6.6. As one can see in Figures 6.5 and 6.6,

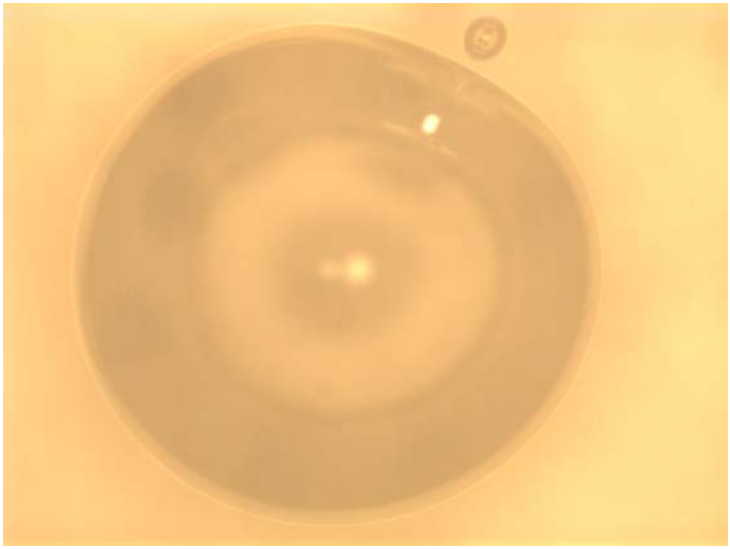

Figure 6.6. Digital micrograph of two adjacent bubbles entrapped in fused quartz with a=0.15 mm and 1.64 mm.

the bubbles are spherical in shape, randomly distributed, and their size distribution is relatively uniform as illustrated in Figure 6.7. The average bubble radius is $\bar{r}$=1.14 mm. The fact that bubbles are randomly distributed assures that radiation characteristics of the medium are independent of the azimuthal angles and that bidirectional transmittances are symmetric with respect to the incident direction. Even though micrographs were taken from two different samples, all the samples were assumed to have the same bubble size distribution and void fraction since the samples were prepared from the same large piece of glass.

6.3.3. Inverse Method

The radiation characteristics of the samples are determined by an inverse method. The inversion consists of determining iteratively the radiation characteristics that minimize the quadratic difference F between the measured and calculated bi-directional

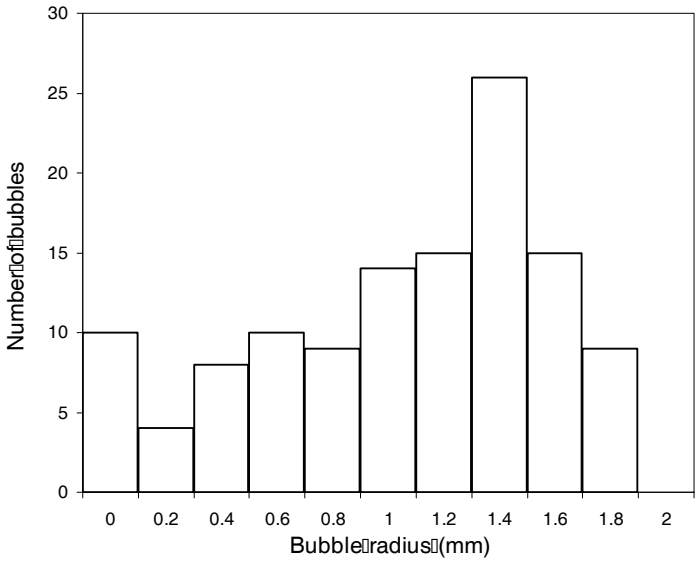

Figure 6.7. Bubble size distribution obtained from more than 120 images of individual bubbles.

transmittance and reflectance at each wavelength λ and in each direction θ_i of interest where F is given by

$$F(\omega_\lambda, \beta_\lambda, \Phi(\theta_i)) = \sum_{i=1}^{n} [T_{t,\lambda}(\theta_i) - T_{e,\lambda}(\theta_i)]^2 \tag{6.6}$$

The function $F(\omega_\lambda, \beta_\lambda, \Phi(\theta_i))$ is minimized by Gauss linearization method, i.e., by setting to zero the derivatives of F with respect to each of the unknown parameters [108].

The theoretical spectral transmittances and reflectances were computed by solving the radiative transfer equation based on the following assumptions: (1) the radiation transfer is assumed to be one-dimensional, (2) azimuthal symmetry prevails, (3) the medium emission term can be disregarded due to the radiation modulation and the phase sensitive detection, (4) the medium is homogeneous and independently scattering, and (5) the effect of polarization on the bi-directional reflectance is not considered.

Solution of the RTE is obtained by using the discrete ordinates method in the n

directions of the quadrature scheme. Under the above assumptions, the discretized one-dimensional RTE in the direction θ_i can be expressed as the following system of n partial differential equations (one for each direction)

$$\mu_i \frac{\partial I_\lambda(\tau_\lambda, \mu_i)}{\partial \tau_\lambda} = -I_\lambda(\tau_\lambda, \mu_i) + \frac{\omega_\lambda}{2} \sum_{j=1}^{n} w_j \left[\Phi(\mu_j, \mu_i) I_\lambda(\tau_\lambda, \mu_j) + \Phi(-\mu_j, \mu_i) I_\lambda(\tau_\lambda, -\mu_j)\right] \tag{6.7}$$

where $\mu_i = cos\theta_i$ is the cosine director, τ_λ is the spectral optical thickness of the sample in the direction μ_i, and w_i is a weighting factor associated with the ordinate direction θ_i. The weighting factors w_i depend on the quadrature scheme [109] and are listed in Table 6.1 and illustrated in Figure 6.8 for the quadrature consisting of 24 directions and corresponding to a half angle θ_0 of 1.27^o. The boundary conditions

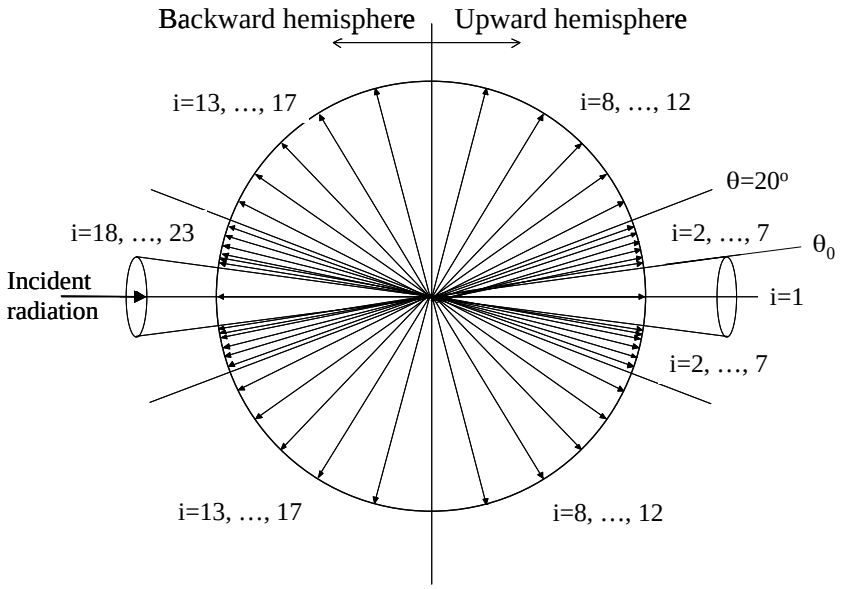

Figure 6.8. Schematic of the 24 directions for the quadrature associated with the divergence half-angle of $\theta_0 = 1.27^o$.

are obtained by assuming that the interfaces are smooth. Indeed, the void fraction is

Table 6.1. 24 directions and corresponding weighting factors for the quadrature with the divergence half-angle equals to 1.27^o.

index i	**Angle,** θ_i $(^o)$	μ_i	**Weight** w_i
1	0.0	1.000000	2.46×10^{-4}
2	1.85	0.999479	7.05×10^{-4}
3	3.32	0.998322	1.60×10^{-3}
4	4.92	0.996315	2.39×10^{-3}
5	6.80	0.992976	3.04×10^{-3}
6	7.99	0.990304	3.49×10^{-3}
7	9.36	0.986680	3.72×10^{-3}
8	16.44	0.959112	6.57×10^{-2}
9	31.58	0.851919	0.14718
10	48.00	0.669092	0.21576
11	64.74	0.426806	0.26518
12	81.57	0.146618	0.29103
13	98.43	-0.146618	0.29103
14	115.27	-0.426806	0.265178
15	132.00	-0.669092	0.21576
16	148.42	-0.851919	0.14718
17	163.56	-0.959112	6.57×10^{-2}
18	170.64	-0.986680	3.72×10^{-3}
19	172.02	-0.990304	3.49×10^{-3}
20	173.51	-0.993586	3.04×10^{-3}
21	175.08	-0.996315	2.39×10^{-3}
22	176.68	-0.998322	1.60×10^{-3}
23	178.15	-0.999479	7.05×10^{-4}
24	180.00	-1.000000	2.46×10^{-4}

relatively small and the effect of open bubbles at the sample surface can be neglected. Then, the boundary conditions are given by

$$I_\lambda(0,\mu_j) = -2r_{12}\sum_{\mu_i<0} w_i\mu_i I(0,\mu_i) + (1-r_{12})\delta_{\mu_0,\mu_j} I_\lambda(0,\mu_0) \qquad \mu_j > 0 \quad (6.8)$$

$$I_\lambda(\tau_{\lambda,L},\mu_j) = 2r_{21}\sum_{\mu_i>0} w_i\mu_i I(\tau_{\lambda,L},\mu_i) \qquad \mu_j < 0 (6.9)$$

where r_{12} and r_{21} are the interface reflectivities as shown in Figure 6.9 and $\tau_{\lambda,L}$ is the optical thickness of the entire sample, i.e., $\tau_{\lambda,L} = \tau_\lambda(x = L)$. As discussed by

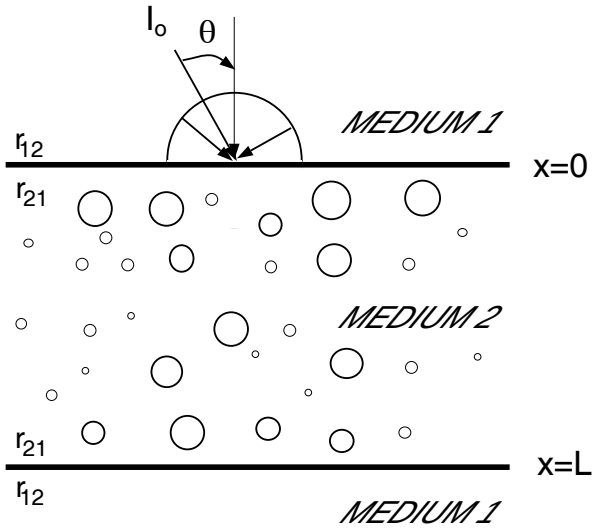

Figure 6.9. Schematic of the idealized liquid layer containing bubbles and the coordinate system.

Fedorov and Viskanta [11], in the case of collimated incident radiation, the external surface reflectivity (r_{12}) can be calculated using Fresnel law of reflection [84]

$$r_{12} = \frac{(n_\lambda^c)^2 - 1}{(n_\lambda^c)^2 + 1} = 1 - r_{21} \quad (6.10)$$

Moreover, due to the presence of a large number of scatterers (bubbles) in the condensed phase layer (medium 2), the radiation field inside the layer can be assumed to be isotropic for both collimated and diffuse external incidence. As such, the internal

surface reflectivity r_{21} for any diffuse media-to-air interface is given by ([110], p. 21 and [111]):

$$r_{21} = 1 - \left\{1 - [0.4399 + 0.7099 n_\lambda^c - 0.3319 (n_\lambda^c)^2 + 0.0636 (n_\lambda^c)^3]\right\} / (n_\lambda^c)^2 \qquad (6.11)$$

The scattering phase function was assumed to follow the Henyey-Greenstein normalized form involving only the asymmetry factor g and expressed as [84]

$$\Phi_\lambda(\theta) = \frac{1 - g^2}{[1 + g^2 - 2gcos\theta]^{3/2}} \qquad (6.12)$$

The shape coefficient g can vary between 0 (isotropic scattering) and ± 1 (+ for strictly forward scattering and - for backward scattering).

Finally, the space is discretized in order to numerically solve the above system of partial differential equations with the associated boundary conditions [Equations (6.7) to (6.9)] by the finite volume method [101, 106]. The results obtained by the discrete ordinates method depend strongly on the number of directions and on the spatial discretizations chosen. In order to reduce the computational time and still provide adequately accurate results grid sensitivity studies have been performed. The numerical results were shown to be independent of the number of control volumes considered and 190 control volumes in each ordinate direction was considered to be the optimum number of spatial discretization. Then, the equations were solved in 24 different angles of ordinate directions and for 337 different wavelengths in the spectral region from 1.67 μm to 4.76 μm.

6.3.4. Infrared Optical Constants of Fused Quartz

The complex index of refraction of fused quartz in the spectral range of the infrared detector ($0.2\mu\text{m} \leq \lambda \leq 15\mu\text{m}$) is necessary for determining the reflectance at the glass sample/surrounding interface used in boundary conditions. These data are also needed for the validation of the model against experimental data.

Table 6.2summarizes the references reporting experimental values of the real part of the complex index of refraction of fused quartz at room temperature along with the

spectral range covered from the relationships: Different correlations for the real part

Table 6.2. Summary of the experimental data reporting the real part of complex index of refraction of fused quartz at room temperature.

Reference	**Wavelengh range**
[47]	$1.31\mu\text{m} \leq \lambda \leq 4.84\mu\text{m}$
[112]	$0.35\mu\text{m} \leq \lambda \leq 3.51\mu\text{m}$
[113]	$0.21\mu\text{m} \leq \lambda \leq 3.71\mu\text{m}$
[114]	$2.1\mu\text{m} \leq \lambda \leq 14.\mu\text{m}$
[115]	$8.13\mu\text{m} \leq \lambda \leq 9.63\mu\text{m}$
[116]	$7.84\mu\text{m} \leq \lambda \leq 12.90\mu\text{m}$
[117]	$0.2\mu\text{m} \leq \lambda \leq 3.4\mu\text{m}$
[118]	$7.14\mu\text{m} \leq \lambda \leq 11.11\mu\text{m}$
[119]	$7.14\mu\text{m} \leq \lambda \leq 50.00\mu\text{m}$

of the complex index of refraction of fused quartz as a function of wavelength have been suggested in the literature [112, 113, 120] for different spectral regions. Rodney and Spindler [112] suggested an expression for n_λ^c over the spectral range from 0.347 to 3.508 μm at 31^{o}C while Tan and Arndt [120] proposed another equation in the spectral region from 1.44 to 4.77 μm at temperatures ranging from 23.5 to 481^{o}C. Over the spectral range from 0.21 to 3.71 μm at 20^{o}C, Malitson [113] fitted experimental data with the following three-term Sellmeier equation,

$$(n_\lambda^c)^2 = 1 - \frac{0.6961663\lambda^2}{\lambda^2 - (0.0684043)^2} \frac{0.4079426\lambda^2}{\lambda^2 - (0.1162414)^2} + \frac{0.8974794\lambda^2}{\lambda^2 - (9.896161)^2} \qquad (6.13)$$

Moreover, Tan [121] confirmed the validity of Equation (6.13) for wavelengths up to 6.7 μm. Therefore, due to its wide range of validity (from 0.21 to 6.7 μm) at room temperature, Equation (6.13) will be used in the present study. Figure 6.10 shows the variations of the real part of the complex index of refraction n_λ^c of fused quartz as a function of wavelength λ as reported in the literature and summarized in Table 6.2.

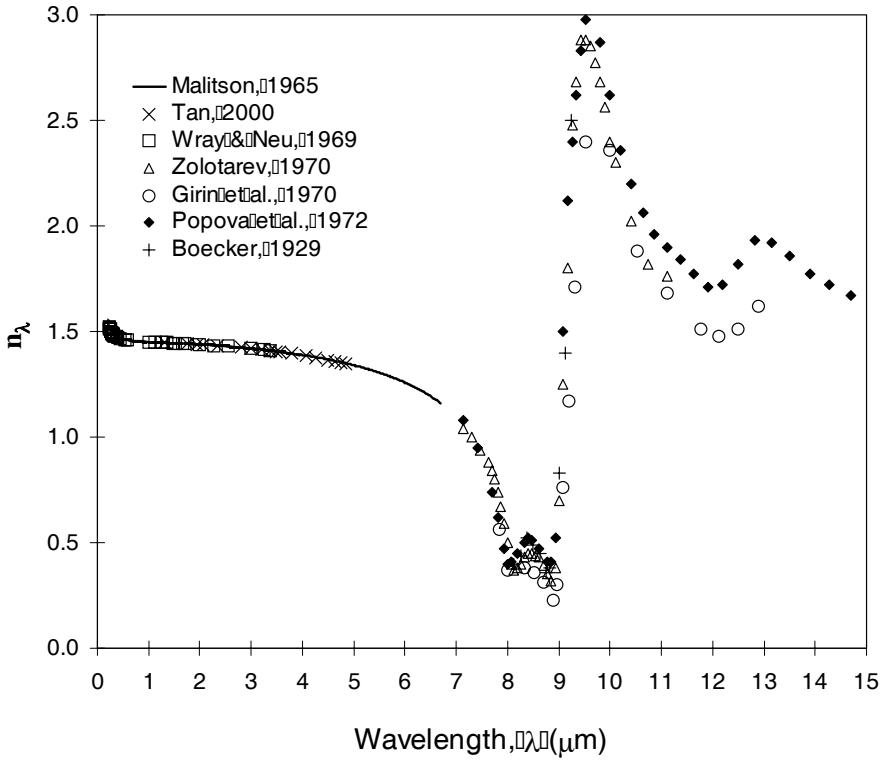

Figure 6.10. Real part of the complex index of refraction of fused quartz n_λ^c.

The absorption coefficient or the imaginary part of the refractive index of fused quartz in the near-infrared (up to 3.5 μm) depends strongly on the purity of the fused quartz [95, 114, 122] and in particular on the hydroxyl content [114, 122]. The value of the extinction index k_λ^c was not always directly available from the literature and had to be recovered from spectral transmittance or emittance measurement data. Table 6.3 lists the references reporting experimental data for fused quartz at room temperature with the spectral range covered, the thickness of the sample, and the measurements performed to recover k_λ^c. The value of k_λ^c can be recovered from the normal spectral transmittance data $T_{0,\lambda}$ based on the relationship between $T_{0,\lambda}$ and k_λ^c in which multiple reflections are accounted for [109]

$$T_{0,\lambda}(L) = \frac{(1-\rho_\lambda)^2 e^{\kappa_\lambda^c L}}{1-(\rho_\lambda^c)^2 e^{2\kappa_\lambda^c L}} \tag{6.14}$$

Table 6.3. Summary of the experimental data reporting the imaginary part of complex index of refraction of fused quartz at room temperature.

Reference	**Wavelengh range**	Comments
[114]	$3.63\mu\text{m} \leq \lambda \leq 14.\mu\text{m}$	
[115]	$8.13\mu\text{m} \leq \lambda \leq 9.63\mu\text{m}$	
[116]	$7.84\mu\text{m} \leq \lambda \leq 12.90\mu\text{m}$	
[118]	$7.14\mu\text{m} \leq \lambda \leq 11.11\mu\text{m}$	
[123]	$0.22\mu\text{m} \leq \lambda \leq 3.5\mu\text{m}$	Data extracted from spectral absorption coefficient
[119]	$7.14\mu\text{m} \leq \lambda \leq 50.00\mu\text{m}$	
[124]	$3.0\mu\text{m} \leq \lambda \leq 14.0\mu\text{m}$	Data extracted from normal emittance measurements at $T = 313K$ (curves 1 on p. 406)
[124]	$7.14\mu\text{m} \leq \lambda \leq 50.00\mu\text{m}$	Data extracted from normal transmittance measurements at $T = 298K$(curves 1, 6, 14, 15, 18, 20, and 29 on p. 423)

where L is the thickness of the layer, ρ_λ and α_λ are the spectral reflectivity of the interface and the spectral absorption coefficient of fused quartz, respectively, and are given by

$$\rho_\lambda^c = \frac{(n_\lambda^c - 1)^2}{(n_\lambda^c + 1)^2} \tag{6.15}$$

$$\text{and} \qquad \kappa_\lambda^c = \frac{4\pi k_\lambda^c}{\lambda} \tag{6.16}$$

This expression can be solved as a quadratic in the exponential factor and after some algebraic manipulation obtain the following expression for k_λ^c as a function of the real part of the complex index of refraction n_λ^c, the sample thickness d, and the sample spectral normal transmittance $T_{0,\lambda}$,

$$k_\lambda^c = -\left(\frac{\lambda}{4\pi L}\right) ln\left[\frac{\sqrt{(1-\rho_\lambda)^4 + 4\rho_\lambda^2 T_{0,\lambda}} - (1-\rho_\lambda)}{2\rho_\lambda^2 T_{0,\lambda}}\right] \tag{6.17}$$

The imaginary part of the complex index of refraction k_λ^c can also be determined from measurements of the spectral normal emittance $\epsilon_{\lambda,0}$ using the following expression [125],

$$k_\lambda^c = \left(\frac{\lambda}{4\pi L}\right) ln\left[\frac{1-\rho_\lambda-\rho_\lambda\epsilon_{\lambda,0}}{1-\rho_\lambda-\epsilon_{\lambda,0}}\right] \tag{6.18}$$

Figure 6.11 shows the variations of the imaginary part of the complex index of refraction k_λ^c of fused quartz as a function of wavelength λ as reported in the literature or derived from Equations (6.17) and (6.18) and summarized in Table 6.3. Note, that

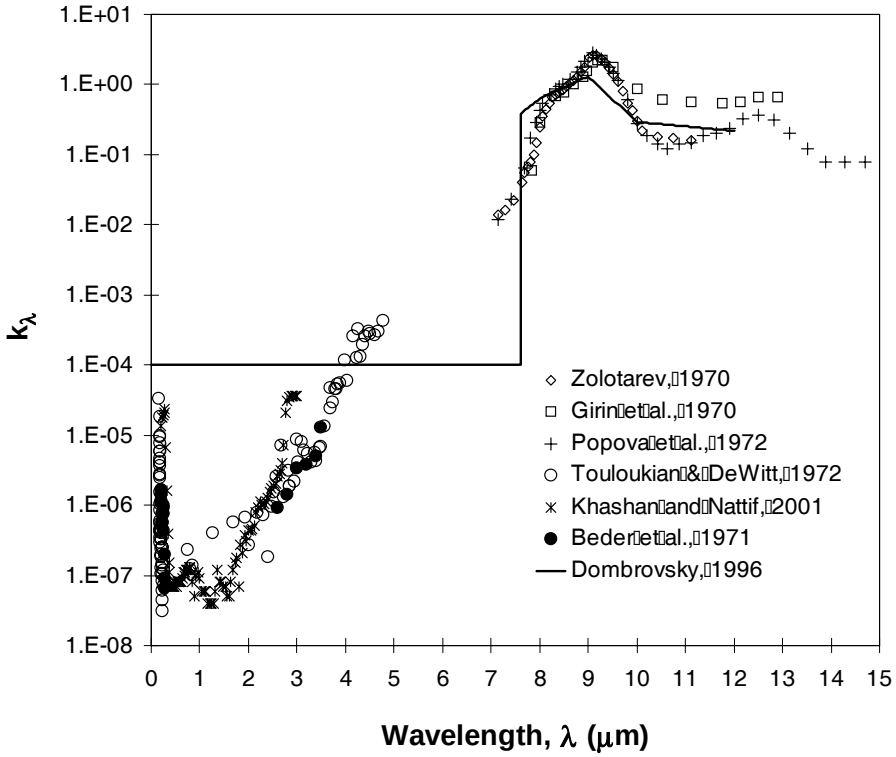

Figure 6.11. Imaginary part of the complex index of refraction of fused quartz k_λ^c.

computation of the complex part of the index of refraction k_λ^c from transmittance and emittance measurements lead sometimes to negative values, particularly in the spectral region where fused quartz is very weakly absorbing (from 0.2 to 4.0 μm). This indicates that in this region, data should be used with care since the experimental

uncertainty for k_λ^c is very large and k_λ^c effectively vanishes as revealed in Figure 6.12 with a linear scale.

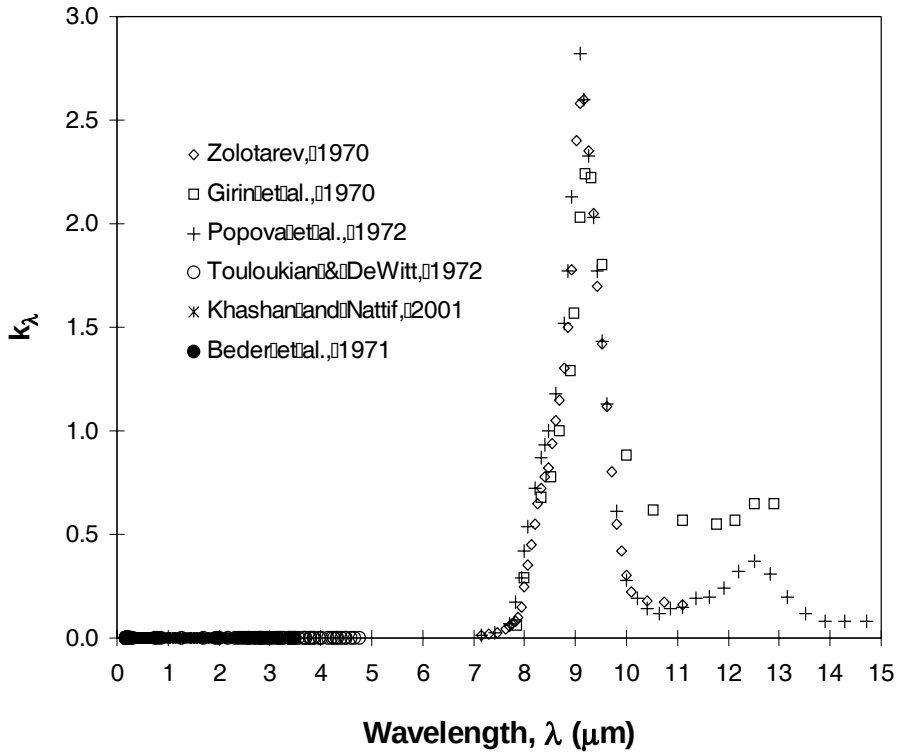

Figure 6.12. Imaginary part of the complex index of refraction of fused quartz k_λ^c plotted with a linear scale.

6.3.5. Experimental Uncertainty

To assess the experimental uncertainty, the spectral bi-directional transmittance and reflectance measurements were performed four times with a sample of thickness 5.6 mm from the alignement of the experimental setup to the inversion method. The

average spectral transmittance or reflectance in direction θ_i and wavelength λ denoted $\bar{T}_\lambda(\theta_i)$ along with the mean square deviations Δ_i have been computed as

$$\bar{T}_\lambda(\theta_i) = \frac{1}{4}\sum_{k=1}^{4} T_{k,\lambda}(\theta_i) \tag{6.19}$$

$$\Delta_i = \frac{1}{\bar{T}_\lambda(\theta_i)}\sqrt{\frac{1}{3}\sum_{k=1}^{4}\left(T_{k,\lambda}(\theta_i) - \bar{T}_\lambda(\theta_i)\right)^2} \tag{6.20}$$

The spectral bi-directional transmittances and reflectances of each sample have been measured for each of the four alignements of the experimental setup. Then, they were averaged and use as an input parameter in the inversion algorithm. The experimental error on the measured transmittances and reflectances depends on the ordinate directions and on the wavelength. Indeed, the signal to noise ratio decreases as one moves away from the incident direction corresponding to $\theta_i = 0.0^o$. The experimental error is conservatively estimated to be 9 %, i.e., $\Delta_i < 9\%$ in the normal direction and to 25% at $\theta_i = 3.32^o$.

6.4. Results and Discussion

The input parameters for the inverse method are the (i) sample thickness L, (ii) the ordinate directions θ_i and the associated weighting factors w_i, and (iii) the complex index of refraction of fused quartz. The radiation characteristics retrieved from the inversion are the single scattering albedo ω_λ, the extinction coefficient β_λ, and the Henyey-Greenstein asymmetry factor g. Then, the absorption and scattering coefficients can be determined from

$$\kappa_\lambda = \beta_\lambda(1-\omega_\lambda) \qquad \text{and} \qquad \sigma_\lambda = \beta_\lambda\omega_\lambda \tag{6.21}$$

This section presents the radiation characteristics of fused quartz containing bubbles obtained by inverse method. It aims at discussing in details the validity of the results and their sensitivity to input parameters as well as providing physical explanations to the results.

6.4.1. Discussion of the Inverse Method

Since the set of equations solved by the inverse method is ill posed, a small uncertainty in the experimental data could lead to large variations and errors in the recovered results. Therefore, it is essential to perform a sensitivity study to assess the effect of small changes in the input parameters [126]. To do so, uncertainty on the real (n_λ^c) and complex (k_λ^c) parts of the index of refraction of fused quartz were estimated to be 2% and 25 %, respectively, while the uncertainty on the sample thickness L is estimated to be 2 %. It was shown that error on the sample thickness L and the complex part of the index of refraction k_λ^c have negligible influence on the results of the inverse method. However, an uncertainty of 2% in n_λ^c leads to a similar uncertainty on the retrieved extinction coefficient, single scattering albedo, and asymmetric factor g but is still acceptable since experimental data for n_λ^c appear to be very accurate and highly reproducible as discussed previously.

Furthermore, the influence of the number of ordinate directions used for the inversion has been investigated. The study shows that at least three angles θ_i are needed in the forward direction in order to have convergence of the inversion algorithm. The results were shown to be independent of the number of ordinate directions if at least eight different angles θ_i were considered. Note that the number of backward directions considered does not affect the value of the retrieved radiation characteristics probably because the scattering is mainly in the forward direction.

Similarly, sensitivity study for the initial values taken for β_λ, ω_λ, g has been carried out. Two sets of initial radiation characteristics were used ($\beta_\lambda = 99.97$, $\omega_\lambda = 0.8$, $g = 0.9$) and ($\beta_\lambda = 80.97$, $\omega_\lambda = 0.99$, $g = 0.6$). The inverse algorithm always converge to the same solutions for both sets of initial estimates of the radiation characteristics.

Moreover, beyond wavelengths of 4.5 μm fused quartz is strongly absorbing, thus reducing the magnitude of the transmitted signal and increasing the experimental uncertainty. The measurements were performed for wavelengths between 1.67 μm and 3.5 μm. The lower limit corresponds to the limit of the detector while for wavelengths larger than 3.5 μm the inverse algorithm could not converge for certain samples.

Finally, it was not necessary to measure spectral directional-hemispherical transmittance and reflectance as suggested by Baillis *et al.* [99, 100] owing to the good behavior of the inversion algorithm in terms of convergence and sensitivity.

6.4.2. Analysis of the Experimental Results

Figure 6.13 shows the extinction coefficient, the single scattering albedo, and the Henyey-Greenstein asymmetric factor as a function of wavelength retrieved for the different samples. One can see that the retrieved characteristics do not vary significantly with the sample thickness which confirms the good behavior of the inversion algorithm. However, the 3 mm thick sample has a spectral extinction coefficient much larger than that of the other samples. This can be explained by the fact that the sample may be too thin to be treated as homogeneous. Similar observations have been reported by Hale and Bohn [96] for open-cell reticulated alumina foams. Moreover, retrieved radiation characteristics for the 10 mm thick sample deviate slightly from those obtained with 5, 5.6, and 6 mm thick samples. The deviation can be attributed to the fact that the one-dimensional radiation transfer assumption may no longer be valid since the sample thickness to diaphragm diameter ratio equals 1/4. It could also be due to the experimental uncertainties that are larger for thicker samples because they provide stronger absorption thus reducing the transmitted signal and the signal to noise ratio.

Based on the above remarks, the radiation characteristics retrieved for the 3 mm thick sample have not been considered. The spectral data for the four other samples have been averaged at each wavelength and are shown in Figure 6.14 along with the associated standard deviation. The maximum standard deviation is observed for the single scattering albedo and does not exceed 14%. The resulting absorption and scattering coefficients computed from Equation (6.21) are presented in Figure 6.15. The scattering coefficient is relatively small due to the small void fraction and the relatively large bubble size resulting in a small interfacial surface area. Indeed, scattering

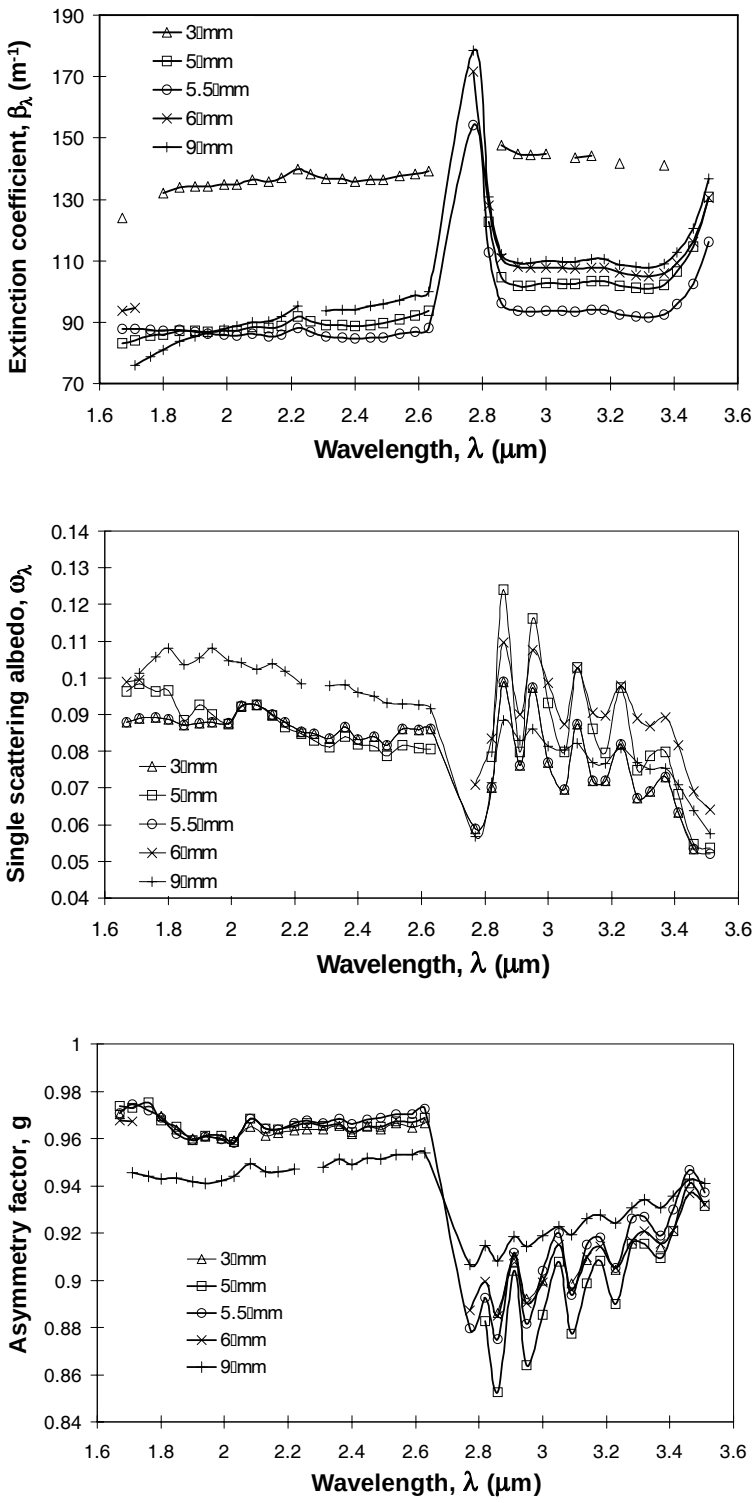

Figure 6.13. Retrieved extinction coefficient, single scattering albedo and Henyey - Greenstein asymmetry factor determined by inverse method for each samples.

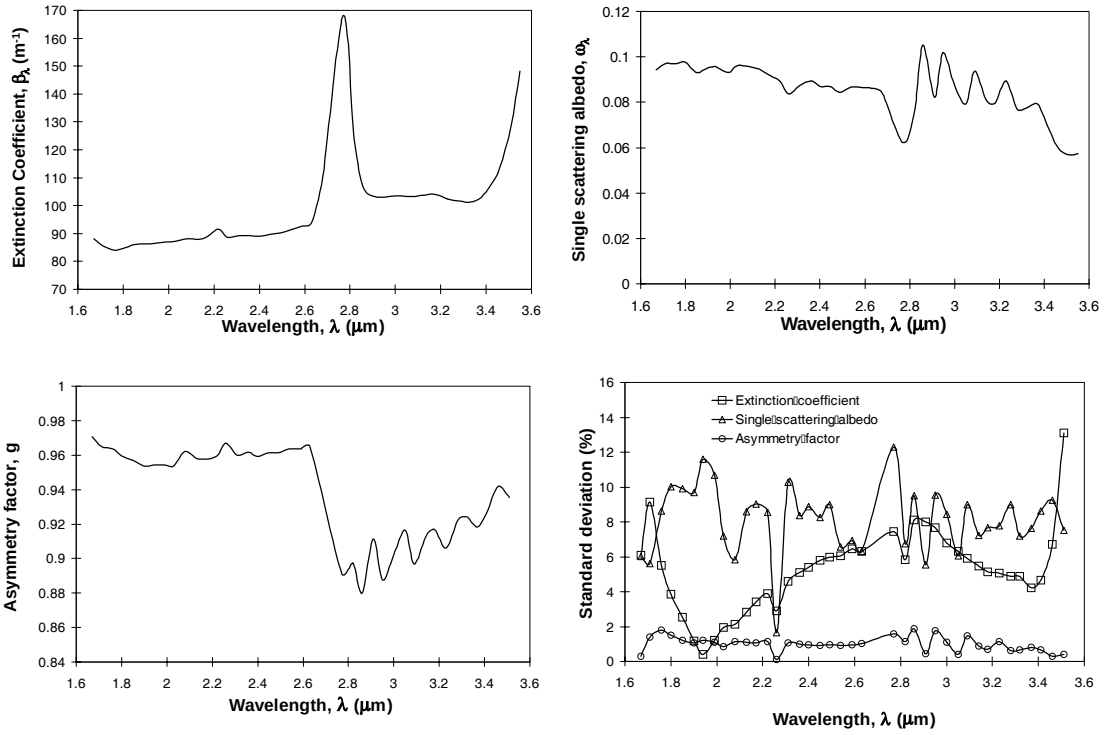

Figure 6.14. Average retrieved extinction, single scattering albedo and Henyey - Greenstein asymmetry factor by inverse method for each samples and their standard deviation.

is caused by the reflection and diffraction of the radiation at the gas/fused quartz interface and should strongly depend on the interfacial surface area. Moreover, the absorption coefficient presents a peak around wavelength of 2.7 μm. It is attributed to hydroxyl groups present as impurities in the fused quartz. Indeed, O-H stretching vibration present a maximum at about 2.72 μm and is believed to consist of four Gaussian components corresponding to different O-H bonding configurations in the SiO_2 matrix [122]. The absorption by the impurities such as hydroxyl groups is particularly noticeable around 2.7 μm since the complex part of the index of refraction and the absorption coefficient of fused quartz are very small over the spectral region from 0.2 to 4.5 μm . One could also mention that carbon dioxide and water vapor present a strong absorption bands at 2.7 μm [109] and could be entrapped in the

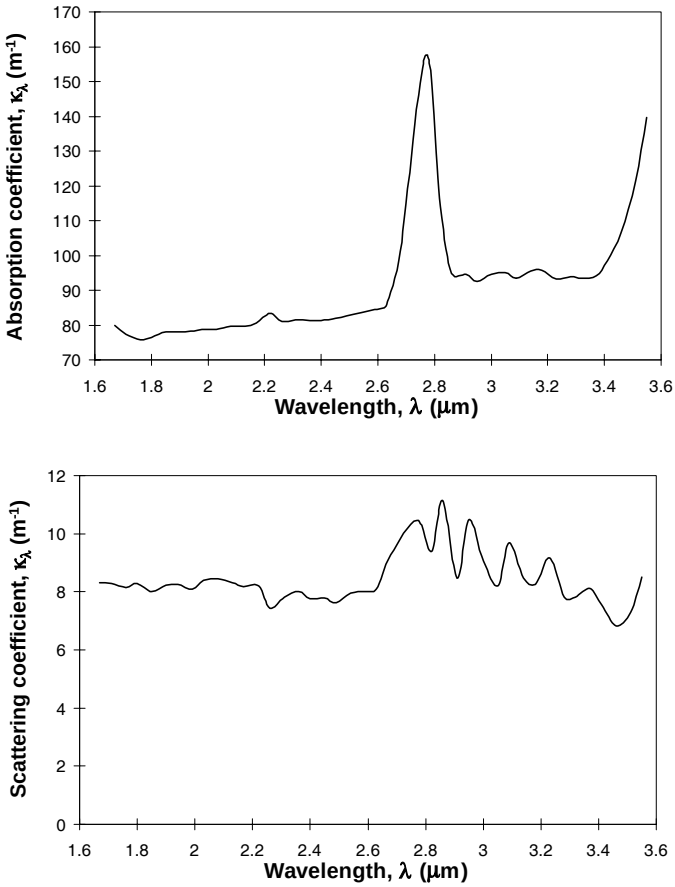

Figure 6.15. Average retrieved absorption (top) and scattering coefficients (bottom).

bubbles as commonly observed in glass manufacturing [86]. However, the industrial process used to manufacture the fused quartz consists of heating pure silicon dioxide electrically in an inert atmosphere of helium and hydrogen [127]. Moreover, analysis of gas bubble content indicates that bubbles contain mainly carbon monoxide, along with helium, and hydrogen [127]. These gases do not absorbe around 2.7 μm [109] and should not influence the radiation characteristics of fused quartz containing bubbles. Consequently, hydroxyl (OH) groups are solely responsible for the absorption peak around 2.72 μm. Finally, the single scattering albedo is small (less than 0.13) indicating that the radiation transfer is dominated by absorption by the fused quartz

matrix. Additional absorption could be due to trapping of radiation by successive inter-reflections within the bubbles caused by the curvature of the bubble surface.

Finally, Figure 6.16 compares the experimental transmittance for typical directions 1 and 3 ($\theta_i = 0^o$ and 3.32^o, respectively) with those obtained numerically by solving the RTE using the discrete ordinates method and the average spectral extinction coefficient, the single scattering albedo, and the asymmetry factor obtained by inverse method. One can see that the computed spectral transmittance falls within the ex-

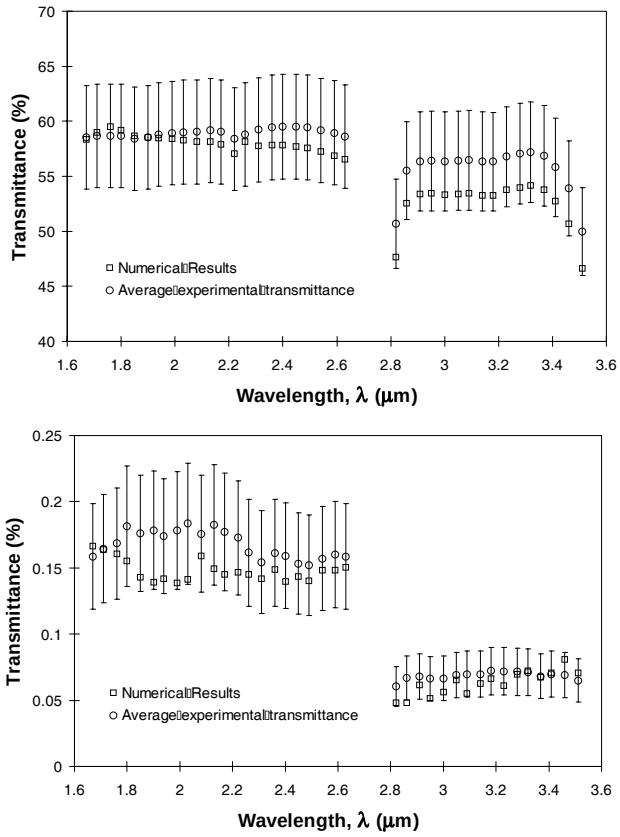

Figure 6.16. Comparison between the average measured spectral transmittance with error bars corresponding to $T_{e,\lambda}(\theta_i) \pm \Delta_i$ and the numerical results obtained with the averaged retrieved radiation characteristics for (top) $\theta_i = 0^o$ and $\Delta_i = 9\%$, and (bottom) $\theta_i = 3.32^o$and $\Delta_i = 25\%$.

perimental uncertainty error bars representing the interval $[T_{e,\lambda}(\theta_i) - \Delta_i, T_{e,\lambda}(\theta_i) + \Delta_i]$.

6.4.3. Model Validation

In order to validate the model presented in Chapter 5 the complex index of refraction of fused quartz reported in the literature and presented in Section 6.3.4 has been used. As a first order approximation, all the bubbles were assumed to have the same diameter, i.e., $a = \bar{a} = 1.14$ mm. A comparison of the model predictions with experimental data for the absorption, scattering, and extinction coefficients and the single scattering albedo over the spectral region from 1.67 to 3.55 μm is provided in Figure 6.17. For each wavelength, two values of k_λ^c were used: (1) data reported in

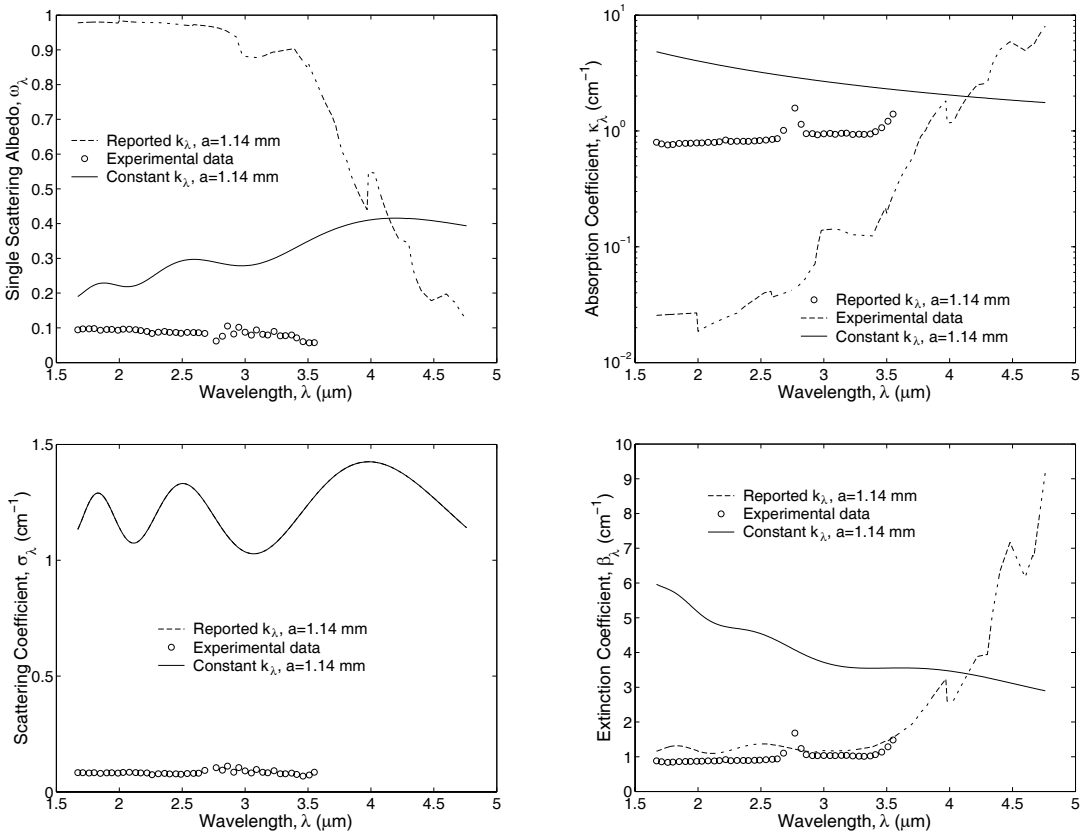

Figure 6.17. Comparison between experimental data and predicted radiation characteristics computed using the reported k_λ (dash line) and $k_\lambda = 10^{-4}$ (solid line).

the literature and presented in Section 6.3.4, and (2) a constant value of $k_\lambda^c = 10^{-4}$

as suggested by Dombrovsky [128]. One can see that the experimentally determined absorption coefficient falls between these two limiting cases, while the model over-predicts the single scattering albedo and the scattering coefficient. Good agreement between experimental data and predictions for the extinction coefficient is observed when k_λ^c reported in the literature is used. However,this is owing to the fact that the overestimation of the scattering coefficient is compensated by the underestimation of the absorption coefficient and this cannot constitute the validation of the model. Note also that the model predictions are very sensitive to the complex part of the index of refraction k_λ^c. The preliminary results are encouraging, but a final validation of the model must await complex index of refraction data for the specific fused quartz (SG25 grade). Since k_λ^c is very sensitive to the fused quartz composition, particularly in the spectral region of interest here, i.e., from 1.67 μm to 3.55 μm. Consequently, the optical properties of the specific fused quartz used in this study should be measured to fully validate the model. This work will be carried out when optical properties data become available. Simultaneously, it will be interesting to estimate the amount of hydroxyl group (in ppm) present in the sample responsible for such a absorption peak.

6.5. Conclusions

For the first time the radiation characteristics of glass containing bubbles have been measured. Experimentally, it has been established that

- The assumption of one-dimensional radiation transfer seems to be appropriate. This assumption could break down for thicker samples such that the sample thickness to diaphragm diameter is smaller than 1/4.

- The homogeneous assumption appears to break for sample thickness less than 3 mm.

As far as the effect of bubbles on the radiation characteristics of fused quartz is concerned, the following conclusions can be drawn:

- The presence of bubbles strongly affects the radiation characteristics of fused quartz even for small void fractions in the spectral region where quartz is weakly absorbing as theoretically predicted in the preceeding chapter.

- The presence of the bubbles significantly increase the extinction coefficient due to the scattering of the radiation at the bubble glass interface in the spectral range 1.67 μm to 3.5 μm.

- The scattering phase function of quartz containing bubbles is directed strongly forward as predicted by the model discussed in Chapter 5.

- In the inversion procedure the boundary conditions have been imposed as expressed by Equations (6.8) and (6.9) that assume specular reflection of the incident radiation at the interface air/porous medium and diffuse reflection for the radiation incident from the interior of the medium and reflected within the medium at the medium/air interface as suggested by Fedorov and Viskanta [11, 12]. However, such an assumption was based on work for a diffusing suspension [111] and its validity should be questioned for fused quartz containing bubbles. Moreover, due to the cutting, grinding, and polishing processes, bubbles at the sample surface have been cut through and are no longer closed. Then, the interface can no longer be treated as optically smooth, the Fresnel law of reflection is no longer valid, and new boundary conditions need to be modeled to account for the presence of open bubbles at the interface.

The same qualitative conclusions have been reached in Chapter 5 for soda-lime silicate glass. However, quantitative validation of the model discussed in Chapter 5 indicates that additional work is needed. The optical properties of the specific dense fused quartz constituting the matrix of the samples must be measured since the absorption coefficient strongly depends on the glass composition. Moreover, the pressure and composition of gases entrapped in the bubbles will have to be modeled in order to quantitatively predict the absorption peak observed experimentally at 2.7 μm and attributed to the carbon dioxide and/or water vapor band.

NOMENCLATURE

a	Bubble radius
$\bar{a}$	Average bubble radius
C_1, C_2	Planck's first and second radiation constants
f_v	Bubble void volume fraction
f_2	Focal distance of the spherical mirror MS2
F	Quadratic difference between measured and calculated bi-directional transmittance
g	Asymmetry factor in the Henyey-Greenstein scattering phase function
I	Radiation intensity
I_b	Blackbody radiation intensity
I_0	Incident intensity of collimated radiation
k	Imaginary part of the complex index of refraction
k_R	Radiative conductivity
L	Thickness of the slab
m	Complex index of refraction, $n - ik$
N_T	Total number of bubbles per unit volume
n	Real part of the complex index of refraction
r_{12}, r_{21}	External and internal surface reflectivity, respectively
R_A	Diaphragm diameter
$\hat{s}$	Spatial coordinate vector
T	Temperature
T_e	Experimental transmittance
T_t	Theoretical transmittance
w	Weighting factor for discrete ordinates method

Greek symbols

β	Extinction coefficient
β_R	Rosseland mean extinction coefficient
Δ	Standard deviation
γ	Surface tension

φ	Azimuth angle
κ	Absorption coefficient
λ	Wavelength of the incident radiation
$\hat{\Omega}$	Line-of-sight direction
μ	Cosine of the transmitted angle, $\mu = cos\theta$
Φ	Effective scattering phase function
ϕ	Scattering phase function of the single bubble
σ	Scattering coefficient or Stefan-Boltzman constant
θ	Scattering angle
θ_0	Divergence half angle
τ	Optical depth, $\int_0^s (\kappa_\lambda + \sigma_\lambda) ds$
ω	Single scattering albedo, $\sigma_\lambda / (\kappa_\lambda + \sigma_\lambda)$

Subscripts

λ	Refers to wavelength-dependent quantity
i	Refers to ordinate directions

Superscripts

d	refers to dispersed phase (gas bubble)
c	refers to the continuous phase

7. BUBBLE TRANSPORT IN THREE-DIMENSIONAL LAMINAR GRAVITY DRIVEN FLOW - MATHEMATICAL MODEL

7.1. Introduction

As shown in Chapters 5 and 6, even a small number of entrapped bubbles can strongly affect the radiation characteristics of semitransparent media provided that the bubble radius is much larger than the wavelength of radiation and that the medium is weakly absorbing. Moreover, bubbles are often generated and transported in the liquid phase like bubbles at the surface of the ocean or in glass melting furnaces. These bubbles may accumulate or rise to the free liquid surface and form a foam layer. Finally, in some industrial applications, the presence of bubbles strongly affects the product quality leading to larger losses in productivity.

The goal of the present work is to develop a general model for bubble transport, growth and shrinkage in three-dimensional flows. The flow is assumed to be laminar for the sake of simplicity. The bubbles can grow or shrink due to diffusion of gases in and out of the bubbles. The analysis presented is as general as possible and can find applications in many materials processing situations for at least one of the following reasons: (1) for predicting the radiation transfer in liquid containing bubbles, (2) for predicting the foam formation, and/or (3) for improving the quality of manufactured products. Applications to glass melting furnaces appear to be the most natural one since glass is one of the most common and available semitransparent media that is weakly absorbing in the infrared spectral region from 0.2 to 4.5 μm [46,47]. Moreover, radiation transfer is main mode of heat transfer in glass melting furnaces, and the quality of glass products is degraded if gas bubbles and unfused silica grains remain in the molten glass as it is being pulled from of the furnace [86, 129].

7.1.1. General Description of The Glass Melting Process

Moreover, as previously discussed radiation transfer is main mode of heat transfer in glass melting furnaces and the quality of glass products is degraded if gas bubbles and unfused silica grains remain in the molten glass as it is being pulled from of the furnace [86, 129]. Fewer defects, especially fewer remaining bubbles, has become a major requirement in the new quality standards for many commercial glass products. For example, in the TV-glass production, a presence of six bubbles per ton of glass results in 10% rejection rate of the final product, and for new products such as High Definition Television, the quality requirements are even more stringent [130]. For automotive window glass, the most demanding specification requires that gas bubbles be less than 0.5 mm in diameter for transparency purposes [131]. Moreover, for automobile windshield glass, reducing by half the defect density would increase the profitability by more than 2 millions dollars per year per plant [131].

Figure 7.1 shows a schematic of a typical glass melting furnace. During the glass

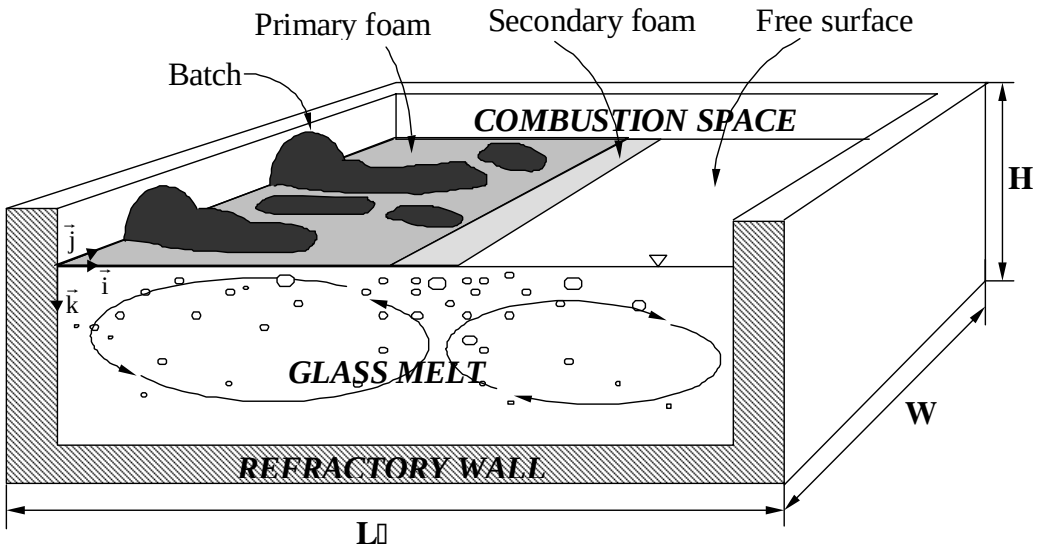

Figure 7.1. Schematic of a glass melting furnace and the coordinate system.

making process, the glass batch is introduced in the glass melting furnace where it spreads due to convection currents in the molten glass and melts due to the heating

from the flames in the combustion space and/or from Joule heating in electric melters. Melting of raw batch materials is a complex physicochemical process which involves a large number of chemical reactions and phase transformations occurring over the wide temperature range from 800 to 1200^{o}C [132]. For example, in the typical container glass manufacturing the basic and most important reaction in the batch involve silica, sodium carbonate, and calcium carbonate [9],

$$CaCO_3 + Na_2CO_3 \rightarrow Na_2Ca(CO_3)_2 \qquad \text{around } 550^oC \tag{7.1}$$

$$Na_2Ca(CO_3)_2 + 2SiO_2 \rightarrow Na_2O \cdot SiO_2 + CaO \cdot SiO_2 + 2CO_2 \qquad 600\text{-}830^oC \tag{7.2}$$

$$Na_2CO_3 + SiO_2 \rightarrow Na_2 \cdot SiO_2 + CO_2 \qquad 720\text{-}900^oC \tag{7.3}$$

$$2CaCO_3 + SiO_2 \rightarrow CaO \cdot SiO_2 + 2CO_2 \qquad 600\text{-}900^oC \tag{7.4}$$

Carbon dioxide gas is produced as a result of the last three reactions and it mainly diffuses in the melt [86]. A small fraction of the gas contributes to heterogeneous nucleation of bubbles within or just below the batch. Some of these bubbles pass through the batch and reach the combustion space, while the others are trapped in the melt and are carried with the convection currents in the glass bath. Refining agents, which are involved in the equilibrium redox reactions producing or consuming gases, are usually added to the batch in order to remove undesirable bubbles from the glassmelt [86, 133, 134]. Three types of refining agents are commonly used [135]:

1. Variable-valence metal oxides which release only oxygen, e.g., the antimony oxide (Sb_2O_5/Sb_2O_3), the arsenic oxide (As_2O_5/As_2O_3), and the cesium oxide (CeO_3/CeO_2) [134, 136–139].

2. Sulphates and sulphites which release a mixture of sulfure dioxide (SO_2) and oxygen [139]. For example, sodium sulfate, (Na_2SO_4) is used as a refining agent at high temperatures (around 1800^{o}C) but it also accelerates the melt formation if introduced in suitable proportions [140]. However, a detailed explanation of the beneficial effects of sulphate is not yet available.

3. Chlorides, bromides, and iodines which evaporate at refining temperature [135].

The fusion of raw materials in the batch and the fining reactions taking place in the glassmelt generate a large number of gas bubbles. A fraction of these bubbles is entrapped on the free surface of the glass to produce the primary foam [9]. Resorption of the remaining small fining gas bubbles, taking place during the conditioning of the glassmelt as it flows from the hot spot in the middle towards the throat of the furnace, also leads to formation of the so-called secondary foam [9]. Visual observations and laboratory scale studies of furnace operations indicate that the foam layers of various thickness can cover a large fraction of the free surface of the molten glass [9, 141].

7.1.2. Literature Review

Previous studies of the bubble behavior in glassmelt were mainly concerned with individual bubbles in an infinitely large quiescient pool of molten glass at a uniform temperature. The simplest of such studies consists of studying the shrinkage or growth of a stationary bubble containing a single gas [142, 143] sometimes accounting for refining reactions [136, 137]. Other studies were concerned with a stationary bubble containing several gases with or without refining reactions [137, 144, 145]. More realistic situations were investigated by accounting for the bubble rise due to buoyancy for a single gas bubble [129, 146] or a bubble containing several gases [147, 148], including the presence of refining reactions [134, 135, 138]. All of these studies show that in the presence of refining agents, only two mechanisms are mainly responsible for the removal of gas bubbles from the melt. They are:

- First, in high temperature regions, the equilibrium of the refining reaction shifts to gas production [86]. Then, the fining gas produced diffuses from the molten glass into already existing gas bubbles. In addition, gases already contained in bubbles are being diluted by the incoming fining gas [86, 149], and, in turn, this enhances the diffusion of gases from the melt into the growing bubbles.

Diffusion of fining gases makes bubbles grow in size until the buoyancy force is large enough to enable them to rise to the glassmelt free surface.

- Second, at low temperatures, the equilibrium of the fining reaction shifts to gas consumption resulting in gas diffusion from the bubbles to the melt. Small bubbles, which did not yet grow to a sufficiently large size, then dissolve in the glassmelt [139]. However, recent studies [150, 151] demonstrate that the refining reaction involving antimony oxide in TV panel glass was complete and irreversible, i.e., bubble shrinkage due to gas consumption at low temperatures was not clearly evident.

Even though modeling the behavior of individual bubbles gives an insight into the mechanism of bubble generation, growth, and shrinkage, it does not lead to any conclusions about the overall performance of the refining process. To accomplish the latter objective, one approach is to trace bubbles as they grow and shrink while being transported in the glass bath through regions of different temperatures, gas concentrations and pressures [86, 133, 149, 150]. In this approach, bubbles are introduced at the batch/glassmelt interface and are followed individually. All the studies reported [86,133,149,150] assume that probabilistic events such as the bubble coalescence or breakage or bubble nucleation are negligible. Moreover, they neglected the interdependence of gas concentration in the glassmelt and mass transfer in and out of the bubbles thus enabling them to solve successively (1) the glass flow and thermal structure, (2) the gas concentrations dissolved in the glassmelt, and (3) the trajectory and growth or shrinkage of a large number of individual single or multicomponent gas bubbles. The results are analyzed using statistical methods [86] in order to assess the degasing efficiency of a new tank design or new process conditions. The tracing method is a useful technique to elucidate the bubble trajectories in the molten glass. However, it is tedious to implement and does not provide detailed information about the number of bubbles and their size distribution at any given location throughout the tank. Therefore, the bubble-tracing approach cannot account for the coupling

between the concentration of gases dissolved in the molten glass, the bubble density function, the growth rate, and the glass flow and temperature fields. In addition, it can hardly be used to predict foaming at the surface of the glassmelt.

An alternative approach has been proposed by Ungan *et al.* [152] that consists of solving the conservation equation for the total number of bubbles and taking into account the effect of bubbles on the flow and temperature fields of the molten glass through the reduction of the effective density of the two-phase mixture. However, only monodispersed bubbles with constant radius were considered and refining reactions and bubble growth due to pressure change and gas diffusion were neglected.

In contrast, the population balance theory [58] allows one to predict in detail the radius and gas content of polydispersed bubbles and their density function throughout the glass melter. The only attempts to employ population balance theory to the bubble dynamics in glass tanks are due to Roi *et al.* [153] and Balkanli and Ungan [154]. Roi *et al.* [153] proposed a two-dimensional model for calculating the time dependence of the bubble size distribution assuming that the bubble growth rate is independent of the bubble radius. However, the authors admitted that their model "contains substancial simplifications and cannot be used for the exact quantitative modeling of concrete melting vessels". Balkanli and Ungan [154] presented a more realistic study based on a discretized formulation of the three-dimensional steady state population balance equation. However, the practical application of both works appear to be very limited since several highly simplifying assumptions have been made such as: (1) refining reactions are not considered, (2) bubble nucleation in the melt and at the refractory walls is neglected, (3) each gas bubble contains only one diffusing gas, and (4) the governing equations for the gas concentration in the molten glass, the bubble growth rate, and bubble population equation are solved independently, i.e., the coupling between these equations is neglected. Moreover, Balkanli and Ungan [154] solved the discretized form of the bubble population balance equation with a coarse grid in the bubble radius space. The limitations of these approaches have been discussed by Kumar and Ramkrishna [155]. In brief, the discrete formulation

lacks of *internal consistency*, i.e., some of the moments of the bubble density function f_1 [1] cannot be predicted accurately [155]. In other words, the calculation is designed for certain selected moments of the bubble density function rather than for an estimate of the bubble density function accurate enough for estimating all moments of the population [58]. For example, in gas/liquid flows in which bubbles are defined by their radius r at time t, the mth sectional and total moments of the bubble density function f_1 in terms of bubble radius, denoted by $\mu_m^{(i)}(\vec{x},t)$ and $\mu_m(\vec{x},t)$, respectively, are defined as

$$\mu_m^{(i)}(\vec{x},t) = \int_{r_i}^{r_{i+1}} r^m f_1(\vec{x},r,t)\mathrm{d}r \tag{7.5}$$

$$\text{and} \qquad \mu_m(\vec{x},t) = \int_{r_0}^{r_N} r^m f_1(\vec{x},r,t)\mathrm{d}r = \sum_{i=0}^{N-1} \mu_m^{(i)}(t) \tag{7.6}$$

where r_0 and r_N are the minimum and maximum bubble radius. The total number of bubbles, the average bubble radius, the interfacial area concentration (essential for interfacial mass and momentum transfer [156, 157]), the local volume fraction of gas (for the mass conservation equation) are physically important moments of the bubble density function and correspond to zero, first, second, and third order moments in terms of the bubble radius, respectively. Another important moment is the total mass of gas contained in the bubbles defined as the third order moment in term of variable $4\pi r^3\rho_g/3$. Conservation equations for each key mth order sectional moments obtained by the discretization method should be solved leading to large computational time and thus, reducing the interest of the method [58] for practical applications.

The purpose of the present work is to propose a simplified yet realistic analysis of the bubble behavior in glass melting furnaces by using the population balance theory [58]. For the first time, it presents a complete set of coupled conservation equations for the refining agent concentration, the concentrations of the gases dissolved in the glassmelt, and the bubble density function along with the associated boundary conditions and the closure laws. The model accounts for the three-dimensional con-

[1] This notation is chosen to be consistent with the notations of Ref. [58]

vective transport of refining agent, gases, and bubbles as well as for bubble growth due to multiple gas diffusion and by taking into account bubble nucleation along the refractory walls and refining reactions. Finally, the method of characteristics and the associated numerical scheme used for solving the population balance equation in terms of the bubble density function f_1 are briefly described.

7.2. Physical Model

Physical modeling of multidimensional two-phase flow has been the subject of intense research over the last half century. The two-fluid model is often considered as the most sophisticated multidimensional models available in the literature [156, 157]. In three-dimensional gas/liquid flows, the two-fluid model is comprised of ten scalar partial differential equations, five scalar algebraic interfacial jump conditions, and eleven state variables [157]. However, as reviewed by Lahey and Drew [157], while the rigorous derivation of the two-fluid models has made significant progresses, " no model exists to date which is completely acceptable". Moreover, interfacial and wall closure laws are still needed to accurately model three-dimensional two-phase flow [157]. More recently, Carrica *et al.* [158] have presented a three-dimensional computational model for the two-phase flow around a naval surface ship. The model can calculate the gas volume fraction and bubble radius, and accounts for the coupling between the governing equations for the gas and the liquid phases. However, their model is limited to monodispersed bubble population i.e., all the bubbles in computational grid have the same radius.

The two-fluid model approach does not appear to be appropriate for studying bubble transport in three-dimensional laminar flow since an accurate set of closure laws are not yet available [157] and the numerical algorithm is quite involved. The present analysis simplifies the mathematical formulation by decoupling the liquid and gas phase equations, i.e., the conservation equations for the liquid and gas phases are solved independently and the momentum and energy equation are solved only for the

liquid phase assuming that no bubbles are present. Such an approach can be justified by the small values of the gas void fraction in the molten glass and the small size of the bubbles. Moreover, unlike previous studies [152, 154, 158] the study predicts the bubble density function f_1 of polydispersed bubbles and enables the accurate post-processing calculation of all the moments of the distribution.

7.2.1. Assumptions

In order to make the problem of bubble generation and transport in the glass melting tank mathematically tractable the following assumptions are made:

1. All the processes are steady state or time independent.

2. The effects of bubbles and dissolved gases on the velocity and on the temperature fields as well as on the thermophysical properties of the glassmelt are not considered.

3. Bubbles are perfectly spherical in shape. This assumption holds for air-molten glass flows at the pressures encountered in the glass melting tank.

4. The bubbles have negligible inertia ($\rho_b \ll \rho_\infty$). This hypothesis is reasonable since very small bubbles are present in the glass bath.

5. The components of the bubble velocity vector, are taken to be the same as those of the molten glass (u_∞, v_∞, w_∞), except in the vertical direction where the buoyancy force has to be taken into account. In other words, the slip between the bubble and the glassmelt velocity is neglected except in the vertical direction. This can be justified by the fact that bubble are assumed to be small.

6. The molten glass is considered to be incompressible.

7. Local thermal equilibrium exists between the gas and liquid phases, i.e., $T_\infty = T_b = T$.

8. Coalescence and break up of bubbles are not considered.

9. The gases in a bubble are perfectly mixed, and the gas mixture inside the bubbles behave as an ideal gas.

10. The bubbles are assumed to contain l different gas species.

11. The diffusing gas species "i" is weakly soluble in the condensed phase (i.e., the Henry's law is applicable at the bubble/glassmelt interface).

12. The pressure in the bubbles remains close to the atmospheric pressure (maximum 5 atm [159]) so that the ideal gas approximation for fugacity is valid.

13. The diffusing gases neither react with the condensed phase nor undergo dissociation or association.

14. Neither chemical reactions between gases inside a bubble nor dissociation of gas molecules are taken into account.

15. The equilibration kinetics at the bubble surface is assumed to be very rapid, so that the rate limiting process is diffusion of gases in the melt.

16. The analysis presented is restricted to fining reactions that involve variable-valence metal oxides and produce oxygen only (in particular, the antimony oxide Sb_2O_5).

The above assumptions are commonly used in the treatment of bubble transport in three-dimensional laminar gravity driven flow of molten glass [133, 149–151, 154]. Assumptions regarding the bubble velocity and neglect of the effects of bubbles on the liquid phase flow and temperature fields are the most severe one and their limitations will be discussed later in this document. They have been used to decouple the conservation, momentum, and energy equations of the liquid and gas phases. This approach can be justified by the facts that bubble radius and concentration are small and that the alternative approach solving the coupled governing equations using the

two-fluid model lacks mechanistic closure laws accounting, for example, for the interfacial momentum transfer. Moreover, the effect of bubbles on the thermophysical properties of the glassmelt such as the dynamic viscosity, the thermal conductivity, and the specific heat are not clearly known. This is particularly true for the effect of bubbles on the radiation characteristics of molten glass that have been addressed in Chapter 5.

7.2.2. Refining Agent Concentration in the Glassmelt

7.2.2.1. Refining Reaction

As mentioned in the Introduction, the refining agent is introduced into the melting tank as part of the batch. As the agent is carried by the flow of the molten glass and encounters high temperature regions, the following reversible chemical reaction for variable-valence metal oxides, written in a generalized form, takes place [160]:

$$\mathrm{M^{k+}} + \frac{\mathrm{k-j}}{2}\mathrm{O^{2-}} \rightleftharpoons \frac{\mathrm{k-j}}{4}\mathrm{O_2} + \mathrm{M^{j+}} \tag{7.7}$$

In the case of antimony oxide as a refining agent, Kawachi and Kawase [133, 150] and Kawachi and Kato [151] showed that the rate of the forward reaction can be neglected in the production of TV panel glass. Therefore, the refining reaction can be considered as irreversible with only the decomposition of the refining agent taking place. By assuming a constant oxygen ion activity and by defining q as the order of the refining reaction occurring at constant volume, the rate of the decomposition reaction can be expressed as [133, 151]

$$-\frac{\partial[M^{k+}]}{\partial t} = \left(\frac{k-j}{4}\right)\frac{\partial[O_2]}{\partial t} = k_r[M^{k+}]^q \tag{7.8}$$

where the reaction rate constant k_r is calculated from the Arrhenius' law [150, 151],

$$k_r = Aexp\left(-\frac{E}{RT}\right) \tag{7.9}$$

The pre-exponential parameter A and the activation energy E are constants determined experimentally.

7.2.2.2. Fining Agent Concentration

As follows from Equation (7.8), the oxygen generation rate depends on the concentration of the dissociated form of the refining agent M^{k+}. Therefore, the local refining agent concentration $[M^{k+}]$ is required in order to predict the transport of oxygen dissolved in the glass bath as well as the bubble generation rate. The species conservation equation for the refining agent in the glassmelt is given by

$$\frac{\partial[M^{k+}]}{\partial t} + \nabla \cdot (\vec{v}_\infty[M^{k+}]) = \nabla \cdot \left(D_M \nabla[M^{k+}]\right) - k_r[M^{k+}]^q \tag{7.10}$$

where $[M^{k+}]$ is the molar concentration of metal ions and $\vec{v}_\infty$ is the local glassmelt velocity vector. The first term on the right hand side of Equation (7.10) accounts for the metal ion diffusion through the melt, while the last term represents the mass sink due to consumption of ions M^{k+} by the refining reaction. Although the steady-state solution of the problem is sought, the transient term $(\partial[M^{k+}]/\partial t)$ has been retained for performing iterative numerical integration which results in the steady-state solution of the molar concentration $[M^{k+}]$.

7.2.2.3. Boundary Conditions

Equation (7.10) can be solved provided that boundary conditions are defined. The batch consists of the raw materials and cullet mixed with the refining agent in the form of oxides such as Sb_2O_5. The dissociation of the oxide occurs as the temperature increases leading to production of cations and anions such as M^{k+} and O^{2-}, respectively. Furthermore, assuming that the concentration of the refining agent is uniform within the batch, and the dissociation reaction at the batch/hot molten glass

interface is instantaneous, complete, and irreversible, the concentration of the cations [M^{k+}] should be constant everywhere at the batch/glassmelt interface:

$$[M^{k+}] = \text{constant} \qquad \text{at the batch/glassmelt interface} \tag{7.11}$$

The specific value of [M^{k+}] depends on the process and the type of glass produced; it can be determined from operating data. Typically, antimony oxide is added in 0.1 to 1.0 wt.% [139].

Finally, the gradient of the concentration [M^{k+}] is taken to vanish at the glass/refractory walls and at the free surface of the molten glass

$$\nabla_{\vec{n}}[M^{k+}] = \vec{0} \qquad \text{at the glassmelt/refractories interface} \tag{7.12}$$

$$\nabla_{\vec{n}}[M^{k+}] = \vec{0} \qquad \text{at the glassmelt/combustion space interface} \tag{7.13}$$

Such boundary conditions can be justified by the fact that the diffusion of the cations from the glassmelt to the refractory walls and to the combustion space is negligible.

7.2.3. Dissolved Gas Transport in the Glassmelt

The growth and shrinkage of the bubbles is, in part, caused by gas diffusion into and out of the bubbles due to a difference in concentration of a given gas species between the glassmelt and the gas bubbles. Therefore, one needs to predict the local concentration of each gas species dissolved in the glassmelt.

7.2.3.1. Species Concentration Equation

The transport of major gas species (O_2, H_2O, CO_2, and N_2) in the glassmelt is governed by the following general species concentration equation [133, 161, 162],

$$\frac{\partial C_{\infty,i}}{\partial t} + \nabla \cdot (\vec{v}_\infty C_{\infty,i}) = \nabla \cdot (D_i \nabla C_{\infty,i}) + \dot{m}_{ref,i} - \dot{m}_{diff,i} \tag{7.14}$$

Here, $C_{\infty,i}$ and D_i are the mass concentration and the diffusion coefficient of the dissolved gas species "i" in the glassmelt, respectively. The first term on the right

hand side of Equation (7.14) accounts for mass diffusion of the dissolved gas species "i" in the glassmelt. The source term $\dot{m}_{ref,i}$ is the volumetric gas production rate due to the refining reaction, and the sink term $\dot{m}_{diff,i}$ accounts for the volumetric diffusion rate of gas species "i" from the glassmelt into the bubbles. As before, the transient term $[\partial C_{\infty,i}/\partial t]$ has been retained to enable iterative numerical integration of Equation (7.14). Note that the last two terms on the right-hand side of Equation (7.14) have been neglected by Balkanli and Ungan [161], while Kawachi and Kawase [133] neglected only the last term.

As stated in assumption 2, the analysis presented here is restricted to refining reactions that are complete and irreversible and produce oxygen only. Then, the source term $\dot{m}_{ref,i}$ vanishes in the case of all gas species but oxygen. Solving Equation (7.10) for $[\mathrm{M}^{k+}]$ enables one to compute the oxygen generation rate per unit volume of glassmelt at every location in the glassmelt since

$$k_r[M^{k+}]^q = \left(\frac{4}{k-j}\right)\frac{1}{M_{O_2}}\frac{\partial C_{\infty,O2}}{\partial t} = \left(\frac{4}{k-j}\right)\frac{\dot{m}_{ref,O_2}}{M_{O_2}} \tag{7.15}$$

After some rearrangment,

$$\dot{m}_{ref,O_2} = \left(\frac{k-j}{4}\right) M_{O_2} k_r [M^{k+}]^q \tag{7.16}$$

The sink term $\dot{m}_{diff,i}$ is the total mass of dissolved gas species "i" diffusing from the glassmelt into the bubbles per unit volume of the glassmelt and per unit of time at location $\vec{x}$ and instant of time t. It is given by

$$\dot{m}_{diff,i}(\vec{x},t) = \int_0^1 ... \int_0^1 \left[\int_0^\infty K_i(C_{\infty,i} - C_{e,i}) f_1 \mathrm{d}r\right] \mathrm{d}\gamma_{i,1} ... \mathrm{d}\gamma_{i,l-1} \tag{7.17}$$

where $K_i(C_{\infty,i} - C_{e,i})$ is the total mass flow rate of the gas species "i" from the glassmelt across the surface of a bubble of radius r expressed in [kg/s/bubble]. The concentration difference of gas species "i" between the glassmelt and the bubble/glassmelt interface is $(C_{\infty,i} - C_{e,i})$. The bubble density function, i.e., the number of bubbles per unit volume at location $\vec{x}$ and time t having equivalent radii that lie within the range r to $r + \mathrm{d}r$, and the molar fraction of gas species "i" ranges between γ_i and

$\gamma_i + \mathrm{d}\gamma_i$ with $1 \leq i \leq l-1$ is denoted $f_1 = f_1\,[\vec{x}, r, t, (\gamma_i)_{1\leq i\leq l-1}]$. Note that all the molar fractions of gas species "i" γ_i sum up to unity. Thus, γ_l can be expressed as a function of the remaining $(l-1)$ others and cannot be treated as an independent variable. When $C_{\infty,i} > C_{e,i}$ the gas species "i" diffuses from the glassmelt in the bubbles, whereas when $C_{\infty,i} < C_{e,i}$ it diffuses from the gas bubbles to the glassmelt. Then, $\dot{m}_{diff,i}(\vec{x}, t)$ behaves either as a sink (if $C_{\infty,i} > C_{e,i}$) or as a source (if $C_{\infty,i} < C_{e,i}$). To complete the formulation, the closure laws must be specified as well as the boundary conditions.

7.2.3.2. Closure Laws

To make the problem well-posed, the total mass flow of the gas species from the glassmelt to the bubbles and particularly the mass transfer coefficient K_i, and the gas concentrations at the bubble glassmelt interface, $C_{e,i}$, should be defined.

According to Levich [163], for bubbles moving at low relative velocities w_r (Reynolds number much smaller than unity) in a quiescent liquid containing diffusing gases, the coefficient K_i can be expressed as

$$K_i = 7.98 D_i^{2/3} w_r^{1/3} r^{4/3} \qquad (\text{in m}^3/\text{s}) \tag{7.18}$$

Here, D_i is the diffusion coefficient of gas species "i" in the glassmelt while w_r is the relative velocity of the bubble of radius r with respect to the liquid. Extensive studies have shown that in molten glass small bubbles behave like solid sphere while large spherical bubbles behave like fluid spheres (see Ref. [139] for an in-depth review). According to the Stokes' law for solid spheres, the small gas bubbles rise in the molten glass with the relative vertical velocity given by:

$$w_r = \frac{2}{9} \frac{\rho_\infty g r^2}{\mu_\infty} \tag{7.19}$$

On the other hand, in the case of large spherical bubbles in the molten glass, the vertical velocity relative to the molten glass follows the Hadamar-Rybczynski formula [139, 164]:

$$w_r = \frac{1}{3}\frac{\rho_\infty g r^2}{\mu_\infty} \tag{7.20}$$

Unfortunately, there is no clear criteria regarding what bubbles should be considered as large or small. Experimental results suggested that bubbles of diameter larger than 1 mm can be considered as large and their velocity follows Equation (7.20) [164]. In brief, the bubble rise velocity with respect to liquid phase can be written as

$$w_r = \alpha\frac{\rho_\infty g r^2}{\mu_\infty} \tag{7.21}$$

where α is a parameter that depends on the bubble size according to Equations (7.19) and (7.20):

$$\alpha = \begin{cases} 2/9 & \text{for small bubbles } (2r \leq 1mm) \\ 1/3 & \text{for large bubbles } (2r \geq 1mm) \end{cases} \tag{7.22}$$

Note that Equations (7.19) to (7.21) correspond to the terminal (i.e., steady state) velocity of spherical bubbles, i.e., the transient motion of bubbles have not been considered for the sack of simplificity and since its formulation is still incomplete and quite involved [83].

In the present analysis, it is assumed that the resistance to the mass transport provided by the surfactants concentrated at the bubble/glass interface is negligibly small. It is also assumed that the magnitude of the mass flux is relatively small, so that the variations of mass concentration of gas species "i" in both phases are small as well. Then, the local quasi-equilibrium can be assumed to exist at the bubble/molten glass interface [165], which implies the equality of the chemical potentials of the diffusing gas on both sides of the interface. This fact, combined with assumptions 3, 8 and 10, allows us to apply the generalized Henry's law and obtain the relationship between species concentrations on both sides of the bubble/glassmelt interface [166],

$$C_{e,i} = S_i M_i f_{b,i} \tag{7.23}$$

Here, $C_{e,i}$ is the concentration of the diffusing gas "i" at the interface (assumed to be at equilibrium) and S_i is the solubility of gas species "i" in the glass melt, M_i is the molecular weight of the species "i", and $f_{b,i}$ the fugacity of the species "i" in the bubble. Provided that the pressure is low enough and the ideal gas approximation holds (assumption 9), the fugacity $f_{b,i}$ is approximately equal to the partial pressure of species "i" ($p_{b,i}$) on the gas side of the interface [159], so that

$$C_{e,i} = S_i M_i p_{b,i} \tag{7.24}$$

Using an ideal-gas equation of state (assumption 7), the partial pressure of the gas species "i" in the bubble is given by the Raoult's law:

$$p_{b,i} = \gamma_i p_b \tag{7.25}$$

where γ_i is the molar fraction of gas species"i" inside the bubble and is such that

$$\sum_{i=1}^{l} \gamma_i = 1 \tag{7.26}$$

This results in the following jump condition for the species concentrations at the bubble/glassmelt interface:

$$C_{e,i} = \gamma_i S_i M_i p_b \tag{7.27}$$

7.2.3.3. Boundary Conditions

According to Balkanli and Ungan [154], the concentration of carbon dioxide (CO_2) at the batch/glassmelt interface can be taken as being the saturation concentration owing to the very high intensity of gas generation due to fusion and melting of the raw batch materials. Also, as speculated by Kawachi and Kawase [133], oxygen (O_2) is supplied in sufficiently large amounts from the combustion space or by refining reactions taking place in the batch to saturate the glassmelt beneath the batch/glassmelt interface; similarly, for nitrogen (N_2) in air fired furnaces. However, transport of nitrogen can be neglected in oxy-fired furnaces since it is present in very small amount.

At the glass/refractory wall interface, the gradient of the concentration of gas species "i" in the glassmelt is assumed to vanish owing to the absence of mass transfer through the refractory walls:

$$\nabla_{\vec{n}} C_{\infty,i} = \vec{0} \qquad \text{at the glassmelt/refractories interface} \tag{7.28}$$

In cases when the free surface of the glassmelt is in direct contact with the combustion gases, the gas concentration at the free surface is given by the Henry's law [133, 151, 161], i.e.,

$$C_{\infty,i} = S_i M_i p_i|_{int} \qquad \text{at the glassmelt/combustion space interface} \tag{7.29}$$

where $p_i|_{int}$ is a partial pressure of gas species "i" on the combustion side of the glassmelt/combustion space interface and is obtained from the calculation of the gas species concentrations as well as the flow and temperature fields in the combustion space.

However, if the free surface is covered by a foam blanket then the effect of foam should be accounted for by equating the mass fluxes on both sides of the foam/glassmelt interface, i.e.,

$$D_i(\nabla C_{\infty,i}) = D_{eff}|_{f,i} \nabla(C_{\infty,i}) \qquad \text{at the glassmelt/foam interface} \tag{7.30}$$

where $D_{eff}|_{f,i}$ is the effective diffusion coefficient of gas species "i" through the foam layer and $C_i|_{int}$ is the gas concentration at the foam/glassmelt interface. The left-hand side of Equation (7.30) represents the gas diffusion mass flux on the glass side, while the right-hand side represents that on the foam side. Assuming that the foam thickness is small, a linear approximation of the gas concentration in the foam layer yields the following mixed boundary condition,

$$D_i \nabla C_{\infty,i} = D_{eff}|_{f,i} \left(\frac{C_i|_{comb} - C_{\infty,i}}{H_\infty} \right) \qquad \text{at the glassmelt/foam interface} \tag{7.31}$$

where H_∞ is the steady-state foam thickness (see Chapter 3) and $C_i|_{comb}$ the gas concentration at the foam/combustion space interface, i.e., at the top of the foam

layer. The model for the effective diffusion coefficient of gas species "i" through the foam layer, $D_{eff}|_{f,i}$ is presented in Appendix A.

7.2.4. Bubble Density Population

7.2.4.1. Single Bubble Environment

A schematic of a single bubble in mechanical and thermal equilibrium with the surrounding molten glass is given in Figure 7.2, along with the corresponding p-T diagram. The Young-Laplace equation relates the pressure (p_b) inside a spherical

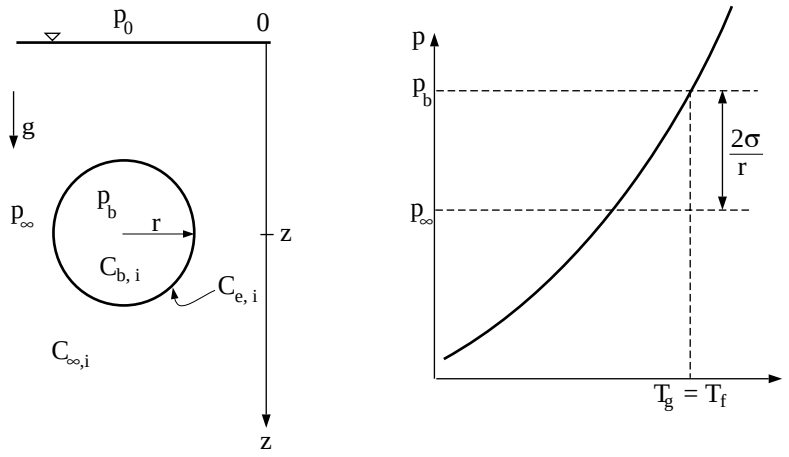

Figure 7.2. Schematic of a single bubble in thermal equilibrium with the glassmelt and the corresponding p-T diagram.

bubble of radius r with the pressure (p_∞) in the surrounding glassmelt and the surface tension σ by

$$p_b = p_\infty + \frac{2\sigma}{r} \tag{7.32}$$

Since the velocity of the viscous molten glass in the glass bath is very small (of the order of 1 cm/s) the pressure field in the tank can be assumed to be purely hydrostatic. Thus, the total pressure inside the bubble is expressed as

$$p_b = p_0 + \rho_\infty g z + \frac{2\sigma}{r} \tag{7.33}$$

where p_0 is the pressure at the free surface of the molten glass and z is the local depth within the glassmelt.

Based on Assumption 5, the components of the bubble velocity vector $\vec{v}_b$ can be expressed as

$$\vec{v_b}(\vec{x}) = u_\infty \vec{i} + v_\infty \vec{j} + (w_\infty - w_r)\vec{k} \tag{7.34}$$

with w_r being the upward bubble velocity relative to the molten glass due to the buoyancy force given by Equation (7.21). Note that according to our convention, the vertical axis is oriented downward. Values of u_∞, v_∞, and w_∞, are obtained from the thermal-flow computation of molten glass circulation in the bath (see, for example, Ref. [167–171]).

7.2.4.2. Population Balance Equation

As discussed in detail by Ramkrishna [58, 172], the bubble population can be described by a state vector defined in a so-called state space. The state space consists not only of the physical space (i.e., the environment of the continuous phase) but also of an abstract "property" space. In the physical space, the state vector coordinates consist of the spatial coordinates [e.g., (x, y, z) in Cartesian coordinates]. In the property space, the system is characterized by its property coordinates. For example, each bubble in the glassmelt is characterized by its radius r and the molar fraction of gas species "i" contained in the bubble γ_i. The spatial and property coordinates are also referred as the external and internal coordinates, respectively. Let $f_1\left(\vec{x}, t, \vec{P}\right) = f_1[\vec{x}, t, r, (\gamma_i)_{1\le i\le l-1}]$ be the average number density function of bubbles. As already discussed, γ_l cannot be treated as an independent variable. The average number density function $f_1[\vec{x}, t, r, (\gamma_i)_{1\le i\le l-1}]$ is assumed to be sufficiently

smooth to allow differentiation with respect to any of its variables as many times as necessary [58]. Note that the temperature of the bubbles is assumed to be the same as that of the glassmelt, i.e., the local thermal equilibrium prevails. Therefore, although the temperature is important to determining the growth rate of a bubble, it is a continuous phase (glassmelt) variable and hence does not enter the characterization of the bubble state. The differential population balance equation that describes the conservation of the bubble population is given by [58]

$$\frac{\partial f_1}{\partial t} + \nabla_x \cdot (\vec{v} f_1) + \nabla_P \cdot (\dot{\vec{P}} f_1) = h \tag{7.35}$$

where $\vec{v}$ and $\dot{\vec{P}}$ are the rate of change of the external and internal coordinates, respectively. The transient term $\partial f_1/\partial t$ represents the time rate of change of the bubble density, and the other two terms on the left-hand side of Equation (7.35) represent advection of the bubble density function in the physical space and in the property space, respectively. Finally, $h = h(\vec{x}, t, \vec{P})$ represents the net rate of production of bubbles of a particular state ($\vec{x}$, $\vec{P}$) at time t. Considering the bubbles generated and transported by the flow of the glassmelt, and assuming that there are l gases diffusing into or out of each bubble, the state vector $\vec{S}$ can be expressed as $\vec{S} = [x, y, z, t, r, (\gamma_i)_{1 \le i \le l-1}]$. Then, the population balance equation can be expressed as

$$\frac{\partial f_1}{\partial t} + \frac{\partial}{\partial x}(u_\infty f_1) + \frac{\partial}{\partial y}(v_\infty f_1) + \frac{\partial}{\partial z}[(w_\infty - w_r) f_1] + \frac{\partial}{\partial r}(\dot{r} f_1) + \sum_{i=1}^{l-1} \frac{\partial}{\partial \gamma_i}(\dot{\gamma}_i f_1) = h \tag{7.36}$$

where, w_r is given by Equation (7.21). The time rate of change of the bubble radius and of the molar fraction of gas species "i" inside the bubble are denoted by $\dot{r}$ and $\dot{\gamma}_i$, respectively.

The molar fraction of gas species "i" can be expressed as a function of the mass concentrations $C_{b,i}$ since by definition

$$\gamma_i = \frac{C_{b,i}/M_i}{\sum_{j=1}^{l} (C_{b,j}/M_j)} = \frac{C_{b,i} R T}{M_i p_b} \tag{7.37}$$

Then, the time derivative of the molar fraction of gas species "i" in the bubble γ_i can be expressed as

$$\dot{\gamma}_i = \gamma_i \left[\frac{\dot{C}_{b,i}}{C_{b,i}} - \frac{\rho_\infty g(w_\infty - w_r) - 2\sigma\dot{r}/r^2}{p_b} \right] \tag{7.38}$$

where $\dot{r}$ and $\dot{C}_{b,i}$ are the time rate of change of the bubble radius and of the mass concentration of gas species "i" contained in the bubbles, respectively. Expressions for $\dot{r}$ and $\dot{C}_{b,i}$ can be derived from assumptions 8 to 10 by writing the time rate of change of the mass of gas species "i" contained in a spherical bubble of radius r as [163]

$$\frac{\mathrm{d}m_i}{\mathrm{d}t} = \frac{\mathrm{d}\left(C_{b,i}V_b\right)}{\mathrm{d}t} = K_i \left(C_{\infty,i} - \gamma_i S_i M_i p_b\right) \tag{7.39}$$

where $C_{b,i}$ and $C_{\infty,i}$ are the mass concentrations of gas species "i" in the bubble and in the glassmelt, respectively. Equation (7.39) indicates that if a bubble contains a single gas, the bubble can only shrink since the concentration of gas dissolved in the glassmelt $C_{\infty,i}$ (in kg/m^3) cannot be larger than the gas solubility given by $S_i M_i(p_0 + \rho_\infty g z)$. The mass transfer coefficient of gas species "i" from the glassmelt to a bubble of volume V_b ($=4\pi r^3/3$) is denoted K_i. Substituting the expression for K_i given by Equation (7.18) and that of $C_{e,i}$ given by Equation (7.27) and differentiating the left-hand side of Equation (7.39) yields

$$\frac{4\pi}{3} r^3 \dot{C}_{b,i} + C_{b,i} 4\pi r^2 \dot{r} = 7.98(C_{\infty,i} - \gamma_i S_i M_i p_b) D_i^{2/3} w_r^{1/3} r^{4/3} \tag{7.40}$$

Then, solving for $\dot{C}_{b,i}$ results in

$$\dot{C}_{b,i} = \frac{1.905}{r} \left(\frac{\alpha \rho_\infty g D_i^2}{\mu_\infty} \right)^{1/3} (C_{\infty,i} - \gamma_i S_i M_i p_b) - \frac{3\dot{r}}{r} C_{b,i} \tag{7.41}$$

According to the Dalton's law for ideal gases, the total pressure of the gas mixture in the bubble is given by

$$p_b = \sum_{i=1}^{l} (p_{b,i}) = \left[\sum_{i=1}^{l} \left(\frac{C_{b,i}}{M_i} \right) \right] RT \tag{7.42}$$

The derivative of Equation (7.42) with respect to the time t using the expression for $\dot{C}_{b,i}$ given by Equation (7.41) results in

$$\frac{\partial p_b}{\partial t} = \frac{1.905 RT}{r} \left(\frac{\alpha \rho_\infty g}{\mu_\infty} \right)^{1/3} \sum_{i=1}^{l} \frac{D_i^{2/3}}{M_i} \left[(C_{\infty,i} - \gamma_i S_i M_i p_b) \right] - \frac{3\dot{r}}{r} p_b \tag{7.43}$$

The temperature T is obtained from the steady-state solution of the thermal-flow calculations of the glassmelt. Substituting the expression for p_b given by Equation (7.33) into Equation (7.43), assuming that $\partial p_0/\partial t = 0$ (steady-state), and solving for the growth rate $\dot{r}$ gives

$$\dot{r} = \frac{0.635RT\left(\frac{\alpha\rho_\infty g}{\mu_\infty}\right)^{1/3}\sum_{i=1}^{l}\left[\frac{D_i^{2/3}}{M_i}\left(C_{\infty,i} - \gamma_i S_i M_i p_b\right)\right] - \rho_\infty g(w_\infty - w_r)r/3}{p_0 + \rho_\infty g z + 4\sigma/3r} \tag{7.44}$$

The first term in the numerator of Equation (7.44) takes into account the change of radius due to mass transfer at the bubble interface, while the second term accounts for the change in pressure as the bubbles are transported in the glass bath. Such an expression has been previously derived by Balkanli and Ungan [129], but the expression for the term accounting for growth due to the change in pressure appears to be in error as also confirmed by other studies for quescient glassmelt ($w_\infty = 0$) [134, 148].

Note that the gas and liquid momentum equations have been decoupled and it was assumed that the vertical component of the bubble velocity vector was given by $w_b = w_\infty - w_r$. Thus, assumption 5 implies that the bubble velocity field does not satisfy the continuity equation in steady-state, i.e., $\nabla \cdot \vec{v}_b \neq 0$. Therefore, the conservation of the total number of bubbles cannot be assured. For example, in the case of convective transport of solid particles without generation and growth, Equation (7.36) simplifies to

$$\frac{\partial f_1}{\partial t} + \nabla \cdot (\vec{v}_b f_1) = 0 \tag{7.45}$$

Along the pathlines of the particles ($\mathrm{d}\vec{x}/\mathrm{d}t = \vec{v}_b$), this equation is written as $\mathrm{d}f_1/\mathrm{d}t = f_1 \partial w_r/\partial z$. However, physically it is clear that the bubble density function is transported unchanged along the particle pathlines and the conservation equation should be written as $\mathrm{d}f_1/\mathrm{d}t = 0$. Therefore, Assumptions 2 and 5 introduce an artificial source in the population balance equation. In order to approximately conserve the total number of bubbles the bubble velocity vector $\vec{v}_b$ should satisfy

$$\nabla \cdot \vec{v}_b = \vec{v}_\infty - \frac{\partial w_r}{\partial z} \approx 0 \tag{7.46}$$

Since the molten glass is treated as incompressible, Equation (7.46) is satisfied if $\partial w_r/\partial z \ll 1$. Physically, this corresponds to situation where the bubble growth rate and liquid velocity does not vary significantly along the bubble pathline during the time interval t and $t + \mathrm{d}t$.

7.2.4.3. Bubble Generation

Finally, heterogeneous nucleation can occur on the surface of undissolved sand grains or on refractory walls [86]. Nemec [173]observed in an experimental crucible under uniform temperature conditions that heterogeneous bubble nucleation occurs at the surface of undissolved sand grains only if refining agent is present while homogeneous bubble nucleation could never be observed. It indicates that bubble nucleation takes place if the glassmelt is supersaturated with refining gases, i.e., if the local gas concentration dissolved in the molten glass exceeds the solubility at the local temperature and pressure. Cable and Rasul [174] reported that heterogeneous bubble nucleation occured at the surface of the refractory even at small supersaturations. Finally, Roi *et al.* [175] have discussed bubble generation and formation of a bubble curtain consisting of very small bubbles located close to the refractory walls. The authors attributed the formation of a bubble curtain to the combination of an unfavourable temperature distribution and bubble growth rate.

Solving the gas species concentration equation [Equation (7.14)] for oxygen could possibly yield oxygen concentrations higher than solubility within the glass bath due to the source from the refining reactions. However, such cases are expected only in the refining section of the tank where the number of undissolved sand grains is predicted to be small [176], thus limiting the number of available nucleation sites. Instead, the main mechanism for dissolved oxygen removal from the glassmelt is the diffusion in already existing bubbles to make them grow and rise at the surface. Note also that from a thermodynamics point of view gas diffusion is favored over heterogeneous nucleation. Therefore, given the complexity of the physical phenomena and

the controversy regarding the significance and mechanisms of heterogeneous nucleation in glass melting furnaces, heterogeneous nucleation has not been considered in the present study. The validity of this assumption will be examined in view of the numerical results presented in the second part of this document. Moreover, very fine grids close to the walls should be used to account for the entrainment by the flowing liquid of the very small bubbles generated at the refractory walls. Then, the grid size should be smaller than the typical size of a generated bubble making the calculation even more time consuming.

7.2.4.4. Boundary Conditions

Boundary conditions for the bubble density function f_1 are required to solve the population balance equation (7.36) and are expressed as follows:

- *At the batch/glassmelt interface* bubbles exist in significant numbers due to the fusion/melting transformations taking place in the batch. The batch coverage is assumed to be known and the gas composition and the bubble density function are the same under the entire surface covered by the batch and does not vary with time. Then, the boundary condition at the batch/glassmelt interface is expressed as

$$f_1 = f_{1,0} \qquad \text{at the glassmelt/batch interface} \tag{7.47}$$

  where $f_{1,0} = f_{1,0}[r, (\gamma_i)_{1 \geq i \geq l-1}]$ is the bubble density function depending on the fusion/melting process and determined experimentally.

- *At the glassmelt/refractory wall interface* the boundary conditions appear to be controversial. Balkanli and Ungan [154], suggested the use of the weak boundary conditions at the refractory walls. However, Swarts [131] mentioned that the number of bubbles per unit volume generated at the glass/refractory interfaces

is significant. Until further experimental results are obtained we will assume that the gradient of f_1 in the normal direction vanishes,

$$\nabla_{\vec{n}} f_1 = \vec{0} \qquad \text{at the glassmelt/refractories interface} \tag{7.48}$$

- *At the free surface of the glassmelt* Balkanli and Ungan [154] used the same boundary condition as that used at the glass/melt/refractory wall interface, i.e., $\nabla_{\vec{n}} f_1 = \vec{0}$. Physically, such a boundary condition means that no bubble can escape through the glassmelt free surface. Obviously, such a boundary condition does not represent the physical phenomena occuring since a single bubble reaching a free interface can either merge with the interface almost instantaneously or bounce back one or several times before stabilizing at the free interface to finally burst [76]. Additional complications appear when bubbles accumulate to form a foam layer at the glassmelt surface. Then, rising bubbles aggregate and coalescence with bubbles in the foams. This phenomena is suspected to be of major importance for onset of foaming. To the best of our knowledge, no boundary conditions for the bubble density function f_1 at the glassmelt free surface and at the glassmelt/foam interface accounting for the physical phenomena described above are available in the literature. Note that the finite difference algorithm needs the definition of these boundary conditions. On the other hand, the method of characteristics used in the present study does not require specification of any boundary condition at the glass/combustion space interface.

The local superficial gas velocity $j(x, y)$ at the glassmelt surface can be computed from the bubble density function:

$$j(x,y) = \int_0^1 ... \int_0^1 \left(\int_0^\infty f_1[x, y, z = 0, r, (\gamma_i)_{1 \geq i \geq l-1}] w_r \mathrm{d}r \right) \mathrm{d}\gamma_1 ... \mathrm{d}\gamma_{l-1} \tag{7.49}$$

Then, the transient and steady-state foam thickness can be predicted from the analysis presented in Chapters 2 and 3 for liquid foams generated from viscous liquids. However, the spreading of the foam over the glassmelt surface is not accounted for.

The foam layer strongly affects the radiation heat transfer from the combustion space to the glass bath and can significantly reduce the glassmelt temperature [13, 171]. Model for radiation transfer through foam and combined conduction and radiation transfer have been proposed recently [11–13, 177, 178] and should be used to recompute the glassmelt flow and thermal structures. However, this task is beyond the scope of the present work, and the presence of a foam layer will not be considered further.

7.3. Method of Solution of Model Equations

Figure 7.3 shows the block diagram of essential steps in the procedure which is used to calculate the bubble transport in the glass melting furnace. Previous studies computed the dissolved gas concentration in the melt by neglecting the source term in Equation (7.14) due to the diffusion of gases in and out of the bubbles [154] and assumed that bubbles contain only one gas species. This simplification reduces the number of independent variables and implies that the dissolved gas concentrations $C_{\infty,i}$, the bubble radius r, and the bubbles density function f_1 can be computed consecutively and independently. In this study, the variables $C_{\infty,i}$, r, γ_i, and f_1 are interdependent and determined iteratively until all the solutions are converged as shown in Figure 7.3. Considering refining reactions that are complete and irreversible enables us to compute the refining agent concentration $[M^{k+}]$ independently.

The governing conservation equations and boundary conditions for the thermal-fluid calculations of the molten glass along with the numerical method of solution can be found elsewhere [167–170]. The governing partial differential equations for the refining agent concentration $[M^{k+}]$ and the gas concentrations $C_{\infty,i}$, are of parabolic type with the transient term included as an iteration parameter. For the purpose of numerical solution, the equations are discretized over the spatial coordinates by means of the control volume integration technique [179]. The resulting finite-difference approximation of derivatives produces a system of linear algebraic

equations, which are then solved using line-by-line iterative method. The method solves a line of nodes by applying the tri-diagonal matrix inversion algorithm and sweeps the domain of integration in alternating directions along the coordinates axes. A fully implicit and unconditionally stable Euler method with very large time steps is employed to integrate the equations in time until steady-state solution is achieved. Numerical integration of the source/sink terms corresponding to gas diffusion in and out of the bubbles and given by Equation (7.17) was performed using Simpson's rule for unequally spaced data [2]. The steady-state conditions for the refining agent concentration and the dissolved gas concentrations was assumed to be reached when the residual for each of these variables was less than an arbitrary small value.

The population balance equation [Equation (7.36)] is solved using the method of characteristics. If we assume that the liquid phase can be treated as incompressible, the mass conservation equation for the liquid phase can be expressed as [180]

$$\frac{\partial u_\infty}{\partial x} + \frac{\partial v_\infty}{\partial y} + \frac{\partial w_\infty}{\partial z} = 0 \tag{7.50}$$

Expanding the partial derivatives on the left-hand side of Equation (7.36) and using Equation (7.50) yields

$$\frac{\partial f_1}{\partial t} + u_\infty \frac{\partial f_1}{\partial x} + v_\infty \frac{\partial f_1}{\partial y} + w_\infty \frac{\partial f_1}{\partial z} + \dot{r}\frac{\partial f_1}{\partial r} + \sum_{i=1}^{l-1} \dot{\gamma}_i \frac{\partial f_1}{\partial \gamma_i} = h + f_1 \left[\frac{\partial w_r}{\partial z} - \frac{\partial \dot{r}}{\partial r} - \sum_{i=1}^{l-1} \frac{\partial \dot{\gamma}_i}{\partial \gamma_i} \right] \tag{7.51}$$

By definition, the total time derivative of f_1 with respect to time t can be written as

$$\frac{\mathrm{d}f_1}{\mathrm{d}t} = \frac{\partial f_1}{\partial t} + \frac{\mathrm{d}x}{\mathrm{d}t}\frac{\partial f_1}{\partial x} + \frac{\mathrm{d}y}{\mathrm{d}t}\frac{\partial f_1}{\partial y} + \frac{\mathrm{d}z}{\mathrm{d}t}\frac{\partial f_1}{\partial z} + \frac{\mathrm{d}r}{\mathrm{d}t}\frac{\partial f_1}{\partial r} + \sum_{i=1}^{l-1} \frac{\mathrm{d}\gamma_i}{\mathrm{d}t}\frac{\partial f_1}{\partial \gamma_i} \tag{7.52}$$

[2]The Fortran subroutine is available at
http : //www.sali.freeservers.com/engineering/fortran_codes/unequal_simps.html

We further define the characteristic curves in the particle state space as

$$\frac{\mathrm{d}x}{\mathrm{d}t} = u_\infty(x,y,z) \tag{7.53}$$

$$\frac{\mathrm{d}y}{\mathrm{d}t} = v_\infty(x,y,z) \tag{7.54}$$

$$\frac{\mathrm{d}z}{\mathrm{d}t} = w_\infty(x,y,z) - w_r(x,y,z,r) \tag{7.55}$$

$$\frac{\mathrm{d}r}{\mathrm{d}t} = \dot{r}[x,y,z,,r,(\gamma_i)_{1\le i\le l-1},t] \tag{7.56}$$

$$\frac{\mathrm{d}\gamma_i}{\mathrm{d}t} = \dot{\gamma}_i[x,y,z,r,(\gamma_i)_{1\le i\le l-1},t] \qquad \text{for} \quad i=1,...,l-1 \tag{7.57}$$

where w_r, $\dot{r}$, and $\dot{\gamma}_i$ are given by Equations (7.21), (7.44), and (7.38), respectively. Then, along the characteristic curves in the [x,y,z,r,$(\gamma_i)_{1\le i\le l-1}$, t] space, the population balance equation can be written as

$$\frac{\mathrm{D}f_1}{\mathrm{D}t} = h + f_1\left[\frac{\partial w_r}{\partial z} - \frac{\partial \dot{r}}{\partial r} - \sum_{i=1}^{l-1}\frac{\partial \dot{\gamma}_i}{\partial \gamma_i}\right] \tag{7.58}$$

where $\mathrm{D}f_1/\mathrm{D}t$ denotes the substantial derivative or the total time derivative along the pathline of the bubbles. The partial derivatives of w_r, $\dot{r}$, and $\dot{\gamma}_i$ with respect to z, r, and γ_i, respectively, are derived from Equations (7.21), (7.44), and (7.38) and expressed as

$$\frac{\partial w_r}{\partial z} = \frac{2\alpha\rho_\infty g r\dot{r}}{\mu_\infty(w_\infty - w_r)} - \frac{\alpha\rho_\infty g r^2}{\mu_\infty^2}\frac{\partial \mu_\infty}{\partial z} \tag{7.59}$$

$$\frac{\partial \dot{r}}{\partial r} = \frac{0.63RT\left(\frac{\alpha\rho_\infty g}{\mu_\infty}\right)^{1/3}\sum_{i=1}^{l}\left(2\sigma\gamma_i S_i D_i^{2/3}/r^2\right) - \frac{\rho_\infty g(w_\infty - 3w_r)}{3}}{p_0 + \rho_\infty g z + 4\sigma/3r} + \frac{4\sigma}{3r^2}\frac{\dot{r}}{p_0 + \rho_\infty g z + 4\sigma/3r} \tag{7.60}$$

$$\frac{\partial \dot{\gamma}_i}{\partial \gamma_i} = -\frac{3\dot{r}}{r} - \frac{1.905 S_i RT}{r}\left(\frac{\alpha\rho_\infty g}{\mu_\infty}\right)^{1/3}\left[1 - \frac{\gamma_i(p_0 + \rho_\infty g z)}{p_0 + \rho_\infty g z + 4\sigma/3r}\right] - \frac{\rho_\infty g(w_\infty - w_r) - 2\sigma\dot{r}/r^2}{p_b} \tag{7.61}$$

Equations (7.53) to (7.58) represent a system of ordinary differential equations that can be solved along the characteristic curves by the method of characteristics using inverse marching method with the same staggered grids as those used for computing

the glassmelt velocity $\vec{v}_\infty$, temperature T, refining agent $[M^{k+}]$ and dissolved gas concentrations $C_{\infty,i}$ fields enabling the coupling between all the variables. Detailed description of the numerical scheme is presented in Appendix C.

The modified method of characteristics (or inverse marching method) is an intepretation of the Lagrangian approach that overcomes the difficulties related to mesh deformation. Based on a prespecified grid, it follows the particles backward in time as opposed to foward in the case of direct marching method. The inverse marching method uses a fixed grid that can also be used for solving other transport equations such the momentum equation, the energy equation or the gas concentration in the continuous phase by finite-difference methods using a staggered grid as suggested by Patankar [179]. Thus, interactions between the particles or bubbles and the surrounding fluid can be easily accounted for in the numerical scheme. But unlike finite-difference methods that propagate the information along coordinate lines, the method of characteristics propagates the information along the pathlines and thus matches the physics of the flow resulting in extremely accurate numerical results [181]. Other advantages of the method of characteristics are to overcome the numerical diffusion introduced by finite-difference methods [179] and to eliminate the need for outflow boundary conditions particularly at the glass free surface and glassmelt/foam interface. Moreover, the modified method of characteristics can be used for both transient and steady-state calculations with great accuracy and without problems of numerical instability. However, it possesses significant although not overwhelming disadvantages [181]: (1) it is a relatively complicated procedure, especially for more than three or four independent variables; (2) the method is restricted to flow without discontinuities, and (3) due to the large amount of required interpolations and numerical integration of the governing ODEs, the computer programs require large execution time. As computer becomes faster, more powerful, and cheaper, the present approach favors accuracy and numerical stability concerns over computational time and algorithm complexity.

Numerical interpolation was performed using Lagrangian interpolation formula in

three-dimensional space and the system of ordinary differential equations (7.53) to (7.58) was solved by the fourth order Runge-Kutta method [182]. The computational points at the glass/combustion space interface are treated as internal points of the computational domain and no boundary condition is prescribed.To avoid numerical instabilities, it is necessary to insure that each computational cell traveled by the bubble contains at least two consecutive points on the characteristic curve. Beside this requirement, the time step had no significant effect on the prediction of the bubble density function. The steady-state conditions were assumed to be reached when the maximum relative difference in the predictions of the particle internal coordinates (r and γ_i) and of the density function f_1 between two successive iterations falls below an arbitrarily specified value.

7.4. Conclusion

This paper presented the mathematical formulation of bubble transport and generation in three-dimensional laminar gravity driven flow. The mathematical model has been developed but is not limited to glass manufacturing and can be readily applied to other materials processing problems such as steel, aluminum, and polymers. After careful statement of the physical assumptions, the governing equations for (1) the refining agent concentration, (2) the gas species dissolved in the liquid phase, and (3) the bubble density function are derived. To the best of our knowledge, this study is the first one presenting a complete set of coupled governing equations for the key variables essential to assess the refining performances of a furnace. The method of solution and the convergence criteria are briefly discussed. The results will enable one to predict the quality of the glass, to simulate foaming of the glassmelt, and to determined the number and size distribution of bubbles in the glassmelt which are critical for accurately predicting heat transfer from the combustion space to the glass bath [11–13]. Part II presents the results of sample calculations.

NOMENCLATURE

A	Frequency factor in Arrhenius equation
C	Mass concentration
D	Diffusion coefficient
$D_{eff}\|_f$	Effective diffusion coefficient of the foam layer
E	Activation energy
f	Fugacity
f_1	Bubble density function
g	Specific gravity
h	Bubble generation rate per unit volume in the state space
H_∞	Steady-state foam thickness
$\vec{i}, \vec{j}, \vec{k}$	Unit vectors in the physical space
j, k	Oxidation indices of the refining agent
$j(x, y)$	Superficial gas velocity at the glassmelt surface
k_r	Refining reaction rate constant
K	Mass transfer coefficient
l	Number of gas species diffusing into and out of the bubbles
$\dot{m}$	Mass flux
M	Refining agent ion
M_i	Molecular mass of gas species "i"
$\bar{M}$	Mean molecular mass
p	Pressure
p_i	Partial pressure of gas species "i"
$\vec{P}$	Property or internal coordinates
q	Order of the refining reaction
r	Bubble radius
R	Universal gas constant $= 8.314 J/molK$
S	Solubility of the gas species in the molten glass
T	Temperature

t	Time
u	Projection of the velocity vector on the x-axis
v	Projection of the velocity vector on the y-axis
V	Volume
$\vec{v}$	Velocity vector
w	Projection of the velocity vector on the z-axis
w_r	Vertical upward velocity of the bubble relative to the glassmelt
$\vec{x}$	Spatial or external coordinates
x	Longitudinal location (see Figure 7.1)
x	Spanwise location (see Figure 7.1)
z	Local depth within the glassmelt (see Figure 7.1)

Greek symbols

α	Parameter [Equation (7.22)]
γ_i	Molar fraction of gas species "i" inside the bubble
σ	Surface tension
ρ	Density
μ	Kinematic viscosity
$\mu_m^{(i)}$	Sectional moment of the bubble density function of order m [Equation (7.5)]
μ_m	Total moment of the bubble density function of order m [Equation (7.6)]

Subscripts

b	Refers to the bubbles
$batch$	Refers to the batch
$comb$	Refers to the combustion space
CO_2	Refers to the carbon dioxide
$diff$	Refers to gas diffusion from the the glassmelt to the gas bubbles
e	Equilibrium property at the bubble/glassmelt interface
i	Index of the gas species
int	Refers to the surface of the glassmelt
M	Refers to the refining agent

n	Index of the bubble group
O_2	Refers to the oxygen
ref	Refers to refining reaction
∞	Refers to the bulk of the glassmelt

Notation

$[X]$	Molar concentration of species X in the glassmelt
$\dot{X}$	Derivative of property X with respect to time

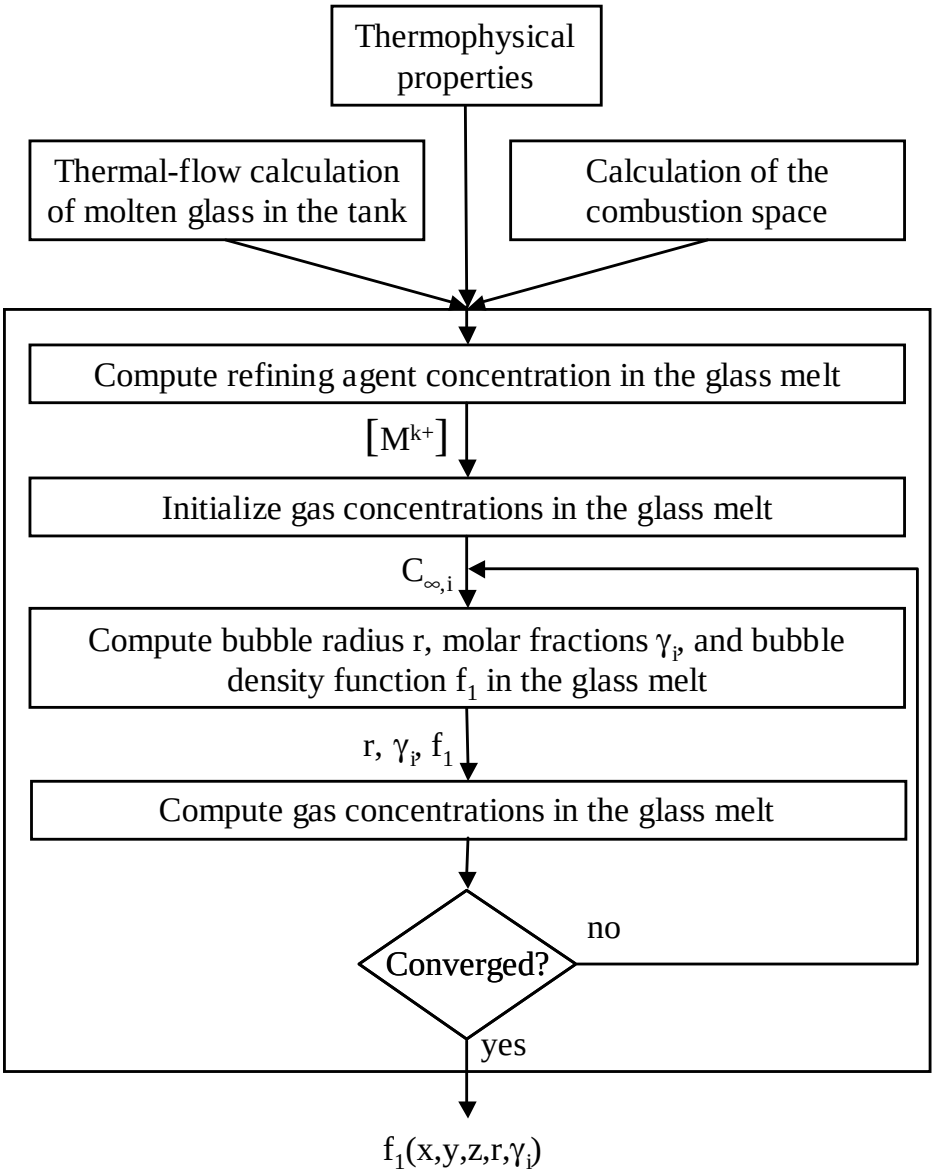

Figure 7.3. Schematic lock diagram of the computational procedure.

8. BUBBLE TRANSPORT IN THREE-DIMENSIONAL LAMINAR GRAVITY DRIVEN FLOW - NUMERICAL RESULTS

8.1. Introduction

Previous studies computed the dissolved gas concentration in the melt by neglecting the source term due to the diffusion of gases in and out of the bubbles [133, 149, 150, 154, 183]. This simplification implies that the dissolved gas concentrations and the number of bubbles in discretized groups can be computed consecutively and independently. In the present study, these parameters are intimately coupled, i.e., $C_{\infty,i}$, r, γ_i, and f_1 are computed iteratively until converged solutions for all the variables are obtained. Considering refining reactions that are complete and irreversible enables one to compute the refining agent concentration $[M^{k+}]$ independently.

The input parameters governing the problem are: (1) the thermophysical properties of the molten glass, (2) the physicochemical properties of gases dissolved in the molten glass, (3) the refining reactions characteristics, (4) the partial pressure of gases at the combustion space/glassmelt or foam interfaces, and (5) the three-dimensional flow and temperature fields of the molten glass. Two sample calculations are presented and discussed in detail for the following physical situations : (1) bubbles contain only CO_2 that diffuse out of the bubbles, and (2) bubbles containing both CO_2 and O_2 but with only O_2 diffusing in and out of the bubbles.

The main interest of this chapter is to demonstrate the feasibility of the calculations by presenting sample results and trends observed in the two-phase flow. Consequently, some simplifications in the model formulation have been made to make the calculations more economical. These include neglecting the effect of bubbles on the liquid flow and thermal structures and assuming that the bubble velocity is the same

as that of the glassmelt except in the vertical direction where buoyancy is accounted for. These simplifications are justified by the fact that bubbles and the void fraction are small and by the inability to validate the numerical results at present due to the lack of experimental data. The study also aims at assessing the effect of the gas diffusion in and out of the bubbles on the concentration of dissolved gases in the glassmelt and neglected in previous studies [133, 149, 150, 154, 161, 183].

8.2. Physicochemical Properties

The thermophysical properties are important input parameters and their appropriate specification is a major concern in modeling glass melting furnaces and bubble behavior [136, 144]. Up to now, no reported simulation of glass melting furnaces has used a consistent set of thermophysical properties for a given glass composition. The assessment of the bubble transport and foam formation models depends strongly on the accuracy of the molten glass thermophysical properties (e.g., viscosity, density, surface tension, thermal diffusivity, and expansion coefficient), the refining reaction characteristics as well as the diffusion coefficient, and the solubility of each gas dissolved in the molten glass. These thermophysical properties depend on many parameters such as the glass composition, the temperature, the dissolved gas partial pressure, and the composition and pressure of the atmosphere [184]. According to Kawachi and Kawase [150] reliable data and measurement methods are not yet available for some of the thermophysical properties needed. The purpose of this work is neither to develop and extensive database nor to provide new experimental results or measurements methods. Instead, its specific aim is to collect and assess the available data for soda-lime silicate glass. Particular attention was paid to the properties of the most common composition [74 SiO_2-16 Na_2O-10 CaO (mol.%)] of soda-lime silicate glass or similar compositions over the temperature range of 1000 to 2000 K. The thermophysical properties of the molten glass have been previously reported [170] and need not be reproduced. Discussion of the gas physicochemical properties used

as input parameters to the numerical simulations is included in the next subsection and is limited to oxygen and carbon dioxide gases. Additional data for nitrogen, water vapor, and sulfure dioxide are given in Appendix B.

8.2.1. Surface Tension

The surface tension depends on the temperature, the bulk glass composition, the atmosphere composition, and the ions dissolved in the melt such as the sulfate [9]. The effect of all those parameters are discussed in detail by Schulze [184]. In brief, surface tension decreases with increasing temperature and the fraction of CaO and Na_2O. The surface tension of the system 74 SiO_2-16 Na_2O-10 CaO (mol.%) soda-lime silicate glass/air is given by [184, 185],

$$\sigma(T) = 321.7 - 0.04 \times (T - 1173.15) \qquad \text{in mN/m} \tag{8.1}$$

The above expression is assumed to be independent of the gas, i.e., Equation (8.1) is used for both carbon dioxide and oxygen. However, it has been observed experimentally that the surface tension of soda-lime silicate glass was reduced by the presence of gases having a non-zero dipole moment in the atmosphere [186]. Water vapor has been identified as having the most significant effect on the surface tension. At temperatures larger than 600 ^{o}C, however, the effect of water vapor has been considered to be negligible [9,184]. The effect of the atmosphere on the surface tension is of great importance in the formation of glass foam [9, 13], and even a small surface tension depression can have a significant effect on the foam thickness as shown experimentally by Ghag *et al.* [26] for water+78% glycerine solution. Unfortunately, no data is reported in the literature for the change of surface tension with water vapor pressure at high temperatures; therefore, this effect will not be considered further.

8.2.2. Gas Diffusion Coefficient in the Glassmelt

The most extensive diffusion measurements have been made for fused silica, since this glass is one of the most permeable to gases. Unfortunately, for other types of glass, a few measurements concerning gases other than helium and hydrogen are available [187]. The variation of the diffusion coefficient of the gas species "i" in a glassmelt as a function of temperature is known to follow an Arrhenius type of law [188]:

$$D_i = D_{0,i} exp\,(-\Delta H_{D,i}/RT) \tag{8.2}$$

where $D_{0,i}$ and $\Delta H_{D,i}$ are empirically determined constants.

Diffusion coefficient of oxygen in the molten glass varies significantly from one type of glass to another as shown by Doremus [189]. Very often the soda-lime silicate glass composition was not available even though it is well known that the gas diffusion coefficients and solubilities can depend significantly on the glass composition. A fit of the experimental data presented by Terai and Oishi [190] gives the following expression for the diffusion coefficient of oxygen in 71.7 SiO_2-15.5 Na_2O-12.8 CaO (mol.%) soda-lime silicate glass:

$$D_{O_2} = 3.2 \times 10^{-6} exp\,(-21076/T) \tag{8.3}$$

A fit of data reported by Doremus [189] for a commercial soda-lime silicate glass leads to the following expression:

$$D_{O_2} = 1.14 \times 10^{-3} exp\,(-24946/T) \tag{8.4}$$

Unfortunately, the composition of the glass studied by Doremus [189] is unknown and it is believed to contain other elements such as MgO and Al_2O_3 [188]. The discrepancies among experimental data are assumed to be due the differences in the glass compositions. It was decided to use the data reported by Terai and Oishi [190] since they cover a wider range of temperatures, and the glass studied has a very similar composition to that of interest in the present study, i.e., 74 SiO_2-16 Na_2O-10 CaO (mol.%).

The only additional information available in the literature concerning the diffusion coefficient of carbon dioxide in soda-lime silicate glass is the following expression proposed by Nemec and Muhlbauer [191]

$$D_{CO_2} = 7.95 \times 10^{-9} exp\left[-11332/\left(T - 473.4\right)\right] \tag{8.5}$$

8.2.3. Gas Solubility in the Glassmelt

Gases can dissolve in the glassmelt by physical and/or chemical dissolution. Physical dissolution consists of occupying free spaces in the network of the molten glass. Physical solubility is higher for small gas molecules and increases slightly with temperature [184]. Gases can also dissolve chemically, i.e., they react chemically and create bonds with the glass structure.

Solubility is the amount of dissolved gas per unit mass of melt per unit of applied pressure and is expressed in many different units. The common unit is the volume of gas at standard temperature and pressure (STP, 0^{o}C and 1 atm) per unit volume of material exposed at one atmosphere of gas (m^3 (STP)/m^{3}atm). It can also be expressed in kg/m^{3}Pa. Doremus [187] pointed out that these definitions contain implicitly a temperature dependence since the applied pressure follows the ideal gas law, P=nRT/V. Instead, Doremus [187] suggested the use of "Ostwald solubility" defined as the ratio of the concentration of the gas in the material C_i and the concentration of the gas in the surrounding atmosphere C_g,

$$S_{i,Os} = \frac{C_i}{C_g} \tag{8.6}$$

However, in the present work solubility will be expressed in moles of gas per unit volume of liquid phase per unit external partial pressure of the gas (mol/m^{3}Pa) as used in the most common form of the Henry's law. The relationships between the different units for solubility are:

$$1[mol/m^3Pa] = \frac{1}{RT_{STP}}[m^3(STP)/m^3atm] = \frac{1}{RT}S_{i,Os} \tag{8.7}$$

where R is the universal gas constant (=8.314J/molK), T is the temperature, and T_{STP} is the temperature at the standard atmosphere (=273.15K). In the following sections the solubility is expressed in mol/m^{3}Pa and is assumed to follows an Arrhenius type of law:

$$S_i = S_{i,0} exp\left(\Delta H_{S,i}/RT\right) \tag{8.8}$$

where $S_{0,j}$ and$\Delta H_{S,i}$ are constants determined experimentally.

The solubility of oxygen depends strongly on the glass composition [192]. The presence of suitable elements of variable valence such as antimony oxide or arsenic can increase the solubility [192]. The only data available concerning the solubility of oxygen in soda-lime silicate is [192],

$$S_{O_2} = 2.2 \times 10^{-4} \qquad \text{in mol/m}^3\text{Pa} \tag{8.9}$$

An expression of solubility of carbon dioxide is available in the literature and compares well with reported experimental data [191]:

$$S_{CO_2} = 3.45 \times 10^{-6} exp\left(3840/T\right) \qquad \text{in mol/m}^3\text{Pa} \tag{8.10}$$

8.2.4. Refining Reactions

The present study is concerned with antimony pentaoxide used as the refining agent and decomposing according to the reaction $Sb_2O_5 \rightleftharpoons Sb_2O_3 + O_2 \uparrow$. Kawachi and Kawase [133, 150] and Kawachi and Kato [151] showed that the rate of the backward reaction can be neglected in the production of TV-panel glass. Therefore, the refining reaction can be considered as irreversible with only the decomposition of Sb_2O_5 taking place. Reaction rate constants and order of the refining reaction involvind antimony oxide can be found in the literature [151]. The same refining reaction characteristics were assumed to hold also for soda-lime silicate glasses. Antimony oxide is considered for the following reasons: the refining reaction produces only oxygen whose concentration in the glassmelt has to be computed, and the reaction is complete and

irreversible so that refining agent concentration can be computed independently from the dissolved gas concentrations $C_{\infty,i}$ and the bubble density function f_1. Treatment of equilibrium refining reactions, such as these involving sodium sulphate Na_2SO_4, would consists of including the computation of the refining agent concentration into the iterative scheme for the dissolved gas concentrations and the bubble density function to account for their interdependence. In addition, when sodium sulfate is used as a refining agent both oxygen and sulfure dioxide SO_2 are generated during the refining process. Then, they dissolve in the glassmelt and can diffuse in and out of the bubbles [9,139]. Therefore, concentrations of both oxygen and sulfure oxide dissolved in the molten glass and their molar fractions in the bubbles should be computed along with those of carbon dioxide. The bubbles are then characterized by six independent variables (e.g., x,y,z,r,γ_{CO_2}, γ_{O_2}) making the numerical scheme quite involved. Such a situation falls beyond the scope of the present study whose main objective is to demonstrate the feasibility of the calculations.

Finally, it has not been possible to find the diffusion coefficient of the refining agent in soda-lime silicate glass.

8.3. Results and Discussion

8.3.1. Model Glass Tank and Parameters

The same glass melting tank as that used for three-dimensional flow and thermal structures of molten glass was considered [170, 171]. It is a rectangular bath 15.85 m long, 7.315 m wide, and 1.03 m deep (see Figure 8.1). The molten glass exits the tank through a throat having a cross-sectional area of 0.386×0.802 m^2 which is located at the bottom and in the middle of the front wall. The raw batch material leading to a glassmelt of composition of 74 SiO_2-16 Na_2O-10 CaO (mol.%) is introduced into the tank at a rate $\dot{m}_b$ of 356 tons/day (or 4.12 kg/s) in the form of a loose blanket covering the entire width of the tank. Since about 200 kg of gases are produced per ton

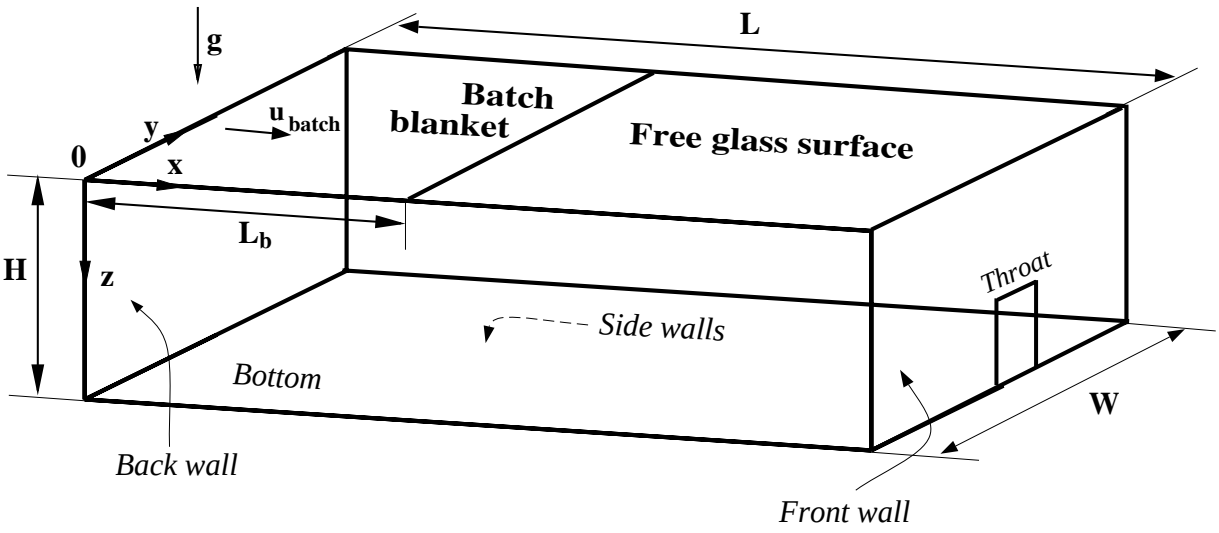

Figure 8.1. Schematic of the modeled glass melting tank and the associated systems of coordinates.

of batch introduced [193], the corresponding glass production rate (pull rate) $\dot{m}_{pull}$ is 297 tons/day (or 3.347 kg/s) of molten glass.

The simulations consider an oxy-fuel furnace burning methane and oxygen at stoichiometric conditions at atmospheric pressure according to reaction $CH_4 + 2O_2 \rightarrow 2H_2O + CO_2$. Thus, the partial pressures of oxygen and carbon dioxide at the glassmelt/combustion space interface are taken as 0.0 and $p_0/3$, respectively.

The energy ΔH_{melt} required to bring the batch from room temperature (320 K) to clear molten glass and the melting temperature T_{melt} were taken equal to 2200 kJ/kg and 1450 K, respectively [194]. A linear decrease of the glassmelt velocity at the batch/glassmelt interface from 0.2 cm/s where the batch enters the furnace to zero at the tip of the batch blanket was chosen to simulate the fact that the batch blanket becomes thinner and less compact from the loading end to the tip. The maximum velocity of 0.2 cm/s was computed based on the pull rate of 4.12 kg/s for a batch blanket covering the entire width and having a density of 1400 kg/m^3 and a thickness of 20 cm. Moreover, from previous work [171] based on the momentum equation for

a batch blanket at rest projected onto the vertical axis, a depth of 11.2 cm of the batch blanket was assumed to be submerged under the free glass surface.

The heat losses between the glassmelt and the ambient surroundings through the walls were computed assuming 1-D heat conduction through the refractories and cooling of the walls by natural convection using an ambiant temperature of 320 K. The construction of the sidewall refractories were considered to be the same, with an overall heat transfer coefficient of 3.86 W/m^{2}K. At the bottom of the tank the overall heat transfer coefficient equals 3.89 W/m^{2}K and that at the back and front wall is equal to 5.57 W/m^{2}K.

The net heat flux incident from the combustion space and reaching the surface of the batch and of the molten glass is assumed to have the longitudinal profile shown in Figure 8.2, where the parameters q''_{max} and q''_0 are the maximum heat flux and the heat flux at the back wall (x = 0 m), respectively. The distance from the back

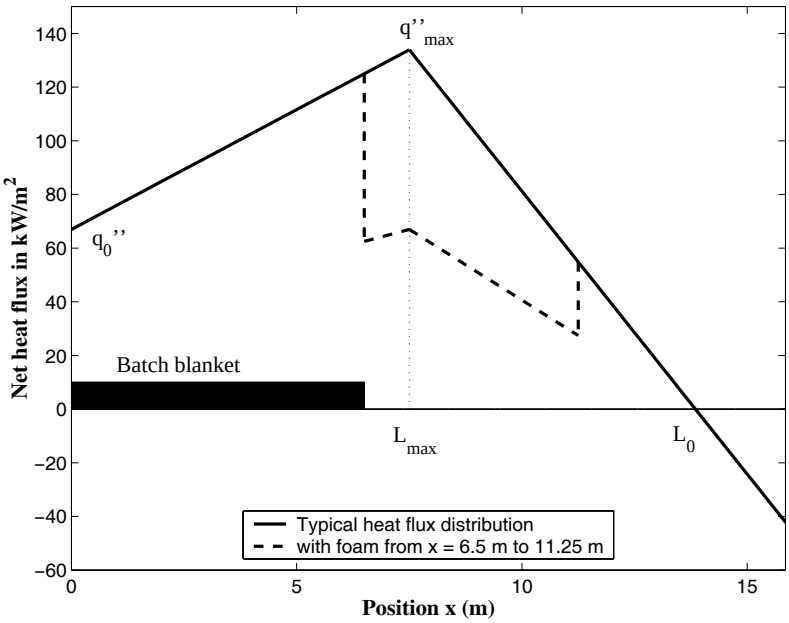

Figure 8.2. Heat flux distribution used as the boundary condition at the glassmelt / combustion space interface.

wall to the location of the maximum heat flux is L_{max} and the distance where the

heat flux vanishes is L_0. They were assumed to be equal to 7.5 m and 13.84 m, respectively. Such a heat flux profile was chosen based on industrial practices [170]. The three-dimensional flow and thermal structures of the molten glass for the above conditions have been presented and discussed in Ref. [171]. Detailed discussion of the flow field is provided and need not be repeated here. Only the temperature, velocity, and streamlines at midplane in the longitudinal direction are reproduced in Figure 8.3. One can see that a part of the pull current flows directly from under the batch

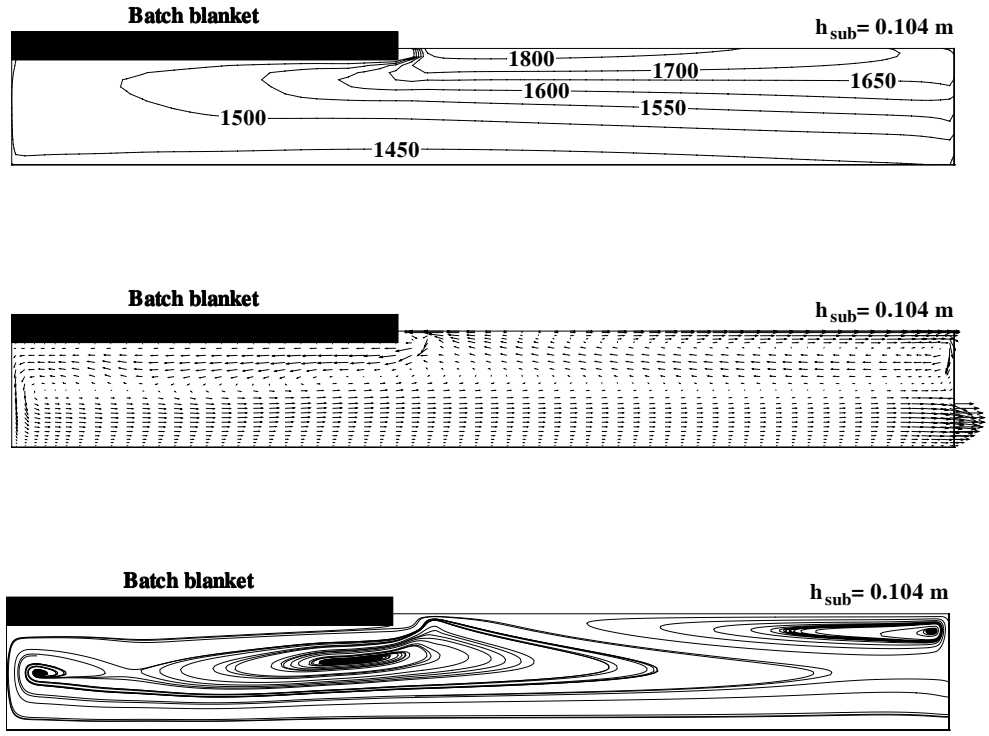

Figure 8.3. Flow field used as input parameter with from top to bottom (top) velocity field, (center) temperature field, and (bottom) streamtraces at the tank midplane.

along the bottom of the tank to the throat as experimentally observed by Zhiqiang and Zhihao [195]. Thus the product quality is expected to be degraded due to the shorter residence time of the glassmelt in the tank.

8.3.2. Analysis of the Results

The calculations yield the value of the bubble density function f_1, the bubble radius r, and the molar fraction of each gas contained in the bubbles γ_i at the scalar nodes of the 66×39×25 staggered grid. The amount of information is very large and not easily interpretable unless it is reduced to physical quantities. Therefore, for a better interpretation of the computational results the bubble density function f_1 and the bubble radius r were converted into more physical and understandable local global variables such as the total number of bubbles N, the interfacial area concentration A_i, the volume fraction of the gas phase f_v, the average bubble radius $\bar{r}$ and the average carbon dioxide molar fraction $\bar{\gamma}_{CO_2}$ at each grid point (x_I,y_J,z_K). For bubbles containing a single gas or a diffusing and a non-diffusing gas, one independent internal variable (r) is considered and N, A_i, f_v, $\bar{r}$, and $\bar{\gamma}_{CO_2}$ are defined, respectively, as

$$0^{th}\text{ moment} \qquad N(x,y,z) = \int_0^\infty f_1(x,y,z,r)\mathrm{d}r \tag{8.11}$$

$$1^{st}\text{ moment} \qquad \bar{r}(x,y,z) = \left[\int_0^\infty r f_1(x,y,z,r)\mathrm{d}r\right] / N(x,y,z) \tag{8.12}$$

$$1^{st}\text{ moment} \qquad \bar{\gamma}_{CO_2}(x,y,z) = \left[\int_0^\infty \gamma_{CO_2} f_1(x,y,z,r)\mathrm{d}r\right] / N(x,y,z) \tag{8.13}$$

$$2^{nd}\text{ moment} \qquad A_i(x,y,z) = \int_0^\infty 4\pi r^2 f_1(x,y,z,r)\mathrm{d}r \tag{8.14}$$

$$3^{rd}\text{ moment} \qquad f_v(x,y,z) = \int_0^\infty \frac{4\pi r^3}{3} f_1(x,y,z,r)\mathrm{d}r \tag{8.15}$$

In the case of single component gas bubbles $\bar{\gamma}_{CO_2}(x,y,z) = 1$. If several diffusing gases are treated, additional internal variables have to be considered and the above integrals become multiple integrals with respect not only to variable r but also to other internal variables γ_i. Note also that, unlike discretized formulations previously suggested [154], which divide the bubble size distribution in groups and solve the population balance equation for the number of bubbles in each group, the present formulation and the associated method of solution compute directly the bubble density function f_1 enabling accurate predictions of any moments of the density function and in particular the zero (N) , first ($\bar{r}$ and $\bar{\gamma}_{CO_2}$), second (A_i), and third (f_v) order moments. The above

single integrals are computed numerically using the Simpson's rule of integration for unequally spaced data [182].

8.3.3. Numerical Method

Numerical difficulties arise due to the fact that many variables (e.g., the pressure inside the bubbles p_b) are functions of $1/r$ which tend to infinity as the bubble radius decreases. However, extremely small bubbles cannot be physically treated in the same manner as macroscale bubbles due, for example, to gas rarefaction effects, and the limits of the concept of surface tension at very small scale. To avoid the numerical problems and account for physical limitations of the model, bubbles are considered to disappear when their radius becomes less than 1.0 μm as suggested by Kawachi and Kawase [150]. Then, the bubble radius r and the bubble density function f_1 are arbitrarily set to 1.0 μm and zero, respectively, corresponding effectively to a sink term in the bubble population balance equation.

The grid sensitivity study for the spatial discretization has been previously performed for the velocity and temperature fields [170]. The entire glass bath was discretized using a 66×39×25 staggered grid. This was a compromise between the computer time required and the resolution needed to resolve details of the glassmelt flow field. The same grid was used for the refining agent concentration and the concentrations of gases dissolved in the molten glass. The steady state was estimated to be reached when the residual for these variables fell below an arbitrarily small constant ϵ_1. The steady-state for the bubble density function f_1, the bubble radius r, and the gas molar fraction γ_{CO_2} is assumed to be reached when the maximum relative variation of the predicted variables between two consecutive iterations over the computational domain fall under an arbitrarily small constant ϵ_2, i.e.,

$$Max\left[\frac{|X_{I,J,K}^{(n-1)} - X_{I,J,K}^{(n)}|}{|X_{I,J,K}^{(n-1)}|}\right] \leq \epsilon_2 \quad \text{for} \quad 1 \leq I \leq 66, 1 \leq J \leq 39, \text{and } 1 \leq K \leq 25 \tag{8.16}$$

where n denotes the iteration number, X is the general symbol for r, f_1, and γ_{CO_2}, while I,J,K are the indices for the scalar nodes of the staggered grid in the x-, y-, and z-directions, respectively. Numerical results for $C_{\infty,i}$, r, f_1, and γ_{CO_2} at steady state were found to be independent of ϵ_1 and ϵ_2 provided that $\epsilon_1 \leq 1.0 \times 10^{-5}$ and $\epsilon_2 \leq 4. \times 10^{-3}$.

Moreover, in order to reduce computational time and still provide adequately accurate results, grid sensitivity studies have been conducted to choose the suitable number of points taken on the initial bubble density function that gives grid-independent numerical results for N, A_i, $\bar{r}$, $\gamma_{\bar{CO_2}}$, f_v, and C_{∞,CO_2}. Numerical sensitivity tests have been made with 6, 11, and 22 points on the initial bubble density function as represented in Figure 8.4. The results for the same number of time steps differed by less

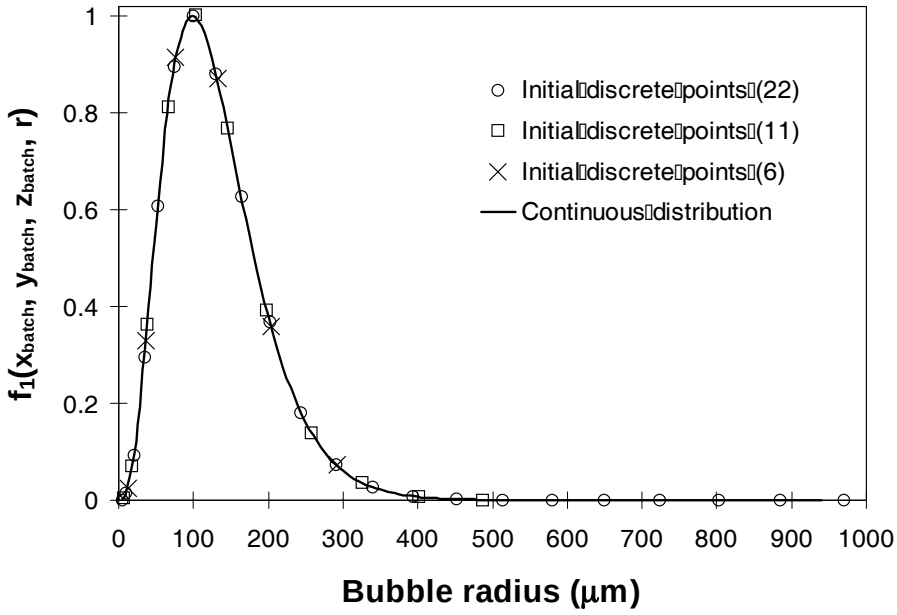

Figure 8.4. Initial bubble density function under the batch and arbitrary discrete set of points chosen for the simulations [Equation (8.17)].

than 1.5% between 11 and 22 points. Therefore, 11 points on the initial distribution are sufficient to obtain a solution independent of the number of points considered on the initial distribution. The time step was proven to have no influence on the final

results as long as at least two consecutive points on the pathlines are contained in any elementary computational volume of the 66×39×25 staggered grid.

In order to validate the numerical implementation of the modified method of characteristics, computations of the bubble radius and density function for simple physical situations having closed-form analytical solutions have been performed. Very good agreement between numerical predictions and analytical solutions for r, and f_1 have been found for one and two dimensional flows and transient and steady-state situation and are summarized in Appendix C.

Unfortunately, no experimental data for full scale industrial glass melters are available to quantitatively validate the numerical results. Comparison with numerical results reported in the literature [150, 154, 183] were made when available. Such comparison with results for the local number of bubbles obtained by Balkanli and Ungan [154] may be misleading since, as pointed out in Chapter 7, the boundary conditions used, the expression for the time rate of change of bubble radius, the decoupling of the gas concentration and the bubble population balance equations are questionable. Moreover, the method of solution based on the discretized formulation cannot predict accurately the other moments of the bubble density function such as $\bar{r}$, $\gamma_{\bar{C}O_2}$, A_i, and f_v [58,155]. The next two sections present results of sample calculations for the physical situations when bubbles contain only CO_2 and when bubbles contain both CO_2 as a non-diffusing gas and O_2 as a diffusing gas, respectively.

8.3.4. Bubbles Containing a Single Gas

Previous studies solving the bubble population balance equation have been concerned only with carbon dioxide bubbles and have neglected the coupling between the concentration of gas dissolved in the molten glass and the bubble population balance equation [154]. This assumption has been made for the sake of simplicity but has not been justified on physically sound arguments. However, the gas contained in single component gas bubbles can only diffuse out of the bubbles since the gas concentra-

tion at the bubble/glassmelt interface at equilibrium $C_{e,i}$ given by the Henry's law is always larger than the gas solubility in the glassmelt [see Chapter 7, Equation (7.27)]. Bubbles shrink due to gas diffusion while they can grow or shrink due to pressure changes; therefore, the presence of bubbles may be a significant source for the gas dissolved in the molten glass and decoupling the gas concentration and the bubble density function may not be appropriate. This section presents and discusses the results when carbon dioxide is the only diffusing gas considered. It represents a limiting case of practical applications since even when no refining agent is added to the batch, water vapor generated in the combustion space, which has a large diffusion coefficient and solubility in the glassmelt, dissolve in the melt and diffuse in the bubbles. The situation considered is highly idealized in order to (1) show the feasability of the calculations, (2) compare with similar simulations previouly reported in the literature [149, 154, 161], and (3) assess the effect of bubbles on the concentration of gases dissolved in the molten glass that was neglected in previous work [133, 149, 150, 183].

The bubble size distribution under the batch and generated by fusion/melting of the raw materials is assumed to follow a gamma distribution defined as

$$f_1(\vec{x}_{batch}, r, t) = Ar^{\eta} exp(-Br) \tag{8.17}$$

the three constants A, B, and η are positive and real numbers determined from experimentally measured quantities such as the radius r_{max} at which the density function reaches a maximum, the total number of bubbles per unit volume of liquid N, and the volumetric void fraction f_v. These quantities can be related to the constants A, B, and η by

$$r_{max} = \left(\frac{\eta}{B}\right), \qquad N = \frac{A\Gamma(\eta+1)}{B^{(\eta+1)}}, \qquad \text{and} \qquad f_v = \frac{4\pi A\Gamma(\eta+4)}{3B^{(\eta+4)}} \tag{8.18}$$

where $\Gamma(z)$ is the gamma function [$\Gamma(z) = \int_0^\infty e^{-t}t^{z-1}dt$] which has been tabulated by Abramowitz and Stegun [87]. Based on experimental results reported in the literature [150, 152, 196], r_{max}, N, and f_v under the batch were taken to be 98 μm, 2,240 bubbles per cubic centimeter of glass, and 4%, respectively, leading to constants A=3.23×10^{26} m^{-7}, B = 3.05×10^4m^{-1}, and η=3. The corresponding average

bubble radius and interfacial area concentration are 112 μm and 609 m^2/m^3 of glass, respectively. Note that the problem of conservation of the total number of bubbles raised in Chapter 7 is not of concern here since the bubble growth rate is very small, owing to the small diffusion coefficient and solubility of carbon dioxide in the glass-melt and due to the small temperature and viscosity gradients, i.e., $\partial w_r/\partial r \approx 0.0$ [see Equation (7.59) in Chapter 7], as checked and confirmed numerically.

First, numerical simulation for the CO_2 concentration in the glassmelt neglecting the presence of bubbles has been performed. Figure 8.5a shows the concentration of carbon dioxide dissolved in the glass bath obtained at the midplane. The figure reveals fairly uniform carbon dioxide concentrations along the glass bath with a sharp concentration gradient close the glass free surface. The relatively uniform carbon dioxide concentration can be explained by the good mixing caused by advective currents and indicates that advection dominates over diffusion [161]. The dominance of advection over diffusion explains also the sharp concentration gradient under the glassmelt surface since in this region the molten glass flows parallel the free surface and transport of carbon dioxide in the normal direction (z-direction) takes place only by diffusion. The lower concentration at the surface of the glass bath is due to the fact that solubility decrease exponentially with temperature [see Equation (8.10)]. The temperatures at the glass free surface are larger than those under the batch by about 250K [171]. Thus, the CO_2 concentration imposed at the glassmelt/combustion space interface is much smaller than that imposed at the glassmelt/batch interface. Overall, numerical predictions of the CO_2 concentration agree well with those reported by Balkanli and Ungan [161]. However, these authors while using the same boundary conditions and the same expression for the carbon dioxide solubility as those of the present study did not mention the partial pressure of carbon dioxide at the glassmelt/combustion space interface used in their numerical simulations. The value of 0.001 kg/m^3 they reported at the glass surface tends to indicate that they imposed a very small partial pressure of CO_2 at the glassmelt/combustion space interface, whereas it should be fairly large since CO_2 and water vapor are the main products of the combustion.

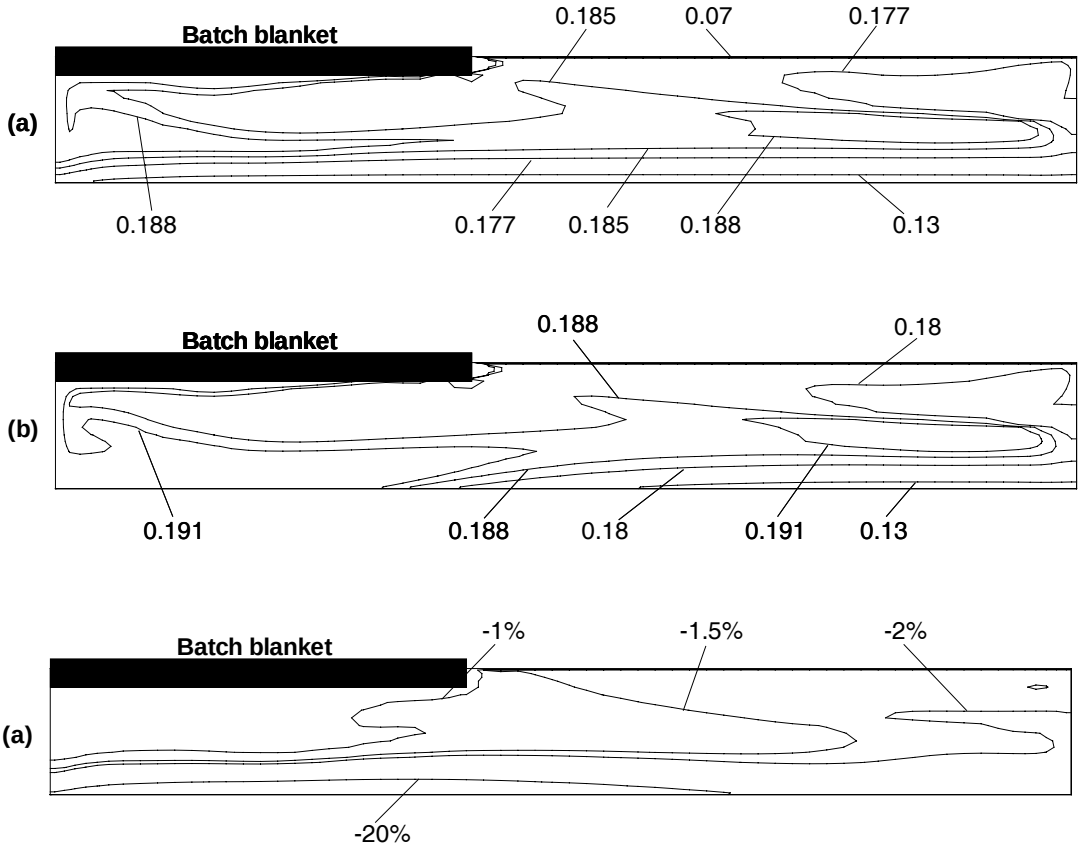

Figure 8.5. Dissolved CO_2 gas iso-concentration lines at midplane (a) without accounting for the presence of bubbles and (b) with accounting for the source term due to gas diffusion in and out of bubbles, and (c) relative difference (in %) between the local CO_2 concentrations in (a) and in (b).

Second, the CO_2 concentration is computed by accounting for the source term owing to CO_2 diffusion out of the bubbles. A converged solution was obtained after two full successive calculations for the CO_2 concentration C_{∞,CO_2} in the glassmelt and the bubble radius r and density function f_1. A grid sensitivity study shows that the maximum deviation in the numerical results between 11 and 22 grid points for N, $\bar{r}$, A_i, f_v, was found to be less than 1.5%, and 11 points is considered sufficient to ensure accuracy. Figure 8.5b shows the concentration of carbon dioxide dissolved in the glass bath at the midplane, while Figure 8.5c shows the relative difference in the CO_2 concentration between Figures 8.5a and 8.5b. It indicates that accounting for gas diffusion out of the bubbles as a source term for carbon dioxide dissolved in the glassmelt does not significantly change the numerical results and the CO_2 concentration increases by less than 2% in most of the glass bath when diffusion out of the bubble is accounted for. Similar spatial distribution of iso-concentration lines can be obtained by shifting the concentration by +0.003 kg/m^3. For example, the 0.185 kg/m^3 iso-concentration line when the presence of bubbles is neglected has the same profile as the 0.188 kg/m^3 concentration line when the presence of bubbles is accounted for.

Finally, note that supersaturation (up to 50 %) of the glassmelt with CO_2 occurs from the tip of the batch to the two third of the tank and underneath the glassmelt free surface (see Figure 8.6). This could lead to heterogeneous bubble nucleation if a large enough amount of undissolved sand grains is present in this region. Bubble nucleation could then result in secondary foam formation in the region beyond the batch tip as commonly observed in industrial glass melting furnaces [9]. Then, secondary foam would be generated not only by bubbles rising from the glassmelt but also from bubbles generated due to oversaturation of the glassmelt and nucleation at the unmelted sand grain surface. However, it is beyond the scope of the present study to investigate such a complex phenomena.

Computations of the bubble density function and of the bubble radius have been performed for different numbers of time steps, i.e., for different simulated times. The

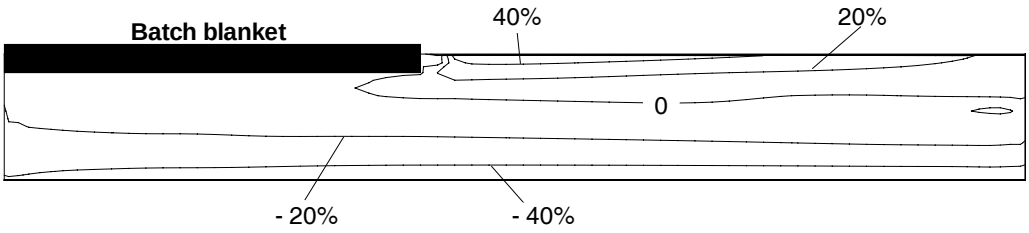

Figure 8.6. Relative difference between the local CO_2 saturation and CO_2 concentration (in %) at midplane accounting for the source term due to gas diffusion in and out of bubbles (negative values correspond to supersaturation).

same iso-concentration lines for the total number of bubbles per unit volume of glass N computed at different times at midplane are presented in Figure 8.7. It simulates the hypothetical situation in which bubbles would be injected a the batch/glassmelt interface at time t=0s and would grow or shrink and be transported by convection. The iso-concentration lines propagates with the glass flow from under the batch to the front wall and then move up toward the free surface before sinking again under the batch. It clearly shows the transport of bubbles by convective currents from under the batch to the refining section and the throat. It also demonstrates the capability of the computer program based on the modified method of characteristics to simulate transient problems. Convergence to steady state is very slow owing to the complexity of the flow field, the small velocities of the glassmelt, and the slow transport phenomena taking place in the glassmelt. In industrial glass melting furnaces, it is estimated that it can take up to two days for the a glassmelt fluid particle to flow from under the batch to throat corresponding to 320,000 time steps to be computed for each points taken on the initial distribution.

Numerical results for the total number of bubbles at steady-state at different cross-sections in the longitudinal direction are shown in Figure 8.8. One can observe the predominance of the bubble transport in the longitudinal direction and no significant changes in the profile of the total number of bubbles from the midplane (y/W=0.5)

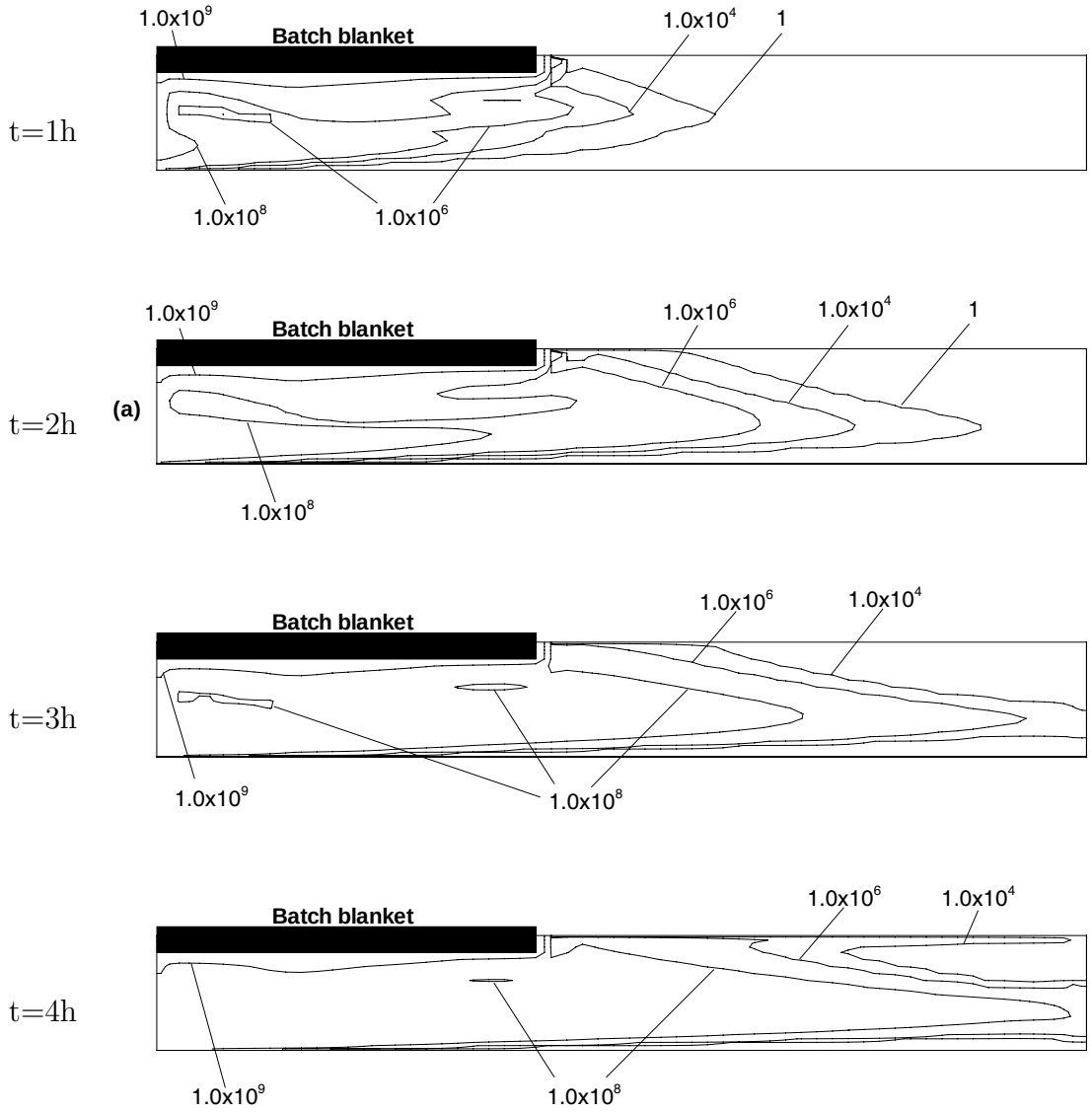

Figure 8.7. Evolution of iso-concentration lines with time for the total number of bubbles N (in $\#/m^3$) at midplane.

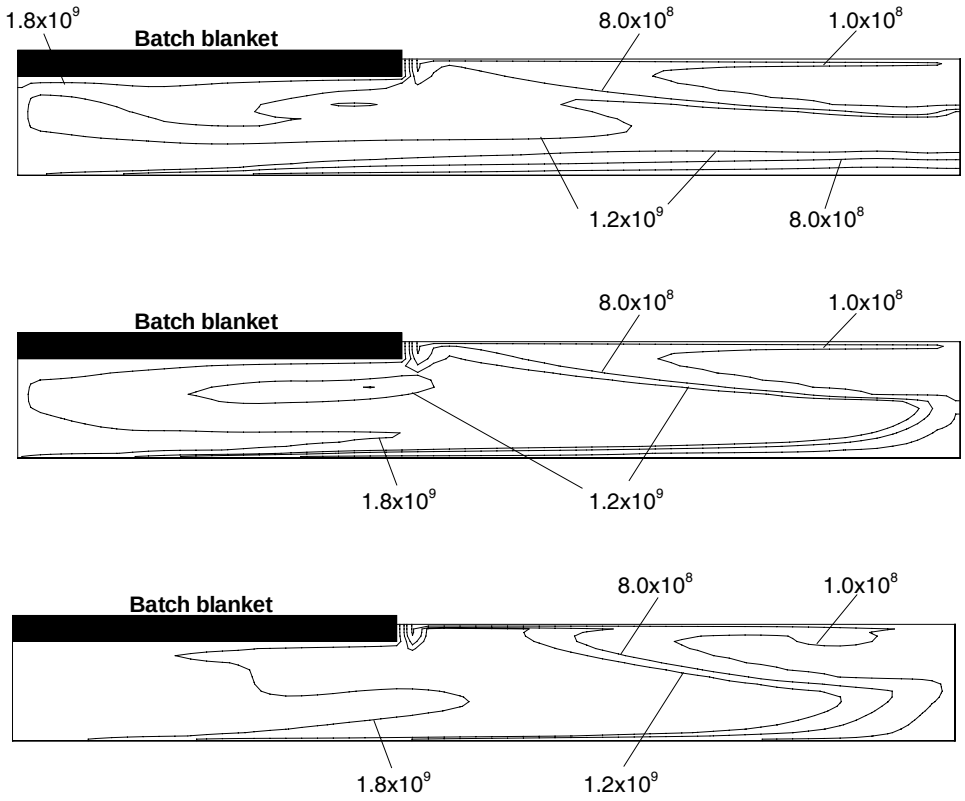

Figure 8.8. Steady-state iso-concentration lines for the total number of bubbles N (in $\#/m^3$) at midplane y/W = 0.5 (top), at y/W=0.25 (center), and y/W=0.01 (bottom).

to the side wall (y=W=0.01) are evident. Moreover, the total number of bubbles entrapped in the glass melt is large and relatively uniform due to the small diffusion coefficient of CO_2 in the glassmelt and the good mixing provided by convection currents.

The steady-state numerical results for the total number of bubbles N, the average bubble radius $\bar{r}$, the interfacial area concentration A_i, and the void fraction f_v, respectively at the midplane (z/W=0.5) are presented in Figures 8.9a to 8.9d and correspond to a simulated time of 48 hours. As one can see, the bubble radius decreases slightly as the bubbles are transported by the convection currents from under the batch to the refining section owing to the small diffusion coefficient of CO_2 in the glassmelt. Only a few bubbles escape to the free glassmelt surface, and the main mechanism of refining is bubble dissolution. The glassmelt flowing near the free surface from the hot spot toward the batch prevents the bubbles from reaching the surface. Indeed, bubbles are too small for the buoyancy force to overcome the strong convection currents in the horizontal plane near the surface of the molten glass. Therefore, as bubbles rise to the glass surface, they are carried away by the glassmelt under the batch and at the bottom of the glass tank. Thus, most bubbles get trapped in the first recirculation loop located in the first half of the tank and significantly fewer bubbles are trapped in the second recirculation loop located closed to the front wall (see Figure 8.3). Finally, Figure 8.9a and b indicate that a large number of bubbles with an average diameter between 70 and 100 μm are transported from the batch through the submerged throat as they are carried by advection when the glassmelt is being pulled. This results in a poor glass quality and energy efficiency but was expected given the glassmelt flow pattern discussed earlier. It is, therefore, interesting to investigate the impact of the refining agent on the bubble behavior since refining gases diffuse in the bubbles to enable the bubbles to rise to the glassmelt surface by buoyancy before reaching the throat.

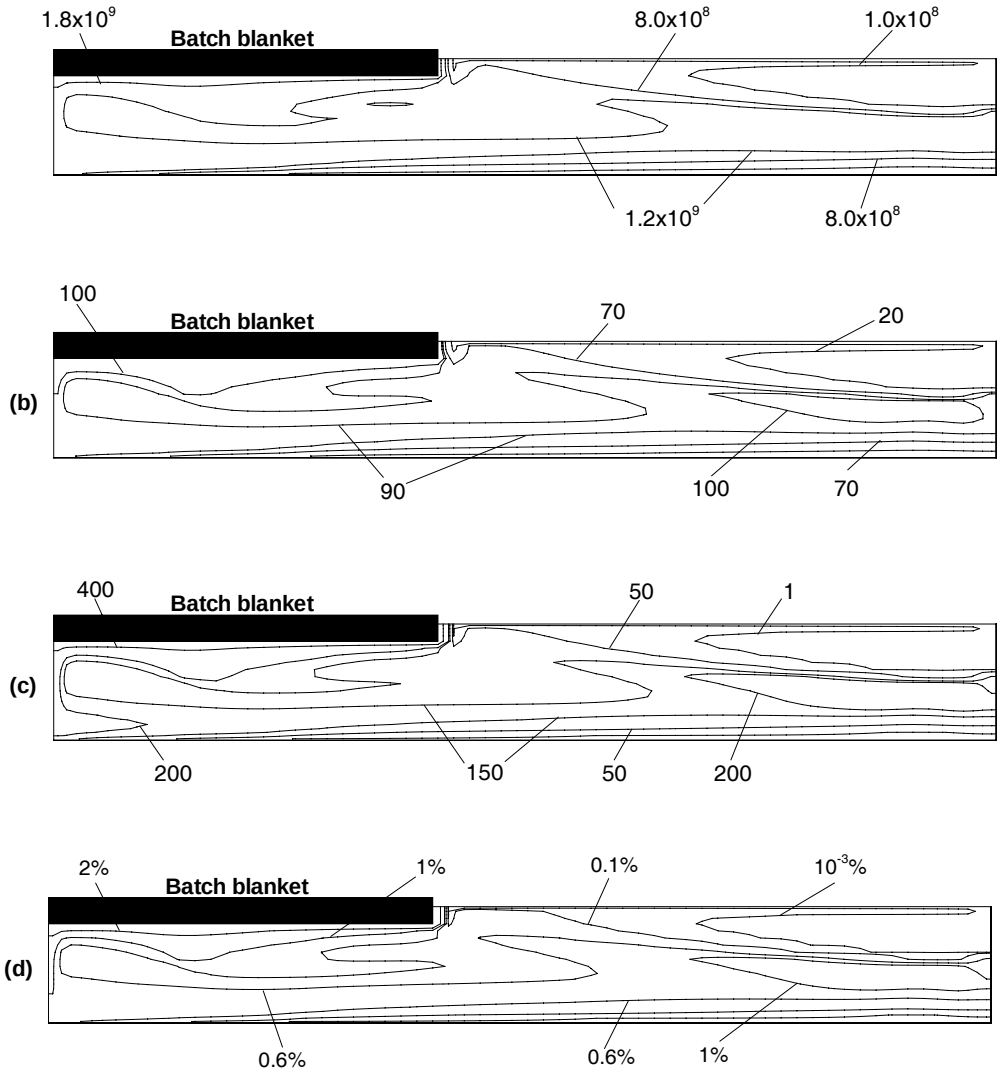

Figure 8.9. Iso-concentration lines at midplane for (a) N (in $\#/m^3$), (b) $\bar{r}$ (in μm), (c) A_i (in m^2 of interface $/m^3$ of glassmelt), (d) f_v (in m^3 of gas in bubbles $/m^3$ of glassmelt) at midplane.

8.3.5. Bubbles Containing Two Different Gases

Bubble growth in the glassmelt can only be due to the diffusion of gases such as oxygen, water vapor, and sulfur oxide that have a large diffusion coefficient and a large enough solubility [174]. Bubble growth is obtained by adding refining agents to the batch that produce such gases. The present example is limited to the important practical situations when antimony pentoxide Sb_2O_5 is added to the raw batch materials as a refining agent. The refining agent concentration is needed to compute the oxygen concentration dissolved in the glassmelt and diffusing in and out of the bubbles. It can be computed independently from the other variables since refining reactions are assumed to be irreversible and complete. However, since the diffusion coefficient of the refining agent and the reaction rate constants of the refining reaction involving antimony oxide in soda-lime silicate glass could not be obtained from the literature, the refining agent concentration has not been computed. Instead, the oxygen concentration dissolved in the glassmelt was assumed to be equal to saturation at the local temperature and pressure everywhere in the glass bath. This can be justified by the fact that oxygen is supplied in great amount during the melting of batch. Thus, its concentration in the glassmelt under the batch should be uniform as shown for CO_2. Furthermore, unlike CO_2, oxygen is also generated by refining reactions in the refining section of the tank where the temperatures are large allowing refining reactions to occur. Finally, convection currents produce good mixing that leads to uniform oxygen concentration in the glassmelt similar to that observed for carbon dioxide. The same sharp concentration gradient at the glassmelt/combustion space interface observed for CO_2 is expected for O_2 since the boundary condition for the oxygen concentration is $C_{\infty,O_2} = 0.0$ at the glassmelt/combustion space interface. This concentration gradient is neglected since it is very sharp and highly localized to a small depth in the glassmelt.

In the case under consideration, both carbon dioxide and oxygen dissolved in the glassmelt or contained in the bubbles have to be considered. Carbon dioxide is generated during the melting of calcium carbonate while oxygen is released by the

decomposition of nitrates such as $NaNO_3$ and of the refining agent [139]. For a typical soda-lime silicate glass batch without refining agent, experimental analysis of gases released during batch melting and fusion [197, 198] indicate that significantly more (at least 15 times) CO_2 is generated than other gases. But, oxygen is generated by refining reactions. Therefore, as a first order approximation, bubbles located under the batch are assumed to contain both CO_2 and O_2 at equal molar fraction, i.e., $\gamma_{CO_2} = \gamma_{O_2} = 0.5$, at the batch/glassmelt interface. Since the diffusion coefficient and solubility of carbon dioxide are at least one order of magnitude smaller than those of oxygen [142, 148, 174] over the temperature range 1000 K to 2000 K, carbon dioxide is treated as a non-diffusing gas and only oxygen is assumed to diffuse in and out of the bubbles.

This assumption has the advantage of simplifying the numerical algorithm by avoiding two-dimensional numerical integration from scattered data points that requires bivariate interpolation and smooth surface fitting onto a equally space fixed grid for initial values given at irregularly distributed points [199,200], before performing the double integration by repeated one-dimensional numerical integration using Simpson's rule [182]. The number of moles of carbon dioxide contained in the bubbles remain constant while the CO_2 molar fraction changes due to oxygen diffusion. The CO_2 molar fraction in the bubbles at location z having radius r and temperature T is expressed as

$$\gamma_{CO_2} = 1 - \gamma_{O_2} = \frac{T(p_0 + 2\sigma/r_0)}{T_{melt}(p_0 + \rho_\infty g z + 2\sigma/r)} \left(\frac{r_0}{r}\right)^3 \gamma^0_{CO_2} \tag{8.19}$$

The initial bubble radius of a point of the initial bubble density function under the batch is r_0. The initial bubble temperature equals the batch melting temperature T_{melt} taken as 1450 K. Finally, the initial molar fraction of CO_2 in the bubbles is given by $\gamma^0_{CO_2}$ while the bubbles are assumed to be initially located in the plane z=0 m. Since CO_2 is assumed not to diffuse into or out of the bubbles, the bubbles can

shrink until the molar fraction of CO_2 becomes unity and the bubble radius reaches its minimum r_{min}, which can be determined by solving the following equation

$$(p_0 + \rho_\infty g z) r_{min}^3 + 2\sigma r_{min}^2 - (p_0 r_0^3 + 2\sigma r_0^2) \frac{T}{T_{melt}} \gamma_{CO_2}^0 = 0 \tag{8.20}$$

Figures 8.10a to 8.10d show the numerical results for the total number of bubbles per unit volume of glass N, the average bubble radius $\bar{r}$, the average molar fraction of CO_2, the interfacial area concentration A_i, and the volumetric gas fraction f_v. As one can see, most of the bubbles are located under the batch where the interfacial area concentration and the void fraction are the largest. Compared with the case when only CO_2 is considered, a larger number of bubbles escape at the glassmelt free surface and the main mechanism of refining is bubble growth and rise to the surface. The addition of refining agents reduces the number of bubbles leaving the tank at the throat but simultaneously increases the foam formation by releasing more bubbles to the glass free surface as observed in actual glass melting furnaces [13]. The average diameter of bubbles leaving the tank at the throat is between 10 and 60 μm compared with 70 to 100 μm when no refining agent is added. The average CO_2 molar fraction (not plotted) increases relatively quickly and is almost uniform across the glass bath except under the batch.

8.4. Conclusions

This chapter presents numerical results for sample calculations of bubble transport, growth or shrinkage in three-dimensional laminar gravity driven flow based on the model developed in Chapter 7 with applications to glass melting furnaces. The following conclusions can be drawn:

- The present study demonstrate the feasibility of solving the bubble population balance equation in three-dimensional laminar gravity driven flow for both transient and steady-state situations using the modified method of characteristics. Detail calculations of the bubble density function enables one to compute any

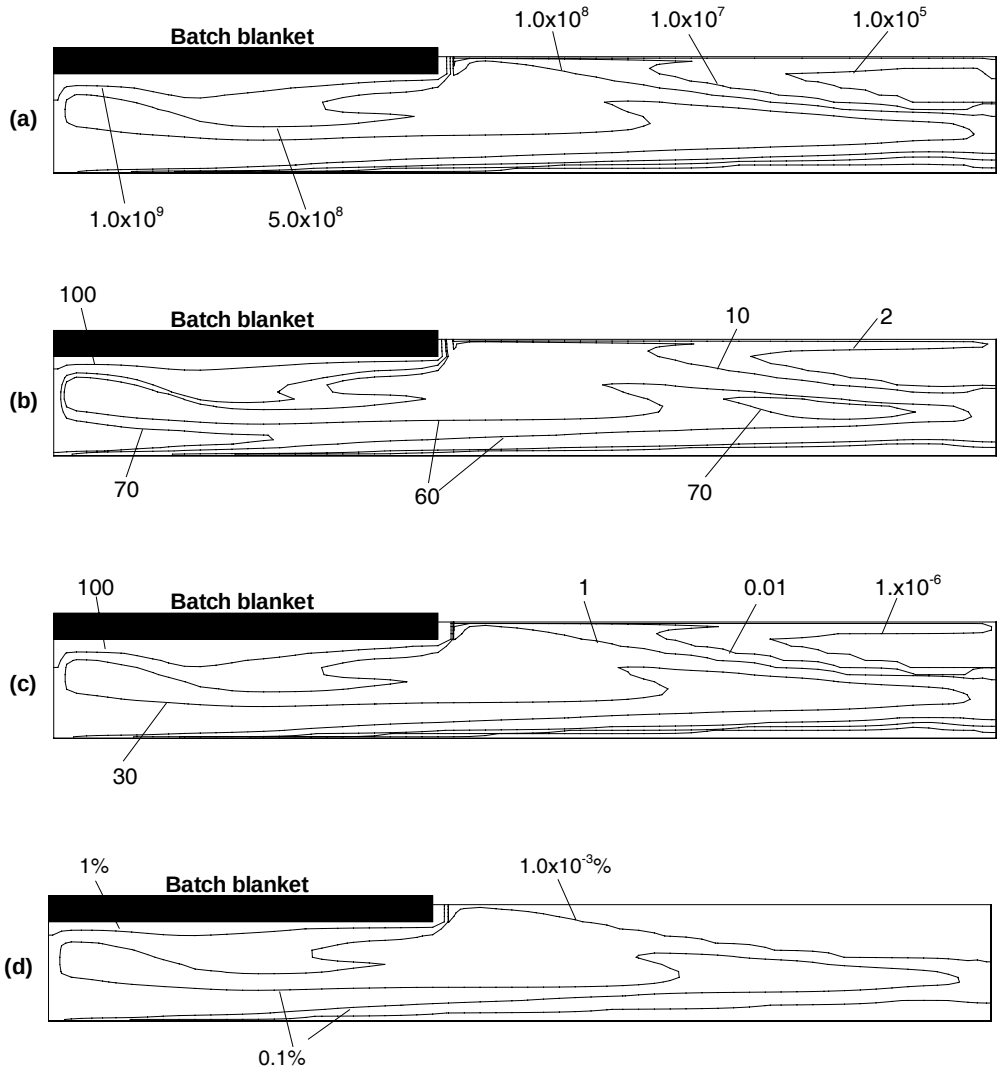

Figure 8.10. Iso-concentration lines at midplane for (a) N (in $\#/m^3$), (b) $\bar{r}$ (in μm), (c) A_i (in m^2 of interface $/m^3$ of glassmelt), (d) f_v (in m^3 of gas in bubbles $/m^3$ of glassmelt).

m^{th} order moments of the density function and in particular, the total number of bubble, the average bubble radius, the average gas molar fraction, the interfacial area concentration and the void fraction.

- Due to the small liquid velocities and the slow diffusion process, the calculation time of the current computer program is excessive and constitutes a limitation to its use. This issue could be easily addressed by parallelizing the computation of the solution of the population balance equation. Indeed, solution of the population balance equation for two different points on the initial bubble density function is currently performed successively on a single microprocessor computer even though they are independent. Therefore, they should be perfomed in parallel on a multiprocessors computer with as many microprocessors as points taken on the initial bubble density function.

- Bubble nucleation at the sand grain surface may be significant and should be modeled since oversaturation of the glassmelt with carbon dioxide and oxygen appear to be important. To do so, the density function of unmelted sand grains is needed in order to know the number of nucleation sites. It could be computed by the same method as that presented here for the bubble density function. A different expression for the growth rate $\dot{r}$ will have to be used and is already available in the literature [176, 201].

- Nucleation at the refractory walls has been neglected for the sake of simplicity. However, it could be easily accounted for by

- It shows that considering the oxygen diffusion in and out of the bubbles significantly reduce the total number of bubbles leaving the throat as well as their radius.

NOMENCLATURE

A	Parameters of the initial bubble size distribution
A_i	Liquid/gas interfacial area concentration
B	Parameters of the initial bubble size distribution
D	Diffusion coefficient
f_1	Bubble density function
f_v	Volumetric gas fraction
g	Specific gravity
M	Molecular mass
N	Total number of bubbles per unit volume of glassmelt
p_0	Atmospheric pressure
p	Pressure
r	Bubble radius
r_0	Initial bubble radius
r_min	Minimum bubble radius
$\dot{r}$	Rate of change of bubble radius
R	Universal gas constant $= 8.314 J/molK$
S	Solubility of the gas species in the molten glass
T	Temperature
t	Time
W	Glass tank width (see Figure 8.1)
w_r	Vertical upward velocity of the bubble relative to the glassmelt
$\vec{x}$	Spatial or external coordinates
x	Longitudinal location (see Figure 8.1)
x	Spanwise location (see Figure 8.1)
z	Local depth within the glassmelt (see Figure 8.1)

Greek symbols

α	Parameter
ϵ_1, ϵ_2	Arbitrarily small constants for convergence criteria

η	Parameters of the initial bubble size distribution
γ	Gas molar fraction in the bubbles
σ	Surface tension
ρ	Density
μ	Kinematic viscosity

Subscripts

$batch$	Refers to the glassmelt/batch interface
CO_2	Refers to the carbon dioxide
i	Index of the gas species
I, J, K	Refers to indices of the scalar nodes of the staggered grid
O_2	Refers to the oxygen
∞	Refers to the bulk of the glassmelt

Notation

$\bar{X}$	Average value of variable X with respect to bubble radius

9. RECOMMENDATIONS

Based on the conclusions of the work described in this document, there is still a number of very important issues that require further research attention. This chapter presents some recommendations and suggestions of future research regarding each one of the topics previously discussed.

Foam Dynamics

- Previous studies have shown that the atmosphere can have a strong influence on the foam dynamics particularly for foams generated from viscous liquids [9, 10, 13, 70]. The effect of the atmospheric conditions (chemical composition, pressure, temperature and their fluctuations) needs to be modeled and validated with carefully designed experiments. To the best of my knowledge, neither physical models nor comprehensive experimental data are available in the literature. However, such a study is of great fundamental and practical interest and would enable one to assess the feasability of controlling the foam thickness by ultrasound or by the change in the temperature or chemical composition of the atmosphere with time.

- In material and food processing, there exists a temperature gradient across the foam layer that can strongly affect physical phenomena key to the foam stability. For example, the temperature gradient results in the Gibbs-Marangoni effects that can destabilize the foam. Moreover, for liquids whose viscosity varies greatly with temperature (e.g., molten glass), the temperature gradient could strongly affects the drainage of the liquid phase in the foam, and therefore the foam stability and its transient and steady-state behaviors. However, to the best of my knowledge, neither a model nor experimental data is available in

the literature to account for the effect of the temperature gradient on the foam dynamics.

- The foam produced in large containers is rarely generated uniformly across the liquid free surface and tends to spread over regions of lower thickness. Experimental data and mathematical models for rheological properties of free foams and their dependence on the foam structure, physicochemical properties of the liquid and gas phases are needed for predicting the spreading of the foam over a liquid free surface.

- The effects of the initial liquid height and the type of gases contained in the bubbles on the foams dynamics (from the onset of foaming to the steady state conditions) remain to be explored. Particular attention should be paid to the transient rise of bubbles to the liquid free surface and to the changes in solubility and diffusion coefficient of the gas in the liquid phase.

- A consistent set of experimental data needs to be collected and used in order to further validate the theoretical model developed for predicting the superficial gas velocity for onset of foaming. This could help refine the model presented in Chapter 4 and understand the very fundamental and still unresolved question "why pure liquids do not foam?".

Radiation Characteristics of Semitransparent Media Containing Bubbles

- Refinements of the simplified model for the radiation characteristics of semitransparent media containing bubbles would consist of (1) developing an approach for calculating the scattering phase function for polyhedral bubbles, (2) explicitely accounting for change in the bubble size, shape and concentration across the foam layer, (3) accounting for the cross-correlation effects on the radiation characteristics due to collective up-rising motion of bubbles in the foam, and (4) accounting for the effect of the surfactant layer at the gas bubble/continuous condensed phase interface.

- The experimental work on radiation characteristics of semitransparent media containing bubbles needs to be extended to specimen having larger void fractions and/or smaller bubbles and/or different bubble size distributions. For larger void fraction the question of dependent vs. independent scattering should be revisited considering the fact that the thickness of the foam lamella could be of the same order of magnitude as the wavelength of incident radiation.

Generation and Transport of Bubbles in Three-Dimensional Laminar Gravity Driven Flow

- The effect of the bubbles on the velocity and temperature fields of the liquid have been neglected for the sake of simplicity. However, coupling of the model for the bubble generation and transport in three-dimensional flow with numerical codes for solving the equations of two-fluid model to account for the coupling between the liquid and the gas phases is needed.

- The calculation time of the current computer program is excessive and constitutes a limitation to its use. This issue could be easily addressed by parallelizing the computation of the solution of the population balance equation. Indeed, solution of the population balance equation for two different points on the initial bubble density function is currently performed successively on a single microprocessor computer even though they are independent. Therefore, they should be perfomed in parallel on a multiprocessors computer with as many microprocessors as points taken on the initial bubble density function.

- The effect of the bubbles on the thermophysical properties such as viscosity, specific heat, thermal conductivity, radiation characteristics of the liquid phase should be accounted for.

- The computer program for bubble transport should be used to simulate the onset of foaming, with the code for solving the bubble population balance equation, for the purpose of validating the model for the onset of foaming.

Specific Recommendation for Glass Melting Furnaces

Several recommendations can be made for the specific application of glass melting furnaces:

- Water vapor concentration in the molten glass should be computed since water vapor has a large diffusion coefficient and solubility in most glasses (see Appendix C) and since it is supplied in great amount in the combustion space by the combustion reactions in particular in modern glass melters using oxy-fuel burners where foam formation is favored due to the increase in the partial pressure of water vapor in the molten glass [13]. The bubble population balance equation should be deduced and solved accordingly, i.e., the bubble density function will have an additional variable.

- A consistent set of thermophysical properties for a given glass composition should be collected and used. In particular data for the gas solubility, diffusion coefficient are badly needed. The effect of water vapor on the glass viscosity and surface tension should be studied more thoroughly.

- The effect of bubbles on the radiation characteristics of molten glass in the spectral region between 0.2 μm and approximately 4.5 μm where most glasses are weakly absorbing should be accounted for since it can greatly affect the three-dimensional gravity driven flow. To do so the algorithm for solving the bubble density function should be coupled to that for solving the radiative transfer equation in the molten glass treating it as an absorbing, emitting, and scattering medium.

- As discussed in Chapter 7, the boundary conditions for the bubble density function at the glassmelt/refractory appear to be controversial and it is not clear wether heterogeneous nucleation takes place at the glassmelt/refractories interface. The effect of bubble nucleation at the refractory walls on the bubble density function leaving the tank through the throat should be investigated as it may strongly affect the product quality. The effect can be studied by

changing the boundary condition at the glassmelt/refractory interface. Since the physical phenomena responsible for bubble generation at the refractor walls is different from bubble entrapment in the batch, the density function, the radius and gas composition of bubbles at the refractory walls is different from that in the glassmelt below the batch. Accounting for the bubble generation at the refractory walls can be accomplished using the principle of superposition of the solution of the population balance equation. Computation could be performed by assuming that only monodispersed bubbles containing oxygen are generated at the refractory wall.

- Experimental data are needed to validate the numerical predictions. For this purpose, experimental techniques to measure the bubble density function within the glassmelt and their gas composition should be developed.

LIST OF REFERENCES

LIST OF REFERENCES

[1] D. Klempner and K. C. Frisch, *Handbook of polymeric foams and foam technology*, Hanser Publishers, Munich, 1991.

[2] A. G. Ostrogorsky and L. R. Glicksman, "Rapid, steady-state measurement of the effective diffusion coefficient of gases in closed-cell foams", *Journal of Heat Transfer*, vol. 110, pp. 500–506, 1988.

[3] A. G. Ostrogorsky and L. R. Glicksman, "Electrical analogy of gas diffusion in closed-cell foams", *Journal of Cellular Plastics*, vol. 24, pp. 215–230, 1988.

[4] J. M. Boulton-Stone and J. R. Blake, "Gas bubbles bursting at a free surface", *Journal of Fluid Mechanics*, vol. 254, pp. 437–466, 1993.

[5] B. Ozturk and R. J. Fruehan, "Effect of temperature on slag foaming", *Metallurgical and Materials Transactions B*, vol. 26B, pp. 1086–1088, 1995.

[6] J. J. Bikerman, *Foams*, Springler-Verlag, New York, 1973.

[7] C. F. Boyd and M. Di Marzo, "The behavior of a fire-protection foam exposed to radiant heating", *International Journal of Heat and Mass Transfer*, vol. 41, pp. 1719–1728, 1998.

[8] P. Gillepsie, "Protecting petrochemical storage tanks", *Fire Journal*, vol. 83, no. 3, pp. 44–48, 1989.

[9] P. R. Laimbock, *Foaming of glass melts*, PhD thesis, Technical University of Eindhoven, Eindhoven, The Netherlands, 1998.

[10] J. Kappel, R. Conradt, and H. Scholze, "Foaming behavior on glass melts", *Glastechnische Berichte*, vol. 60, no. 6, pp. 189–201, 1987.

[11] A. G. Fedorov and R. Viskanta, "Radiative transfer in a semitransparent glass foam blanket", *Physics and Chemistry of Glasses*, vol. 41, no. 3, pp. 127–135, 2000.

[12] A. G. Fedorov and R. Viskanta, "Radiative characteristics of glass foams", *Journal of the American Ceramic Society*, vol. 83, no. 11, pp. 2769–2776, 2000.

[13] A. G. Fedorov and L. Pilon, "Glass foam: formation, transport properties, and heat, mass, and radiation transfer", *Journal of Non-Crystalline Solids (in press)*, 2002.

[14] A. Bhakta and E. Ruckenstein, "Decay of standing foams: drainage, coalescence and collapse", *Advances in Colloid and Interface Science*, vol. 70, pp. 1–124, 1997.

[15] G. Narsimhan and E. Ruckenstein, "Hydrodynamics, enrichment, and collapse in foams", *Langmuir*, vol. 2, pp. 230–238, 1986.

[16] A. D. Barber and S. Hartland, "The collapse of cellular foams", *Transactions of the Institution of Chemical Engineers*, vol. 53, pp. 106–111, 1975.

[17] G. Narsimhan, "A model for unsteady state drainage of a static foam", *Journal of Food Engineering*, vol. 14, pp. 139–165, 1991.

[18] R. J. Germick, A. S. Rehill, and G. Narsimhan, "Experimental investigation of static drainage of protein stabilized foams - Comparison with model", *Journal of Food Engineering*, vol. 23, pp. 555–578, 1994.

[19] A. Bhakta and E. Ruckenstein, "Drainage of standing foam", *Langmuir*, vol. 11, pp. 1486–1492, 1995.

[20] Y. Zhang and R. J. Fruehan, "Effect of bubble size and chemical reactions on slag foaming", *Metallurgical and Materials Transactions B*, vol. 26B, pp. 803–812, 1995.

[21] Y. Zhang and R. J. Fruehan, "Effect of carbonaceous particles on slag foaming", *Metallurgical and Materials Transactions B*, vol. 26B, pp. 813–819, 1995.

[22] Y. Zhang and R. J. Fruehan, "Effect of gas type and pressure on slag foaming", *Metallurgical and Materials Transactions B*, vol. 26B, pp. 1089–1091, 1995.

[23] R. Jiang and R. J. Fruehan, "Slag foaming in bath smelting", *Metallurgical and Materials Transactions B*, vol. 22B, pp. 481–489, 1991.

[24] S-M Jung and R. J. Fruehan, "Foaming characteristics of BOF slags", *ISIJ International*, vol. 40, pp. 348–354, 2000.

[25] S. Hara, T. Takayuki, and K. Ogino, "Effect of surface viscosity on the foaminess of molten oxides", *Journal of the Iron and Steel Institute of Japan*, vol. 12, pp. 2182–2187, 1989.

[26] S. S. Ghag, P. C. Hayes, and H-G Lee, "Physical model studies on slag foaming", *ISIJ International*, vol. 38, pp. 1201–1207, 1998.

[27] S. S. Ghag, P. C. Hayes, and H-G Lee, "Model development of slag foaming", *ISIJ International*, vol. 38, pp. 1208–1215, 1998.

[28] S. S. Ghag, P. C. Hayes, and H-G Lee, "The prediction of gas residence times in foaming CaO-SiO_2-FeO", *ISIJ International*, vol. 38, pp. 1216–1224, 1998.

[29] K. Ito and R. J. Fruehan, "Study of the foaming of CaO-SiO_2-FeO slags: Part I. Foaming parameters and experimental results", *Metallurgical and Materials Transactions B*, vol. 20B, pp. 509–514, 1989.

[30] K. Ito and R. J. Fruehan, "Study of the foaming of CaO-SiO_2-FeO slags: Part II. Dimensional analysis and foaming in iron and steelmaking processes", *Metallurgical and Materials Transactions B*, vol. 20B, pp. 515–521, 1989.

[31] S. A. K. Jeelani, S. Ramaswami, and S. Hartland, "Effect of binary coalescence on steady-state height of semi-batch foams", *Transaction of the Institution of Chemical Engineers*, vol. 68, Part A, pp. 271–277, 1990.

[32] S. Hartland, J. R. Bourne, and S. Ramaswami, "A study of disproportionation effects in semi-batch foams - II. Comparison between experiment and theory", *Chemical Engineering Science*, vol. 48, pp. 1723–1733, 1993.

[33] D. B. Buruk, D. Petrovic, and J. G. Daly, "Flow regime transitions in a bubble column with a paraffin wax as the liquid medium", *Industrial and Engineering Chemistry Research*, vol. 26, pp. 1087–1092, 1987.

[34] L.Z. Pino, M. M. Yepez, A. E. Saez, and G. De Drago, "An experimental study of gas holdup in two-phase bubble columns with foaming liquids", *Chemical Engineering Communications*, vol. 89, pp. 155–175, 1990.

[35] Y. T. Shah, S. Joseph, D. N. Smith, and J. A. Ruether, "On the behavior of the gas phase in a bubble column with ethanol-water mixtures", *Industrial Engineering and Chemistry Process Design and Development*, vol. 24, pp. 1140–1148, 1985.

[36] G. B. Wallis, *One-dimensional two-phase flow*, McGraw-Hill, New York, 1969.

[37] M. U. Vera, A. Saint-Jalmes, and D. J. Durian, "Scattering optics of foams", *Applied Optics*, vol. 40, no. 24, pp. 4210–4214, 2001.

[38] J.-A. Kong, "Polarimetric passive remote sensing of ocean surface", Tech. Rep. ADA372480, Massachussets Institute of Technology, Cambridge, MA, 2000.

[39] A. Ungan, *Three dimensional numerical modeling of glass melting process*, PhD thesis, Purdue University, West Lafayette, IN, USA, 1985.

[40] D. J. Durian, "The diffusion coefficient depends on absorption", *Optics Letters*, vol. 23, pp. 1502–1504, 1998.

[41] M. U. Vera, P.-A. Lemieux, and D. J. Durian, "Angular distribution of diffusely backscattered light", *Applied Optics*, vol. 40, no. 24, pp. 4210–4214, 2001.

[42] L.R. Glicksman, M. Schuetz, and M. Sinofsky, "Radiation heat transfer in foam insulation", *International Journal of Heat and Mass Transfer*, vol. 30, pp. 187–197, 1987.

[43] M. Schuetz and L. Glicksman, "A basic study of heat transfer through foam insulation", *Journal of Cellular Plastics*, vol. 20, pp. 114–121, 1984.

[44] L.R. Glicksman, "Heat transfer and ageing of cellular foam insulation", *Cellular Polymers*, vol. 10 No. 4, pp. 276–293, 1991.

[45] L.R. Glicksman, A.L. Marge, and J.D. Moreno, "Radiation heat transfer in cellular foam insulation", in *HTD Vol. 203, Developements in Radiative Heat Transfer*, ASME, New-York, 1997, pp. 45–54.

[46] M. Rubin, "Optical properties of soda-lime silicate", *Solar Energy Materials*, vol. 12, pp. 275–288, 1985.

[47] C.Z. Tan and J. Arndt, "Refractive index, optical dispersion, and group velocity of infrared wave in silica glass", *Journal of Physics and Chemistry of Solids*, vol. 62, pp. 1087–1092, 2001.

[48] G. Narsimhan and E. Ruckenstein, "Effect of bubble size distribution on the enrichment and collapse in foams", *Langmuir*, vol. 2, pp. 494–508, 1986.

[49] K. Malysa, "Wet foams: formation, properties and mechanism of stability", *Advances in Colloid and Interface Science*, vol. 40, pp. 37–83, 1992.

[50] S. Hutzler, D. Weaire, and S. Shah, "Bubble sorting in a foam under forced drainage", *Philosophical Magazine Letters*, vol. 80, no. 1, pp. 41–48, 2000.

[51] V. V. Krotov, "Theory of syneresis and foams and concentrated emulsions. 3. local equation of syneresis and formulation of boundary conditions", *Colloid Journal of the USSR*, vol. 43, pp. 33–39, 1981.

[52] N. F. Djabbarah and D. T. Wasan, "Foam stability: the effect of surface rheological properties on the lamella rupture", *AIChE Journal*, vol. 31, no. 6, pp. 1041–1043, 1985.

[53] P. Hrma, "Model for a steady state foam blanket", *Journal of Colloid and Interface Science*, vol. 134, no. 1, pp. 161–168, 1990.

[54] S. Hartland and A. D. Barber, "A model for cellular foam", *Transactions of the Institution of Chemical Engineers*, vol. 52, pp. 43–52, 1974.

[55] D. Desai and R. Kumar, "Flow through a plateau border of cellular foam", *Chemical Engineering Science*, vol. 37, no. 9, pp. 1361–1370, 1982.

[56] A. Monsalve and R. S. Schechter, "The stability of foams: dependence of observation on the bubble size distribution", *Journal of Colloid and Interface Science*, vol. 97, no. 2, pp. 327–335, 1984.

[57] S. Ramaswami, S. Hartland, and J. R. Bourne, "A study of disproportionation effects in semi-batch foams - I. Simulation of bubble size distribution", *Chemical Engineering Science*, vol. 48, pp. 1709–1721, 1993.

[58] D. Ramkrishna, *Population balances*, Academic Press, San Diego, CA, 2000.

[59] D. Desai and R. Kumar, "Liquid holdup in semi-batch cellular foams", *Chemical Engineering Science*, vol. 38, no. 9, pp. 1525–1534, 1983.

[60] M. Tenenbaun and H. Pollar, *Ordinary differential equations*, Harper & Row, New York, NY, 1963.

[61] R.E. Pattle, "The control of foaming. II. The breakdown mechanisms and volume of dynamic foams", *Journal of the Society of Chemical Industry*, vol. 69, pp. 368–371, 1950.

[62] J. J. Bikerman, "The unit of foaminess", *Transactions of the Faraday Society*, vol. 38, pp. 634–638, 1938.

[63] R. McElroy, *Air release from mineral oils*, PhD thesis, Department of Pure and Applied Chemistry, Strathclyde University, 1978.

[64] Z. Lin and R. I. L. Guthrie, "A model for slag foaming for the in-bath smelting process", *Iron and Steelmaker*, vol. 22, no. 5, pp. 67–73, 1995.

[65] R. C. Watkins, "An improved foam test for lubricating oils", *Journal of the Institute of Petroleum*, pp. 106–113, 1973.

[66] S. Ross and Y. Suzin, "Measurement of dynamic foam stability", *Langmuir*, vol. 1, no. 1, pp. 145–149, 1985.

[67] M-Y. Zhu and Du Sichen, "Modeling study of slag foaming phenomenon", *Steel Research*, vol. 71, no. 3, pp. 76–82, 2000.

[68] K. C. Mills and B. J. Keene, "Physical properties of BOS slags", *International Materials Reviews*, vol. 32, no. 1-2, pp. 1–120, 1987.

[69] Y. Ogawa, D. Huin, H. Gaye, and N. Tokumitsu, "Physical model of slag faoming", *ISIJ International*, vol. 33, no. 1, pp. 224–232, 1993.

[70] C. F. Cooper and J. A. Kitchener, "The foaming of molten silicates", *Journal of the Iron and Steel Institute*, pp. 48–55, Sept., 1959.

[71] M. Cable, C. G. Rasul, and J. Savage, "Laboratory investigation of foaming and reboil in soda-lime-silicate melts", *Glass Technology*, vol. 9, no. 2, pp. 25–31, 1968.

[72] K. Wu, S. Chu, W. Qian, and Q. Niu, "Investigation into rheological characteristic and foaming behaviour of molten slags", *Steel Research*, vol. 70, no. 7, pp. 248–251, 1999.

[73] M. Ishii, "One-dimensional drift-flux model and constitutive equations for relative motion between phases in various two-phase flow regimes", *Argonne National Laboratory Report ANL-77-47*, 1977.

[74] P.C. Duineveld, "Bouncing and coalescence of bubble pairs rising at high reynolds number in pure water or aqueous surfactant solutions.", *Applied Scientific Research*, vol. 58, pp. 409–439, 1998.

[75] A. K. Chesters, "The modelling of coalescence processes in fluid-liquid dispersions: a review of current understanding", *Transactions of the Institution of Chemical Engineers*, vol. 69 - Part A, pp. 259–270, 1991.

[76] R. D. Kirkpatrick and M. J. Lockett, "The influence of approach velocity on bubble coalescence", *Chemical Engineering Science*, vol. 29, pp. 2363–2373, 1974.

[77] J. W. Kim and W. K. Lee, "Coalescence behavior of two bubbles in stagnant liquids", *Journal of Chemical Engineering of Japan*, vol. 20, pp. 448–453, 1987.

[78] M. Ishii and N. Zuber, "Drag force and relative velocity in bubbly, droplet or particulate flows.", *AIChE Journal*, vol. 25, no. 5, pp. 843–855, 1979.

[79] J. Guitian and D. Joseph, "How bubbly mixture foam and foam control using fluidized bed.", *International Journal of Multiphase Flow*, vol. 24, no. 1, pp. 1–16, 1998.

[80] M. Ishii and T. C. Chawla, "Local drag laws in dispersed two-phase flow", *Argonne National Laboratory Report ANL-79-105, NUREG/CR-1230*, 1979.

[81] R. Clift, J. R. Grace, and M. E. Weber, *Bubbles, drops, and particles*, Academic Press, New York, 1978.

[82] A. J. De Vries, "Morphology, coalescence, and size distribution of foam bubbles", in *Adsorptive Bubble Separation Techniques*, R. Lemlich, Ed., vol. 1, pp. 7–31. Academic Press, New York, NY, 1972.

[83] J. J. M. Magnaudet, "The forces acting on bubbles and rigid particles", in *ASME Fluids Engineering Division Summer Meeting, FEDSM'97, Part 16, Vancouver, Canada*, June 22-26 1997, vol. 16, pp. 1–7.

[84] M. F. Modest, *Radiative heat transfer*, McGraw-Hill, New York, NY, 1993.

[85] R. Viskanta and M. P. Mengüç, "Radiative transfer in combustion system", *Progress in Energy and Combustion Sciences*, vol. 13, pp. 97–160, 1987.

[86] R. G. C. Beerkens, "The role of gases in glass melting processes", *Glastechnische Berichte*, vol. 71, no. 12, pp. 369–380, 1995.

[87] M. Abramowitz and I. A. Stegun, *Handbook of mathematical functions*, Dover Publications, New York, 1965.

[88] H. C. van de Hulst, *Light scattering by small particles*, John Wiley & Sons, New York, NY, 1957.

[89] D. Deirmendjian, *Electromagnetic scattering on spherical polydispersions*, Elsevier, New York, NY, 1969.

[90] C. L. Tien and B. L. Drolen, "Thermal radiation in particulate media with dependent and independent scattering", in *Annual Review of Numerical Fluid Mechanics and Heat Transfer*, T.C. Chawla, Ed., vol. 1, pp. 1–32. Hemisphere, New York, NY, 1987.

[91] E. Franses, *Chapter 2. Interfacial phenomena: principles, data, and applications*, Purdue University - Class Notes ChE 668, 2000.

[92] J. Kuhn, H.-P. Ebert, M.C. Arduini-Schuster, D. Büttner, and J. Fricke, "Thermal transport in polystyrene and polyurethane foam insulations", *International Journal of Heat and Mass Transfer*, vol. 35, no. 7, pp. 1795–1801, 1992.

[93] G. Eeckhaut and A. Cunningham, "The elimination of radiative heat transfer in fine celled pu rigid foams", *Journal of Cellular Plastics*, vol. 32, pp. 528–552, 1996.

[94] F. P. Incropera and D. P. DeWitt, *Fundamentals of heat and mass transfer*, John Wiley & Sons, New York, Fourth edition, 1996.

[95] L.A. Dombrovsky, *Radiation heat transfer in disperse systems*, Begell House, New York, NY, 1996.

[96] M. J. Hale and M. S. Bohn, "Measurement of the radiative transport properties of reticulated alumina foams", in *Proceedings of the ASME/ASES Joint Solar Engineering Conference*, A. Kirkpatrick and W. Worek, Eds., ASME, New York, 1993, pp. 507–515.

[97] T. J. Hendricks and J. R. Howell, "Absorption/scattering coefficients and scattering phase functions in reticulated porous ceramics", *Journal of Heat Transfer*, vol. 118, pp. 79–87, 1996.

[98] D. Baillis, M. Raynaud, and J.-F. Sacadura, "Determination of spectral radiative properties of open-cell foam: model validation", *Journal of Thermophysics and Heat Transfer*, vol. 14, no. 2, pp. 137–143, 2000.

[99] D. Baillis, M. Arduini-Schuster, and J.-F. Sacadura, "Identification of spectral radiative properties of polyurethane foam from hemispherical and bi-directional transmittance and reflectance measurements", in *Proceedings of the 3rd International Symposium on Radiation Transfer*, M. P. Mengüc and N. Selcuk, Eds. , Begell House, Inc., New York, 2001, pp. 474–482.

[100] D. Baillis and J.-F. Sacadura, "Identification of polyurethane foam radiative properties - influence of transmittance measurements number", *Journal of Thermophysics and Heat Transfer*, vol. 16, no. 1, pp. 200–206, 2002.

[101] L. M. Moura, *Identification des propriétés radiatives des matèriaux semi-transparent diffusants en situation de non-symmetrie azimutale du champ radiatif*, PhD thesis, Institut National des Sciences Appliquées de Lyon, France, Lyon, France, 1998.

[102] W. L. Dunn, "Inverse Monte Carlo analysis", *Journal of Computational Physics*, vol. 41, pp. 154–166, 1981.

[103] S. Subramaniam and M. P. Mengüç, "Solution of the inverse radiation problem for inhomogeneous and anisotropically scattering media using a Monte Carlo technique", *International Journal of Heat and Mass Transfer*, vol. 14, pp. 253–266, 1991.

[104] Take-Uchi, Y. Kurosaki, T. Kashiwagi, and J. Yamada, "Determination of radiation properties of porous media by measuring emission", *JSME International Journal*, vol. 31, no. 3, pp. 581–585, 1988.

[105] J. Yamada and Y. Kurosaki, "Estimation of a radiative property of scattering and absorbing media", *International Journal of Thermophysics*, vol. 18, no. 2, pp. 547–556, 1997.

[106] D. Doermann, *Modélisation des transferts thermiques dans des matériaux semi-transparents de type mousse à pores ouverts et prédiction des propriétés radiatives*, PhD thesis, Institut National des Sciences Appliquées de Lyon, France, 1995.

[107] V.P. Nicolau, *Identification des propriétés radiatives des matèriaux semi-transparent diffusants*, PhD thesis, Institut National des Sciences Appliquées de Lyon, France, 1994, (94 ISAL 0001.

[108] J.V. Beck and K. J. Arnold, *Parameter estimation in engineering and science*, John Wiley & Sons, New York, NY, 1977.

[109] R. Siegel and J.R. Howell, *Thermal radiation heat transfer, Third Edition*, Hemisphere Publishing Co., New York, NY, 1992.

[110] S. E. Egan and T. W. Hilgeman, *Optical properties of inhomogeneous materials: applications to geology, astronomy, chemistry and engineering*, Academic Press, New York, 1979.

[111] S. E. Orchard, "Reflection and transmission of light by diffusing suspensions", *Journal of the Optical Society of America*, vol. 59, no. 12, pp. 1584–1597, 1969.

[112] W.S. Rodney and R.J. Spindler, "Index of refraction of fused quartz for ultraviolet, visible, and infrared wavelengths", *Journal of the Optical Society of America*, vol. 44, No. 9, pp. 677–679, 1954.

[113] I.H. Malitson, "Interspecimen comparison of the refractive index of fused silica", *Journal of the Optical Society of America*, vol. 55, No. 10, pp. 1205–1209, 1965.

[114] V.A. Petrov and S.V. Stepanov, "Radiation characteristics of quartz glasses spectral radiating power", *Teplofizika Vysokikh Temperatur*, vol. 13, no. 2, pp. 335–345, 1975.

[115] C. Boeckner, "A method of obtaining the optical constants of metallically reflecting substances in the infrared", *Journal of the Optical Society of America*, vol. 19, pp. 7–15, 1929.

[116] O.P. Girin, Y.N. Kondratev, and E.L. Raaben, "Optical constants and spectral microcharacteristics of NaO_2-SiO_2 glasses in the IR region of the spectrum", *Optics and Spectroscopy*, vol. 29, pp. 397–403, 1970.

[117] J.H. Wray and J.T. Neu, "Refractive index of several glasses as a function of wavelength and temperature", *Journal of the Optical Society of America*, vol. 59, no. 6, pp. 774–776, 1969.

[118] V.M. Zolotarev, "The optical constants of amorphous sio2 and geo2 in the valence band region", *Optics and Spectroscopy*, vol. 29, pp. 34–37, 1970.

[119] S.I. Popova, T.S. Tolstykh, and V.T. Vorobev, "Optical characteristics of amorphous quartz in the 1400-200 cm^{-1} region", *Optics and Spectroscopy*, vol. 33, pp. 444–445, 1972.

[120] C.Z. Tan and J. Arndt, "Temperature dependence of refractive index of glass SiO_2 in the infrared wavelength range", *Journal of Physics and Chemistry of Solids*, vol. 61, pp. 1315–1320, 2000.

[121] C.Z. Tan, "Determination of refractive index of silica glass for infrared wavelengths by ir spectroscopy", *Journal of Non-Crystalline Solids*, vol. 223, pp. 158–163, 1998.

[122] V.G. Plotnichenko, V.O. Sokolov, and E.M. Dianov, "Hydroxyl groups in high-purity silica glass", *Journal of Non-Crystalline Solids*, pp. 186–194, 2000.

[123] E.C. Beder, C.D. Bass, and W.L. Shackleford, "Transmittivity and absorption of fused quartz between 0.2 and 3.5 μm from room temperature to 1500^{o}C", *Journal of the American Ceramic Society*, vol. 10, no. 10, pp. 2263–2268, 1971.

[124] Y.S. Touloukian and D.P. DeWitt, *Thermal Properties of Matter, Radiative, Volume 8 - Thermal Radiative Properties Nonmetallic Solids*, IFI/Plenum, New York, NY, 1972.

[125] A. V. Dvurechensky, V.A. Petrov, and V. Yu Reznik, "Spectral emissivity and absorption coefficient of silica glass at extremely high temperatures in the semitransparent region", *Infrared Physics*, vol. 19, pp. 465–469, 1979.

[126] M. Raynaud, "Strategy for the experimental design and the estimation of parameters", *High Temperatures-High Pressures*, vol. 31, pp. 1–15, 1999.

[127] Osram Sylvania R. Marlor, ", *Personal Communication*, July 2002.

[128] L.A. Dombrovsky, "Quartz-fiber thermal insulation: infrared radiative properties and calculation of radiative-conductive heat transfer", *Journal of Heat Transfer*, vol. 118, pp. 408–414, 1996.

[129] B. Balkanli and A. Ungan, "Numerical simulation of bubble behaviour in glass melting tanks. Part 1. under ideal conditions", *Glass Technology*, vol. 37, no. 1, pp. 29–34, 1996.

[130] J. M Hermans and A. C. Verbeeks, "Gas exchange between bubbles and molten glass", *Glastechnische Berichte*, vol. 67, no. 2, pp. 49–51, 1994.

[131] E. L. Swarts, "Bubble generation at glass/refractory interfaces: A review of fundamental mechanisms and practical considerations", *Glastechnische Berichte*, vol. 65, no. 4, pp. 87–92, 1992.

[132] A. Ungan and R. Viskanta, "Melting behavior of continuously charged loose batch blankets in glass melting furnaces", *Glastechnische Berichte*, vol. 59, no. 10, pp. 279–291, 1986.

[133] S. Kawachi and Y. Kawase, "Evaluation of bubble removing performance in a TV glass furnace. Part 1. mathematical formulation", *Glastechnische Berichte*, vol. 71, no. 4, pp. 83–91, 1998.

[134] E. Itoh, H. Yoshikawa, H. Miura, and Y. Kawase, "A quasi-stationary model for bubble behaviour in glass melts with refining reactions", *Glass Technology*, vol. 38, no. 4, pp. 134–140, 1997.

[135] L. Nemec, "The behaviour of bubbles in glass melts. Part 1. bubble size controlled by diffusion", *Glass Technology*, vol. 21, no. 3, pp. 134–138, 1980.

[136] R. G. C Beerkens and H. De Wall, "Mechanism of oxygen diffusion in glassmelts containing variable-valence ions", *Journal of the American Ceramic Society*, vol. 73, no. 7, pp. 1857–1861, 1990.

[137] H. Yoshikawa and Y. Kawase, "Significance of redox reactions in glass refining processes", *Glastechnische Berichte*, vol. 70, no. 2, pp. 31–40, 1997.

[138] H. Yoshikawa, H. Miura, and Y. Kawase, "Dissolution of bubbles in glass-melts with equilibrium redox reactions: approximations for a moving bubble boundary", *Journal of Materials Science*, vol. 33, no. 10, pp. 2701–2707, 1998.

[139] J. E. Shelby, *Handbook of gas diffusion in solids and melts*, ASM International, Materials Park, OH, 1996.

[140] M. Cable and D. Martlew, "The dissolution of silica in melts containing sodium carbonate, sodium sulphate, and silica", *Glass Technology*, vol. 37, no. 4, pp. 137–142, 1996.

[141] J. Shell, "Representative video and operating conditions of the Techneglas furnace C", *Personal Communication*, July 1999.

[142] M. C. Weinberg, P. I. K. Onorato, and D. R. Uhlmann, "Behavior of bubles in glassmelts: I, dissolution of a stationary bubble containing a single gas", *Journal of the American Ceramic Society*, vol. 63, pp. 175–180, 1980.

[143] L. Nemec, "Diffusion-controlled dissolving of water vapor bubbles in molten glass", *Glass Technology*, vol. 10, pp. 176–181, 1969.

[144] M. Cable and J.R. Frade, "Theoretical analysis of the dissolution of multicomponent gas bubbles", *Glastechnische Berichte*, vol. 60, no. 11, pp. 355–362, 1987.

[145] M. C. Weinberg, P. I. K. Onorato, and D. R. Uhlmann, "Behavior of bubles in glassmelts: II, dissolution of a stationary bubble containing a diffusing and a non-diffusing gas", *Journal of the American Ceramic Society*, vol. 63, pp. 435–438, 1980.

[146] P. I. K. Onorato, M. C. Weinberg, and D. R. Uhlmann, "Behavior of bubles in glassmelts: III, dissolution and growth of a rising bubble containing a diffusing a single gas", *Journal of the American Ceramic Society*, vol. 64, pp. 676–682, 1981.

[147] E. Itoh, H. Yoshikawa, and Y. Kawase, "Modeling of bubble removal from glassmelts at fining temperatures", *Glastechnische Berichte*, vol. 70, no. 1, pp. 8–16, 1997.

[148] J. I. Ramos, "Behavior of multicomponent gas bubbles in glass melts", *Journal of the American Ceramic Society*, vol. 69, no. 2, pp. 149–154, 1986.

[149] B. Balkanli and A. Ungan, "Numerical simulation of bubble behaviour in glass melting tanks. Part 3. bubble trajectories", *Glass Technology*, vol. 37, no. 4, pp. 137–142, 1996.

[150] S. Kawachi and Y. Kawase, "Evaluation of bubble removing performance in a TV glass furnace. Part 2. verification using real furnace data", *Glastechnische Berichte*, vol. 71, no. 5, pp. 111–119, 1998.

[151] S. Kawachi and M. Kato, "Evaluation of reaction rate of refining agents", *Glastechnische Berichte*, vol. 72, no. 6, pp. 182–187, 1999.

[152] A. Ungan, W.H. Turner, and R. Viskanta, "Effect of gas bubbles on three-dimensional circulation in a glass melting tank", *Glastechnische Berichte*, vol. 56K, pp. 125–129, 1983.

[153] O. T. Roi, G. Nölle Seidel, and D. Höhne, "Modeling of bubble population in glass melts", *Glastechnische Berichte*, vol. 67, no. 10, pp. 263–271, 1994.

[154] B. Balkanli and A. Ungan, "Numerical simulation of bubble behaviour in glass melting tanks. Part 4. bubble number density distribution", *Glass Technology*, vol. 3, no. 5, pp. 164–168, 1996.

[155] S. Kumar and D. Ramkrishna, "On the solution of population balance equation by discretization - III nucleation, growth, and aggregation of particles", *Chemical Engineering Science*, vol. 52, no. 4, pp. 4659–4679, 1997.

[156] M. Ishii, *Thermo-fluid dynamics theory of two-phase flow*, Eyrolles, Paris, 1975.

[157] R.T. Lahey and D.A. Drew, "On the development of multidimensional two-fluid models for vapor/liquid two-phase flows", *Chemical Engineering Communications*, vol. 118, pp. 125–139, 1992.

[158] P.M. Carrica, F.J. Bonetto, D.A. Drew, and R.T. Lahey Jr., "The interaction of background ocean air bubbles with a surface ship", *International Journal for Numerical Methods in Fluids*, vol. 28, pp. 571–600, 1998.

[159] M. B. King, *Phase equilibrium in mixtures*, Pergamon Press, Oxford, 1969.

[160] R. Pyare, S. P. Singh, A. Singh, and P. Nath, "The As^{3+}-As^{5+} equilibrium in borate and silicate glasses", *Physics and Chemistry of Glasses*, vol. 23, no. 5, pp. 158–168, 1982.

[161] B. Balkanli and A. Ungan, "Numerical simulation of bubble behaviour in glass melting tanks. Part 2. gas concentration", *Glass Technology*, vol. 37, no. 3, pp. 101–105, 1996.

[162] J.-M. Rousseaux, C. Vial, H. Muhr, and E. Plasari, "CFD simulation of precipitation in the sliding-surface mixing device", *Chemical Engineering Science*, vol. 56, pp. 1677–1685, 2001.

[163] V. G. Levich, *Physicochemical hydrodynamics*, Englewood Cliffs, Prentice-Hall, NJ, 1962.

[164] E.M. Hornyak and M.C. Weinberg, "Velocity of a freely rising gas bubble in a soda-lime silicate glass melt", *Communications of the American Ceramic Society*, vol. 67, no. 11, pp. C244–246, 1984.

[165] R. B. Bird, W.E. Stewart, and E. N. Lightfoot, *Transport Phenomena*, John Wiley & Sons, New York, 1960.

[166] I. M. Klotz and R. M. Rosenberg, *Chemical thermodynamics*, Krieger Publishing Company, Malabar, FL, 1991.

[167] A. Ungan and R. Viskanta, "Three-dimensional numerical modeling of circulation and heat transfer in a glass melting tank. Part. 1 mathematical formulation", *Glastechnische Berichte*, vol. 60, no. 3, pp. 71–78, 1987.

[168] A. Ungan and R. Viskanta, "Three-dimensional numerical modeling of circulation and heat transfer in a glass melting tank. Part. 2 sample simulations", *Glastechnische Berichte*, vol. 60, no. 4, pp. 115–124, 1987.

[169] R. Viskanta, "Review of three-dimensional mathematical modeling of glass melting", *Journal of Non-Crystalline Solids*, vol. 177, pp. 347–362, 1994.

[170] L. Pilon, G. Zhao, and R. Viskanta, "Three-dimensional flow and thermal structures in glass melting furnaces. Part I. Effects of the heat flux distribution", *Glass Science and Technology*, vol. 75, no. 2, pp. 55–68, 2002.

[171] L. Pilon, G. Zhao, and R. Viskanta, "Three-dimensional flow and thermal structures in glass melting furnaces. Part II. Effects of the presence of batch and bubbles", *Glass Science and Technology*, vol. 75, no. 3, pp. 115–124, 2002.

[172] D. Ramkrishna, "The status of population balances", *Review in Chemical Engineering*, vol. 3, no. 1, pp. 49–95, 1985.

[173] L. Nemec, "Refining in the glassmelting process", *Journal of the American Ceramic Society*, vol. 60, no. 9-10, pp. 436–440, 1977.

[174] M. Cable and C. G. Rasul, "Spontaneous bubble formation in silicate melts at high temperatures: II, effect of we atmospheres and behavior of mixed alkali glasses", *Journal of the American Ceramic Society*, vol. 50, no. 10, pp. 528–531, 1967.

[175] O. T. Roi, G. Nölle Seidel, and D. Höhne, "Formation and behavior of bubble curtains in glass melts", *Glastechnische Berichte*, vol. 68, no. 7, pp. 222–227, 1995.

[176] A. Ungan, R. U. Payli, and B. Balkanli, "Numerical model of polydispersed silica grain dissolution in glass melting furnaces", *Journal of the American Ceramic Society*, vol. 77, no. 7, pp. 1921–1927, 1994.

[177] M. Varady and A.G. Fedorov, "Combined conduction and radiation in glass foams", *ASME Journal of Heat Transfer*, 2002 , (in press).

[178] M. Varady and A. G. Fedorov, "Combined conduction and radiation in glass foams", in *International Mechanical Engineering Congress & Exposition IMECE'01, New York City*. ASME, November 2001.

[179] S. Patankar, *Numerical heat transfer and fluid flow*, Hemisphere, Washington, DC, 1980.

[180] R.W. Fox and A.T. McDonald, *Introduction to fluid mechanics*, John Wiley & Sons, New York, NY, Fifth edition, 1998.

[181] D.L. Marcum and J.D. Hoffman, "Calculation of three-dimensional flowfields by the unsteady method of characteristics", *AIAA Journal*, vol. 23, no. 10, pp. 1497–1505, 1985.

[182] J. D. Hoffman, *Numerical methods for engineers and scientists*, McGraw Hill, New York, NY, 1998.

[183] S. Kawachi and Y. Iwatsubo, "Diagnosis and treatment of bubbles in glass production using a numerical simulator", *Glastechnische Berichte*, vol. 72, no. 7, pp. 207–213, 1999.

[184] H. Scholze, *Glass nature, structure and properties, 3rd. Edition*, Springer-Verlag, Berlin, 1991.

[185] A. Dietzel, "Praktische Bedeutung von Berechnung der Oberflächenspannung von gläsern, Glasuren und Emails", *Sprechsaal*, vol. 75, pp. 82–85, 1942.

[186] N. M. Parikh, "Effect of atmosphere on surface tension of glass", *Journal of the American Ceramic Society*, vol. 41, pp. 18–22, 1958.

[187] R. H. Doremus, *Glass science*, John Wiley & Sons, New York, NY, 1994.

[188] N. P. Bansal and R. H. Doremus, *Handbook of glass properties*, Academic Press, Inc., 1986.

[189] R. H. Doremus, "Diffusion of oxygen from contracting bubbles in molten glass", *Journal of the American Ceramic Society*, vol. 43, pp. 655–661, 1960.

[190] R. Terai and Y. Oishi, "Self-diffusion of oxygen in soda-lime silicate glass", *Glastechnische Berichte*, vol. 50, pp. 68–73, 1977.

[191] L. Nemec and M. Mühlbauer, "Verhalten von gasblasen in der glasschmelze bei konstanter temperatur", *Glastechnische Berichte*, vol. 54, pp. 99–108, 1981.

[192] M. Cable, "A study of refining. Part 2. Mechanisms of refining", *Glass Technology*, vol. 2, no. 2, pp. 60–70, 1961.

[193] C. Madivate, F. Müller, and W. Wilsmann, "Calculation of the theoretical energy requirement for melting technical silicate glasses", *Journal of the American Ceramic Society*, vol. 81, pp. 3300–3306, 1998.

[194] C. Madivate, "Calculation of the theoretical energy requirement for melting technical silicate glasses", *Journal of the American Ceramic Society*, vol. 81, pp. 3300–3306, 1998.

[195] Y. Zhiqiang and Z. Zhihao, "Basic flow pattern and its variation in different types of glass tank furnaces", *Glastechnische Berichte*, vol. 70, pp. 165–172, 1997.

[196] M. Cable and A. A. Naqvi, "The refining of a soda-lime-silica glass with antimony", *Glass Technology*, vol. 16, no. 1, pp. 2–11, 1975.

[197] J. Mukerji, A. K. Nandi, and K.D. Sharma, "Reaction in container glass batch", *Ceramic Bulletin*, vol. 59, pp. 790–793, 1980.

[198] F. Kramer, "Gasprofilmessugen zur bestimmung der gasabgabe beim glasschmeltprozeß", *Glastechnische Berichte*, vol. 53, no. 7, pp. 177–188, 1980.

[199] H. Akima, "A method of bivariate interpolation and smooth surface fitting for values given at irregularly distributed points", *ACM Transactions on Mathematical Software*, vol. 4, no. 2, pp. 148–159, 1978.

[200] H. Akima, "On estimating partial derivatives for bivariate interpolation of scattered data", *Rocky Mountain Journal of Mathematics*, vol. 14, pp. 41–52, 1984.

[201] M. K. Choudhary, "Dissolution of polydisperse silica grains in glass melts - analysis", *Journal of the American Ceramic Society*, vol. 73, pp. 3053–3058, 1990.

[202] A. G. Ostrogorsky and L. R. Glicksman, "Aging of polyurethane foams", *International Journal of Heat and Mass Transfer*, vol. 29, no. 8, pp. 1169–1176, 1986.

[203] D. A. Brandreth, "Insulation foam aging - a review of the relevant physical phenomena", in *Improved Thermal Insulation: Problems and Perspectives*, D. A. Brandreth, Ed., Lancaster, PA, 1997, Technomic Pub., pp. 165–173.

[204] G. M. R. du Cauzé de Nazelle, G. C. J. Bart, A. J. Damners, and A Cunningham, "A fundamental characterization of the ageing of polyurethane rigid foam", in *International Workshop on Long-Term Thermal Performance of Cellular Platics*, Huntsville, Ontario, Canada, Sept. 1989.

[205] I. R. Shankland, "Diffusion of gases in closed-cell foams: a comparison of experiment with theory", in *Annual Technical Conference ANTEC '86*, Boston, MA, 1986, Society of Plastics Engineers, pp. 34–37.

[206] M. C. Page and L. R. Glicksman, "Measurements of diffusion coefficients of alternate blowing agents in closed cell foam insulation", *Journal of Cellular Plastics*, vol. 28, pp. 268–283, 1992.

[207] Y. Fan and E. Kokko, "Measurement of gaseous diffusion within zero ODP cellular plastic insulation", *Journal of Cellular Plastics*, vol. 33, pp. 72–90, 1997.

[208] I. R. Shankland, "Measurement of gas diffusion in closed-cell foams", in *Insulation Materials: Testing and Applications, ASTM STP 1030*, D. L. McElroy and J. F. Kimpflen, Eds., Philadelphia, PA, 1990, American Society for Testing and Materials, pp. 174–188.

[209] D. W. Reitz, M. A. Schuetz, and L.R. Glicksman, "A basic of aging of foam insulation", *Journal of Cellular Plastics*, vol. 20, pp. 104–113, 1984.

[210] S. Alsoy, "Modeling of diffusion in closed cell polymeric foams", *Journal of Cellular Plastics*, vol. 35, pp. 247–271, 1999.

[211] G. C. J. Bart and G. M. R. du Cauzé de Nazelle, "Certification of the thermal conductivity aging of PUR foam", *Journal of Cellular Plastics*, vol. 29, pp. 29–42, 1993.

[212] G. C. J. Bart, "Comments on a paper in Journal of Cellular Plastics, vol. 29, 1993, pp.29-42", *Personal Communication*, 2000.

[213] J. Brandrup, E. H. Immergut, and Eds. E. A. Grulke, *Polymer handbook, Fourth edition*, John Wiley & Sons, New York, 1999.

[214] G. P. Mitilas and M. K. Kumaran, "Methods to calculate gas diffusion coefficients of cellular plastic insulation from experimental data on gas absorption", *Journal of Thermal Insulation*, vol. 14, pp. 342–357, 1991.

[215] B. J. Briscoe and T. Savvas, "Gas diffusion in dense poly(ethylene) foams", *Advances in Polymer Technology*, vol. 17, no. 2, pp. 87–106, 1998.

[216] W. A Kaplan and R. L. Tabor, "The effect of polymer structure on the gas permeability of model polyurethanes", *Journal of Cellular Plastics*, vol. 30, pp. 242–272, 1994.

[217] M. C. Page, "*Effects of alternate blowing agents on the aging of closed-cell foam insulation*", Master's thesis, Department of Mechanical Engineering, Massachusetts Institute of Technology, Cambridge, MA, 1991.

[218] E. Kokko, "Comments on a paper in Journal of Cellular Plastics, vol. 33, 1997, pp.72-90", *Personal Communication*, 1999.

[219] M. Svantröm, O. Ramnäs, M. Olsson, and U. Jarfelt, "Determination of effective diffusion coefficients in rigid polyurethane foam", *Cellular Polymers*, vol. 16, no. 3, pp. 182–193, 1997.

[220] J. R. Booth and D. Bhattarcharjee, "The effective diffusivity of cyclopentane and n-pentane in PU and PUIR foams by thin-slice gravimetric analysis", *Journal of Thermal Insulation and Building Envelops*, vol. 20, pp. 339–349, 1997.

[221] J. R. Booth, "Some factors affecting the long-term thermal insulating performance of extruded polystyrene foams", in *Insulation Materials: Testing and Applications Vol. 2, ASTM STP 1116*, R.S. Graves and D. C. Wysocki, Eds., Philadelphia, PA, 1991, American Society for Testing and Materials, pp. 1857–1861.

[222] C. L. Babcock, *Silicate glass technology methods*, John Wiley & Sons, New York, 1977.

[223] M. Coenen, "Dichte von ,,schlierengläsern bei hohen temperaturen", *Glastechnische Berichte*, vol. 39, pp. 81–89, 1966.

[224] T. Lakatos, L.-G. Johansson, and B. Simmingsköld, "Viscosity temperature relations in the glass system SiO_2-Al_2O_3-Na_2O-K_2O-CaO-MgO in the composition range of technical glasses.", *Glass Technology*, vol. 13, pp. 88–95, 1972.

[225] A. Dietzel and E. Wegner, "Wirkung von Schwefelverbindungen auf Dieoberflächenspannung von Emails", *Mitt. Ver. dtsch emailfachl*, vol. 2, pp. 13–14, 1954.

[226] D. E. Sharp and L. B. Ginther, "Effect of composition and temperature on the specific heat of glass", *Journal of the American Ceramic Society*, vol. 34, pp. 260–271, 1951.

[227] C. L. Babcock and D. L. McGraw, "Controlling conductivity in silicates", *Glass Industry*, vol. 38, pp. 147–151, 1957.

[228] A. F. Van Zee and C. L. Babcock, "A method for the measurement of thermal diffusivity of molten glass", *Journal of the American Ceramic Society*, pp. 244–250, 1951.

[229] H. Scholze and H. O. Mulfinger, "Der Einbau des Wassers in gläsern. V. die Diffusion des Wassers in Gläsern bei hohen Temperaturen", *Glastechnische Berichte*, vol. 32, pp. 381–386, 1959.

[230] P. B. McGinnis and J.E. Shelby, "Diffusion of water in float glass melts", *Journal of Non-Crystalline Solids*, vol. 177, pp. 381–388, 1994.

[231] H. Franz and H. Scholze, "Die lslichkeit von H_2O-dampf in glasschmelzen verschiedener Basizitt", *Glastechnische Berichte*, vol. 36, no. 9, pp. 347–356, 1963.

[232] H. Scholze, "Der Einbau des Wassers in Gläsern. IV. UR-Der einflub der temperatur", *Glastechnische Berichte*, vol. 32, pp. 314–320, 1959.

[233] H. Meyer, G. H. Frischat, and F. U. A. Kramer, "Diffusion von stisckstoff in glasschmelzen für den fall physikalischer lösung.", in *XI Internat. Glaskongre, Prag. Sammelbd..II. Prg:CVTS-Dum techn.*, 1977, pp. 317–326.

[234] F. Kramer, "Mathjematische modelle der veranderung von gasblasen in glasschmelzen", *Glastechnische Berichte*, vol. 52, no. 2, pp. 43–50, 1979.

[235] G.H. Frischat, O. Bushman, and H. Meyer, "Diffusion von stickstoff in glasschmelzen", *Glastechnische Berichte*, vol. 51, no. 12, pp. 321–327, 1978.

[236] G. Mertens, F. Schouppe-Zubac, and F. M. Boffe, "Recherche de l'origine des bulles par analyse des gaz au spectromètre de masse", in *Symposium sur l'élaboration du verre (fusion et affinage), Madrid*, Charleroi, 1973, vol. Bd. 1, pp. 2–75, Union Scientifique Continental du Verre.

[237] H. Scholze, "Gases in glass", in *Eighth International Congress on glass. Sheffield*. 1969, pp. 69–83, Society of Glass Technology.

[238] H. O. Mulfinger, A. Dietzel, and J. M. Fernandez Navarro, "Physikalische löslichkeit von helium, neon und stickstoff in glasschmelzen", *Glastechnische Berichte*, vol. 45, pp. 386–396, 1972.

[239] H. O. Mulfinger, "Physical and chemical solubility of nitrogen in glass melts", *Journal of the American Ceramic Society*, vol. 49, no. 9, pp. 462–467, 1966.

[240] F. Mahieux, "Contribution a l'étude des gaz dans le verre", *Verre et Réfractaire*, vol. 10, pp. 342–356, 1956.

[241] M.J. Hounslow, R.L. Ryall, and V.R. Marshall, "A discretized population balance for nucleation, growth, and aggregation", *AIChE Journal*, vol. 34, no. 11, pp. 1821–1832, 1988.

[242] S. Kumar and D. Ramkrishna, "On the solution of population balance equation by discretization - I a fixed pivot technique", *Chemical Engineering Science*, vol. 51, no. 8, pp. 1311–1332, 1996.

[243] A. Allievi and R. Bermejo, "Finite element modified method of characteristics for Navier-Stokes equations", *International Journal for Numerical Methods in Fluids*, vol. 32, pp. 439–464, 2000.

[244] B. N. Wang and J.D. Hoffman, "Calculation of annular nozzle trisonic flowfields by the method of characteristics", *Journal of Propulsion and Power*, vol. 4, no. 3, pp. 228–235, 1988.

[245] D.L. Marcum, *Calculation of three-dimensional inviscid flowfields*, PhD thesis, Purdue University, 1985.

[246] I. H. Parpia, *Multidimensional time dependent method of characteristics*, PhD thesis, Purdue University, 1986.

[247] M. M. Dabral, S. Roy, and A. N. Bhaskarwar, "General kinetic invariant model of dissolution of large polydisperse particles", *The Chemical Engineering Journal*, vol. 61, pp. 161–170, 1996.

[248] J.B. Hunter and J.A. Asenjo, "A population balance model of enzymatic lysis of microbial cells", *Biotechnology and Bioengineering*, vol. 35, pp. 31–42, 1990.

[249] B.H. Shah and D. Ramkrishna, "A population balance model for mass transfer in lean liquid-liquid dispersion", *Chemical Engineering Science*, vol. 28, pp. 389–399, 1973.

APPENDICES

A. GAS DIFFUSION IN CLOSED-CELL FOAMS

Reproduction of L. Pilon, A. G. Fedorov and R. Viskanta, "Gas diffusion in closed-cell foams", *Journal of Cellular Plastics*, Vol. 36, No. 6, pp. 451-474, 2000.

ABSTRACT

The objective of this paper is to present an engineering model based on fundamentally sound but simplified treatment of mass diffusion phenomena for practical predictions of the effective diffusion coefficient of gases through closed-cell foams. A special attention was paid to stating all assumptions and simplifications that define the range of applicability of the proposed model. The model developed is based on the electrical circuit analogy, and on the first principles. The analysis suggests that the effective diffusion coefficient through the foam can be expressed as a product of the geometric factor and the gas diffusion coefficient through the foam membrane. Validation against experimental data available in the literature gives satisfactory results. Discrepancies between the model predictions and experimental data have been observed for gases with high solubility in the condensed phase for which Henry's law does not apply. Finally, further experimental data concerning both the foam morphology and the diffusion coefficient in the membrane are needed to fully validate the model.

Keywords: gas diffusion, aging, effective diffusion coefficient, closed-cell foam.

A.1. Introduction

Closed-cell foams consists of gas bubbles separated one from another by a thin membrane of a continuous condensed phase. The condensed phase can be solid or liquid. Among foams having solid membrane, the polymeric foams are the most commonly used [1]. They can be rigid or flexible and the cell geometry can be open or closed. Open-cell polymeric foams are generally flexible and best for automobile seats, furniture, and acoustic insulation. Closed-cell polymeric foams are usually rigid and mostly used for thermal insulation in the construction and refrigeration industries. Indeed, closed-cell foams are very effective thermal insulators due to entrapped blowing agents used for foaming and having a low thermal conductivity. Unfortunately, the thermal insulating properties and dimensional stability of rigid closed-cell foams decay significantly with age due to the outward diffusion of the low conductivity blowing agent and the inward diffusion of higher conductivity air constituents [2, 3]. Typically, air constituents diffuse through foam much faster than commonly used blowing agents such as chlorofluorocarbons [1, 2]. As a result, the short and intermediate term aging of polymeric foams are due to in-diffusion of air constituents, while long-term aging depends on depletion of blowing agents.

Liquid foams are frequently encountered as a by-product in bioprocessing (protein separation) and materials processing (glass melting and casting) or generated for special ap-

plications (firefighing). For example, in glass manufacturing liquid foams are formed at the free surface of the molten glass due to entrapment of gas bubbles produced as a result of the batch fusion and fining reactions in the glass melt [9, 10]. Glass foams consist of spherical and/or polyhedral gas bubbles surrounded by liquid lamellae. In the glass melting process, foaming is undesirable since it reduces significantly heat transfer rates from the combustion space to the melt [9, 10], thereby increasing the operating temperature, the NO_x-formation rate, and the energy consumption [9].

Understanding and modeling of the mass diffusion process in foams is, therefore, of major importance from both fundamental and practical viewpoints. The objective of this paper is to present an engineering model based on fundamentally sound but simplified treatment of mass diffusion phenomena for practical predictions of the effective diffusion coefficient of gases through a foam layer. The model developed is based on the electrical circuit analogy, and available experimental data are used for model validation.

A.2. Analysis

A.2.1. Current state of knowledge

In general, the effective diffusion coefficient of a gas species "i" in the foam depends not only on the diffusion coefficients in the gas and the condensed phases (denoted $D_{g,i}$ and $D_{c,i}$, respectively) but also on the foam morphology parameters such as the membrane (or wall) thickness, the unit cell size and shape, the spatial distribution of the cells, the total number of open cells and on the foam porosity [2,3,202,203]. The foam porosity ϕ is defined as

$$\phi = \frac{\rho_c - \rho_f}{\rho_c - \rho_g} \tag{A.1}$$

and it can be easily computed from the experimental measurements of the foam density (ρ_f) and the gas and condensed phases densities, denoted by ρ_g and ρ_c, respectively. The geometry of the unit cell may vary substantially within the same foam, but an idealized unit cell of high porosity foams can be represented by a regular pentagonal dodecahedron [1, 14]. The presence of open cells tends to increase the effective diffusion coefficient and in polymeric foams, open cells account for 5% to 15% of the total number of cells [203].

The prediction of gas diffusion through the closed-cell foam can be accomplished via two different types of models [203]: 1) permeability models and 2) diffusion models. Both models use either continuous or discrete approaches. Brandreth [203] reviewed advantages and drawbacks of each model. In brief, the permeability models are based on the assumption that the permeability coefficient for species "i" through the membrane ($Pe_{c,i}$) can be expressed as the product of the diffusion coefficient ($D_{c,i}$) and the solubility ($S_{c,i}$) of the species "i" in the membrane, i.e.,

$$Pe_{c,i} = D_{c,i} S_{c,i} \tag{A.2}$$

This relationship is strictly valid only if steady state conditions are attained, the wall material is mainly amorphous, and the Henry's law is applicable. Brandreth [203] questioned the appropriateness of Equation (A.2) in studying the aging of polymeric foams by virtue of the fact that the steady state and the Henry's law conditions are hardly satisfied in practice.

Ostrogorsky and Glicksman [3, 202] developed a discrete permeability model based on the electrical circuit anology and Equation (A.2) resulting in the following expression for the effective diffusion coefficient through the foam layer:

$$D_{eff}|_{f,i}(T) = \epsilon \frac{< l >}{d} \frac{T}{T_{STP}} Pe_{c,i} \tag{A.3}$$

where $< l >$ is the average distance between successive membranes, d is the membrane thickness, and $Pe_{c,i}$ is the permeability coefficient of the gas through the membrane that follows an Arrhenius type of law [202]. The parameter ϵ is defined as the ratio of the membrane area to the cross-section area of a unique cell, and it is assumed to be equal to 2 corresponding to spherical shape gas bubbles. The effective diffusion coefficients were found to underpredict the experimental results by as much as 29% [202], while in other studies [204] the discrepancies between predictions and measurements were in the range of 25% to 45%. Shankland [205] modified Equation (A.3) as follows:

$$D_{eff}|_{f,i}(T) = G p_{_{STP}} \left(\frac{T}{T_{_{STP}}} \right) Pe_{c,i} \tag{A.4}$$

where G is a dimensionless geometric factor depending on the foam structure. Equation (A.4) suggests that a plot $D_{eff}|_{f,i}(T)$ versus $p_{_{STP}} \left(\frac{T}{T_{_{STP}}} \right) Pe_{c,i}$ should be a straight line passing through the origin and whose slope is the geometric factor G [205]. Indeed, experimental data obtained for extruded polystyrene foams [205] support the mathematical form of Equation (A.4), but the author emphasized a need for additional information about the foam morphology to fully validate the model. However, there appears a clear lack of consistency in the experimental data presented by various authors. Specifically, Page and Glicksman [206] as well as Fan and Kokko [207] reported the experimental results obtained for different foams over the temperature range of 30^oC to 80^oC. Their experimental data indicate that the effective diffusion coefficient follows an Arrhenius type of law, thereby restricting the applicability of the model proposed by Shankland [205].

The continuous diffusion models consider the foam as a homogeneous and isotropic medium through which gas species "i" diffuses with an effective diffusion coefficient $D_{eff}|_{f,i}$. The effective diffusion coefficient is determined via an inverse solution of the following species conservation equation:

$$\frac{\partial C_i}{\partial t} = D_{eff}|_{f,i} \nabla^2 C_i \tag{A.5}$$

The discrete diffusion models consider the foam layer as the repetition of unit cells characterized by their geometry (membrane thickness, cell size and shape) as well as the diffusion coefficients of the species through the condensed phase (liquid or solid) and through the gas phase. Several studies showed the significant influence of the foam morphology on the diffusion process through closed-cell foams [208, 209]. The continuous model is by its essence unable to account for the discreteness of the foam morphology. In contrast, the discrete approach enables one to express the effective diffusion coefficient in terms of parameters characterizing the foam structure and composition.

Recently, Alsoy [210] reviewed the discrete diffusion models, and a reader is referred to this publication for citations of the relevant literature. In short, she concluded that the model developed by Bart and Du Cauzé de Nazelle [211] represents the current state-of-the-art. In this work, one-dimensional diffusion through a series of three-dimensional cubic

cells of uniform wall thickness was considered. The authors neglected the diffusion through the gas phase, and used the Henry's law at the membrane/gas phase interface to obtain the following expression for the effective diffusion coefficient both in a unit cell and in the entire foam [211, 212]:

$$D_{eff}|_{f,i}(T) = \left(\frac{L}{b}\right)\left(\frac{D_{c,i}S_{c,i}RT}{(1-\phi)S_{c,i}RT+\phi}\right) \tag{A.6}$$

Here, $D_{eff}|_{f,i}(T)$ is the effective diffusion coefficient of gas "i" expressed as a function of geometric parameters of the foam [the size of the unit cubic cell (L), the thickness of the membrane (b), and porosity (ϕ)], and thermophysical properties [the diffusion coefficient ($D_{c,i}$) and the solubility ($S_{c,i}$) of the gas in the condensed phase]. Alsoy [210] reported an extensive comparison of the effective diffusion coefficient predicted by Equation (A.6) with the experimental data obtained for different types of polymeric foams and diffusing gases. The author observed that Bart and Du Cauzé de Nazelle's model underpredicted the effective diffusion coefficients by about one to three orders of magnitude [210].

To conclude this overview, there is a great deal of controversy about what type of model should be used for predicting the effective properties of a foam. In this paper, an attempt is made to derive an expression of the effective diffusion coefficient of the foam based on the first principles. It is hoped that the theoretical model developed will contribute to clarifying at least some of the controversial issues and will provide a framework for developing physically consistent models. In the present work, a cubic unit cell is used as representative model to predict mass diffusion through the closed-cell foams using electrical circuit analogy. A special attention was paid to stating all assumptions and simplifications that define the range of applicability of the proposed model. Finally, the analysis considers multi-gas diffusion through the foam layer with either liquid or solid condensed phase. The theoretical model developed is validated against the experimental data available in the literature.

A.2.2. Model Assumptions

A model for mass diffusion of the gas species "i" through a unit cell of the foam layer is developed using the following assumptions:

1. Foam cells are taken to be closed and separated by the continuous solid or liquid membranes.
2. The condensed phase of the membranes is assumed to be at rest.
3. Gas diffusion of gas species "i" through the condensed phase is considered to be a thermally activated process, i.e., the mass diffusion coefficient ($D_{c,i}$) depends on the temperature via the Arrhenius' law [213]:

$$D_{c,i} = D_{c,0,i}exp\left(\frac{-E_{c,i}}{RT}\right) \tag{A.7}$$

   where $D_{c,0,i}$ and $E_{c,i}$ are experimentally determined constants.
4. The gas mixture contained in the pores (voids) of the foam behaves as an ideal gas.

5. Mass diffusion only in the vertical z-direction is considered.
6. The diffusing gas species "i" is weakly soluble in the condensed phase (i.e., Henry's law is applicable)[1].
7. The temperature is uniform throughout the unit cell.
8. The pressure in the void remains close to the atmospheric pressure (maximum 5 atm [159]) so that the ideal gas approximation for fugacity is valid.
9. The diffusing gas neither reacts with the condensed phase nor undergoes dissociation or association.
10. The condensed phase is continuous (i.e., poreless).
11. The foam consists of a succession of identical stacked layers of juxtaposed unit cells. Thus, the effective diffusion coefficient of gas "i" through the entire foam layer ($D_{eff}|_{f,i}$) can be expressed as:

$$D_{eff}|_{f,i} = \left(\frac{L}{H_f}\right) D_{eff,i} = \frac{1}{n} D_{eff,i} \tag{A.8}$$

    where $D_{eff,i}$ is the effective diffusion coefficient of gas species "i" through a unit cell, H_f is the foam thickness, and L is the characteristic length of the cubic unit cell. The ratio H_f/L $(=n)$ represents the number of unit-cell-thick layers constituting the foam. Note that, as the number of closed-cells in the diffusion direction increases, the resistance to gas diffusion increases and the effective diffusion coefficient becomes smaller.
12. Convective gas transport inside the pores is neglected [206].
13. The changes of the effective diffusion coefficient due to the variation of the foam porosity with temperature (i.e., due to thermal expansion) are neglected compared to the changes due to the variation of the diffusion coefficients $D_{c,i}$ and $D_{g,i}$ with temperature.

Using the above listed assumptions, a model for effective diffusion coefficient in closed-cell foams is developed based on the cubic representation of the foam unit cell.

A.2.3. Cubic Unit Cell Model

Figure A.1 shows a representative unit cell that is used to describe the microstructure of the foam. The unit cell is a cube of characteristic length L with the pore (void) represented by a smaller cube. The space between the two cubes is occupied by a condensed phase (solid or liquid), while the internal cube contains a gas mixture. Based on the definition of porosity (the volume fraction of the cell occupied by the gas mixture), the relationship between the wall (membrane) thickness b and the porosity ϕ can be expressed as

$$\phi = \left(1 - 2\frac{b}{L}\right)^3 \tag{A.9}$$

[1]This assumption appears not to be valid for $CFCl_3$ (R-11) in rigid polyurethane foams as discussed by Brandreth [203].

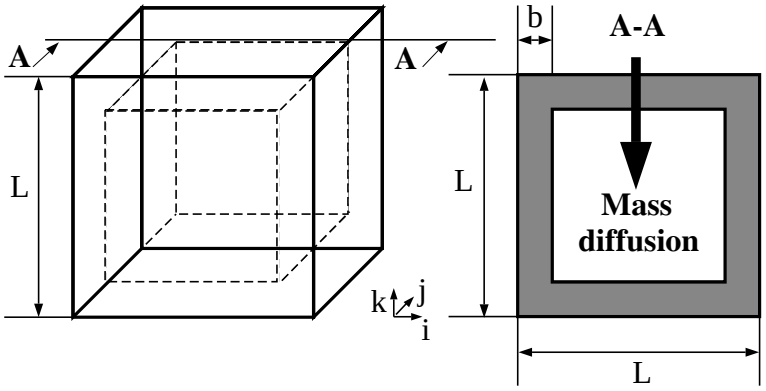

Figure A.1. Schematic of a cubic unit cell of the foam.

or, in terms of the dimensionless wall thickness $\beta = b/L$, as

$$\beta = \frac{1}{2}(1 - \sqrt[3]{\phi}) \tag{A.10}$$

Three different resistances to diffusion of species "i" in the vertical direction from the top to the bottom of the unit cell should be considered: 1) the resistance of the condensed phase, 2) the interface resistance and 3) the resistance of the gas. Wet foams are often stabilized by the surface active chemicals present at the interface of the lamella. In this analysis, it is assumed that the resistance to the mass transport provided by the surfactants is negligibly small. It is also assumed that the magnitude of the mass flux is relatively small, so that the variations of mass concentration of gas species "i" in both phases are small as well. Then, the quasi-equilibrium conditions can be assumed to exist at the gas/condensed phase interface [165] which imply the equality of the chemical potentials of the diffusing gas on both side of the interface. This fact, combined with assumptions 6, 7, 8 and 9, allows us to apply the generalized Henry's law to obtain a relationship between species concentrations on both sides of the gas/condensed phase interface [166]:

$$C_{c,i} = S_{c,i} M_i f_{g,i} \tag{A.11}$$

Here, $C_{c,i}$ is the concentration and $S_{c,i}$ is the solubility of the diffusing gas "i" in the condensed phase, M_i is the molecular weight of the species "i", and $f_{g,i}$ the fugacity of the species "i" in the gas phase. Provided that the pressure is low enough and ideal gas approximation holds (assumption 8), the fugacity $f_{g,i}$ is approximately equal to the partial pressure of species "i" (p_i) on the gas side of the interface [159], so that

$$C_{c,i} = S_{c,i} M_i p_i \tag{A.12}$$

Using an ideal-gas equation of state (assumption 4), the concentration of the gas species "i" in the gas phase can be expressed as

$$C_{g,i} = \frac{M_i}{RT} p_i \tag{A.13}$$

This results in the following jump condition for the species concentrations at the interface:

$$C_{c,i} = S_{c,i} RTC_{g,i} \tag{A.14}$$

Figure A.2 schematically illustrates the mass concentration profile of gas species "i" across the foam unit cell with the jump condition at the gas/condensed phase interfaces given by Equation (A.14). Note that, although the concentration profile may appear counter-

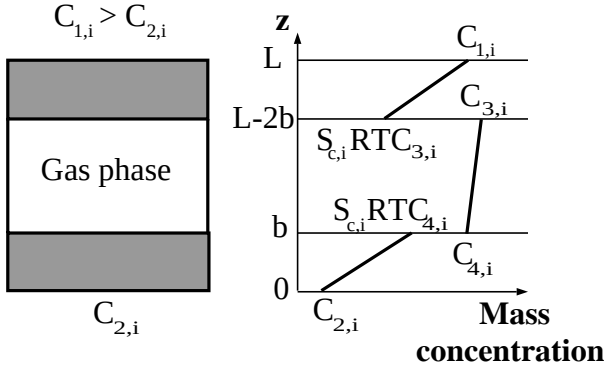

Figure A.2. Concentration profile in the center part of the cubic cell for $S_{c,i}RT \leq 1.0$.

intuitive, the chemical potential profile, if plotted, would be a continuous, decreasing function from top to bottom indicating the direction of the mass transfer.

Using the electric circuit analogy [94], the equivalent diffusion resistance circuit for the given unit cell can be constructed as shown on Figure A.3.

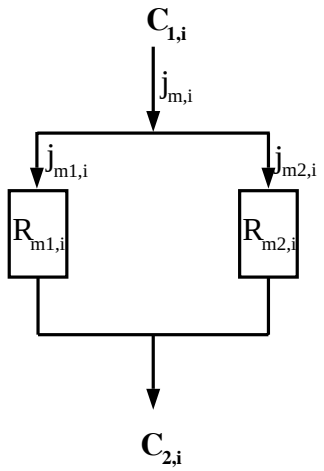

Figure A.3. The equivalent diffusion resistance circuit for a cubic cell.

Here, $R_{m1,i}$ denotes the resistance of the surrounding cubic envelope, and $R_{m2,i}$ is the total resistance of the top condensed phase + void gas + bottom condensed phase layers in

the center part of the unit cell. The resistance $R_{m1,i}$ can be computed in a straight-forward fashion as

$$R_{m1,i} = \frac{L}{4D_{c,i}b(L-b)} \tag{A.15}$$

Considering only the center part of the cube, the concentration difference across each phase can be expressed in term of the local mass-transfer rate $j_{m2,i}$ (in kg/s) and the mass diffusion coefficient of the species "i" in the given phase:

$$\begin{aligned} j_{m2,i} &= D_{c,i}(L-2b)^2 \frac{(C_{1,i} - S_{c,i}RTC_{3,i})}{b} \\ &= D_{g,i}(L-2b)^2 \frac{(C_{3,i} - C_{4,i})}{(L-2b)} \\ &= D_{c,i}(L-2b)^2 \frac{(S_{c,i}RTC_{4,i} - C_{2,i})}{b} \end{aligned} \tag{A.16}$$

Solvation of Equation (A.16) for $C_{3,i}$ and $C_{4,i}$ yields

$$(C_{3,i} - C_{4,i}) = \frac{D_{c,i}(L-2b)}{2D_{g,i}b + S_{c,i}RTD_{c,i}(L-2b)}(C_{1,i} - C_{2,i}) \tag{A.17}$$

By definition, the diffusion resistance in the center part of the cubic cell is given by

$$R_{m2,i} = \frac{(C_{1,i} - C_{2,i})}{j_{m2,i}} \tag{A.18}$$

or, after using Equations (A.16) and (A.17), by the following expression:

$$R_{m2,i} = \frac{2b}{D_{c,i}(L-2b)^2} + \frac{S_{c,i}RT}{D_{g,i}(L-2b)} \tag{A.19}$$

It is clear from Equation (A.19) that the total diffusion resistance in the center part of the cell ($R_{m2,i}$) consists of the resistances of the two layer of the condensed phase (the first term on the right-hand side) in series with the resistance of the gas phase (the second term on the right-hand side).

If the resistances $R_{m1,i}$ and $R_{m2,i}$ are specified, the total resistance of a unit cubic cell $R_{m,i}$ is computed as follows:

$$R_{m,i} = \frac{R_{m1,i}R_{m2,i}}{R_{m1,i} + R_{m2,i}} \tag{A.20}$$

Finally, the effective mass diffusion coefficient of the unit cubic cell ($D_{eff,i}$) is defined as

$$D_{eff,i} = \frac{j_{m,i}}{L(C_{1,i} - C_{2,i})} = \frac{1}{R_{m,i}L} \tag{A.21}$$

and, by substituting Equations (A.15) and (A.19) into Equations (A.20) and (A.21), it is given by

$$D_{eff,i} = D_{c,i}\left[4\beta(1-\beta) + \frac{D_{g,i}(1-2\beta)^2}{2D_{g,i}\beta + S_{c,i}RTD_{c,i}(1-2\beta)}\right] \tag{A.22}$$

where the dimensionless wall thickness β can be calculated from Equation (A.10) if the foam porosity (ϕ) is known.

In most of the practical cases, the cell interior (void volume) does not introduce a significant resistance to mass diffusion [2, 3, 211] since diffusion coefficient in the gas phase is much larger than diffusion in the condensed phase ($D_{g,i} \gg D_{c,i}$). Then, the concentration across the gas phase can be assumed as essentially constant and Equation (A.22) simplifies to

$$D_{eff,i} = \frac{D_{c,i}}{2\beta}(1 - 4\beta + 12\beta^2 - 8\beta^3) \tag{A.23}$$

Substituting an expression for β from Equation (A.10) into Equation (A.23) yields:

$$D_{eff,i} = D_{c,i}\left(1 + \frac{\phi}{1 - \sqrt[3]{\phi}}\right) \tag{A.24}$$

Note that if the diffusion within the void is neglected, the total diffusion resistance of the cell consists only of that of the condensed phase, and the interfacial jump conditions and the solubility of the gas in the condensed phase have no influence on the effective diffusion coefficient.

Finally, by accounting for the temperature dependence of the mass diffusion coefficient in the condensed phase $D_{c,i}$ [see Equation (A.7)] and considering multiple unit-cell structure of the foam layer [see Equation (A.8)], the following expression for the effective diffusion coefficient of the entire foam layer can be suggested:

$$D_{eff}|_{f,i} = G(\phi, n) D_{c,0,i} exp\left(\frac{-E_{c,i}}{RT}\right) \tag{A.25}$$

where the geometric factor $G(\phi, n)$ is expressed as

$$G(\phi, n) = \frac{1}{n}\left(1 + \frac{\phi}{1 - \sqrt[3]{\phi}}\right) \tag{A.26}$$

Note that the effective diffusion coefficient of the foam [Equation (A.25)] is expressed as the product of a geometric factor, $G(\phi, n)$, and the diffusion coefficient in the foam condensed phase, $D_{c,i}(T)$. The geometric factor $G(\phi, n)$ depends on the foam porosity (ϕ) and on the average number of cells (n) across the foam thickness in the direction of the diffusion flux. The cubic cell geometry is, obviously, a simplified representation of the real morphology of the foam. Therefore, the parameter n (=H_f/L) should be viewed as the number of equivalent cubic cells that best represent the real foam. Assigning an appropriate value of the linear dimension of the unit cubic cell L could be used to account for the discrepancy between the model and the reality. For example, one can derive the characteristic length by preserving one or several foam parameters (e.g., the wall thickness, the interfacial area, the cell volume or the projected interfacial area onto a plan perpendicular to the direction of diffusion) in the actual and idealized (model) settings.

The diffusion coefficient of gas species "i" in the condensed phase depends on the physical and the chemical characteristics of the condensed phase. For example, the gas diffusion coefficient in a polymeric condensed phase depends not only on the chemical structure of the specific polymer but also on morphology, density, crystallinity and orientation of molecular chains in the polymer [213]. However, the chemical structure can be considered to be a predominant factor [213], and one should carefully consider it in validating and making practical calculations using the theoretical models developed.

A.3.1. Parametric Calculations

First, a critical analysis of the model developed by Bart and Du Cauzé de Nazelle [211] [see Equation (A.6)] is presented and important trends are discussed. A main input parameter for the Bart and Du Cauzé de Nazelle's model is the product $S_{c,i}RT$, whose typical values at O^oC in polyurethane foams range between 0.1 and 10 for nitrogen and CFC-11, respectively [211]. Figure A.4 shows the ratio of the effective diffusion coefficient through a unit cell and that through the condensed phase alone, predicted by Equations (A.24) and (A.6) [for different values of the parameter $S_{c,i}RT$] ploted against the porosity (ϕ). Intuitively, one expects that as the membrane becomes thinner, the diffusion resistance de-

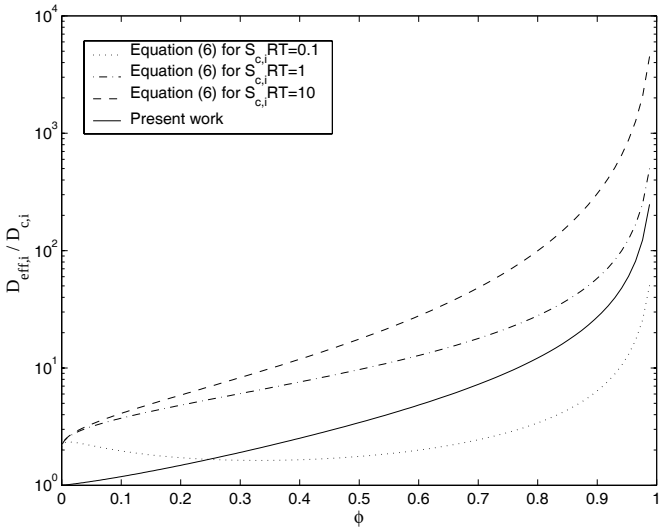

Figure A.4. Parametric analysis of Bart and Du Cauzé de Nazelle model [16].

creases leading to a larger effective diffusion coefficient. In other words, the effective diffusion coefficient should increase continuously as the porosity increases since the resistance of the gas phase is much smaller than that of the condensed phase, and experimental observations confirm these expectations for low pressures [2,206,214]. However, when $S_{c,i}RT \leq 1.0$ (that is for nitrogen and oxygen in polyurethane membrane [211]), Equation (A.6) exhibits an unexpected non-monotonic trend with the local minima. This trend has also been observed by Briscoe and Savvas [215] in their numerical study of oxygen and nitrogen gas diffusion through dense polyethylene foams having an initial pressure in cavities of 4.8 MPa. The authors speculate that the medium size voids act as "buffers" which prevent rapid variation of the gas pressure in the medium porosity range, thereby leading to a local minima in the effective diffusion coefficient. In low porosity foams, the cells are too small to significantly buffer the pressure fluctuations, whereas in high porosity foams the cavities are much larger than the cell walls and their effect on pressure is negligible compared to that of the walls.

For such high pressure applications, the ideal gas approximation is not valid [159] and this case falls beyond the scope of this study.

The simplified cubic model [see Equation (A.22)] developed here predicts a continuous increase in the effective diffusion coefficient as the foam porosity increases. The parametric analysis of the cubic model indicates that if the diffusion coefficient through the membrane is at least two orders of magnitude greater than the diffusion coefficient through the gas, then the resistance to gas diffusion presented by the gas phase can be neglected. Thus, for all practical applications with either liquid or solid condensed phase, one can neglect the resistance of the gas phase and the simplified models given by Equations (A.25) and (A.26) should be adequate for practical calculations.

A.3.2. Validation Against Experimental Data

Tables A.1 and A.2 summarize the experimental conditions used in the studies concerned with the effective diffusion coefficients through different polyurethane (PUR) and related polyisocyanurate (PIR) foams as well as other polymeric foams, respectively. Polyurethane foams and related polyisocyanurate foams comprise the largest family of rigid closed-cell foams [1]. Polyurethane membranes are formed by exothermic chemical reactions between an polyisocyanate and a polyol, and foaming is achieved by evaporation of low boiling point liquids (blowing agents) such as chlorofluorocarbons (CFC or R) (see Ref.[1] for an in depth discussion)". Note that the specific type of polyols used for polyurethane foams is rarely mentioned and often unknown to the authors [212]. This is unfortunate since previous studies [216] showed that the gas diffusion coefficient through polyurethane membranes depends on the type of polyol used, whereas the influence of the isocyanate functionality has not been clearly observed. Since $D_{c,i}$ and $S_{c,i}$ may vary by several orders of magnitude from one polyurethane foam to another [216], any reliable assessment of gas diffusion models through polyurethane foams should be performed for polyurethane foams made out of the same polyol. For instance, Alsoy [210] used the experimental data for the diffusion coefficient of an unknown type of polyurethane membrane [211] to validate the Bart and Du Cauzé de Nazelle's model against the experimental data taken from other studies without checking if the polyurethane foams were generated using the same polyol.

To assess the validity of Equations (A.25) and (A.26) for predicting the effective gas diffusion coefficient through the closed-cell foams, one needs to know (*i*) the chemical structure of the condensed phase (membrane), (*ii*) the mass diffusion coefficient of the gas through the specific membrane and its temperature dependence $[D_{c,i}(T)]$, (*iii*) the foam porosity or the foam density, and (*iv*) the average number of equivalent cubic cells in the direction of the diffusion process. Unfortunately, the authors were unable to find a consistent set of data supplied with all the necessary parameters. Therefore, an indirect approach will be used to validate the simplified diffusion models against available experimental data.

A.3.3. Temperature Dependence of the Effective Diffusion Coefficient

Temperature has been identified as having a significant influence on the effective gas diffusion coefficient through closed-cell foams [2]. In some cases the effective diffusion coefficient can change by one order of magnitude when the temperature is increased from

25^oC to 80^oC [2, 206]. Figure A.5 shows the temperature dependence of the effective diffusion coefficient of carbon dioxide through an extruded low density polyethylene (LDPE) foam [208] and the diffusion coefficient of carbon dioxide through a polyehtylene membrane obtained in the literature [213]. One can observe that both lines have practically the same

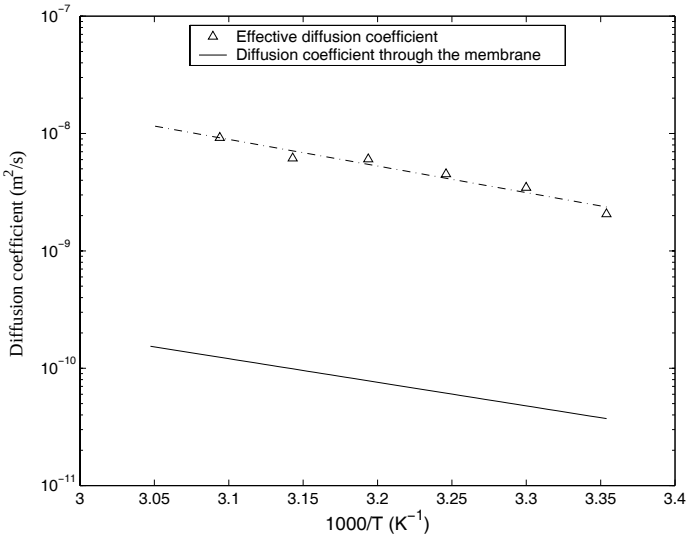

Figure A.5. CO_2 diffusion coefficients through extruded LDPE foam [13] and LDPE membrame [18] vs. inverse temperature.

slopes, and this is in agreement with the trend predicted by the theoretical model developed in this study assuming that the variation of the geometric factor with temperature is negligible (i.e., no thermal expansion/construction occurs). Indeed, Equation (A.25) states that the slope of the $ln(D_{eff}|_{f,i})$ vs. $1/T$ plot and the slope of the $ln(D_{c,i})$ vs. $1/T$ plot should be the same. Note that for the cases when a temperature gradient exists across the foam layer in the direction of the diffusion flux, the discrete model can still be applied by approximating the temperature gradient as a step function with constant but different average temperatures for each unit cell in the foam layer.

A.3.4. Geometric Factor

As evident from Equations (A.25) and (A.26) that the ratio of the foam effective diffusion coefficient to the diffusion coefficient in the membrane is a geometric factor $G(\phi, n)$ depending on the foam morphology only. A plot $D_{eff}|_{f,i}(T)$ vs. $D_{c,i}(T)$ should, therefore, feature a straight line passing through the origin. Figure A.6 depicts the experimental effective diffusion coefficient for carbon dioxide in the extruded low density polyethylene foam [208] against the diffusion coefficient through the membrane reported in the literature [213]. It appears that Equation (A.25) is capable of correctly predict of the trend over the temperature range of 25^oC to 50^oC within an error corresponding to the uncertainty in the experimental data.

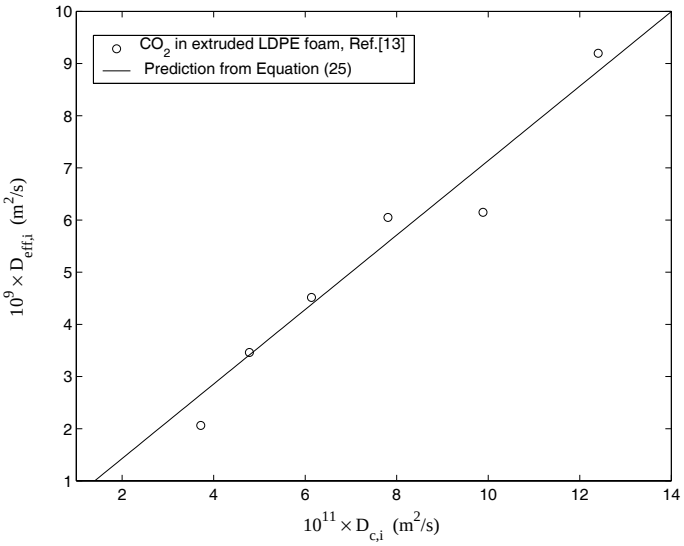

Figure A.6. Effective diffusion coefficient vs. the diffusion coefficient through the membrane for CO_2 in extruded LDPE foam [13].

Bart and Du Cauzé de Nazelle [211] reported data for the effective diffusion coefficient and the diffusion coefficient through the membrane for an unspecified polyurethane foam with diffusing gases being oxygen, nitrogen, carbon dioxide, CFC-11 and CFC-22. It is interesting to note that, in general, the geometric factor varies significantly from one gas to another within the same foam. However, the low solubility gases in polyurethane foam, namely oxygen and nitrogen, yield approximately the same geometric factors within the uncertainty of the measurements. The geometric factors obtained for the other gases are higher by one to two orders of magnitude without providing any clear trend. Earlier studies have shown that the Henry's law is not valid for CFC-11 in polyurethane foams due to its high solubility [203]. Note that for the polyurethane membrane considered, the solubilities of CO_2, CFC-11, and CFC-22 are of the same order of magnitude [211], indicating that Henry's law may not be applicable for any of these gases in polyurethane foams.

Due to the lack of consistent and complete set of experimental data, the proposed theoretical model can be only approximately validated indirectly. Specifically, Equation (A.26) suggests that the geometric factor is the function of the foam porosity $\Gamma(\phi)$ divided by the equivalent number of cubic cells in the foam layer in the diffusion direction, i.e.,

$$G(\phi, n) = \frac{\Gamma(\phi)}{n} \tag{A.27}$$

Then, by considering two foam samples with different porosities but with the membrane made of the same polymer material, the ratio of the effective diffusion coefficients should be independent of the temperature and equals to the ratio of the geometric factors only:

$$\frac{D_{eff}|_{f_1,i}}{D_{eff}|_{f_2,i}} = \frac{G(\phi_1, n_1)}{G(\phi_2, n_2)} \tag{A.28}$$

Figure A.7 shows the ratio of the geometric factors computed from the experimental data [208] for diffusion of CO_2 and He through two similar polystyrene foams having different porosities, 0.974 and 0.917. The effective diffusion coefficients through the two samples are quite

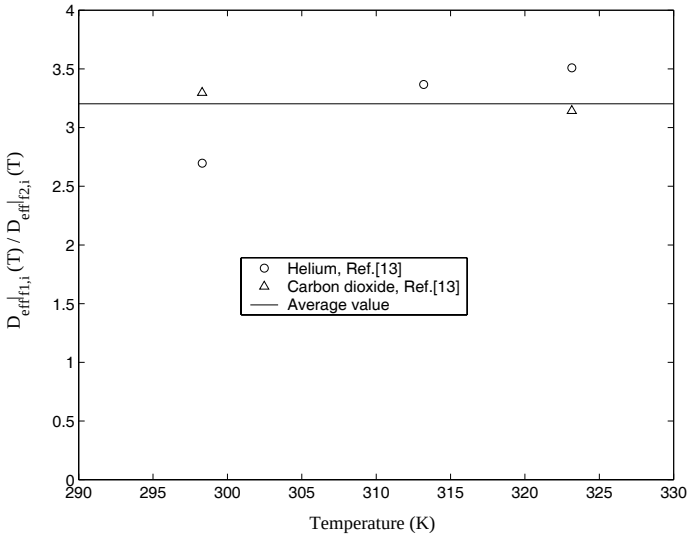

Figure A.7. Ratio of geometric factors for polystyrene foams at different temperatures [13].

different as well as the porosities, but one can note that the geometric factor appears to be practically independent of the temperature and of the nature of the gas. The same analysis has been performed using the experimental data for two polyisocyanurate foam samples (samples 17 and 18) containing between 10 to 15 cells and made of terate-203-mutranol-9171 (T) as the polyol and the isocyanate Mondur [217]. Figure A.8 shows the experimentally determined ratio of the effective diffusion coefficients through the two foams for oxygen and carbon dioxide. The same ratio has been predicted from Equation (A.27) by assuming, as a first approximation, that the equivalent number of cubic cells is the same as the number of cells in the real foam. Then, considering the limiting cases for which one foam has 10 cells while the other has 15 cells and vice versa, the ratio of the effective diffusion coefficients should vary between the following limits:

$$\frac{10}{15}\frac{\Gamma(\phi_1)}{\Gamma(\phi_2)} \leq \frac{D_{eff}|_{f_1,i}}{D_{eff}|_{f_2,i}} \leq \frac{15}{10}\frac{\Gamma(\phi_1)}{\Gamma(\phi_2)} \tag{A.29}$$

where the values for the porosity function $\Gamma(\phi)$ are 154.9 and 134.9 for samples 17 and 18, respectively. As noted on Figure A.8), inequality (A.29) predicts the correct range for the ratio of the effective diffusion coefficients for two different gases in foam samples made of the same condensed phase. These results, using the reported number of cells across the foam layer as the equivalent number of cubic cells n, tend to confirm the theoretical model developed. Unfortunately, experimental data providing the precise number of closed-cells across the foam layer are not available.

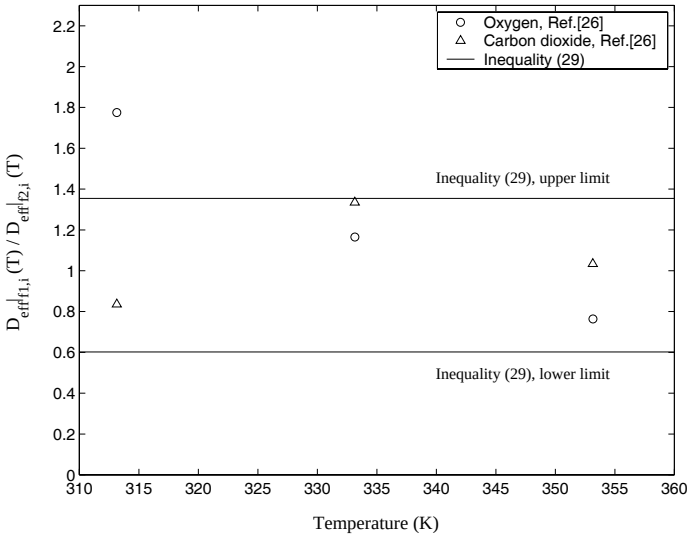

Figure A.8. Effective diffusion coefficient ratio for two PIR (MR/T) foams at different temperatures and predicted range [26].

A.4. Conclusions

This paper deals with an analysis of the gas diffusion process through closed-cell foams. A theoretical model has been developed for predicting the effective diffusion coefficient of the weakly soluble, low pressure gases through solid and wet foams based on the first principles. The analysis suggests that the effective diffusion coefficient through the foam can be expressed as a product of the geometric factor and the gas diffusion coefficient through the foam membrane. The model has been validated by comparing its predictions with available experimental data, and the following conclusions can be drawn:

- No consistent and complete set of data is available in the literature for comprehensive model validation. In particular, the reported experimental data lack information on the temperature dependence of the diffusion coefficient in the polymer membrane and on the average number of unit cell in the foam layer. This data is critically important for the development of reliable foam diffusion models.
- The available data for different types of polymeric foams support the validity of the model developed both qualitatively and quantitatively. Discrepancies between the model predictions and experimental data have been observed for gases with high solubility in the condensed phase for which Henry's law does not apply.
- Further work is needed to extend the analysis from ideal gases to real gases as well as to perform accurate and consistent model validations through carefully designed experiments.

ACKNOWLEDGEMENTS

This work was supported by the US Department of Energy/ Glass Industry/ Argonne National Laboratory/ University collaborative research project. The authors are indebted

to the glass industry representatives for numerous technical discussions and exchange of information.

NOMENCLATURE

b	Wall thickness in the cubic model
C	Mass concentration
d	Cell wall thickness
D	Diffusion coefficient
E	Activation energy, Equation (A.7)
f	Fugacity
G	Geometric factor, Equation (A.26)
H_f	Thickness of the foam layer
$\vec{i}, \vec{j}, \vec{k}$	Unit vectors in the x-, y-, and z-directions, respectively
j_m	Mass transfer rate
$< l >$	Average distance between successive membranes in the foam, Equation (A.3)
L	Linear dimension of the unit cubic cell
M	Molecular weight of the gas
n	Average number of cells across the foam layer in the direction of the diffusion process ($= H_f/L$)
p	Pressure of the gas in the void
Pe	Permeability coefficient
R_m	Species diffusion resistance
R	Universal gas constant $= 8.314 J/mol.K$
S	Solubility of the gas species in the condensed phase
T	Temperature
z	Axial coordinate

Greek symbols

β	Dimensionless wall thickness in the cubic model (=b/L)
ϵ	Parameter, Equation (A.3)
Γ	Foam porosity function, Equation (A.27)
ϕ	Porosity
φ	Function of number of closed-cells in the diffusion direction, Equation (A.27)

Subscripts

0	Refers to a reference state
c	Refers to condensed phase (liquid or solid)
eff	Refers to effective property
f	Refers to foam
g	Refers to gas phase
i	Index of the gas species
STP	Standard temperature and pressure

Table A.1. Compilation of experimental studies on gas effective diffusion coefficient through polyurethane (PUR) and related polyisocyanurate (PIR) foams.

Ref.	**Type of Foam**	**Polyiso-cyanate**	**Polyol**	**Blowing Agent**	**Density** (kg/m^3)	**Diffusing Gases**	**Coeff.** $D_{c,i}(T)$	**Morpho -logy**
[2]	PUR	MDI	N.A.	N.A.	25.2	N_2, O_2, and R-11	N.A.	N.A.
[202]	PUR	MDI	N.A.	N.A.	22.5 to 28.4	CO_2, N_2, O_2	N.A.	A.
[204]	PUR	MDI	AP	R-11 and	30.4	CO_2	A.	A.
	PUR	MDI	ASA	CO_2	34.1	air	A.	A
[206]	PIR	MR200	S-PS	HCFC-123	32.36	CO_2, O_2,	N.A.	A.
	PIR	MR	T	HCFC-123	30.11	N_2, R-11, and	N.A.	A.
	PIR	MR	T	HCFC-141b	28.19	HCFC-123,-141b	N.A.	A.
[207]	PUR	MDI [218]	N.A.	n-pentane iso-pentane	33 to 44.4	CO_2, N_2, and O_2	N.A.	N.A.
[208]	PUR	MDI	N.A.	R-11	27.2	CO_2, He, Ne	N.A.	N.A.
[209]	PUR	TDI	N.A.	N.A.	20.82	CO_2 and O_2	N.A.	A.
	PUR	MDI	N.A.	N.A.	28.3 to 48.1		N.A.	A.
[211]	PUR	N.A.	N.A.	N.A.	about 30 [212]	CO_2, O_2, N_2, R-11, R-22,-123,-141b	A.	N.A.
[214]	PUR	N.A.	N.A.	N.A.	31.2	N_2 and O_2	N.A.	N.A.
	PIR	N.A.	N.A.	N.A.	30.5	N_2 and O_2	N.A.	N.A.
[219]	PUR	N.A.	N.A.	cyclopentane, pentane	43 to 49	N_2, O_2, and CO_2	N.A.	N.A.
[220]	PUR	MDI	N.A.	cyclopentane,	N.A.	cyclopentane,	N.A.	N.A.
	PIR	MDI	polyester	and n-pentane	N.A.	n-pentane	N.A.	N.A.

MR: Mondur, MDI: diphenylmethane diisocyanate, TDI: toluene diisocyanate, S-PS: Stepan PS2852, ASA: Aromatic Sucrose Amine, AP: aromatic Polyether, T: Terate 203-Multranol 9171, N.A.: not available, A.: available.

Table A.2. Compilation of experimental studies on gas diffusion through polymeric foams other than PUR and PIR foams.

Ref.	**Type of Foam**	**Blowing Agent**	**Density** (kg/m^3)	**Diffusing Gas**	**Diffusion Coeff.** $D_{c,i}(T)$	**Morphology**
[207]	XPS	N.A.	31.4	O_2, N_2, CO_2	N.A.	N.A.
[208]	XPS	R-12	34.8 to 87.5	He and CO_2	N.A.	N.A.
[208]	extruded LDPE	R-12 and R-114	25.2	He, CO_2, and Ne	A. [213]	N.A.
[214]	XPS	N.A.	31.4	N_2 and O_2	N.A.	N.A.
[221]	XPS	R-12 and methyl chloride	28 to 34	HCFC-22,-142b R-12 and N_2	N.A.	N.A.

N.A.: not available, A.: available, XPS: extruded polystryene, LDPE: low density polyethylene.

B. THERMOPHYSICAL PROPERTIES OF SODA-LIME SILICATE GLASS

B.1. Introduction

Appropriate specification of the thermophysical properties is a major concern in modeling of glass melting furnaces [136]. Up to now, no reported simulation of glass melting furnaces has used a consistent set of thermophysical properties for a given glass melt. The assessment of the bubble transport and foam formation models depends very strongly on the accuracy of the molten glass thermophysical properties (viscosity, density, surface tension, thermal diffusivity...), the refining reaction characteristics, as well as the diffusion coefficients, and the solubilities for each gas dissolved in the molten glass. These thermophysical properties depend on many parameters such as the glass composition, the temperature, the dissolved gas partial pressure, and the composition and pressure of the atmosphere . According to Kawachi and Kawase [150] reliable data and measurement methods are not yet available for some of the mentioned thermophysical properties. The purpose of this work is neither to develop an extensive database nor to provide new experimental results or measurement methods. Instead, it aims at collecting and assessing the available data concerning soda-lime silicate and in some cases at highlighting discrepancies and lack of available data. Soda-lime silicate glass is the most widespread and inexpensive form of glass used to manufacture many different products such as containers, windows, lamps, lenses, etc. [187, 222]. Particular attention was paid to the thermophysical properties of the most common composition [74 SiO_2-16 Na_2O-10 CaO (mol.%)] soda-lime silicate glass[1] or very similar compositions over the temperature range of 1000 to 2000 K. Very often the soda-lime silicate glass composition was not available even though it is well known that the gas diffusion coefficients and the solubilities may depend significantly on the glass composition. Four different gases diffusing molecularly in glass melts are considered: oxygen, nitrogen, carbon dioxide and water. Note that it has been impossible to obtain a consistent set of data of all the thermophysical properties needed. Obtaining such a consistent set of reliable data and developing measurement methods should be the concern of future work.

B.2. Glass Melt Properties

The necessary glass melt properties for the bubble transport model are the density, the dynamic viscosity, the surface tension, and the thermal properties. Following, are the empirical equations of these properties. Their variations with temperature in the range of 1000 K to 2000 K are shown in Figure B.1 through B.6. Experimental data, when available, are reported in Table B.1 to B.3.

[1]This composition is equivalent to 74.1 SiO_2-16.5 Na_2O-9.4 CaO (wt.%)

B.2.1. Density and Thermal Expansion Coefficient

The density depends on the glass composition, the temperature, and the prior history [184]. In the present study, only the two first parameters are considered. The change of the glass density with temperature is approximated by

$$\rho_\infty(T) = \rho_0[1 - \beta(T - T_0)] \qquad \text{in kg/m}^3 \tag{B.1}$$

where ρ_0 is the density of the melt at T_0 and β the linear coefficient of expansion.

The thermal expansion is not only of interest for the usage of glass products but also for the calculation of the gravity driven flow of the glass melt [167]. Thermal expansion is strongly dependent on the glass composition [184, 222, 223]. Analysis of data reported by Coenen [223] and reproduced in Table B.1 leads to a thermal expansion coefficient of 6.59×10^{-5} K^{-1} for 73.8 SiO_2-15.5 Na_2O-10.7 CaO[2] (mol.%) soda-lime silicate glass. Then, Equation (B.1) becomes

$$\rho_\infty(T) = 2406.5[1 - 6.6 \times 10^{-5}(T - 1123.15)] \qquad \text{in kg/m}^3 \tag{B.2}$$

As shown in Figure B.1, the variation of the glass density in the temperature range of interest is very small: the density decreases only by 6.5% from 1000 K to 2000 K; therefore the glass density will be considered as a constant in the computations except for the calculation of the gravity driven flow of the glass melt for which the Boussinesq's assumption will be used. The glass melt density will be taken as the value given by Equation (B.2) at 1500 K: ρ_∞(T)

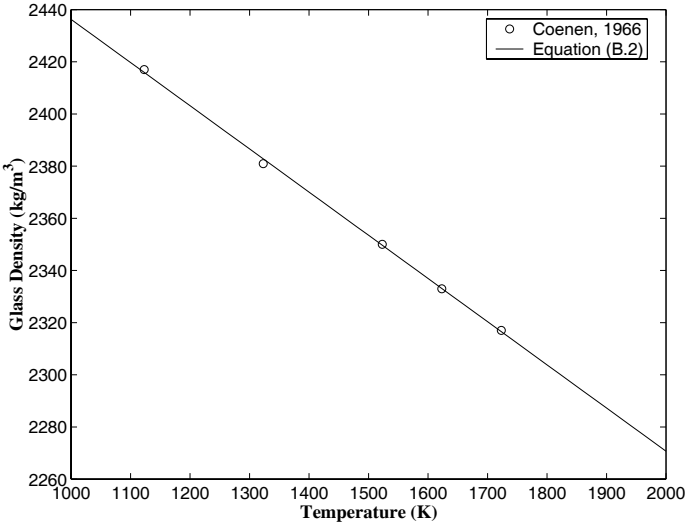

Figure B.1. Effect of temperature on the density of in 74 SiO_2-16 Na_2O-10 CaO (mol.%) soda-lime silicate glass.

= 2346.6 kg/m^3.

[2]This composition is equivalent to 74 SiO_2-16 Na_2O-10 CaO (wt.%)

B.2.2. Dynamic Viscosity

The viscosity of soda-lime silicate glass is strongly dependent on the temperature and less strongly on the glass composition [184]. According to Lakatos *et al.* [184, 224], the viscosity of 74 SiO_2-16 Na_2O-10 CaO (mol.%) soda-lime silicate glass can be expressed as

$$\mu_\infty = 4.448 \times 10^{-3} exp\left[\frac{8982}{T - 539.4}\right] \qquad \text{in Pa s} \tag{B.3}$$

Figure B.2 compares the expression given by Equation (B.3) and the experimental data [188] for the dynamic viscosity of a soda-lime silicate glass melt reproduced in Table B.2 and corresponds to a similar composition (75 SiO_2-15 Na_2O-10 CaO (mol.%)) . Good agreement

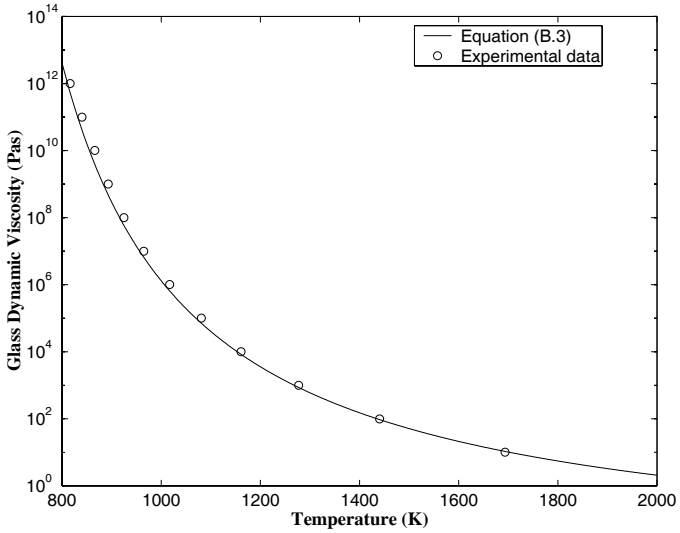

Figure B.2. Effect of temperature on the viscosity of soda-lime silicate glass. The solid line corresponds to a composition of 74 SiO_2-16 Na_2O-10 CaO (mol.%) and experimental data are for 75 SiO_2-15 Na_2O-10 CaO (mol.%) CaO soda-lime silicate.

between Equation (B.3) and experimental data is found. Moreover, it has been shown that the water vapor dissolved in the glass melt greatly lowers its dynamic viscosity at low temperatures (between 1250 and 1450 K) [184]; at higher temperatures the effect of water vapor on the glass melt viscosity is very small [9, 184] and will be neglected in the present study.

In the above expressions, neither the density of the melt ρ_∞ nor its dynamic viscosity μ_∞ depends on the volume fraction of gas bubbles present in the melt since we assumed that bubbles had no effect on the thermophysical properties of the melt (assumption 4). However, if the local gas void fraction in the melt is sufficiently large the density of the mixture decreases, and its viscosity increases [80]. Then, the density of the mixture ρ_m should be expressed as [36]

$$\rho_m = \rho_g \alpha + \rho_\infty (1 - \alpha) \tag{B.4}$$

where α is the local gas void fraction and ρ_g the density of the gas contained in the bubbles. On the other hand, Ishii [80] recommended the following expression for the viscosity of the mixture μ_m for a bubbly flow

$$\frac{\mu_m}{\mu_\infty} = (1-\alpha)^{-1} \tag{B.5}$$

Equation (B.5) indicates that the viscosity of the mixture increases as the gas void fraction increases due to the resistance of the bubbles to the deformation of the flow field caused by their presence. If one wants to consider the effect of the bubbles on the thermophysical properties of the melt, one has to compute simultaneously the thermal flow field of the glass melt and the bubble population balance equation. This calculation is very time consuming and requires significant computational resources; therefore, it will not be considered further.

B.2.3. Surface Tension

The surface tension is a very important property in product glass manufacture. Indeed, it affects the wetting of silicate grains by the first appearing molten glass phase, the corrosion of the refractories as well as the forming process [9]. The surface tension depends on the temperature, the bulk glass composition, the atmosphere composition, and the ions dissolved in the melt such as the sulfate [9]. The effect of all those parameters are discussed in detail in Ref. [184]. In brief, surface tension decreases with increasing temperature and the fraction of CaO and Na_2O. The surface tension σ of 74 SiO_2-16 Na_2O-10 CaO (mol.%) soda-lime silicate glass is given by the following expression [184, 185]:

$$\sigma(T) = 321.7 - 0.04 \times (T - 1173.15) \qquad \text{in mN/m} \tag{B.6}$$

Figure B.3 shows the influence of the temperature on the surface tension of the soda-lime silicate glass of interest as expressed by Equation (B.6). Moreover, it has been observed experimentally that the surface tension of soda-lime silicate was reduced by the presence of gases having a non-zero dipole moment in the atmosphere [186]. Water vapor has been identified as having the most significant effect on the surface tension. The surface tension of soda-lime silicate glass is reduced from 315 mN/m in dry atmosphere to 215 mN/m with a water vapor pressure of 2.13×10^3 Pa at 550^oC [186]. Dietzel and Wegner [225] measured a decrease of the surface tension of 5 mN/m at 850^oC. At higher temperature the effect of water vapor has been considered to be negligible [9, 184]. However, the effect of the atmosphere on the surface tension is of great importance in the formation of glass foam [9], and even a small surface tension depression can have a significant effect on the foam thickness as shown experimentally by Ghag [26] for water+78% glycerine solution. Unfortunately, no data is reported in the literature for the change of surface tension with water vapor pressure at high temperature, therefore this effect will not be considered further.

B.2.4. Specific Heat

Sharp and Ginther [226] studied the effect of temperature and composition on the mean specific heat c_p of soda-lime silicate glasses. They observed that the specific heat varies

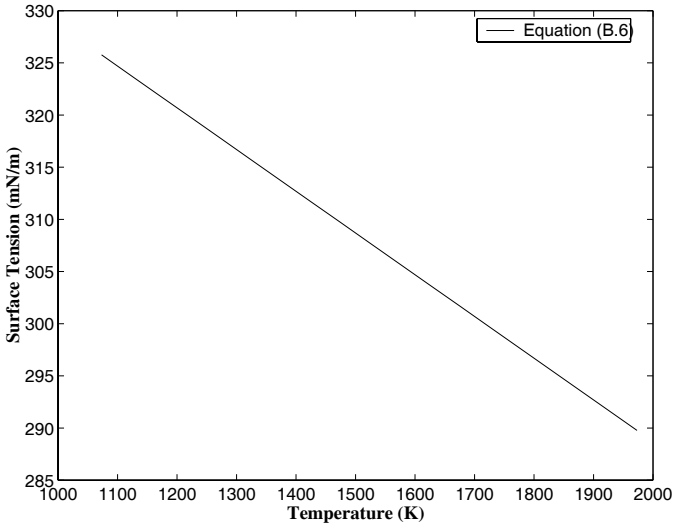

Figure B.3. Effect of temperature on the surface tension of 74 SiO_2-16 Na_2O-10 CaO (mol.%) soda-lime silicate glass, according to Equation (B.6).

slightly with glass composition [227] and for 74 SiO_2-16 Na_2O-10 CaO (mol.%) soda-lime silicate glass they proposed the following expression,

$$c_p(T) = \frac{2.18667T + 138.12}{0.00146T + 0.6012} \qquad \text{in J/kgK} \tag{B.7}$$

As one can see on Figure B.4, the specific heat does not vary significantly over the temperature range of 1000 to 2000 K. Therefore, in the rest of this study the specific heat will be taken as constant and equals to its average value between 1000 and 2000 K, i.e., $c_p = 1231 J/kgK$. This assumption leads, at most, to an error of 5%.

B.2.5. Thermal Diffusivity

The thermal diffusivity α of the glass melt is an important thermophysical property for the thermal flow calculation in the glass melt as well as for the calculation of bubble generation and transport. Van Zee and Babcock [228] reported data for 72.6 SiO_2-14 Na_2O-13.4 CaO (mol.%) soda-lime silicate glass over the temperature range of 1000 to 1700 K (see Table B.3). Those data are shown in Figure B.5 along with the second order polynomial fitting the data and expressed as

$$\alpha(T) = 6.8765 \times 10^{-5} - 1.1948 \times 10^{-7}T + 5.3816 \times 10^{-11}T^2 \qquad \text{in m}^2/\text{s} \tag{B.8}$$

From the experimental thermal diffusivity data and knowledge of the specific heat and the density, an expression for the effective thermal conducitivity k_{eff} of the glass melt can be obtained:

$$k_{eff}(T) = \frac{\alpha(T)}{\rho_\infty c_p} = 213.0084 - 0.3698T + 1.6577 \times 10^{-4}T^2 \qquad \text{in W/mK} \tag{B.9}$$

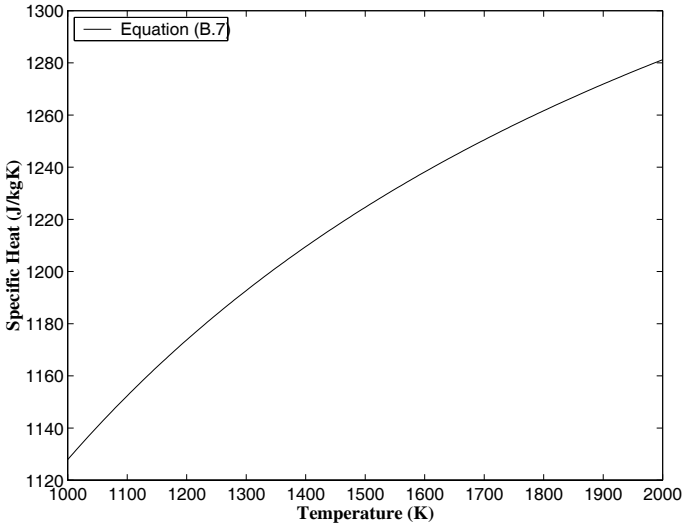

Figure B.4. Effect of temperature on the specific heat of 72.6 SiO_2-14 Na_2O-13.4 CaO (mol.%) soda-lime silicate glass.

Note that the effective conductivity k_{eff} accounts for both conduction and radiative heat transfer in the glass sample and is shown in Figure B.6..

B.3. Gas Properties

Gases can dissolved in the glass melt by physical and/or chemical dissolution. Physical dissolution consist of occupying holes in the network of the molten glass. Physical solubility is higher for small gas molecules and increases slightly with temperature [184]. Gases can also react chemically and create bonds with the glass structure. The latter phenomenon is called chemical solubility and concerns for example oxygen, carbon dioxide, water vapor, and sulfure dioxide [9]. Four gases are considered in this study: nitrogen, oxygen, carbon dioxide, and water vapor, the molar masses of which are reported in Table B.4. The diffusion coefficient and the solubility of each gas in soda-lime silicate melts are discussed in the next few sections.

B.3.1. Gas Diffusion Coefficient in Glass Melt

The most extensive diffusion measurements have been made using fused silica, since this glass is one of the most permeable to gases. Unfortunately, for other types of glass, a few measurements concerning gases other than helium and hydrogen are available [187]. The variation of the diffusion coefficient of the gas species "i" in glass melts as a function of temperature is known to follow an Arrhenius type of law [188]:

$$D_i = D_{0,i} exp\left(-\Delta H_D / RT\right) \tag{B.10}$$

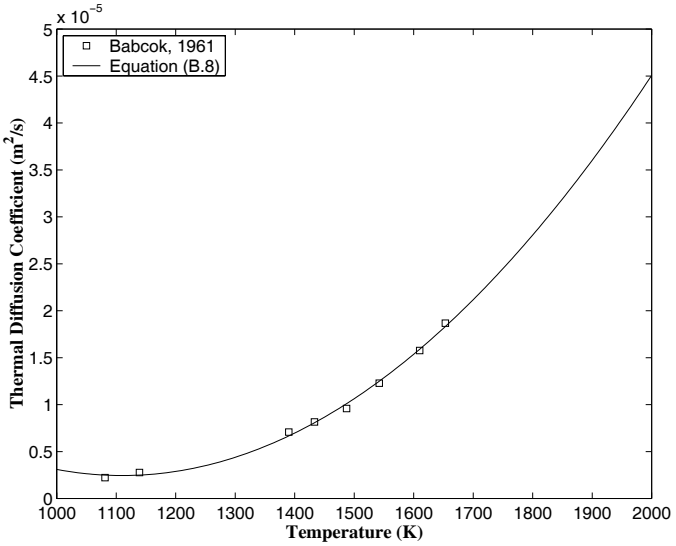

Figure B.5. Effect of temperature on the thermal diffusivity of 75 SiO_2-15 Na_2O-10 CaO (mol.%) soda-lime silicate glass.

where $D_{0,i}$ and ΔH_D are empirically determined constants.

- **Nitrogen**
  The diffusion coefficient of nitrogen in soda-lime silicate melts increases slightly with increasing temperature and varies very little with glass composition [139]. Table B.5 gives the diffusion coefficient of nitrogen in soda-lime silicate melts obtained by different authors. A fit of the experimental data has been performed leading to the following expression of the diffusion coefficient of nitrogen in 74 SiO_2-16 Na_2O-10 CaO (mol.%) soda-lime silicate glass:

$$D_{N_2} = 8.1 \times 10^{-5} exp\,(-20103/T) \tag{B.11}$$

  Figure B.7 shows the temperature dependence of the diffusion coefficient of nitrogen in soda-lime silicate glass reported in Table B.5 and the expression given by Equation (B.11). Even though the number of available data were limited, the reported data appear to agree remarkably well.

- **Oxygen**
  Diffusion coefficient of oxygen in the molten glass varies significantly from one type of glass to another as shown by Doremus [189] for soda-lime silicate, barium aluminum alkali silicate and borosilicate melts. Table B.6 summarizes the diffusion coefficients of oxygen in soda-lime silicate melts obtained by different authors. A fit of the experimental data presented by Terai and Oishi [190] gives the following expression for the diffusion coefficient of oxygen in 71.7 SiO_2-15.5 Na_2O-12.8 CaO (mol.%) soda-lime silicate glass:

$$D_{O_2} = 3.2 \times 10^{-6} exp\,(-21076/T) \tag{B.12}$$

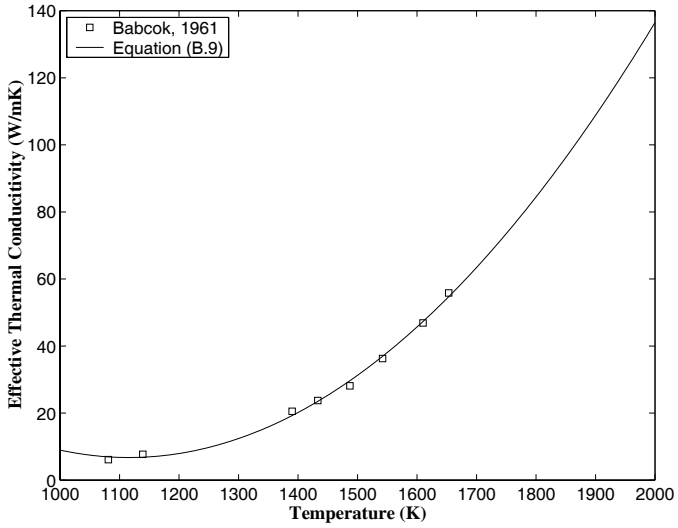

Figure B.6. Effect of temperature on the effective thermal conductivity of 75 SiO_2-15 Na_2O-10 CaO (mol.%) soda-lime silicate glass.

A fit of data reported by Doremus [189] for a commercial soda-lime silicate glass leads to the following expression:

$$D_{O_2} = 1.14 \times 10^{-3} exp\left(-24946/T\right) \tag{B.13}$$

Unfortunately, the composition of the glass studied by Doremus [189] is unknown and it is believed to contain other elements such as MgO and Al_2O_3 [188]. Figure B.8 is a plot of the experimental data summarized in Table B.6 and the expression of the diffusion coefficient as a function of temperature given by Equations (B.12) and (B.13). The discrepancies among experimental data are assumed to be due the differences of the glass compositions. It was decided to use the data reported by Terai and Oishi [190] since they cover a wider range of temperatures, and the glass studied had a very similar composition as the one of interest in the present study i.e., 74 SiO_2-16 Na_2O-10 CaO (mol.%).

- **Carbon Dioxide**
  The only piece of information available in the literature concerning the diffusion coefficient of carbon dioxide in soda-lime silicate glass is the following expression proposed by Nemec and Muhlbauer [191] and ploted in Figure B.9

$$D_{CO_2} = 7.95 \times 10^{-9} exp\left(-11332/\left(T - 473.4\right)\right) \tag{B.14}$$

- **Water Vapor**
  Only a few data have been reported for the diffusion coefficient of water in soda-lime

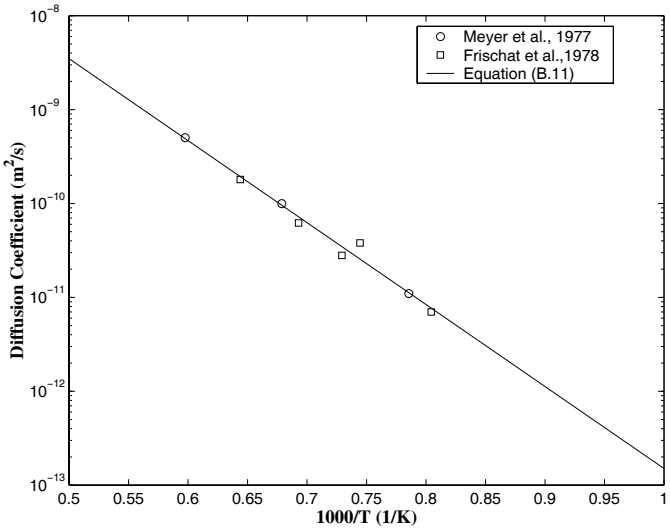

Figure B.7. Effect of temperature on the diffusion coefficient of nitrogen in soda-lime silicate melt.

silicate glass [143, 191, 229, 230]. Data for 74 SiO_2-16 Na_2O-10 CaO (mol.%) soda-lime silicate glass reported by Scholze and Mulfinger [229] are reproduced in Table B.7. Fit of those data gives

$$D_{H_2O} = 1.83 \times 10^{-6} exp\,(-13830/T) \tag{B.15}$$

Finally, a comparison of the expressions of the diffusion coefficient of the four gas considered in this study in the 74 SiO_2-16 Na_2O-10 CaO (mol.%) soda-lime silicate glass, over the temperature range of 1000 K to 2000 K, is provided in Figure B.11. Nitrogen appears to have the highest diffusion coefficient while carbon dioxide has the smallest one.

B.3.2. Gas Solubility in Glass Melt

Solubility is the amount of dissolved gas per unit mass of melt per unit of applied pressure. Solubility is expressed in many different unit. The common unit is the volume of gas at standard temperature and pressure (STP, 0^oC and 1 atm) per unit volume of material exposed at one atmosphere of gas (m^3 (STP)/m^3atm). It can also be expressed in kg/m^3Pa. Doremus [187] pointed out that these definitions contain implicitly a temperature dependence since the applied pressure follows the ideal gas law, $P = nRT/V$. Instead, Doremus [187] suggested the use of "Ostwald solubility" defined as the ratio of the concentration of the gas in the material and the concentration of the gas in the surrounding atmosphere:

$$S_{i,Os} = \frac{C_i}{C_g} \tag{B.16}$$

where C_i and C_g are the concentration of the gas in the material and the concentration of the gas in the surrounding atmosphere, respectively. However, in the present work solubility

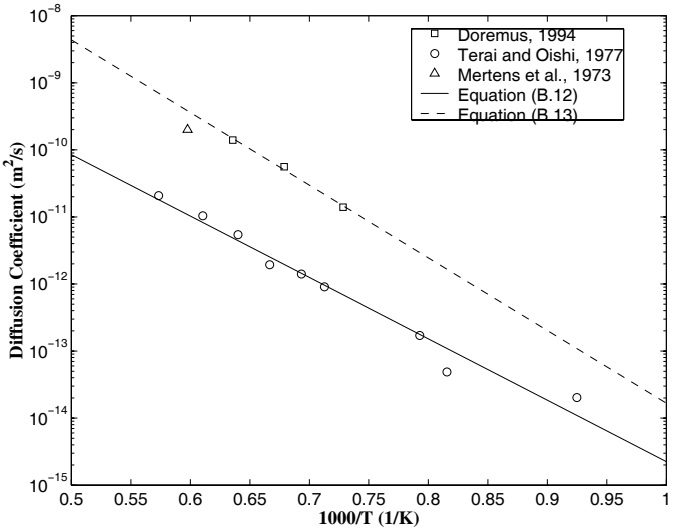

Figure B.8. Effect of temperature on the diffusion coefficient of oxygen in soda-lime silicate melt.

will be expressed in mol of gas per unit volume of liquid phase per unit external partial pressure of the gas (mol/m^{3}Pa) as used in the most common form of the Henry's law. The relationships between the different units for solubility are:

$$1[mol/m^3Pa] = \frac{1}{RT_{STP}}[m^3(STP)/m^3atm] = \frac{1}{RT}S_{i,Os} \tag{B.17}$$

where R is the universal gas constant (=8.314J/molK), M_i is the molar mass of gas species "i" expressed in kg/mol, ρ_∞ is the glass melt density, T is the experimental temperature, and T_{STP} is the standard temperature (=273.15K). In the following sections we have assumed that the solubility expressed in mol/m^{3}Pa follows an Arrhenius type of law:

$$S_i = S_{i,0}exp\,(-\Delta H_i/RT) \tag{B.18}$$

where $S_{0,j}$ andΔH_S are constants determined experimentally.

- **Nitrogen**
  Solubility of nitrogen in soda-lime silicate melts increases slightly with increasing temperature [139]. A fit of the data reported in Table B.8 for the solubility of nitrogen in 74 SiO_2-16 Na_2O-10 CaO (mol.%) soda-lime silicate melts give the following expression,

  $$S_{N_2} = 9.3 \times 10^{-6}exp\,(-6414/T) \qquad \text{in mol/m}^3\text{Pa} \tag{B.19}$$

  Figure B.12 plots the experimental data reported in Table B.8 and compares the data with Equation (B.19).

- **Oxygen**
  The solubility of oxygen depends strongly on glass composition and may vary from 0 to 9.33×10^{-4} mol/m^{3}Pa [192]. The increase in solubility is due to the presence

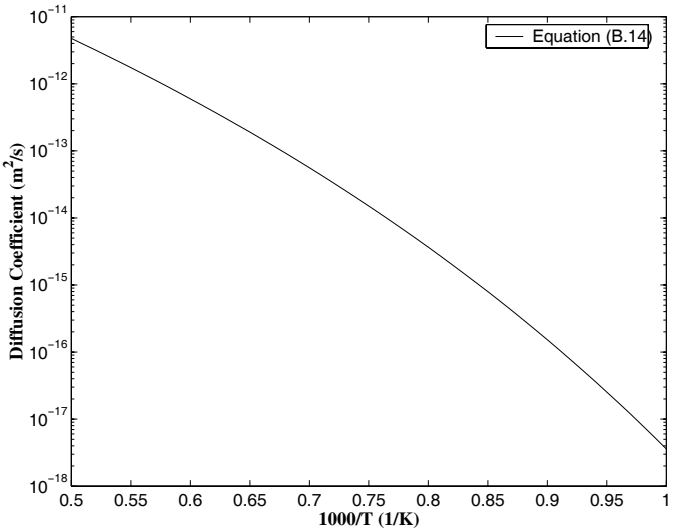

Figure B.9. Effect of temperature on the diffusion coefficient of carbon dioxide in soda-lime silicate melt.

of suitable elements of variable valence such as antimony oxide or arsenic [192]. The only data available concerning the solubility of oxygen in soda-lime silicate is [134],

$$S_{O_2} = 3.0 \times 10^{-6} \qquad \text{in mol/m}^3\text{Pa} \tag{B.20}$$

- **Carbon Dioxide**
  Table B.9 provides the solubility of carbon dioxide in soda-lime silicate melt. An expression of solubility of carbon dioxide is available in the literature [191]:

  $$S_{CO_2} = 3.45 \times 10^{-6} exp\,(3840/T) \qquad \text{in mol/m}^3\text{Pa} \tag{B.21}$$

  Figure B.13 shows the experimental data reported in Table B.9 and Equation (B.21), reasonable agreement is found.

- **Water Vapor**
  Table B.10 summarizes some experimental data for solubility of water vapor in soda-lime silicate. An expression for water vapor solubility in a glass melt of complex composition is available in the literature [191]. However, it has been noted that the water vapor solubility in glass melts depends on glass composition [231] and slightly on temperature [230,232]. Therefore, data for 74 SiO_2-16 Na_2O-10 CaO (mol.%) soda-lime silicate reported in Table B.10 were fitted and the solubility of water vapor is expressed as

  $$S_{H_2O} = 1.8 \times 10^{-3} exp\,(-407/T) \qquad \text{in mol/m}^3\text{Pa} \tag{B.22}$$

Finally, Figure B.15 compares the expressions for the solubility of the four gas considered in this study over the temperature range of 1000 K to 2000 K. Nitrogen appears to have the

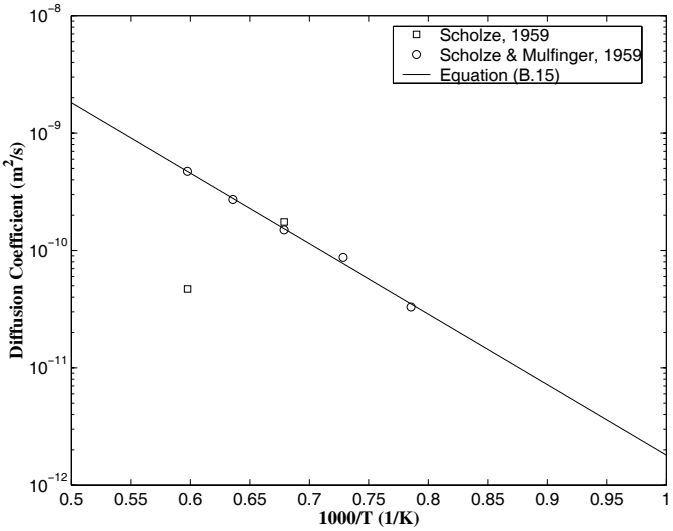

Figure B.10. Effect of temperature on the diffusion coefficient of water in soda-lime silicate melt.

highest diffusion coefficient in soda-lime silicate glass while carbon dioxide has the lowest one.

B.4. Refining Reactions

The refining reaction involving variable-valence metal oxides can be written in the following generalized form [160],

$$M^{k+} + \frac{k-j}{2} O^{2-} \rightleftharpoons \frac{k-j}{4} O_2 + M^{j+} \tag{B.23}$$

By assuming a constant oxygen ion activity and by defining q as the order of the refining reaction occurring at constant volume, the rate of the decomposition reaction can be expressed as

$$-\frac{\partial[M^{k+}]}{\partial t} = \frac{k-j}{4}\frac{\partial[O_2]}{\partial t} = k_r[M^{k+}]^q \tag{B.24}$$

where the reaction rate constant k_r is calculated from the Arrhenius' law,

$$k_r = Aexp(-\frac{E}{RT}) \tag{B.25}$$

with the constants A and E determined experimentally. In the case of antimony oxide as a refining agent, Kawachi and Kawase [133, 150] and Kawachi and Kato [151] showed that the rate of the forward reaction can be neglected in the production of TV-panel glass. Therefore, the refining reaction can be considered as irreversible with only the decomposition

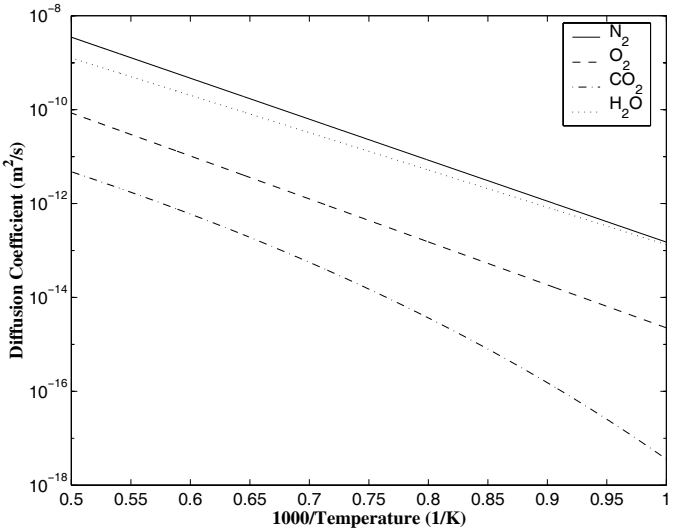

Figure B.11. Comparison of the diffusion coefficient of nitrogen, oxygen, carbon dioxide, and water in 74 SiO_2-16 Na_2O-10 CaO (mol.%) soda-lime silicate melt as a function of the temperature over the range of 1000K to 2000K.

of the refining agent taking place. The decompositon of the antimony oxide is characterized by [151]

$$\begin{cases} q = 3.3 \\ A = 2.347 \times 10^{11}\mathrm{s}^{-1} \\ E = 4.247545 \times 10^{5}\mathrm{J/mol} \end{cases} \tag{B.26}$$

Table B.1. Density of 74 SiO_2-16 Na_2O-10 CaO (wt.%) soda-lime silicate glass melt.

SiO_2 mol.%	**CaO mol.%**	**Na_2O mol.%**	**Temperature** (K)	**Density (kg/m^3)**	**References**
73.8	10.7	15.5	1123.15	2406.5	
73.8	10.7	15.5	1323.15	2373.9	
73.8	10.7	15.5	1523.15	2344.5	Coenen [223]
73.8	10.7	15.5	1623.15	2325.5	
73.8	10.7	15.5	1723.15	2311.7	

Table B.2. Dynamic viscosity of 75 SiO_2-15 Na_2O-10 CaO (mol.%) soda-lime silicate glass melt.

SiO_2 mol.%	**CaO mol.%**	**Na_2O mol.%**	**Temperature** (K)	**Dynamic Viscosity (Pa s)**	**References**
75	10	15	816.15	10^{12}	
75	10	15	840.15	10^{11}	
75	10	15	866.15	10^{10}	
75	10	15	893.15	10^{9}	
75	10	15	925.15	10^{8}	
75	10	15	965.15	10^{7}	Bansal and Doremus [188]
75	10	15	1017.15	10^{6}	
75	10	15	1081.15	10^{5}	
75	10	15	1161.15	10^{4}	
75	10	15	1277.15	10^{3}	
75	10	15	1440.15	10^{2}	
75	10	15	1693.15	10	

Table B.3. Thermal diffusivity of 75 SiO_2-15 Na_2O-10 CaO (mol.%) soda-lime silicate glass melt.

SiO_2 mol.%	**CaO mol.%**	**Na_2O mol.%**	**Temperature** (K)	**Thermal Diffusivity (m^2/s)**	**References**
72.6	13.4	14	1653.15	1.868×10^{-5}	
72.6	13.4	14	1610.15	1.576×10^{-5}	
72.6	13.4	14	1542.15	1.228×10^{-5}	
72.6	13.4	14	1487.15	9.59×10^{-6}	Van Zee and Babcock [228]
72.6	13.4	14	1433.15	8.15×10^{-6}	
72.6	13.4	14	1390.15	7.08×10^{-6}	
72.6	13.4	14	1139.15	2.77×10^{-6}	
72.6	13.4	14	1081.15	2.22×10^{-6}	

Table B.4. Molar mass for oxygen, nitrogen, carbon dioxide and water vapor.

	O_2	**N_2**	CO_2	H_2O
Molar Mass(g/mol)	32.00	28.01	44.01	18.02

Table B.5. Diffusion coefficient of nitrogen in 74 SiO_2-16 Na_2O-10 CaO (mol.%) soda-lime silicate glass melt.

SiO_2 mol.%	**CaO mol.%**	**Na_2O mol.%**	**Temperature** (K)	**Diffusion Coefficient (m^2/s)**	**References**
			1273.15	1.1×10^{-11}	
			1473.15	1.0×10^{-10}	Meyer *et al.* [233, 234]
			1673.15	5.0×10^{-10}	
76	10	14	1243.15	7.0×10^{-12}	
76	10	14	1343.15	3.8×10^{-11}	
76	10	14	1371.15	2.8×10^{-11}	Frischat *et al.* [235]
76	10	14	1443.15	6.2×10^{-11}	
76	10	14	1553.15	1.8×10^{-10}	

Table B.6. Diffusion coefficient of oxygen in soda-lime silicate glass melt.

SiO_2 mol.%	**CaO mol.%**	**Na_2O mol.%**	**Temperature** (K)	**Diffusion Coefficient (m^2/s)**	**References**
			1373.15	1.4×10^{-11}	
			1473.15	5.6×10^{-11}	Doremus [189]
			1573.15	1.4×10^{-10}	
71.7	12.8	15.5	1081.15	2.03×10^{-14}	
71.7	12.8	15.5	1226.15	4.90×10^{-14}	
71.7	12.8	15.5	1261.15	1.70×10^{-13}	
71.7	12.8	15.5	1403.15	9.04×10^{-13}	
71.7	12.8	15.5	1442.15	1.40×10^{-12}	Terai and Oishi [190]
71.7	12.8	15.5	1500.15	1.93×10^{-12}	
71.7	12.8	15.5	1562.15	5.47×10^{-12}	
71.7	12.8	15.5	1638.15	1.04×10^{-11}	
71.7	12.8	15.5	1744.15	2.08×10^{-11}	
			1673.15	2.0×10^{-10}	Mertens *et al.* [236]

Table B.7. Diffusion coefficient of water in soda-lime silicate glass melt.

SiO_2 mol.%	**CaO+MgO mol.%**	**Na_2O mol.%**	**Temperature** (K)	**Diffusion Coefficient (m^2/s)**	**References**
			1473.15	1.75×10^{-10}	Scholze [237]
			1673.15	4.70×10^{-11}	
74.1	9.4	16.5	1273.15	0.33×10^{-10}	
74.1	9.4	16.5	1373.15	0.87×10^{-10}	Scholze and
74.1	9.4	16.5	1473.15	1.50×10^{-10}	Mulfinger [229]
74.1	9.4	16.5	1573.15	2.72×10^{-10}	
74.1	9.4	16.5	1673.15	4.72×10^{-10}	

Table B.8. Solubility of nitrogen in 74 SiO_2-16 Na_2O-10 CaO (mol.%) soda-lime silicate glass melt.

SiO_2 mol.%	**CaO mol.%**	**Na_2O mol.%**	**Temperature** (K)	**Solubility mol/Pa m^3**	**References**
			1673.15	2.2×10^{-7}	
			1673.15	2.47×10^{-7}	Meyer *et al.* [233, 234]
			1673.15	2.33×10^{-7}	
74	10	16	1573.15	1.63×10^{-7}	
74	10	16	1673.15	1.85×10^{-7}	Mulfinger *et al.* [238]
74	10	16	1783.15	2.51×10^{-7}	
74	10	16	1673.15	1.7×10^{-7}	Mulfinger [239]

Table B.9. Solubility of carbon dioxide in soda-lime silicate glass melt.

SiO_2 mol.%	**CaO mol.%**	**Na_2O mol.%**	**Temperature** (K)	**Solubility mol/Pa m^3**	**References**
74	10	16	1673.15	in progress	Mahieux [234, 240]

Table B.10. Solubility of water vapor in soda-lime silicate glass melt.

SiO_2 mol.%	**CaO mol.%**	**Na_2O mol.%**	**Temperature** (K)	**Solubility mol/Pa m^3**	**References**
74	10	16	1523.15	1.35×10^{-3}	
74	10	16	1593.15	1.36×10^{-3}	Scholze [188]
74	10	16	1673.15	1.37×10^{-3}	
74	10	16	1753.15	1.40×10^{-3}	

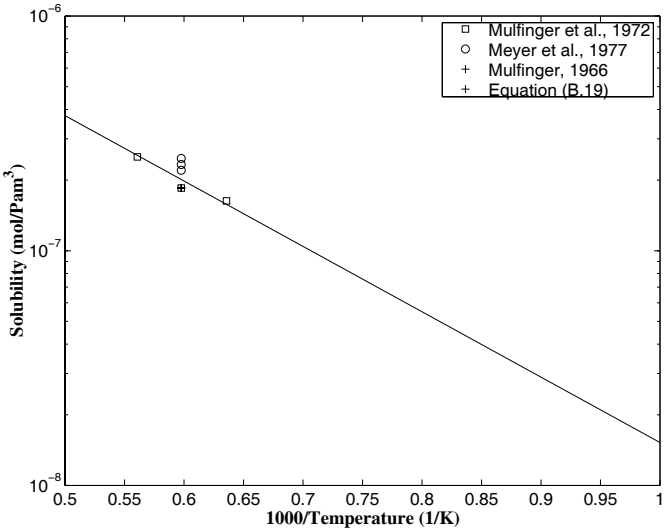

Figure B.12. Effect of temperature on the solubility of nitrogen in soda-lime silicate melt.

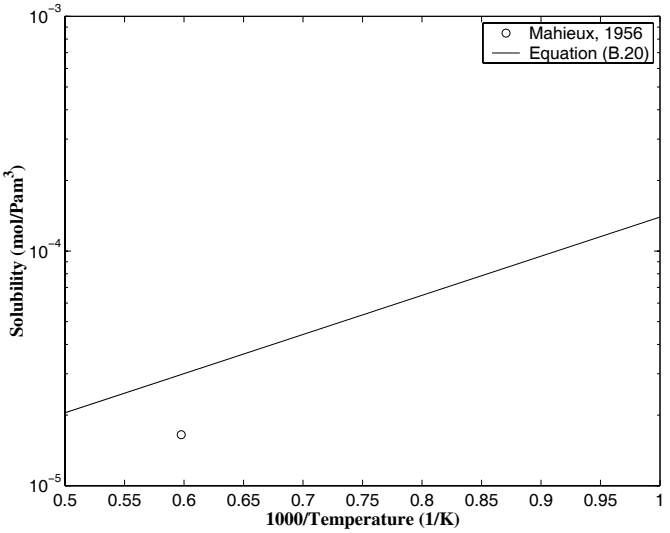

Figure B.13. Effect of temperature on the solubility of carbon dioxide in soda-lime silicate melt.

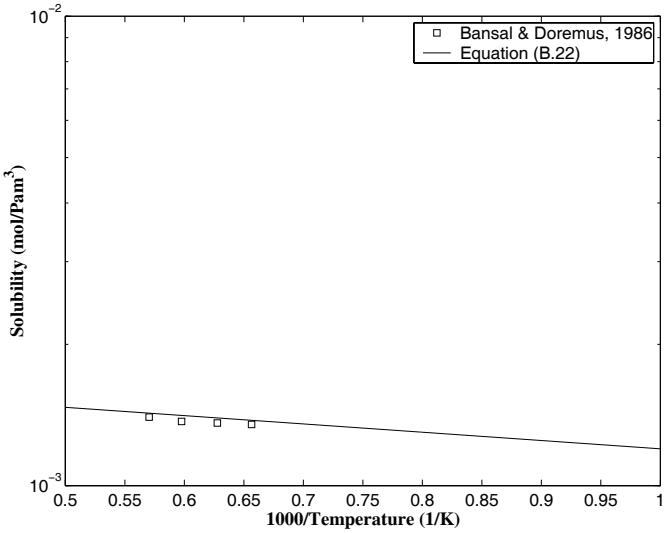

Figure B.14. Effect of temperature on the solubility of water vapor in soda-lime silicate melt.

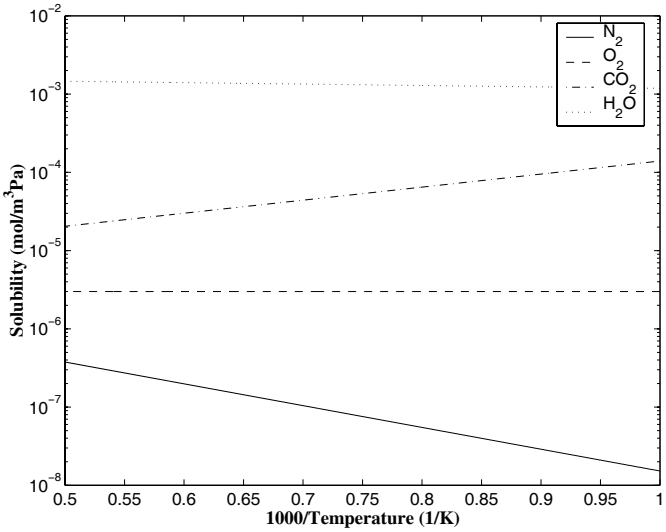

Figure B.15. Comparison of the solubility of nitrogen, oxygen, carbon dioxide, and water in 74 SiO_2-16 Na_2O-10 CaO (mol.%) soda-lime silicate as a function of the temperature over the range of 1000K to 2000K.

C. MODIFIED METHOD OF CHARACTERISTICS FOR SOLVING POPULATION BALANCE EQUATION

C.1. Introduction

Physical modeling of multidimensional two-phase flow has been the subject of intense research over the last half century. The two-fluid model is often considered as the most sophisticated multidimensional models available in the literature [156, 157]. In three-dimensional gas/liquid flows, the two-fluid model is comprised of ten scalar partial differential equations, five scalar algebraic interfacial jump conditions, and eleven state variables. However, as reviewed by Lahey and Drew [157], while the rigorous derivation of the two-fluid models has made significant progresses, " no model exists to date which is completely acceptable". Moreover, mechanistic interfacial and wall closure laws are still needed to accurately model three-dimensional two-phase flow [157]. More recently, Carrica *et al.* [158] have presented a three-dimensional computational model for two-phase flow around a naval surface ship. The formulation is based on a multidimensional two-fluid model consisting of the continuity and the momentum equations for both the gas and the liquid phases combined with the conservation equation for the total number of bubbles. The numerical algotrithm is based on a finite-difference method and can calculate the gas volume fraction and bubble radius, and accounts for the coupling between the gas and the liquid equations. However, it is limited to monodispersed bubble population, i.e., all the bubbles at each location have the same radius. This was recognized as an obvious limitation. However, such limitation could be overcome by solving the bubble population balance equation for a polydisperse bubble density function.

Both analytical and numerical methods for solving the population balance equation have been recently reviewed by Ramkrishna [58]. For most practical problems, numerical methods are required if one wants to avoid simplistic assumptions. Discretization of the density function has been one of the most popular numerical methods [58,154,162,176,241]. It consists of discretizing the particle density function in the internal space, thus forming groups of particles and solving the resulting equations for the total number of particles in each group by a finite-difference method. Such method has the advantage to reduce computational times, a valuable feature in control and optimization of particulate systems [58]. However, the discrete formulation has major drawbacks that have been discussed extensively by Kumar and Ramkrishna [155, 242]. In brief, the discrete formulation lacks of *internal consistency*, i.e., some of the moments of the particle density function cannot be predicted accurately. In other words, the calculation is designed for certain selected moments of the particle density function rather than for an estimate of the particle density function accurate enough for estimating all moments of the population [58]. For example, in gas/liquid flows in which bubbles are defined by their radius r at time t, the m^{th} sectional and total

moments of the bubble density function f_1 in terms of bubble radius, denoted by $\mu_m^{(i)}(\vec{x},t)$ and $\mu_m(\vec{x},t)$, respectively, are defined as

$$\mu_m^{(i)}(\vec{x},t) = \int_{r_i}^{r_{i+1}} r^m f_1(\vec{x},r,t)\mathrm{d}r \qquad \text{and} \qquad \mu_m(\vec{x},t) = \int_{r_0}^{r_N} r^m f_1(\vec{x},r,t)\mathrm{d}r = \sum_{i=0}^{N-1} \mu_m^{(i)}(t) \tag{C.1}$$

where r_0 and r_N are the minimum and maximum bubble radius. The total number of bubbles, the average bubble radius, the interfacial area concentration the local volume fraction of gas (for the mass conservation equation) are physically important moments of the bubble density function and correspond to zero, first, second, and third order moments in terms of the bubble radius, respectively. Another important moment is the total mass of gas contained in the bubbles defined as the third order moment in term of variable $4\pi r^3\rho_g/3$. The total number of particles, the average particle radius, the interfacial area concentration, the local volume fraction of gas are essential physically important moments of the particle density function and correspond to zero, first, second, and third order moments in terms of the particle radius, respectively. Another important moment is the total mass of gas contained in the particles defined as the third order moment in term of variable $4\pi r^3\rho_g/3$. In addition to the total number of particles for each discrete group, the discretized formulation for all these moments should also be solved if one wants to accurately predict (1) the interfacial mass and momentum transfer between the phases [156, 157]), [156, 157], (2) the flow regime often determined from the void fraction, and (3) other closure laws of the two-fluid model [156]. A simplified version of this approach has been developed by Rousseaux *et al.* [162] who solved the coupled conservation equations for the first four total moments of the density function of pseudo-boehmite particles accounting for growth and precipitation in sliding surface mixing device.

The method of characteristics, on the other hand, consists of transforming the partial differential population balance equation into an ordinary differential equation (ODE) which is then solved along the pathline of the particles (characteristic curves). Unlike finite-difference methods that propagate the information along coordinate lines, the method of characteristics propagates the information along the pathlines and thus matches the physics of the flow resulting in extremely accurate numerical results [181]. Another advantage of the method of characteristics is to overcome the numerical diffusion introduced by finite-difference methods [179]. The conventional implementation (*or direct marching method*) of the method of characteristics is based on the Lagrangian formulation. The particles or the particle density function are identified and located at initial time $t = t_0$ and followed at subsequent time as the particles are transported. However, the deformation that the initial mesh undergoes as time progresses might lead to deterioration of the numerical solution particularly in three-dimensional flows [243]. The modified method of characteristics (*or inverse marching method*) is an intepretation of the Lagrangian approach that overcomes the difficulties related to mesh deformation [243]. Based on a pre-specified grid, it follows the particles backward in time as opposed to foward in the case of direct marching method. Unlike the direct marching method, the inverse marching method uses a fixed grid that can also be used for solving other transport equations such the continuity, momentum, and energy equations or the gas concentration in the continuous phase by finite-difference methods using a staggered grid as suggested by Patankar [179]. Thus, interactions between the particles and the surrounding fluid can be easily accounted for in the numerical

scheme. Moreover, the modified method of characteristics can be used for both transient and steady-state calculations with great accuracy and without problems of numerical instability. However, it possesses significant although not overwhelming disadvantages [181]: (1) it is a relatively complicated procedure, especially for more than three or four independent variables, (2) the method is restricted to flows without discontinuities, and (3) due to the large amount of required interpolations and integration of the governing ODEs, the computer programs require long execution times.

The modified method of characteristics has been successfully used for predicting high speed three-dimensional inviscid flows in subsonic and supersonic propulsion nozzles [181, 244–246] and combined with finite elements method for solving unsteady incompressible Navier-Stokes equations [243]. The conventional method of characteristics for solving the population balance equation has been mainly used (1) for mathematical arguments to show the existence of solution [58], (2) for obtaining analytical solutions [58, 247–249], and (3) for obtaining numerical solution for two independent variables problems [155]. However, to the best of our knowledge, no attempt has been made to solve the population balance equation by the modified method of characteristics. As computers become more powerful and cheaper, the present approach favors accuracy and numerical stability over short computational time and algorithm simplicity. This document presents a numerical implementation of the modified method of characteristics for solving the population balance equation in multiphase particulate systems that could be coupled to other numerical schemes for solving the two-fluid model equations.

C.2. Population Balance Model

The present study is concerned with solving the population balance equation for solid or fluid particle transport in three-dimensional multiphase flow using the modified method of characteristics. A Cartesian coordinate system was employed in the analysis. The formulation of the population balance equation is based on the following general assumptions that hold for many different multiphase particulate systems:

1. The effects of particles and dissolved gases on the velocity and on the temperature fields as well as on the thermophysical properties of the liquid phase are not considered.
2. The particles are perfectly spherical in shape.
3. The particles have negligible inertia ($\rho_b \ll \rho_\infty$). This hypothesis is reasonable since very small particles are considered.
4. The liquid is incompressible.
5. Local thermal equilibrium exists between the gas and liquid phases, i.e., $T_\infty = T_b = T$.
6. Aggregation and break up of particles are not considered.
7. The components of the particle velocity vector, are taken to be the same as those of the molten glass (u_∞, v_∞, w_∞), except in the vertical direction where the buoyancy force has to be taken into account, i.e.,

$$\vec{v_b}(r) = u_\infty \vec{i} + v_\infty \vec{j} + (w_\infty - w_r)\vec{k} \tag{C.2}$$

with w_r being the upward particle velocity relative to the liquid phase due to the buoyancy force and is assumed to follow Stokes' law, i.e.,

$$w_r = \frac{2}{9}\frac{\rho_\infty g r^2}{\mu_\infty} \tag{C.3}$$

Note that (i) according to our convention, the vertical axis is oriented downward, (ii) Equation (C.3) corresponds to the terminal (i.e., steady state) velocity of spherical bubbles, i.e., the transient motion and inertia of bubbles have not been considered for the sack of simplificity and since its formulation is still incomplete and quite involved [83].

As discussed in detail by Ramkrishna [58, 172], the bubble population can be described by a state vector defined in a so-called state space. The state space consists not only of the physical space (i.e., the environment of the continuous phase) but also of an abstract "property" space. In the physical space, the state vector coordinates consist of the spatial coordinates [e.g., (x, y, z) in Cartesian coordinates]. In the property space, the system is characterized by its property coordinates. For example, each particle is characterized by its radius r and other properties denoted p_i such as gas molar fractions in the case of bubbles. The spatial and property coordinates are also referred as the external and internal coordinates, respectively. Considering the particles transported by the liquid flow and characterized by their radius r and l other internal properties p_i the state vector $\vec{S}$ can be written as $\vec{S} = [x, y, z, t, r, (p_i)_{1\leq i\leq l}]$. Then, the population balance equation can be expressed as

$$\frac{\partial f_1}{\partial t} + \frac{\partial}{\partial x}(u_\infty f_1) + \frac{\partial}{\partial y}(v_\infty f_1) + \frac{\partial}{\partial z}[(w_\infty - w_r) f_1] + \frac{\partial}{\partial r}(\dot{r} f_1) + \sum_{i=1}^{l} \frac{\partial}{\partial p_i}(\dot{p}_i f_1) = h \tag{C.4}$$

The time rate of change of the radius and of the other properties of the particles are denoted by $\dot{r}$ and $\dot{p}_i$, respectively. Finally, $h = h(\vec{x}, t, r, p_i)$ represents the net rate of production of particles of a particular state ($\vec{x}$, r, $(p_i)_{1\leq i\leq l}$) at time t.

C.3. Method of Characteristics

The population balance equation [Equation (C.4)] is solved using the method of characteristics. If we assume that the liquid phase can be treated as incompressible, the mass conservation equation for the liquid phase can be expressed as [180]

$$\frac{\partial u_\infty}{\partial x} + \frac{\partial v_\infty}{\partial y} + \frac{\partial w_\infty}{\partial z} = 0 \tag{C.5}$$

Expanding the partial derivatives on the left-hand side of Equation (C.4) and using Equation (C.5) yields

$$\frac{\partial f_1}{\partial t} + u_\infty \frac{\partial f_1}{\partial x} + v_\infty \frac{\partial f_1}{\partial y} + w_\infty \frac{\partial f_1}{\partial z} + \dot{r}\frac{\partial f_1}{\partial r} + \sum_{i=1}^{l} \dot{p}_i \frac{\partial f_1}{\partial p_i} = h + f_1 \left[\frac{\partial w_r}{\partial z} - \frac{\partial \dot{r}}{\partial r} - \sum_{i=1}^{l} \frac{\partial \dot{p}_i}{\partial p_i} \right] \tag{C.6}$$

By definition, the total time derivative of f_1 with respect to time t can be written as

$$\frac{\mathrm{d}f_1}{\mathrm{d}t} = \frac{\partial f_1}{\partial t} + \frac{\mathrm{d}x}{\mathrm{d}t}\frac{\partial f_1}{\partial x} + \frac{\mathrm{d}y}{\mathrm{d}t}\frac{\partial f_1}{\partial y} + \frac{\mathrm{d}z}{\mathrm{d}t}\frac{\partial f_1}{\partial z} + \frac{\mathrm{d}r}{\mathrm{d}t}\frac{\partial f_1}{\partial r} + \sum_{i=1}^{l}\frac{\mathrm{d}p_i}{\mathrm{d}t}\frac{\partial f_1}{\partial p_i} \tag{C.7}$$

We further define the characteristic curves in the particle state space as

$$\frac{\mathrm{d}x}{\mathrm{d}t} = u_\infty(x,y,z) \tag{C.8}$$

$$\frac{\mathrm{d}y}{\mathrm{d}t} = v_\infty(x,y,z) \tag{C.9}$$

$$\frac{\mathrm{d}z}{\mathrm{d}t} = w_\infty(x,y,z) - w_r(x,y,z,r) \tag{C.10}$$

$$\frac{\mathrm{d}r}{\mathrm{d}t} = \dot{r}[x,y,z,,r,(p_i)_{1\le i\le l},t] \tag{C.11}$$

$$\frac{\mathrm{d}p_i}{\mathrm{d}t} = \dot{p}_i[x,y,z,r,(p_i)_{1\le i\le l},t] \qquad \text{for} \quad i=1,...,l \tag{C.12}$$

Then, along the characteristic curves in the [x,y,z,r,$(p_i)_{1\le i\le l}$, t] space, the population balance equation can be written as

$$\frac{\mathrm{D}f_1}{\mathrm{D}t} = h + f_1\left[\frac{\partial w_r}{\partial z} - \frac{\partial \dot{r}}{\partial r} - \sum_{i=1}^{l}\frac{\partial \dot{p}_i}{\partial p_i}\right] \tag{C.13}$$

where $\mathrm{D}f_1/\mathrm{D}t$ denotes the substantial derivative, i.e., the total time derivative along the pathline of the particle. The partial derivative of w_r with respect to z is obtained from Equation (C.3) and is expressed as

$$\frac{\partial w_r}{\partial z} = \frac{4\rho_\infty g r\dot{r}}{9\mu_\infty(w_\infty - w_r)} - \frac{2\rho_\infty g r^2}{9\mu_\infty^2}\frac{\partial \mu_\infty}{\partial z} \tag{C.14}$$

Similarly, expressions for $\dot{r}$ and $\dot{p}_i$ and their derivatives with respect to r and p_i, respectively, can be obtained based on physical considerations of the specific process to be modeled.

In the method of characteristics, no boundary condition is required at the outflow while particle density function is specified at the inlet boundary,

$$f_1(x_0,y_0,z_0,t) = f_{1,0}[r,(p_{0,i})_{1\le i\le l},t] \tag{C.15}$$

At the container walls/liquid interface the gradient of the particle density function f_1 in the normal direction vanishes,

$$\nabla_{\vec{n}} f_1 = \vec{0} \qquad \text{at the liquid/walls interface} \tag{C.16}$$

Assumptions regarding the bubble velocity and neglect of the effects of bubbles on the liquid phase flow and temperature fields are the most severe one and their limitations will be discussed later in this document. They have been used to decouple the conservation, momentum, and energy equations of the liquid and gas phases. This approach can be justified by the facts that bubble radius and concentration are small and that the alternative approach in solving the coupled governing equations using the multidimensional two-fluid

model lacks mechanistic closure laws accounting, for example, for the interfacial mass and momentum transfer [157].

C.4. Numerical Method

In the present model, the liquid flow is assumed not to be affected by the presence of particles; therefore, the velocity and temperature fields in the liquid phase are treated as fixed input parameters. The system of equations for the velocity and temperature fields are parabolic in nature and can be discretized in space using a $(l_1 \times m_1 \times n_1)$ staggered grids for the scalar and vector variables and can be solved, for example, by the SIMPLER algorithm [179]. Indices i, j, k correspond to the vector grid points while indices I, J, K correspond to the scalar grid points as illustrated in Figures C.1 and C.2 for two-dimensional geometry. Other external variables related to the liquid phase, such as the dissolved gas

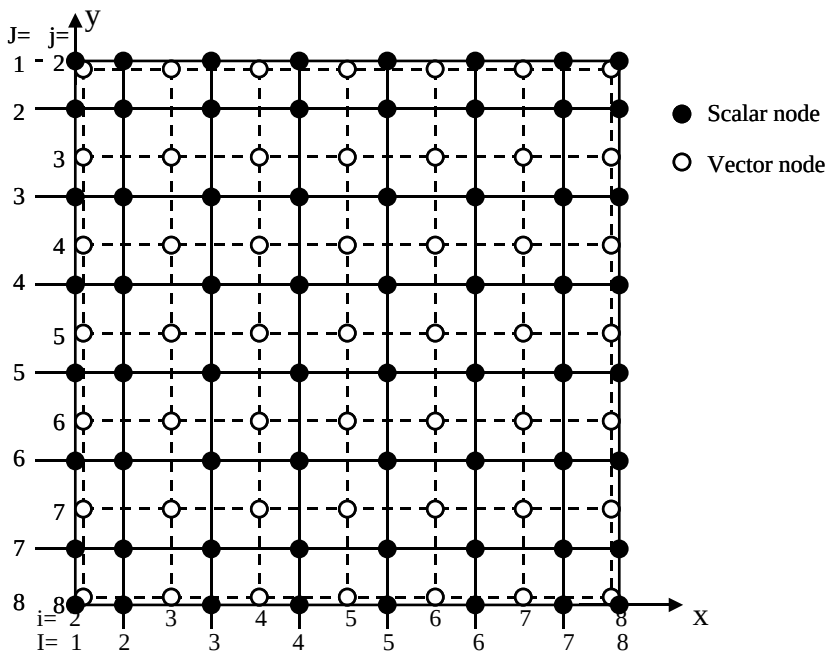

Figure C.1. Schematic of a staggered grid in a two-dimensional representative longitudinal plane for $l_1 = m_1 = 8$.

concentrations, can be computed in a similar manner.

The governing equations [Equations (C.8) to (C.16)] for the particle density function are solved by the modified method of characteristics [181, 244, 246]. Figure C.3 shows a three-dimensional computational cell whose corner points belong to the vector component grid. The modified method of characteristics consists of determining the coordinates (x_n, y_n, z_n) of the point in space from where the particles located at the grid point (x_a, y_b, z_c) at time $t + \Delta t$ originate at time t. In other words, for each point of a specified grid, the pathline

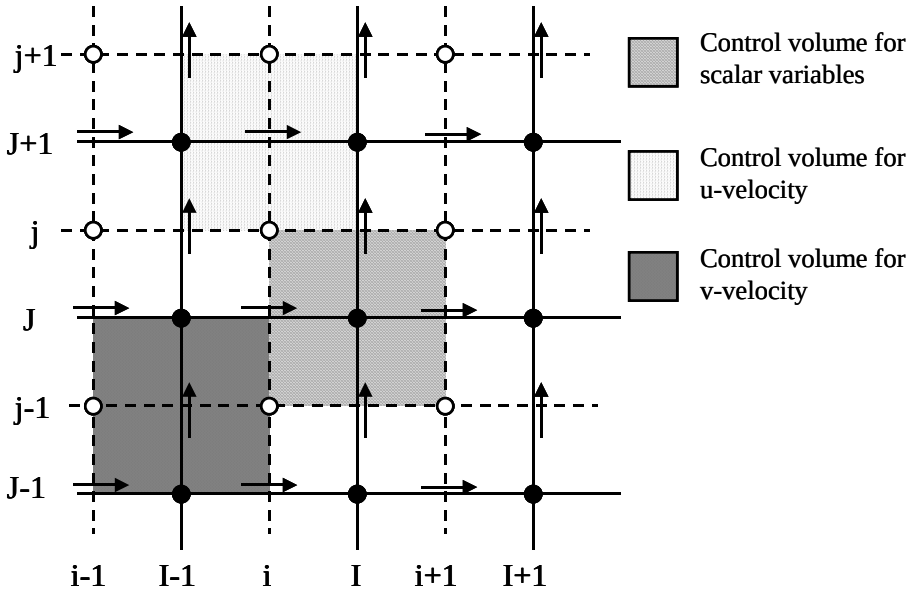

Figure C.2. Definition of control volume in a two-dimensional representative longitudinal plane.

is projected rearward to the initial-data surface to determine the initial data point. For example, in Figure C.3 the point (x_a, y_b, z_c) is the point $(x_{i+1}, y_{j+1}, z_{k+1})$. The solid line represents the section of the characteristic curve along which the particle traveled from location (x_n, y_n, z_n) to location (x_a, y_b, z_c) during the time interval between t and $t + \Delta t$.

To avoid numerical instabilities, it is necessary to insure that the particles do not leave the computational cell between the time t and $t+\Delta t$. In other words, each computational cell traveled by the particle should contain at least two consecutive points on the characteristic curve. Therefore, the initial time step Δt is determined by the equation,

$$\Delta t = \min_{\substack{2\le i\le l_1-1\\ 2\le j\le m_1-1\\ 2\le k\le n_1-1}} \left\{ \left| \frac{x_{i+1}-x_i}{2u_\infty(i,j,k)} \right|, \left| \frac{y_{j+1}-y_j}{2v_\infty(i,j,k)} \right|, \left| \frac{z_{k+1}-z_k}{2[w_\infty(i,j,k)-w_r(i,j,k)]} \right| \right\} \qquad \text{(C.17)}$$

The factor 2 appearing in the denominator was arbitrarily introduced to assure that each computational cell contains at least two consecutive points on the characteristics curve. A larger value of the factor could have been chosen but was proven to have no significant effect on the final numerical results, while slowing down the convergence. However, when particles can growth, the particle radius and upward velocity can change and the time step may have to be reduced in order to assure the stability requirement.

Figure C.4 shows the general block diagram of the computational procedure in performing a steady-state calculation for a given particle size distribution at the inlet boundary. First, the variables across the computational domain are all initialized to an arbitrarily small value except at the inlet boundary where the variables r, $(p_i)_{1\le i\le l}$, and f_1 are set to be equal to r_0, $(p_{0,i})_{1\le i\le l}$, and $f_{1,0}$, respectively, corresponding to an arbitrary point

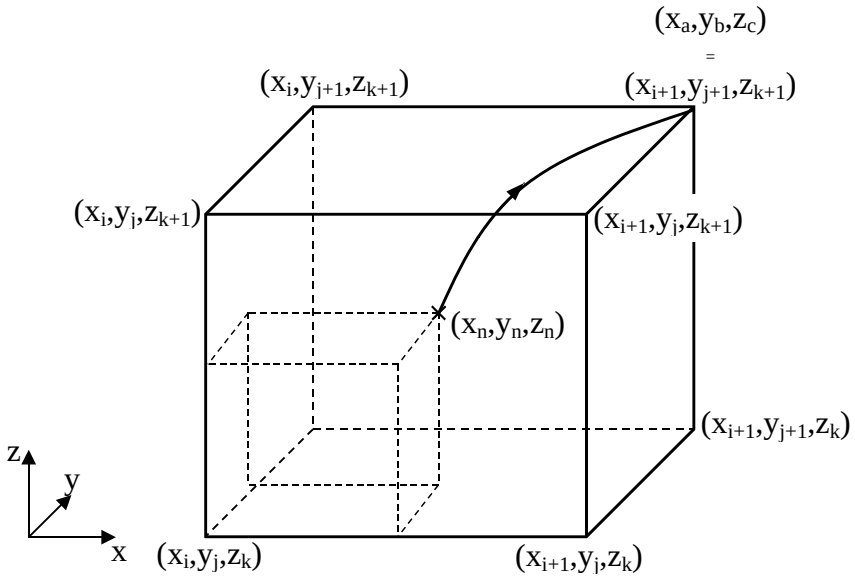

Figure C.3. Typical computational cell used for inverse marching method containing the pathline of the bubbles.

on the initial particle density function $f_{1,0}[x_0, y_0, z_0, r_0, (p_{0,i})_{1\leq i\leq l}]$. Then, the time step is computed according to Equation (C.17). Finally, the ordinary differential equations for the variables r, $(p_i)_{1\leq i\leq l}$, and f_1 [Equations (C.8) to (C.13)] are solved at all interior points, followed by the computation of the variables at the boundary points. The solution of the governing ODE at the interior points and specification of the variables at the boundaries is repeated until a steady state has been reached. The same sequence takes place for another arbitrary point on the initial particle density function $f_{1,0}[x'_0, y'_0, z'_0, r'_0, (p'_{0,i})_{1\leq i\leq l}]$ at the inlet boundary.

The computational domain for solving the particle density function, the particle radius, and the other particle internal coordinates consists of four basic types of points (or nodes): interior, solid boundary, inlet, and exit points. The basic features of the interior point unit process are presented in the following discussion followed by a brief description of the other three unit processes.

C.4.1. Interior Point Unit Process

Figure C.5 shows the detailed numerical procedure used for solving the governing ordinary differential equations [Equations (C.8) to (C.13)] at every interior point (x_a, y_b, z_c) such that $2 \leq a \leq l_1 - 1$, $2 \leq b \leq m_1 - 1$, and $2 \leq c \leq n_1 - 1$ as well as at the outlet boundary.

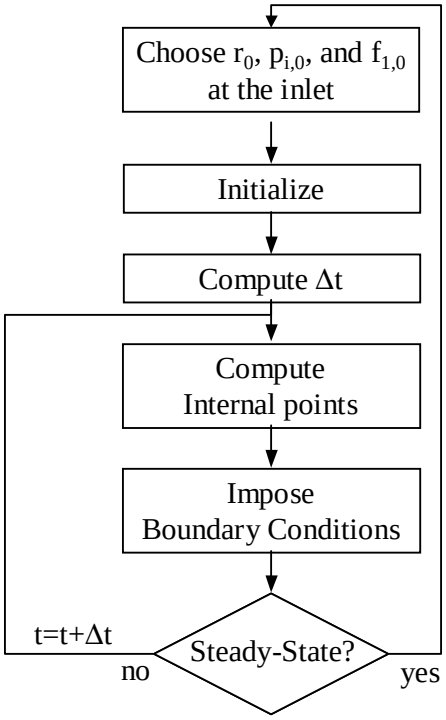

Figure C.4. Block diagram of the numerical procedure for solving the population balance equation by the method of characteristics using inverse marching method.

1. First, the coordinates (x_n, y_n, z_n) are determined by assuming that the velocity component (u_n, v_n, w_n) and the particle radius r_n at location (x_n, y_n, z_n) and time t are the same as those at location (x_a, y_b, z_c) at time $t + \Delta t$ and are calculated as

$$x_n = x_a - u_\infty(x_a, y_b, z_c)\Delta t \quad \text{(C.18)}$$
$$y_n = y_b - v_\infty(x_a, y_b, z_c)\Delta t \quad \text{(C.19)}$$
$$z_n = z_c - [w_\infty(x_a, y_b, z_c) - w_r(x_a, y_b, z_c, r)]\Delta t \quad \text{(C.20)}$$

2. Second, let us call (x_i, y_j, z_k) the closest point to (x_n, y_n, z_n) in the **vector** grid such that $x_i \le x_n \le x_{i+1}$, $y_j \le x_n \le y_{j+1}$, $z_k \le x_n \le z_{k+1}$. Similarly, let us call (x_I, y_J, z_K) the closest point to (x_n, y_n, z_n) in the **scalar** grid such that $x_I \le x_n \le x_{I+1}$, $y_J \le x_n \le y_{J+1}$, $z_K \le x_n \le z_{K+1}$. Then, the computational cells containing the point (x_n, y_n, z_n) in both the vector grid and the scalar grid of the staggered grid system, i.e., i, j, k and I, J, K, are determined.

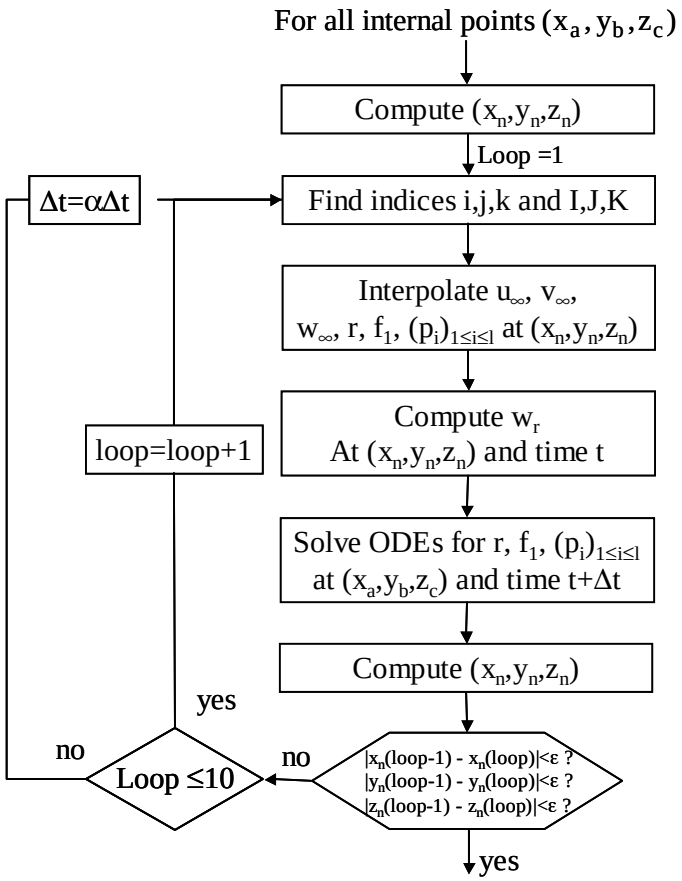

Figure C.5. Block diagram of the computation of the interior point for solving the population balance equation by the method of characteristics using inverse marching method.

3. Third, the velocity components at (x_n, y_n, z_n) are determined by Lagrangian interpolation using their values at the eight corners of the computational cell in the vector grid containing the point (x_n, y_n, z_n),

$$\begin{aligned}\phi_n \;=\; & (1-w_u)(1-w_v)(1-w_w)\phi_{i,j,k} + w_u(1-w_v)(1-w_w)\phi_{i+1,j,k} + \\ & (1-w_u)w_v(1-w_w)\phi_{i,j+1,k} + w_u \times w_v(1-w_w)\phi_{i+1,j+1,k} + \\ & (1-w_u)(1-w_v)w_w\phi_{i,j,k+1} + w_u(1-w_v)w_w\phi_{i+1,j,k+1} + \\ & (1-w_u)w_v \times w_w \times \phi_{i,j+1,k+1} + w_u \times w_v \times w_w \times \phi_{i+1,j+1,k+1} \qquad \text{(C.21)}\end{aligned}$$

where the variable ϕ corresponds to the liquid velocity components u_∞, v_∞, and w_∞ and ϕ_n is their interpolated value at location (x_n, y_n, z_n), while $\phi_{i,j,k}$ is their value

computed at the vector grid point (x_i, y_j, z_k). The weights w_u, w_v, and w_w vary between zero and unity and are defined as

$$w_u = \frac{(x_n - x_i)}{(x_{i+1} - x_i)}, \qquad w_v = \frac{(y_n - y_j)}{(y_{j+1} - y_j)}, \qquad and \qquad w_w = \frac{(z_n - z_k)}{(z_{k+1} - z_k)} \tag{C.22}$$

Similarly, the scalar variables ψ such as the temperature T, the radius of the particles r, the internal coordinate $(p_i)_{1 \le i \le l}$, and the thermophysical properties are interpolated at location (x_n, y_n, z_n) and time t using the equation

$$\begin{aligned} \psi_n \;=\; & (1-w_x)(1-w_y)(1-w_z)\psi_{I,J,K} + w_x(1-w_y)(1-w_z)\psi_{I+1,J,K} + \\ & (1-w_x)w_y(1-w_z)\psi_{I,J+1,K} + w_x \times w_y(1-w_z)\psi_{I+1,J+1,K} + \\ & (1-w_x)(1-w_y)w_z \times \psi_{I,J,K+1} + w_x(1-w_y)w_z \times \psi_{I+1,J,K+1} + \\ & (1-w_x)w_y \times w_z \times \psi_{I,J+1,K+1} + w_x \times w_y \times w_z \times \psi_{I+1,J+1,K+1} \end{aligned} \tag{C.23}$$

where the function ψ corresponds to scalar variables such as the liquid temperature T, the particle radius r, and ψ_n is their extrapolated value at location (x_n, y_n, z_n) and time t from the knowledge of the values at the scalar grid points (x_i, y_j, z_k). The weights w_x, w_y, and w_z vary between zero and unity and are defined as

$$w_x = \frac{(x_n - x_I)}{(x_{I+1} - x_I)}, \qquad w_y = \frac{(y_n - y_J)}{(y_{J+1} - y_J)}, \qquad and \qquad w_z = \frac{(z_n - z_K)}{(z_{K+1} - z_K)} \tag{C.24}$$

4. The coordinates (x_n, y_n, z_n) of the particle at time t are recomputed using the interpolated values of the liquid velocity components, while the relative particle velocity w_r is computed from Equation (C.3) using the relative particle radius r_n and the thermophysical properties of the liquid interpolated at location (x_n, y_n, z_n) and time t:

$$x_n = x_a - u_{\infty,n}\Delta t \tag{C.25}$$

$$y_n = y_b - v_{\infty,n}\Delta t \tag{C.26}$$

$$z_n = z_c - (w_{\infty,n} - w_{r,n})\Delta t \tag{C.27}$$

with

$$w_{r,n} = \frac{2}{9}\frac{\rho_\infty g r_n^2}{\mu_{\infty,n}} \tag{C.28}$$

5. The ordinary differential equations for the particle internal coordinates (r, p_i) and for the density function f_1 [Equations (C.11) to (7.58)] at location (x_a, y_b, z_c) and time $t + \Delta t$ can then be integrated by the fourth order Runge-Kutta method [182].

6. Steps 2 to 5 are repeated until the difference between two successive computed values of x_n, y_n, and z_n is less than an arbitrary value ϵ, i.e.,

$$Max[|x_n(iter+1) - x_n(iter)|, |y_n(iter+1) - y_n(iter)|, [|z_n(iter+1) - z_n(iter)|] \le \epsilon \tag{C.29}$$

where *iter* is the iteration step number. Sensitivity study has been performed and showed that the numerical solution was independent of ϵ provided that it is less than 1.0×10^{-4}m.

7. Steps 1 to 6 are repeated for all interior points (x_a, y_b, z_c).
8. For steady state calculations, steps 1 to 7 are repeated until the maximum relative difference in the predictions of the particle internal coordinates and of the density function f_1 between two successive iterations fall under an arbitrary constant:

$$\max_{\substack{2\le i\le l_1-1\\ 2\le j\le m_1-1\\ 2\le k\le n_1-1}} \left[\frac{|X(iter+1)-X(iter)|}{X(iter)|}\right] \le 1.0\times 10^{-6} \tag{C.30}$$

   where X represents the internal coordinates r, $(p_i)_{1\le i\le l}$, and f_1.
9. Steps 1 to 8 are repeated for all the points on the initial particle density function $f_1(x_0, y_0, z_0, r, (p_i)_{1\le i\le l}], t = 0)$

C.4.2. Boundary Point Unit Processes

The boundary conditions used at the inlet points are that the particle properties r_0, $f_{1,0}$, and $p_{i,0}$ are all known and constant. Their values are determined from physical considerations or based on experimental data. The exit points are treated as interior points and the same procedure as that previously described is followed. Finally, Dirichlet, Neuman or mixted boundary conditions can be applied at the solid boundary points. In the present work, the weak boundary conditions was assumed for r, f_1, and p_i.

C.5. Computer Program Validation

A set of examples has been chosen in order to compare the numerical predictions against practical problems whose analytical solutions are known and can be summarized as follows:

1. Solid particle in one-dimensional laminar flow - transient and steady-state situations.
2. Bubble transport and growth due to pressure change in one-dimensional vertical laminar flow.

In all the cases considered for validation, the liquid temperature, the liquid viscosity and density are assumed to be uniform over the entire computational domain. Moreover, the liquid is assumed to be incompressible. The container is taken to be a parallelopiped of height, length, and width denoted by H, L, and W, respectively.

C.5.1. Solid Particles in One-Dimensional Laminar Flow

For validation purposes, we consider the physical situation when monodispersed solid particles of constant radius r are injected at the bottom of a vertical container. The liquid under one-dimensional laminar flow conditions with a uniform and constant upward velocity of 0.2 m/s, i.e., $\vec{v}_\infty = w_\infty \vec{k} = -0.2\vec{k}$, is considered. The particles are subject to buoyancy and are assumed to be small and in low concentration so that their presence does not affect the liquid flow. Then, the population balance equation simplifies to

$$\frac{\partial f_1}{\partial t} + (w_\infty - w_r)\frac{\partial f_1}{\partial z} = 0 \tag{C.31}$$

Transient Situation

In this example, the particles are injected uniformly across the bottom of the container (at z=H) and the injection rate varies with time so that the particle density function at the bottom of the tank ($z = H$) and time t is denoted $F(t)$. Thus, the transient particle density distribution at time t and location z solution of Equation (C.31) is

$$f_1(z,t) = F(u) \qquad \text{where} \qquad u = t - (H-z)/(w_\infty - w_r) \tag{C.32}$$

In the present study we assume that the particle density function at the bottom of the column varies with time according the following Fermi function,

$$F(t) = f_0 \left[\frac{e^{a(t-t_0)}}{1 - e^{a(t-t_0)}} \right] \tag{C.33}$$

where a, t_0, and f_0 are arbitrary constants. The exact analytical solution to this problem is given by

$$f_1(z,t) = \left\{ \frac{e^{a[t-(H-z)/(w_\infty - w_r)]}}{1 - e^{a[t-(H-z)/(w_\infty - w_r) - t_0]}} \right\} f_0 \tag{C.34}$$

The numerical calculations were performed with the particle radius and the fluid properties such that the fluid flow is laminar and that the particle upward velocity $(w_\infty - w_r)$ is equal to 4 cm/s while the parameters at the particle injection cross-section (i.e., at z=H) are $a = 1.4s^{-1}$, $t_0 = 2s$, and $f_0 = 1/m^3$of liquid/m. Figure C.6 shows a comparison of the particle density function using dimensionless variables along the z-axis at time $t = 20.4$ s obtained numerically using the method of characteristics with the exact solution. One can see that as the grid size is reduced, the predictions of the numerical model converge toward the exact solution [Equation (C.34)]. The rapid changes in the particle injection rate with time forces one to reduce the grid size significantly in order to capture the sharp variation of the injection rate.

Steady-State Situation

Here, the particles are not injected uniformly at the bottom of the container, instead the particle density function at $z = H$ varies in the x-direction, i.e., $f_1(x, y, z = H, r, t) = G(x)$ as illustrated in Figure C.7. Then, under steady-state conditions, the particle density function at any location z should be the same as that at the bottom of the container, i.e.,

$$f_1(x, y, z, r) = G(x) \tag{C.35}$$

Figure C.8 illustrates a comparison of the numerical results with the analytical solution for the particular example when

$$G(x) = \left[\frac{e^{a(x-x_0)}}{1 - e^{a(x-x_0)}} \right] f_0 \tag{C.36}$$

with the parameters $a = 1.5m^{-1}$, $x_0 = 0.7m$, and $L = 1m$. The tank was discretized in Cartesian coordinates using a $24 \times 15 \times 9$ grid. All the particles were assumed to be 1 mm in radius. Very good agreement between the numerical and the analytical solutions even with a coarse grid.

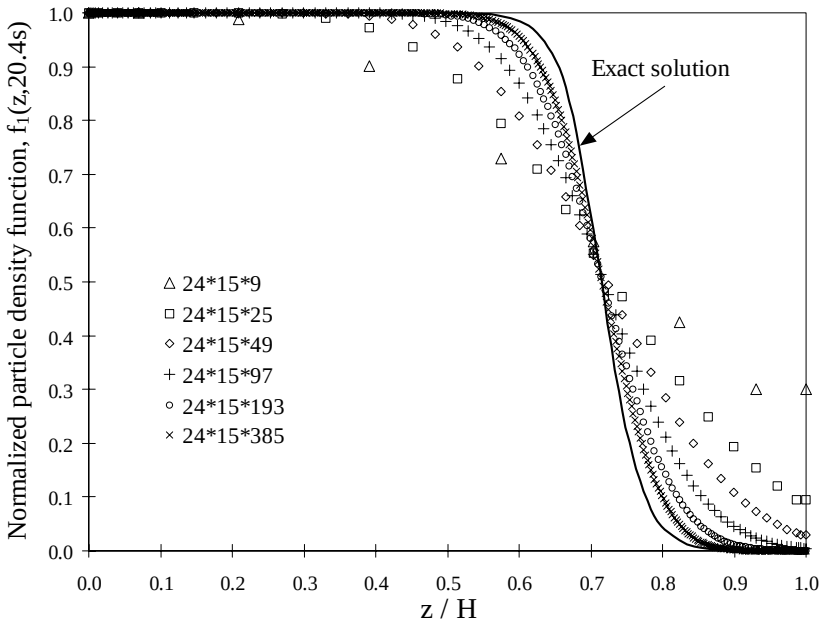

Figure C.6. Comparison between the predictions of the method of characteristics and the analytical solution for bubble density function under one-dimensional transient flow at time t=20.4s.

Similar results can be obtained for any arbitrary polydispersed population of solid particles. It suffices only to perform the same calculation for different radii and corresponding particle density functions.

In conclusion, for solid particles transport in a one-dimensional vertical flows, the numerical scheme based on the modified method of characteristics yields results which are in very good agreement with theoretical solutions for both transient and steady-state conditions.

C.5.2. Bubbles Rise at Constant Growth Rate

This section is limited to bubble transport in steady-state one-dimensional laminar flow with constant particle growth rate $\dot{r}$ as shown in Figure C.9. The population balance equation to be solved is written as

$$\frac{\partial}{\partial z}[(w_\infty - w_r)f_1] + \frac{\partial}{\partial r}(\dot{r}f_1) = 0 \qquad \text{(C.37)}$$

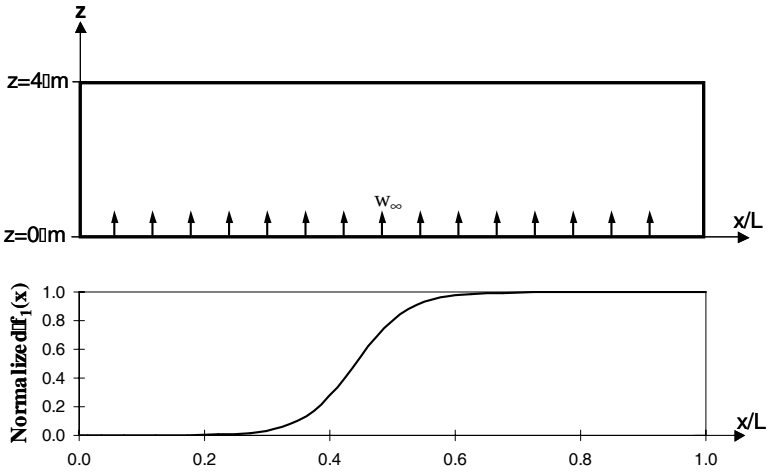

Figure C.7. Schematic of the rectangular container for the code validation for the steady-state flow of solid bubbles.

where w_r is given by Equation (C.3). The liquid upward velocity is assumed to be $w_\infty = -0.2$ m/s and the growth rate is taken as constant and equal to $\dot{r} = \dot{r}_0 = 1.0 \times 10^{-5}$ m/s. The governing equations to be solved simplify to

$$\frac{\mathrm{d}z}{\mathrm{d}t} = w_\infty(z) - w_r(r,z) \tag{C.38}$$

$$\frac{\mathrm{d}r}{\mathrm{d}t} = \dot{r}_0 \tag{C.39}$$

$$\frac{\mathrm{d}f_1}{\mathrm{d}t} = f_1 \frac{\partial w_r(r,z)}{\partial z} \tag{C.40}$$

The bubble density function at the injection cross-section $z = H$ is assumed to follow a normal distribution , i.e.,

$$f_1(r, z = H, t) = \frac{1}{\sigma_0\sqrt{2\pi}} exp\left[-\frac{(r-\mu_0)^2}{2\sigma_0^2}\right] \tag{C.41}$$

with a mean value $\mu_0 = 1$ mm and a deviation $\sigma_0 = 0.25$ mm.

In this specific case, an analytical solution to the population balance equation can be found if one recognizes that the bubbles are small and their relative velocity with respect to the liquid w_r is negligible compared with the velocity of the liquid ($w_r \ll w_\infty$). In other words, the bubble density function $f_1(z,r)$ is shifted toward larger r in the r-space when bubbles are transported from location $z = H = 4$ m to $z = 0$ m, i.e., a bubble entering the column at $z = H$ with a radius r reaches the location z with a radius $r + \dot{r}(H - z)/w_\infty$. Then, the bubble density function f_1 at location z is given by

$$f_1(z,r) = \frac{1}{\sigma_0\sqrt{2\pi}} exp\left[-\frac{[(r + \dot{r}(z-H)/w_\infty) - \mu_0]^2}{2\sigma_0^2}\right] \tag{C.42}$$

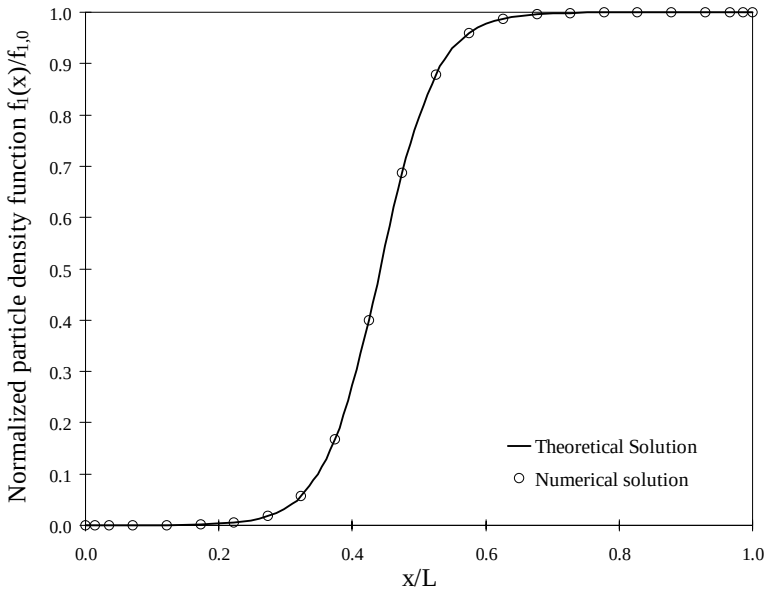

Figure C.8. Comparison between the numerical solutions and the analytical solution for bubble density function under one-dimensional steady-state flow.

Figure C.10 compares the bubble density function at locations $z = 0$ m obtained numerically with the analytical solution given by Equation (C.42). The results clearly indicate that the numerical model agrees very well with the exact solution.

C.5.3. Bubbles Transport, and Growth Due to Pressure Changes

In this section, the gas bubbles are transported with the upward flowing liquid and by buoyancy while they can grow due the change in hydrostatic pressure as shown in Figure C.9. The pressure drop in the liquid phase is neglected and the pressure at z = 0 m is assumed to equal the atmospheric pressure p_0. The following equations are to be solved by the modified method of characteristics,

$$\frac{\mathrm{d}z}{\mathrm{d}t} = w_\infty(z) - w_r(r,z) \tag{C.43}$$

$$\frac{\mathrm{d}r}{\mathrm{d}t} = \dot{r}(r,z) \tag{C.44}$$

$$\frac{\mathrm{d}f_1}{\mathrm{d}t} = f_1\left[\frac{\partial w_r(r,z)}{\partial z} - \frac{\partial \dot{r}(r,z)}{\partial r}\right] \tag{C.45}$$

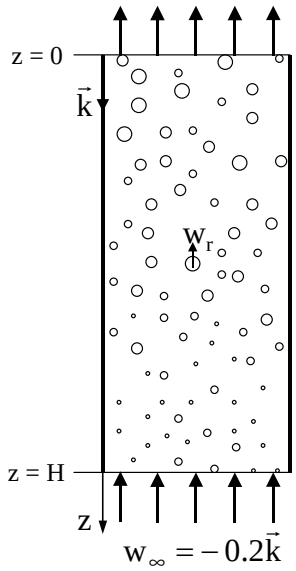

Figure C.9. Schematic of a rectangular vertical container used for the code validation.

where w_r and its derivative with respect to z are given by Equations (C.3) and (C.14), respectively. The bubble growth rate $\dot{r}$ and its derivative with respect to bubble radius are expressed as

$$\dot{r} = -\frac{\rho_\infty g(w_\infty - w_r)r/3}{p_0 + \rho_\infty g z + 4\sigma/3r} \tag{C.46}$$

$$\frac{\partial \dot{r}}{\partial r} = -\frac{\rho_\infty g}{3}\left[\frac{(w_\infty - 3w_r)}{p_0 + \rho_\infty g z + 4\sigma/3r}\right] - \frac{4\sigma}{3r^2}\left[\frac{\dot{r}}{p_0 + \rho_\infty g z + 4\sigma/3r}\right] \tag{C.47}$$

Here, the liquid density, viscosity and surface tension correspond to those of soda-lime silicate glass at 1800 K and are equal to 2406 kg/m^3, 5.53 Pa.s, and 296 mN/m, respectively. The initial bubble density function is assumed to follow a normal distribution [Equation (C.41)] with a mean value of $\mu_0 = 1$ mm and a deviation $\sigma_0 = 0.25$ mm.

C.5.3.1. Bubble Rise Dominated by the Upward Liquid Flow

In the present example, the relative velocity of the bubble with respect to the liquid w_r can be neglected compared with the liquid velocity w_∞. Its partial derivative with respect to z is also negligible in comparison with that of $\dot{r}$ with respect to the bubble radius r. Moreover, the term due to surface tension in the denominator is assumed to be negligible, i.e., $4\sigma/3r \ll (p_0 + \rho_\infty g z)$. This assumption is valid for bubble radii larger than 0.2 mm.

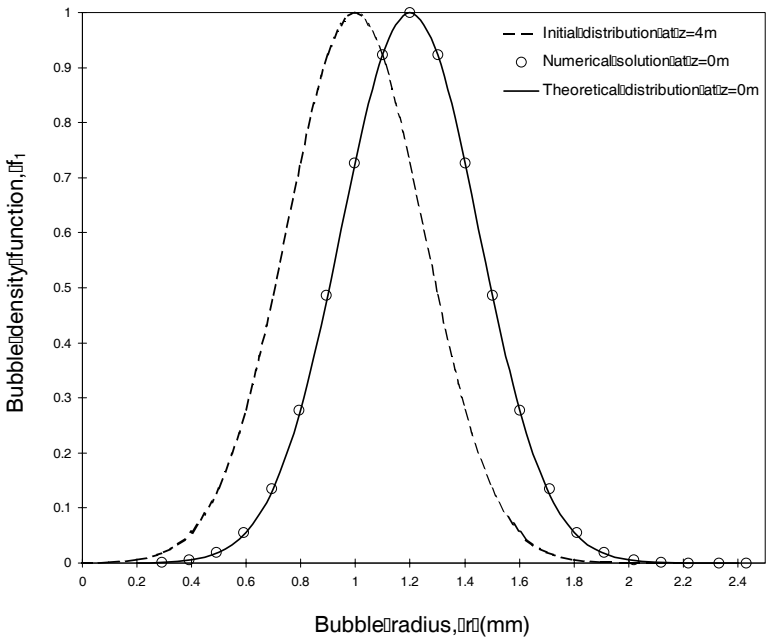

Figure C.10. Comparison between the numerical solution and the analytical solution for bubble rise at constant growth rate ($\dot{r} = 0.01mm/s$) under one-dimensional steady state flow at $z = 0$ m with $\mu_0 = 1mm$, $\sigma_0 = 0.25mm$, $\vec{w}_\infty = -0.2\vec{k}$.

Note that, if the liquid flows upward ($w_\infty < 0$), the bubbles grow and the growth rate $\mathrm{d}r/\mathrm{d}t$ is positive. The approximate solution to the problem of interest can be written as

$$z(t) = H + w_\infty t \tag{C.48}$$

$$r(t) = r_0 \left(\frac{p_0 + \rho_\infty g H}{p_0 + \rho_\infty g z} \right)^{1/3} \tag{C.49}$$

$$f_1(r) = f_1(r_0) \left(\frac{r_0}{r} \right) \tag{C.50}$$

where r_0 is the bubble radius at location z=H=4 m at time t=0 s. Note that the approximate analytical solution satisfies the conservation of the same total number of bubbles N,

$$N(z) = \int_0^\infty f_1(r)\mathrm{d}r = \int_0^\infty f_1(r_0)\frac{r_0}{r}\mathrm{d}r = \int_0^\infty f_1(r_0)\mathrm{d}r_0 = N(H) \tag{C.51}$$

Figure C.11 illustrates a comparison of the approximate analytical solution given by Equation (C.50) with the numerical results for Equations (C.45) to (C.47). The numerical solutions compare very well with the approximate analytical solution. The slight discrepancies may be explained by the approximation made to solve the problem analytically that tend to underestimate the bubble growth. One can see that unlike the results for constant growth rate, the bubble density function at the top of the column (z=0 m) is not symmetric around the mean value due to the fact that the growth rate increases linearly with the

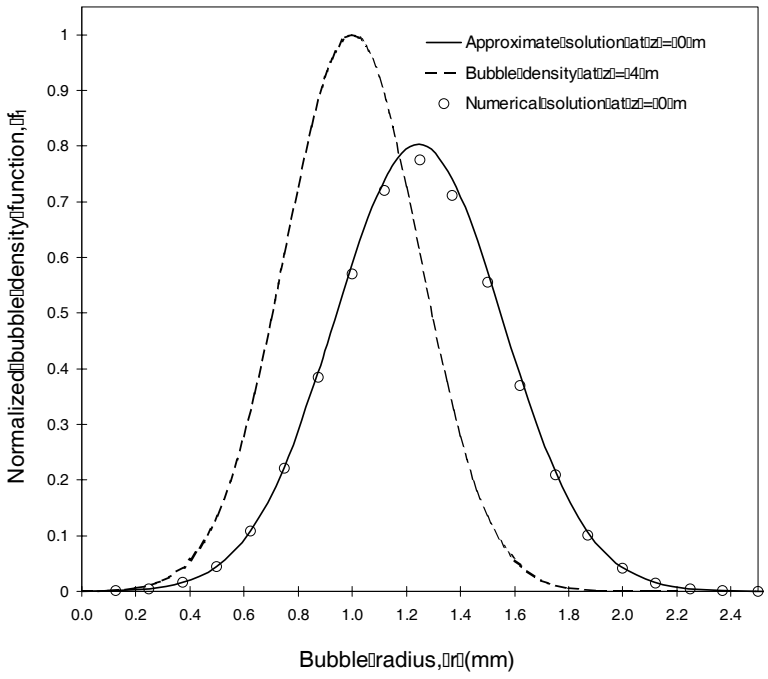

Figure C.11. Comparison between the method of characteristics and the approximate analytical solution for bubble rise and growth due to pressure change under one-dimensional steady state flow at $z = 4m$ with $\mu_0 = 1mm$, $\sigma_0 = 0.25mm$, $\vec{w}_\infty = -0.2\vec{k}$ m/s.

bubble radius as given by Equation (C.46) when w_r is negligible compared with w_∞, i.e., the large bubbles grow faster than the smaller ones. Finally, the variation of the bubble radius $r(z)$ and the bubble density function $f_1(r, z)$ with the vertical location z for an initial bubble radius $r_0 = 2$ mm at $z = 4$m is shown in Figures C.12 and C.13, respectively. Again, good agreement between the approximate analytical and the numerical solution is observed.

C.5.3.2. Bubble Rise Dominated by Buoyancy

Here, the gas bubbles rise by buoyancy only, i.e., $w_\infty = 0.0$, and can grow due the changes in the hydrostatic pressure. Similarly, assuming that the term due to surface tension in the denominator is negligible compared with the hydrostatic pressure, i.e., $4\sigma/3r \ll (p_0+\rho_\infty gz)$,

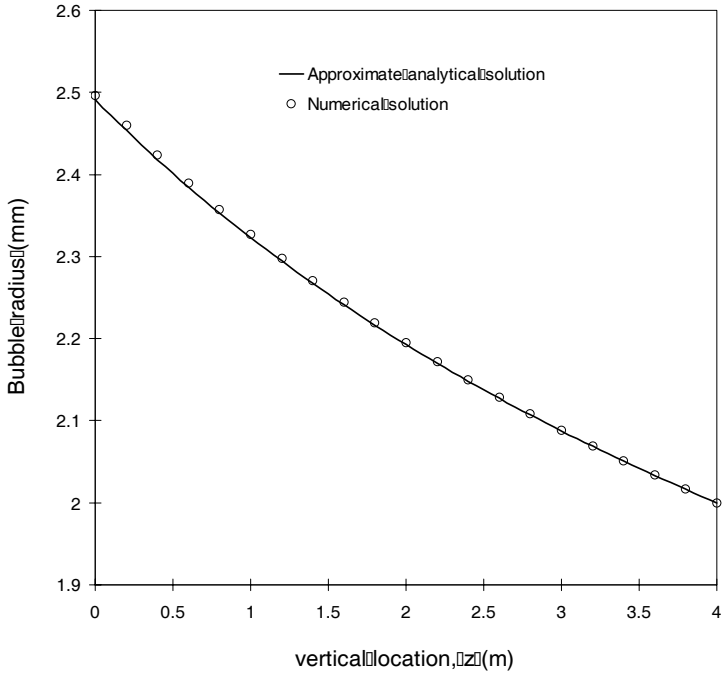

Figure C.12. Comparison between the method of characteristics and the approximate analytical solution [Equation (C.49)] for the profile of bubble radius $r(z)$ as a function of z with $r_0 = 2$mm at $z = 4$m, and $\vec{w}_\infty = -0.2\vec{k}$ m/s.

an analytical solution can be found for the radius r and the bubble density function f_1 at every location z in the column are given by

$$r(z) = r_0 \left(\frac{p_0 + \rho_\infty g H}{p_0 + \rho_\infty g z} \right)^{1/3} \tag{C.52}$$

$$f_1(z) = f_1(r_0) \left(\frac{r_0}{r} \right)^5 \tag{C.53}$$

where r_0 and $f_1(r_0)$ are the bubble radius and the bubble size distribution at location $z = H = 4$ m, respectively.

Figure C.14 shows a comparison of the approximate analytical solution given by Equation (C.53) and the numerical results. The latter are in very good agreement with the approximate analytical solution. Note that the variations of the bubble radius $r(z)$ with the vertical location z for an initial bubble radius $r_0 = 2$ mm at $z = 4$m are the same as those when the bubble rise is dominated by the upward liquid flow (see Figure C.12) and need not be repeated. The bubble density function $f_1(r, z)$ with the vertical location z for an initial bubble radius $r_0 = 2$ mm at $z = 4$m is shown in Figure C.15. Excellent agreement between the approximate analytical solution and the numerical solution is evident. Note that in the present case, the total number of bubbles is not conserved, i.e., $\int_0^\infty f_1(r)\mathrm{d}r \neq \int_0^\infty f_1(r_0)\mathrm{d}r_0$. This is due to the fact that the gas and liquid momentum

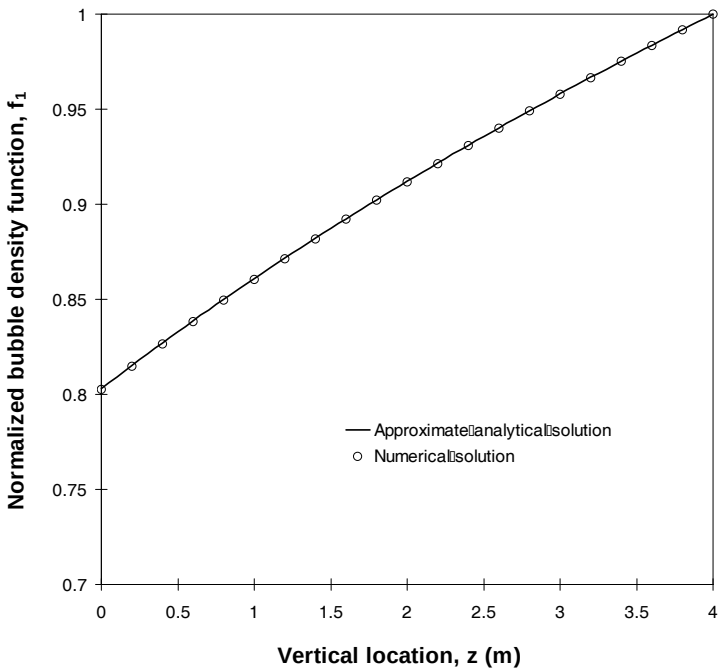

Figure C.13. Comparison between the method of characteristics and the approximate analytical solution [Equation (C.50)] for the profile of bubble density function $f_1(z)$ as a function of z with $r_0 = 2$mm at $z = 4$m, and $\vec{w}_\infty = -0.2\vec{k}$ m/s.

equations have been decoupled and it was assumed that the vertical component of the bubble velocity vector was given by $w_b = w_\infty - w_r$. Thus, this assumption implies that the bubble velocity field does not satisfy the steady-state continuity equation, i.e., $\nabla \cdot \vec{v}_b \neq 0$. Therefore, the conservation of the total number of bubbles cannot be assured. For example, in the case of convective transport of solid particles without generation and growth, the conservation equation [Equation (C.31)] along the pathlines of the particles is written as $\mathrm{d}f_1/\mathrm{d}t = f_1 \partial w_r/\partial z$. However, physically it is clear that the bubble density function is transported unchanged along the particle pathlines and the conservation equation should be written as $\mathrm{d}f_1/\mathrm{d}t = 0$. Therefore, the assumption on the bubble velocity introduces an artificial source in the population balance equation. In order to approximately conserve the total number of bubbles the bubble velocity vector should satisfy

$$\nabla \cdot \vec{v}_b \approx 0 \tag{C.54}$$

Since the liquid is treated as incompressible, Equation (C.54) is satisfied if $\partial w_r/\partial z \ll 1$. Physically, this corresponds to situation when the bubble growth rate and liquid velocity do not vary significantly with position and time. This problem does not occur either in the case of bubble growth and rise dominated by the liquid flow since $\nabla \cdot \vec{v}_b \approx \nabla \cdot \vec{v}_\infty \approx 0$ or for solid particle rise by buoyancy without growth since then $\partial w_r/\partial z = 0$. However, for bubble rise dominated by buoyancy, the simplifying assumption $w_b = w_\infty - w_r$ must be

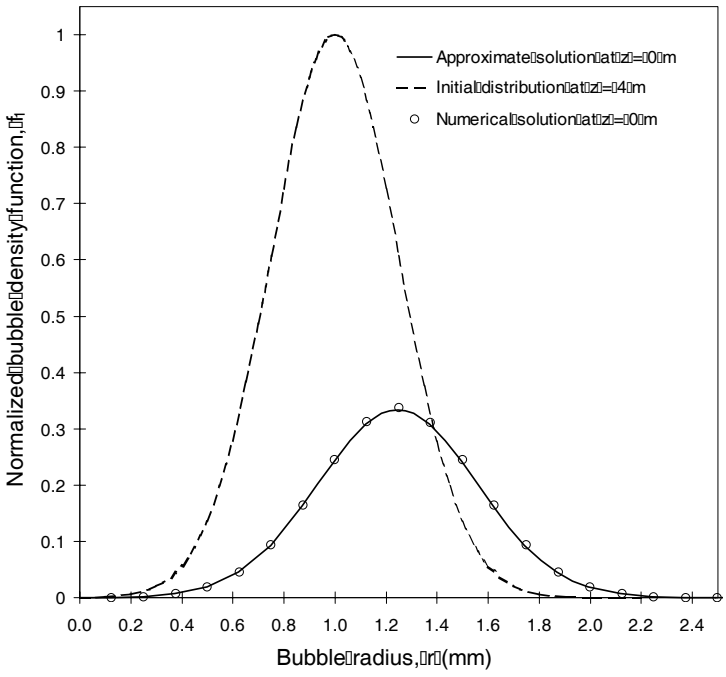

Figure C.14. Comparison between the method of characteristics and the approximate analytical solution for bubble rise due to buoyancy and growth due to pressure change under one-dimensional steady state flow at $z = 4m$ with $\mu_0 = 1mm$, $\sigma_0 = 0.25mm$, $\vec{w}_\infty = 0.0\vec{k}$ m/s.

relaxed and the coupling between the bubble rise and the liquid flow should be accounted for. To do so, one could couple the mass and momentum conservation equations for both phases using the two-fluid model [156, 157]. However, this task is complicated and beyond the scope of this study.

In conclusion, the results reported in this section validate the numerical computer program. Previous examples have analytical solutions and could have been solved using the conventional method of characteristics (direct marching method) since they were concerned with one-dimensional flow and with bubbles having one internal coordinate (their radius r). The numerical results obtained compare well with the analytical solution and validate the numerical scheme.

C.6. Conclusion

This Appendix has described in detail the numerical method for solving the population balance equation by the method of characteristics. The numerical solution has been compared with the analytical solution for simple cases when it was possible. Good agreement between the numerical and the theoretical solutions has been obtained confirming the va-

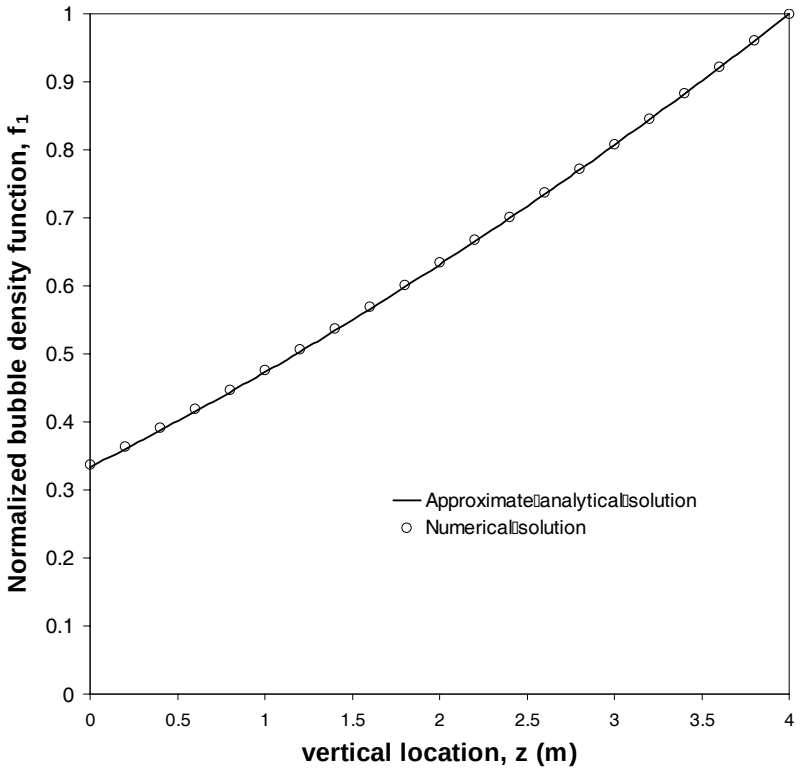

Figure C.15. Comparison between the method of characteristics and the approximate analytical solution [Equation (C.53)] for the profile of bubble density function f_1 as a function of vertical location - one-dimensional steady state flow with $\mu_0 = 1mm$, $\sigma_0 = 0.25mm$, $\vec{w}_\infty = -0.2\vec{k}$ m/s.

lidity of the numerical procedure and the associated computer program.

Moreover, Carrica *et al.* [158] have presented a three-dimensional computational model for the two-phase flow around a naval surface ship. The model can calculate the gas volume fraction and bubble radius, and accounts for the coupling between the gas and the liquid equations. However, their model is limited to monodispersed bubble population, i.e., all the bubbles in the computational grid have the same radius. The numerical scheme developed in the present study could easily be coupled to the three-dimensional two-fluid model to solve for polydispersed bubble size distribution.

Finally, since computations for each initial point on the bubble density function are independent from one another, parallel computing is recommended to significantly reduce the computational time. Indeed, in reality the local particle density function and the conditions in the surrounding liquid phase (temperature, velocity vector, gas concentration) are interdependent thus requiring iterations that are very time consuming.

NOMENCLATURE

f_1	Particle density function
g	Specific gravity
h	Particle generation rate per unit volume in the state space
H	Depth at which particles are injected
$\vec{i}, \vec{j}, \vec{k}$	Unit vectors in the physical space
l	Number of internal coordinates other than the particle radius
N	Total number of particles
p_i	Particle internal coordinates other than radius ($1 \leq i \leq l$)
p	Pressure
r	Particle or bubble radius
$\dot{r}$	Time rate of change of particle or bubble radius
R	Universal gas constant $= 8.314 J/molK$
t	Time
u	Projection of the velocity vector on the x-axis
v	Projection of the velocity vector on the y-axis
$\vec{v}$	Velocity vector
w	Projection of the velocity vector on the z-axis
w_r	Vertical upward velocity of the particle relative to the glass melt
$\vec{x}$	Spatial or external coordinates
x	Longitudinal location
y	Spanwise location
z	ocal depth within the glass melt
Greek symbols	
α	Arbitrary constant with values between 0 and 1
ϵ	Arbitrary small constant for numerical converge criteria
σ	Surface tension
σ_0	Standard deviation of the particle density function
ρ	Density
μ	Kinematic viscosity
μ_0	Mean value of the particle density function
$\mu_m^{(i)}$	Sectional moment of the bubble density function of order m
Subscripts	
0	Refers to initial values
b	Refers to the particles or bubbles
i, j, k	Indices for the vector nodes of a staggered grid (see Figure C.1)
I, J, K	Indices for the scalar nodes of a staggered grid (see Figure C.1)
i	Index of the internal variable
n	Index of the particle group
∞	Refers to the bulk of the liquid phase
Notation	
$\dot{X}$	Derivative of property X with respect to time

D. ARTICLES IN PRINT OR SUBMITTED FOR PUBLICATION BASED ON THE DOCTORAL WORK

[1] L. Pilon, A. G. Fedorov, and R. Viskanta, 2000. "Gas diffusion in closed-cell foams", *Journal of Cellular Plastics*, Vol. 36, pp. 451-474.

[2] L. Pilon, A. G. Fedorov, and R. Viskanta, 2001. "Steady-state foam thickness of liquid-gas foams", *Journal of Colloid and Interface Science*, Vol. 242, pp. 425-436.

[3] L. Pilon, A. G. Fedorov, and R. Viskanta, 2002. "Analysis of transient thickness of pneumatic foams", *Chemical Engineering Science*, Vol. 57, pp. 977-990.

[4] L. Pilon, G. Zhao, and R. Viskanta, 2002. "Three-dimensional flow and thermal structures in glass melting furnaces. Part I. Effects of the heat flux distribution",*Glass Science and Technology*, Vol. 75, No. 2, pp. 55-68.

[5] L. Pilon, G. Zhao, and R. Viskanta, 2002. "Three-dimensional flow and thermal structures in glass melting furnaces. Part II. Effects of the presence of batch and bubbles", *Glass Science and Technology*, Vol. 75, No. 3, pp. 115-124.

[6] L. Pilon and R. Viskanta, 2002. "Radiation characteristics of glass containing bubbles", *Journal of the American Ceramic Society*, Vol. 86, No.8, pp. 1313-1320.

[7] A.G. Fedorov and L. Pilon, 2002. "Glass Foams: Formation, Transport Properties, Heat, Mass, and Radiation Transfer", *Journal of Non-Crystalline Solids*, Vol. 311, No.2, pp. 154-173.

[8] L. Pilon and R. Viskanta, 2003. "Solution of the Population Balance Equation by the Modified Method of Characteristics", *International Journal for Numerical Methods in Fluids*, Vol. 42, pp.1211-1236.

[9] L. Pilon and R. Viskanta, 2004. "Superficial gas velocity for onset of foaming", *Chemical Engineering and Processing*, Vol.43, No.2, pp.149-160.

[10] L. Pilon and R. Viskanta, 2004. "Bubble transport and generation in glass melting furnaces. Part II. Numerical Results", *Journal of the American Ceramic Society*, Vol. 336, No.2, pp.71-83.

[11] L. Pilon, A. G. Fedorov, and R. Viskanta, 2004. "Bubble transport and generation in glass melting furnaces. Part I. Mathematical Formulation", *Journal of the American Ceramic Society*,Vol. 336, No.2, pp.84-95..

[12] D. Baillis, L. Pilon, F. Randrianalisoa, and R. Gomez and R. Viskanta, 2004.

"Radiation Characteristics of Fused Silica Containing Bubbles", Journal of the Optical Society of America, A. Vol. 21, No.1, pp. 149-159.

[13] L. Pilon and R. Viskanta. "Apparent radiation characteristics of semitransparent media containing gas bubbles", *Proceedings of the12th International Heat Transfer Conference*, Grenoble, France, August 18-23, 2002, pp.645-650.

VITA

VITA

Laurent Pilon was born in Nantes, France in 1973. He graduated from the Grenoble National Polytechnic Institute, France in 1997 with a Bachelor of Science in Applied Physics (minor in Nuclear Engineering) and a Master of Science in Energy Engineering and Applied Physics. Before starting his doctoral studies in August 1999, he worked for two years for the French Atomic Energy Commission including 16 months in the School of Nuclear Engineering at Purdue University. After his PhD he became Assistant Professor in the Mechanical and Aerospace Engineering Department at the University of California, Los Angeles.